UNIVERSITY OF MINNESOTA

This is to certify that I have examined this copy of a doctoral dissertation by

Bálint Vanek

and have found that it is complete and satisfactory in all respects,
and that any and all revisions required by the final
examining committee have been made.

Gary J. Balas

Name of Faculty Adviser

Signature of Faculty Adviser

Date

GRADUATE SCHOOL

# Control Methods for High-Speed Supercavitating Vehicles

A DISSERTATION
SUBMITTED TO THE FACULTY OF THE GRADUATE SCHOOL
OF THE UNIVERSITY OF MINNESOTA
BY

Bálint Vanek

IN PARTIAL FULFILLMENT OF THE REQUIREMENTS
FOR THE DEGREE OF
DOCTOR OF PHILOSOPHY

Gary J. Balas

June 2008

# Acknowledgements

I am grateful to numerous people who helped my career during the last few years. First and foremost I would like to thank Professor Gary Balas, my advisor for his constant support and his enthusiasm on topics related to control theory and beyond. His mindset greatly influenced my attitude to research and to life. I would also like to thank Professor József Bokor, my former advisor, for introducing me to the interesting world of control theory and for his constant support during my Phd studies.

I am also grateful for my committee members, Professors Tryphoon Georgiou, Roger Arndt and Demoz Gebre-Egziabher not only for serving as a member on my committee but also for helping me along with comments and insight on problems related to my research.

The control lab was a great place to work, due to numerous exceptional colleagues and visitors. I enjoyed the discussions with Tamás, Francesco, Paolo, Paw, Arnar, Rohit and Balázs, they helped me enhancing my knowledge on various topics related to control theory and vehicle dynamics.

My stay in Minneapolis would not be as great as it was without the swimming team, they welcomed me as friend on the first day I went to the swimming pool and helped me to forget all the difficulties I encountered during these years. Of course, I am grateful for the support of my friends and teammates in Hungary, who kept me connected to home. Without them and the will power I got from sports it would have been much more difficult to keep on track with my research.

Finally, I thank to my family for their constant support and love, they inspire me to be brave enough to achieve my dreams.

Hálás szeretettel családomnak.

# Abstract

Supercavitation is an emerging technology that enables underwater vehicles to reach unprecedented speed. With proper design of cavitator attached to the vehicle nose, the vehicle body is surrounded by water vapor cavity, eliminating skin friction drag. This technology offers unprecedented drag reduction, though poses problems for vehicle design. The gas bubble surrounding the hull introduces highly coupled dynamic behavior, representing a challenge for the control designer. Development of stable, controllable supercavitating vehicles requires solution for several open problems. This dissertation addresses the problem of control oriented modeling, stability augmentation, and reference tracking using parameter dependent control techniques for supercavitating vehicles.

The thesis is divided into three parts. A nonlinear dynamical model capturing the most important properties of the vehicle motion is developed from a control design perspective. The model includes memory effects associated with the time evolution of the cavity and uses lookup tables to determine forces.

To aid understanding the cavity-vehicle interaction, a longitudinal control scenario is developed for a simplified longitudinal dynamical model with guaranteed properties. Significant insight is gained on planing behavior and operating envelope using constrained control inputs.

Extending the longitudinal control problem, a linear parameter varying model of the coupled motion is developed to provide a platform for parameter dependent control synthesis. The mathematical model is scheduled with aerodynamic angles, uses steady-state approximation of the cavity, leading to uncertainty in the governing equations. Two Linear Parameter Varying (LPV) controllers are synthesized for the angle rate tracking problem, taking uncertainty into account. One uses traditional decoupled loops for pitch-, roll- and yaw-rate tracking. Ignoring the cross coupling, leads to more tractable subproblems . A controller, taking advantage of the coupling, is also presented in the thesis. The complexity of the coupled dynamics prohibits the synthesis of the controller as a single entity. Several LPV controllers synthesized for smaller overlapping regions of the parameter space are blended together, providing a single controller for the full flight envelope. Time-domain simulations of different vehicle-controller configurations, implemented on high-fidelity simulations, provide insight into the capabilities of the supercavitating vehicle.

# Contents

# List of Tables

# List of Figures

# List of Symbols

| | | |
|---|---|---|
| $x_E, y_E, z_E$ | Vehicle position in the Earth frame | $(m)$ |
| $\psi, \theta, \phi$ | Vehicle Euler angles relative to the Earth frame | $(rad)$ |
| $DCM_{B\rightarrow E}$ | Direction Cosine Matrix between body and Earth frame | |
| $u, v, w$ | Vehicle speed in body frame | $(m/s)$ |
| $p, q, r$ | Vehicle angular rates | $(rad/s)$ |
| $L$ | Vehicle length | $(m)$ |
| $L_{cav}$ | Distance between c.g. and cavitator | $(m)$ |
| $R$ | Body diameter | $(m)$ |
| $\sigma$ | Cavitation number | $(m/s)$ |
| $\mathcal{F}$ | Froude number | |
| $\mathcal{C}_Q$ | Ventillation coefficient | |
| $p_\infty$ | Ambient pressure | $Pa$ |
| $p_c$ | Cavity pressure | $Pa$ |
| $\rho$ | Water density | $kg/m^3$ |
| $V_m$ | Total vehicle speed | $m/s$ |
| $g$ | Gravitational acceleration | $m/s^2$ |
| $d_c$ | Cavitator diameter | $m$ |
| $d_{max}$ | Maximum cavity diameter | $m$ |
| $Q$ | Ventillation flow rate | $m^3/s$ |
| $l_c$ | Cavity length | $m$ |
| $C_D$ | Cavitator drag coefficient | |
| $\alpha_c$ | Cavitator angle-ofattack | $rad$ |
| $R_{cav}$ | Cavitator radius | $m$ |
| $y_c, z_c$ | Cavity centerline body x-axis offset | $m$ |
| $a_{buoy}$ | Buoyancy acceleration on air in water | $m/s^2$ |

| | | |
|---|---|---|
| $\tau$ | Delay in propagation from nose to tail | $s$ |
| $t$ | time | $s$ |
| $\phi_p$ | Angle of the plane of immersion | $rad$ |
| $\phi_i$ | Relative angle of the i-th fin | $rad$ |
| $I_i$ | Relative immersion of the i-th fin | |
| $r_s$ | Fin length | $m$ |
| $r_{piv}$ | Fin pivot point offset | $m$ |
| $h$ | Immersion depth | $m$ |
| $\alpha_p$ | Immersion angle | $rad$ |
| $\alpha$ | angle-of-attack | $rad$ |
| $\beta$ | Sideslip angle | $rad$ |
| $\delta_{cav,y}$ | Cavitator yaw deflection | $rad$ |
| $\delta_{cav,p}$ | Cavitator pitch deflection | $rad$ |
| $\delta_{fin,i}$ | i-th find deflection | $rad$ |
| $C_{F_{x,i}}$ | x directional force coefficient in the i-th fin | |
| $C_{M_{x,i}}$ | x directional moment coefficient in the i-th fin | |
| $\varepsilon$ | Nominal cavity gap $(R_c - R)$ | $m$ |
| $m$ | Vehicle mass | $kg$ |
| $I_{xx}$ | Inertia around the x-axis | $kgm^2$ |
| $x_f$ | Fin pivot c.g. offset | $m$ |
| $\alpha_s$ | Fin sweepback angle | $rad$ |
| $p_{ref}$ | Roll rate reference command | $rad/s$ |
| $A, B, C, D$ | State space matrices | |
| $\rho(t)$ | Parameter vector | |
| $\mathcal{P}_1$ | First scheduling parameter | |
| $\mathbb{R}$ | Field of real numbers | |
| $\bar{\nu}_i, \underline{\nu}_i$ | Upper, lower rate bound on the i-th parameter | |
| $G_\rho$ | LPV system | |

# Chapter 1

# Introduction

The velocity of conventional manned or unmanned underwater vehicles is limited by the drag introduced by skin friction, interaction of liquid with the vehicle surface. Since drag increases exponentially with velocity, the amount of thrust propelling an underwater vehicle has to increase exponentially to achieve increase in speed, as shown on Figure 1.1. Since new technologies in underwater and rocket propulsion does not offer radical increase in specific impulse, the only way to increase propelling force by increasing the rate of fuel burnt in the engine, which becomes highly inefficient if we consider the decrease in range associated with the higher consumption. Due to this reason, current underwater vehicles are limited to approximately 50 $m/s$. Instead it is more beneficial to reduce the surface area in contact with water. Since the conventional ways of improving propulsion and streamlining the vehicle did not lead to significant speed increase, Russian designers in the 1970s proposed a radically different approach, the surface area of the vehicle in contact with the liquid phase from the vehicle hull was reduced, eliminating skin friction by enveloping the vehicle with a gas bubble. The water vapor cavity generated by *supercavitation* led to the Skhval [3] underwater rocket which can reach speeds up to 100 $m/s$. Supercavitation can drastically reduce the wetted surface area by enveloping the vehicle with gaseous water vapor, leading to an order of magnitude reduction in drag if the body is shaped properly. Research in cavitation was active in the Unites States since the mid 1950's led my Marshall Tulin [6], and the US Navy funded research programs focused on development of supercavitating propellers. The first use of supercavitation for reducing vehicle drag appeared during the

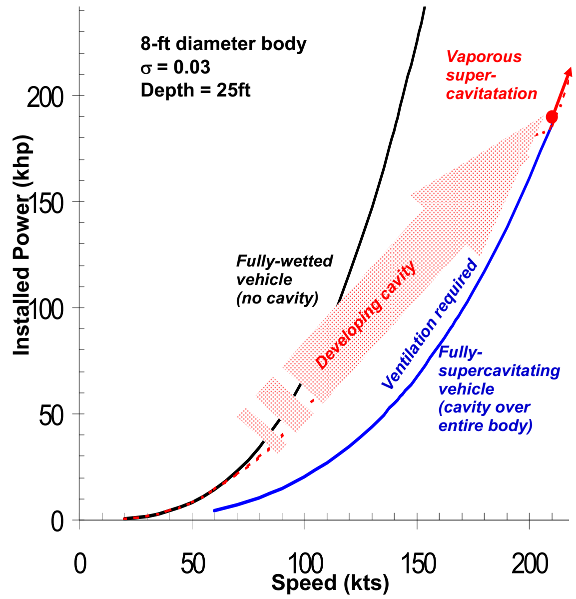


Figure 1.1: Benefit of using supercavitation.

development of the Rapid Airborne Mine Clearance System (RAMICS) in the late 1990's. The U.S. Navy currently has no supercavitating vehicles though it is pursuing two major development programs, the Office of Naval Research (ONR) Supercavitating High-Speed Bodies Program and the Defense Advanced Research Projects Agency (DARPA) Underwater Express Program. The ONR program focuses on developing a counter weapon for the threat of the Russian Skhval (Fig. 1.2). The DARPA Underwater Express Program has a

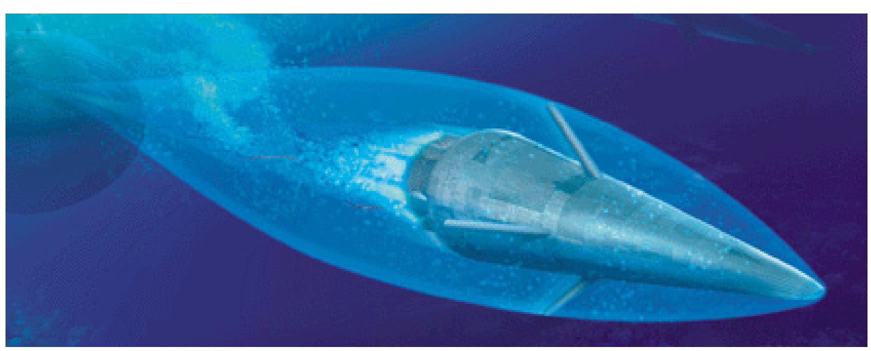

Figure 1.2: The VA-111 Skhval Supercavitating Vehicle Launched from a Submarine (Courtesy: [3]).

different objective, to demonstrate stable and controllable high-speed underwater transport through supercavitation. The intent is to determine the feasibility for supercavitation technology to enable a new class of high-speed underwater craft for future littoral missions that could involve the transport of high-value cargo and/or small units of personnel. The Underwater Express program is a technology development and demonstration program: It will require the investigation and resolution of critical technological issues associated with the physics of supercavitation and culminate in a credible demonstration at a significant scale to prove that a supercavitating underwater craft is controllable at speeds up to 50 $m/s$, which is a significant technological leap compared with the fastest submarine, the Russian Alpha-class, capable of 25 $m/s$.

Although the current focus of research is related to military, several other applications of supercavitation are possible. NASA scientists proposed using supercavitating technology for the exploration of Jupiter's moon, Europa. Magnetic and surface features indicate that this unique water world may contain under ice an ocean more vast than all the seas of Earth combined. It is possible that water, plus energy, plus nutrients kicked up by volcanoes and vents could create life there.

Supercavitating vehicles could also revolutionize ocean farming. A supercavitating torpedo with a mooring line fired down from the water's surface could maintain the force needed to slam an anchor deep into the sea floor, whereas such a remote system in deep seas using existing technology would slow and then simply clunk onto the sediment below. A report by Stanley Associates Inc. and Designers and Planners USA proposed using the technology to moor open ocean platforms for aquaculture instead of using divers or extensive underwater operations as with traditional drag embedment anchors.

Another example of using gas cavity to improve efficiency is under development by Dutch DK Group, who claim 15% fuel reduction on large ocean ships by using the Air Cavity System as seen on Figure 1.3.

As described above it is advantageous to use supercavitation to reduce friction on underwater objects but it is not a widespread method. To better understand the reasons why supercavitation is only emerging recently as a technology to help making underwater vehicles more efficient, some fundamental properties of hydrodynamics, the physics behind supercavitation, have to be reviewed.

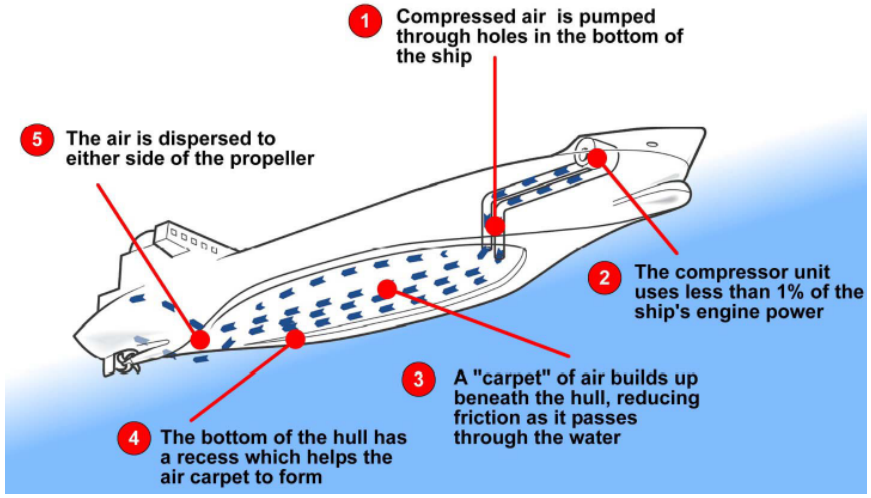


Figure 1.3: The Air Cavity System under development (Courtesy: DK Group).

## 1.1 Cavitation

Cavitation was first studied by Lord Rayleigh in the late 19th century when he considered the collapse of a spherical void within a liquid [7]. When a volume of liquid is subjected to a sufficiently low pressure it may rupture and form a cavity. This phenomenon is termed cavitation inception and may occur behind the blade of a rapidly rotating propeller or on any surface vibrating underwater with sufficient amplitude and acceleration. Other ways of generating cavitation voids involve the local deposition of energy such as an intense focussed laser pulse (optic cavitation) or with an electrical discharge through a spark. Vapor gasses evaporate into the cavity from the surrounding medium, thus the cavity is not a perfect vacuum but has a relatively low gas pressure. Such a low pressure cavitation bubble in a liquid will begin to collapse due to the higher pressure of the surrounding medium. As the bubble collapses, the pressure and temperature of the vapor within will increase. The bubble will eventually collapse to a fraction of its original size, at which point the gas within dissipates into the surrounding liquid via a rather violent mechanism, which releases a significant amount of energy in the form of an acoustic shock-wave and as visible light. At the point of total collapse, the temperature of the vapor within the bubble may be several thousand kelvin, and the pressure several hundred atmospheres.

The physical process of cavitation inception is similar to boiling. The major difference

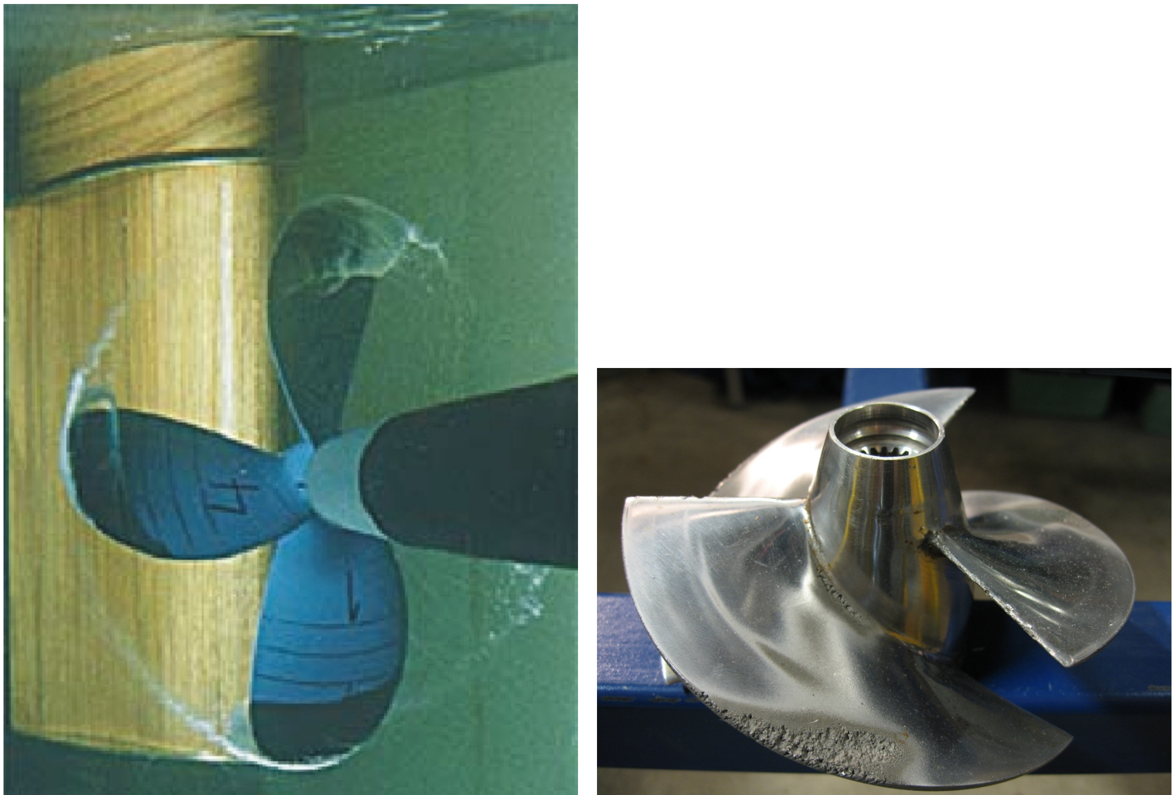

(a) Cavitating propeller. (b) Propeller damaged by cavitation.

Figure 1.4: Cavitation examples

between the two is the thermodynamic paths which precede the formation of the vapor. Boiling occurs when the local vapor pressure of the liquid rises above its local ambient pressure and sufficient energy is present to cause the phase change to a gas. Cavitation inception occurs when the local pressure falls sufficiently far below the saturated vapor pressure, a value given by the tensile strength of the liquid.

In order for cavitation inception to occur, the cavitation “bubbles” generally need a surface on which they can nucleate. This surface can be provided by the sides of a container or by impurities in the liquid or by small undissolved microbubble within the liquid. It is generally accepted that hydrophobic surfaces stabilize small bubbles. These pre-existing bubbles start to grow unbounded when they are exposed to a pressure below the threshold pressure, termed Blake’s threshold.

Cavitation is an undesired phenomena in most engineering applications. It can limit the efficiency of propellers, turbine blades have to run at lower speeds, and properly maintained due to the erosion made by collapse of cavity bubbles, as seen on Figure 1.4. For general information on the subject refer to [8].

## 1.2 Supercavitation

A supercavitating object uses the cavitation phenomena in a larger, and sustained manner. The main features of a supercavitating object are a sharp leading edge (or nose), typically flat with sharp edges, and streamlined, hydrodynamic and aerodynamic shape. When the object is traveling through water at high speeds, the nose deflects the water outward so fast that the pressure of the fluid aft of the nose drops (Bernoulli's principle). The water vaporizes when the pressure drops below the vapor pressure. The pressure of the surrounding water forces the bubble to collapse, which takes time. Hence, the nose opens an extended bubble of water vapor behind it. Given sufficient speed, or the injection of gas into a partially-developed bubble, the cavity can extend to envelop the entire vehicle body.

Recent developments in supercavitation, motivated by the demand for high-speed underwater vehicles [3, 9], has generated renewed interest in cavitation. Supercavitation can provide significant benefit for drag reduction by maintaining a stable, single vaporous bubble around the vehicle resulting in extended velocity and range of underwater applications.

The fundamental problems of maintaining supercavitation are solved. The current challenge is to fuse the components into a vehicle which can be operated on a day-to-day basis, not just only demonstrate technology which can be sustained under laboratory environment with several limitations. The next step of developing a supercavitating vehicle is using feedback control to augment stability and steer the vehicle to successfully execute its tasks. Vehicle control is challenging due to the complex nonlinear vehicle dynamics interacting with the gas filled cavity, the sensors are severely limited due to operation under the water. The wetted surface creating significant drag is desired to be low, only the cavitator must be in contact with the water, hence all other control actuators must have limited control authority to keep the overall drag low. Moreover the control actuators have to keep the cavity intact. For these reasons even the optimal vehicle configuration is under analysis. Different set of control actuators can produce distinctive control action leading to diverse platforms for sensors. This is a fundamental problem, since most sensors including the sonar and pressure probes must be in contact with water and have to be operated under low noise environment.

(a) Propeller shaped to use cavitation.

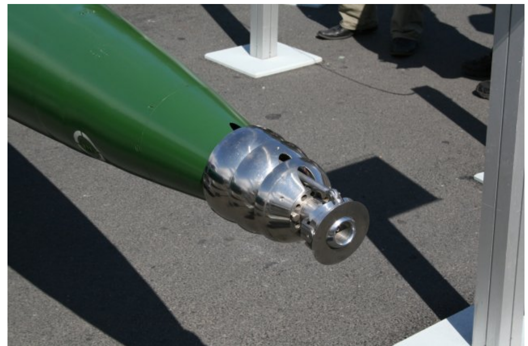

(b) Nose section of the Shkval-E (Courtesy: Wikipedia).

Figure 1.5: Supercavitation examples

# Chapter 2

# High-Speed Supercavitating Vehicle

The present dissertation focuses on the challenges associated with the Office of Naval Research (ONR) Supercavitation Science and Technology Program [10]. Objectives of the program are understanding and quantifying the critical phenomena governing the guidance, stability, control and maneuvering of supercavitating, high-speed, underwater vehicles. The overall goal is developing a supercavitating vehicle which accurately tracks trajectories. For this reason, the system description, equations-of-motion and the control results are applicable for a fairly general vehicle. Beyond the purpose of aiding the design of a prototype vehicle manufactured by Applied Research Laboratory at Penn State University, the goal of this thesis is to provide general control synthesis guidelines for highly-coupled nonlinear underwater vehicles via the understanding of limitations imposed by the vehicle architecture.

Before analyzing the individual vehicle components it is beneficial to review a few general problems associated with the overall objective of supercavitation. Important trade-offs can be understood with placing each vehicle component in the context of the associated challenges.

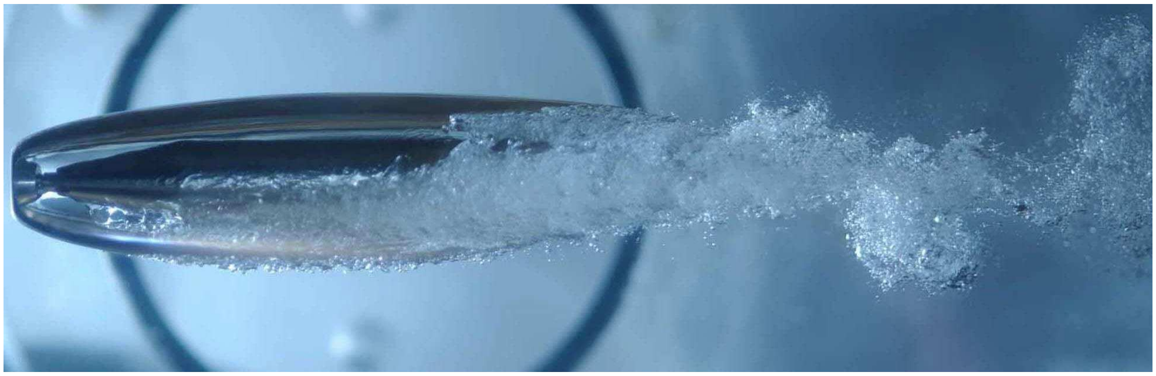

Figure 2.1: Supercavitation water tunnel test at Saint Anthony Falls Laboratory (UMN).

## 2.1 Vehicle Concept

The cavitator diameter, drag coefficient and forward velocity determine the dimensions of the cavity bubble in which the body must fit. Any other contact with fluid phase is undesirable from a drag reduction standpoint. In this vehicle configuration, with no additional lift components, the vehicle is unstable inside the cavity. One means to address the vehicle stability involves the body itself. When the aft end penetrates the cavity surface, a large restoring force, known as *planing*, directs the vehicle back inside the cavity. Planing can be used as a support force to improve maneuverability and eliminate the need for fins. This leads to a reduced cost and system complexity, but it can result in limit cycle oscillations and increased drag.

Three dimensional trajectory tracking requires cavitator actuation in two degrees-of-freedom. In absence of fins planing has to support the vehicle weight, to balance the moment and stabilize the pitch motion. Since planing force has oscillatory nature the cavitator has to constantly counteract. This is undesired, since it focuses all important tasks into the most complex part of the vehicle to the cavitator.

If planing does not support the vehicle weight, then fins at the aft end have to provide a lift force to balance the moment and stabilize the pitch motion and may be used for guidance level control tasks. While the contact of the hull with the fluid can be avoided. Fins can provide roll control, unlike using only cavitator for control. The drawback of using fins from a control design point of view is the added coupling between the cavity and vehicle. Since the cavity shape, which influences planing, and the immersion of fins, is a function of the past vehicle path. Due to this property the cavity-vehicle interaction has memory effects. Note that even when fins are used for control planing can occur, since the gap between the body and the cavity wall is on the order of $1 - 5$ $cm$ at vehicle speeds between 75 to 100 $m/s$. Compared to the body length of $1 - 2$ meters the small cavity clearance poses a challenging task for control design.

The Russian navy has a supercavitation vehicle, the Shkval, currently in operation [3], and the German Diehl BGT Defence has also demonstrated successful stable, straight and curved path maneuvers with the Barracuda [11] supercavitating vehicle. Despite these successes, active three dimensional trajectory tracking problem for supercavitating vehicles is an open problem in the literature. The Shkval use open-loop control algorithms, which cannot provide precise steering due to uncertainties in system parameters and outside disturbances. Since the vehicle with most forces generated on the cavitator tends to be unstable, open-loop stability, with no active feedback control, is achieved by passive side-skids used as dampers. The Barracuda has a flexible nose cone which provides steering. The current focus of Diehl BGT's research program is on stabilization, guidance and maximization of agility, which is an important objective for engaging rapidly moving underwater targets. Active control has the potential advantage of handling open-loop unstable plants providing more freedom for optimizing the hydrodynamics of the body and enable the required maneuverability.

Significant research on supercavitation vehicle control has been done in the past years. It has focused on the use of linear regulators [12–15]. These model-based designs rely on linearized dynamics around operating points. None of these approaches provide a planing-free operation which is a potential requirement in the future Underwater Express program [9]. Other control approaches, using nonlinear techniques [16, 17] are in the early development phase. Hence there are great opportunity for the development of control algorithms to accurately and robustly control a supercavitating vehicle.

The vehicle configuration used in this thesis is similar to existing underwater vehicles with two set of control surfaces, one in front of the c.g. the other behind. The current layout uses an actuated cavitator, and four actuated fins, see Fig. 2.2. The cavitator may have a single degree of freedom in pitch, this would require the vehicle to use bank-to-turn maneuvering, or a two-degree of freedom cavitator which would allow skid-to-turn maneuvers. The later configuration is more advantageous from control design perspective since, disturbance attenuation in yaw channel is difficult with only fin control inputs on the lateral dynamics (see Chapter 6). The vehicle exhibits non-minimum phase response on the yaw dynamics when only fin control inputs are available, severely restricting the achievable control bandwidth and disturbance attenuation properties. Although initial results showed that tail-slapping could be used to provide the balancing moment at the aft-end it is not possible to completely remove the fins from the vehicle. They are required in the subtle initial phase, since the cavity has to fully develop after the launch. Tail slapping creates drag, similar to fins, and result in oscillatory behavior, hence it can be more advantageous to use small fins as seen on Figure 2.2. With the minimal disadvantage of increased drag, oscillatory motion can be attenuated, providing a lower noise level platform for the inertial measurement unit, and for the homing sensors.

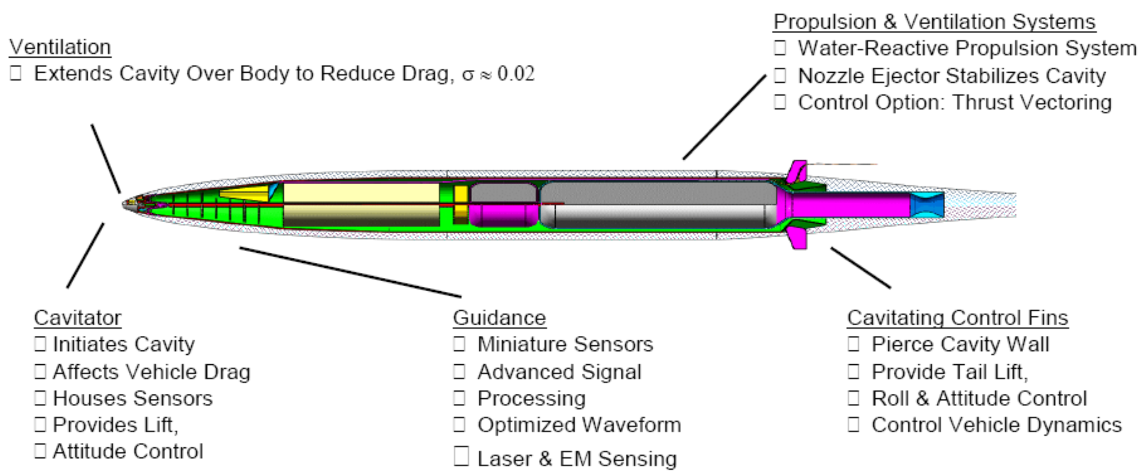


Figure 2.2: Vehicle components of the ONR test bed.

### 2.1.1 Body

The body is assumed to be built by three sections, a conical first section holding the cavitator and providing low drag coefficient in the initial fully wetted phase, for simplicity. A slender cylindrical body houses the main components of the vehicle, while a smaller diameter conical section accounts for the nozzle. The geometric components with the control effectors surrounded by the cavity can be seen on Figure 2.3.

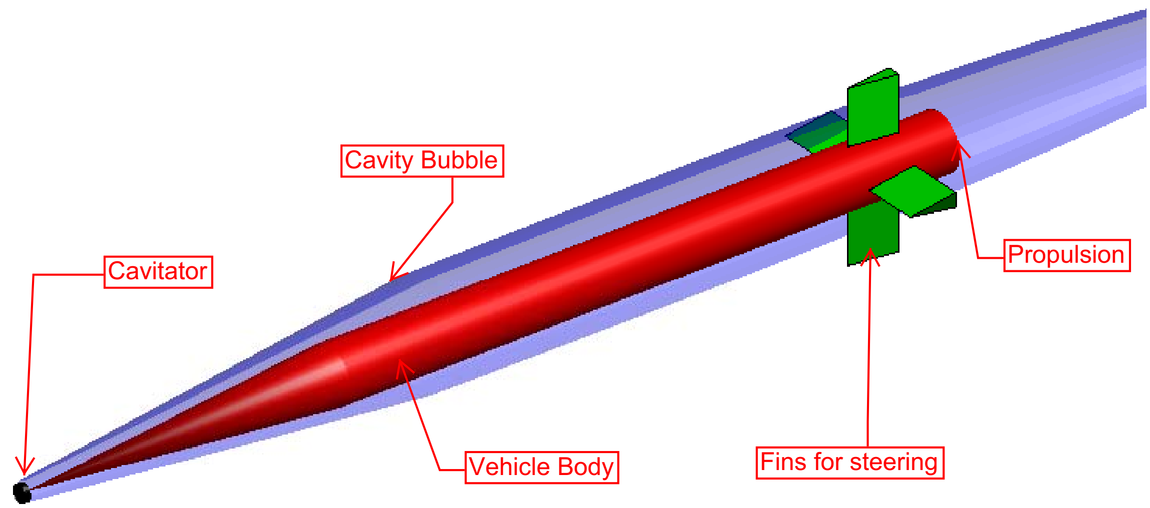


Figure 2.3: Vehicle components of the ONR test bed.

### 2.1.2 Cavitator

The cavitator is the most critical part of the supercavitating vehicle. It generates the cavity, provides control forces, and supports the ventilation gas flow rate. The cavitator is also the only part of the vehicle which is continuously in contact with water. The selection of disk cavitator might not be the ideal choice for all requirements, especially due to limited surface area for sensors and low lift coefficient at moderate angles-of-attack. However the current study does not consider these additional requirements and only focuses on control design, hence the disk cavitator is sufficient for control purposes. It is important to notice that the cavitator actuator has rate and deflection limits, which restricts the achievable level of performance in closed loop control.

### 2.1.3 Fins

Four swept back, wedge shaped fins at the aft end of the vehicle are used for control. The importance of these surfaces are obvious, since supercavitating vehicles have to provide the necessary control forces with the small portions of body in contact with the liquid.

Conventional underwater vehicles operate under the influence of buoyancy, and vortex shedding helps providing forces during maneuvers. The unique features influencing the forces acting on the fins include not just only the presence of cavity during normal flight, but also the transition from fully wetted to supercavitating condition during launch. The fins are individually actuated around rotation axis, no elevator or rudder coupling is enforced among them to be able to account for asymmetric immersion on different sides. A CFD database is used to calculate the forces on each individual fin. The database accounts for the partial cavity developing on the suction side of the fin, forming a supercavity at higher angles of attack, though the data does not consider the hysteresis effect [18], that developed supercavity detaches at lower angle of attack then it is formed. It is also assumed that the fins have rate and deflection limits.

### 2.1.4 Cavity

Behavior of the cavity plays a central role in the vehicle dynamics. It causes the dynamical system to be highly nonlinear, and depend on the history of the vehicle motion. The interaction of the vehicle with the cavity is via the fins and via afterbody contact with the liquid phase. The offset between the cavity centerline and the body $x$-axis determines the immersion of the fins, which changes as the vehicle follows non-steady maneuvers, continuously influencing the control authority on the fins. Afterbody planing have a hybrid nature, it does not always appear, it is present when the tail-cavity offset is sufficiently high and the surface of the body is in contact with the water. Then planing exerts a high impulsive force to direct the tail back to the cavity.

The cavity closure zone influences both planing and fin immersion is the most difficult problem when describing the cavity shape though it is out of the scope of this thesis. Cavity self oscillation can happen in the zone where the gas cavity transitions to liquid even when the vehicle is assumed to travel straight and level with constant speed. These oscillation becomes more significant when the cavity is ventilated, as high gas flow rates can destabilize the cavity, making fin immersion and planing rapidly changing and highly uncertain.

There are four different cavity closure models that have been postulated [6]:

- *Ryabushinsky* scheme: A cavity is closed on the "image" of the body placed in the closure region so that the streamlines close smoothly onto this image.

- *Zhukovsky-Roshko* solves the closure problem by satisfying the dynamic free surface condition only up to a certain point on the free streamlines and then somehow continuing these streamlines to downstream infinity, thus simulating a wake extending to infinity. This is known as the “open-wake model”. The cavity terminates on a surface perpendicular to the flow.
- The *reentrant jet* model, which was first formulated by Kreisel (1946) and Efros (1946). In this model, a jet flows into the cavity from the closure region. Thus the rear stagnation point, has been shifted off the free surfaces into the body of the fluid. One of the motivations for the model is that reentrant jets are often observed in real cavity flows. In practice the jet impacts one of the cavity surfaces and is reentrained in an unsteady and unmodeled fashion.
- Two additional models for planar, two-dimensional flow were suggested by Tulin. In these models, termed the “single spiral vortex model” and the “double spiral vortex model,” the free streamlines terminate in a vortex.

Another difficulty not elaborated in this thesis is the interaction of rocket plume with the cavity closure. Since the cavity closure has influence on the entire cavity bubble it is important to investigate the effects of this interaction, but in the thesis it is assumed the exhaust gas has no influence on the vehicle and on the cavity diameter and the cavity terminates smoothly according to the Ryabushinsky scheme.

### 2.1.5 Critical Technologies

The main objective of the vehicle is to follow reference maneuvers with high precision. This task poses difficulties for the inner-loop control due to the complex vehicle dynamics. The guidance level control have to address the challenges of sensing under water, since the amount of information on the surrounding environment is limited. Conventional underwater vehicles use sonars for guidance, which uses acoustic signals, but the cavity has high self-noise level and the gas layer around the vehicle limits the place ment for sonar sensors. One of the key challenges facing the development of supercavitating vehicles is to provide a platform for homing, using reliable navigation solution. This means that the control has to account for providing smooth flight, with the absence of high noise tail slapping.

For the initial phase of the project normal rocket propulsion is used to propel the vehicle, without thrust vectoring. The drawback of using conventional propulsion is the vehicle have to carry the oxidizer onboard, hence the specific impulse is not maximized. The Shkval mentioned above, uses rocket propulsion and has only 7 $km$ range. The proposed alternative, water reactive propulsion, uses seawater for oxidizer, improving the efficiency of propulsion. Another advantage of water reactive propulsion is using the byproduct of reaction, hydrogen, to ventilate the cavity. It uses aluminum as fuel reacting with the high velocity radially injected seawater, melting and breaking the solid oxidizer. The required water is obtained via inlets on the cavitator, which can provide enough flow rate to support the reaction and augment thrust, but assign another task for the cavitator and reduces its control authority.

# Chapter 3

# Nonlinear Equations-of-Motion of the Supercavitating Vehicle

The dynamical model of a high-speed supercavitating vehicle has been previously described in several articles [1,15]. A feedback control oriented model is developed in this thesis, based on the models described in [1,4,15] and several recent results in hydrodynamics [19–21]. A six degrees-of-freedom motion model of the vehicle is derived that approximates the cavity vehicle interaction with a simple bubble model, while refines the planing equations with relative velocity dependent "dynamic-planing" [20,22]. The unique aspect of the proposed model is it neglects the complete time evolution of the cavity and only assumes contact with the liquid phase in the vicinity of the fins at the transom region. Shallow planning is assumed, while the governing equations exhibit delay-differential properties important to account for memory-effect in the propagation of the cavity shape.

The specific vehicle dimensions capture the characteristics of the test vehicle developed by Applied Research Lab at Penn State University [23]. Additional models have been developed [1,4,15] which provide accurate description of the vehicle dynamics. The present model is different from them in the aspect of being control oriented. The equations are organized in state space form, to serve as a platform for further control design oriented tasks like trim and linearization. The chapter is divided into two parts, the first section on kinematics places the vehicle into the Earth fixed reference frame and describes the vehicle motion relative to the surrounding environment. The second section on dynamics focuses on kinetics, the response of the vehicle for outside influences, forces and moments acting on the body, leading to translational and angular acceleration. The kinematic equations have direct coupling via the bubble dynamics with the kinetics as described later, which makes the equations-of-motion unique, different from air or ground vehicles.

## 3.1 Kinematics

The definition of coordinate systems and degrees of freedom is fundamental for describing the equations of motion. Since the vehicle has several moving components and the time evolution of the cavitator position is required to describe the cavity shape, several relative coordinate frames are defined. The states associated with kinematics are described in the Earth fixed North-East-Down (NED) frame. Position coordinates measured in meters are $x_E$, $y_E$, and $z_E$ in the Earth frame (see Fig. 3.1), and in the sequence of rotation $\psi$ yaw angle, $\theta$ pitch angle, and $\phi$ roll angle in radians describe the relative attitude.

### 3.1.1 Orientation of the Vehicle

The HSSV Vehicle is considered to be a rigid body, hence six degrees of freedom are required to describe its position and orientation. All motions are relative to the Earth fixed inertial coordinate frame (Fig.3.1). The time evolution of motion requires the definition of an inertial frame. The origin of the body coordinate frame is measured in meters, and is located at $X_E = [x_E; y_E; z_E]$ distance from the origin of the inertial frame. The vehicle body is described by three angles, measured in radians: $\psi$ yaw angle, $\theta$ pitch angle and $\phi$ roll angle. The inertial coordinate system is, by convention [24], chosen to be the North-East-Down (NED) frame centered at any conveniently chosen point as shown on Figure 3.1, with $z_E$ measuring the depth under see level for simplicity. To simplify the derivation of the equations-of-motion the body coordinate system is placed at the center of gravity, with $x$ axis pointing towards the vehicle nose, $y$ pointing in starboard direction and $z$ in nominal level flight pointing down, according to right hand rule. The position and orientation of the vehicle is determined by the position coordinate $X_E$ and the direction cosine matrix $DCM_{B\rightarrow E}(\psi, \theta, \psi)$ (Eq.3.7), connecting the Earth and body coordinate frames. The Euler angles are denoted by $\psi$ (heading), $\theta$ (attitude) and $\phi$ (bank), using the aerospace standard

$3-2-1$ rotation sequence [25]. First, the position of the HSSV with respect to the Earth is determined using the navigational equations:

$$\dot{x}_E = u\cos\psi\cos\theta + v[-\cos\phi\sin\psi + \cos\psi\sin\phi\sin\theta] \\ + w[\sin\phi\sin\psi + \cos\psi\cos\phi\sin\theta] \tag{3.1}$$

$$\dot{y}_E = u\sin\psi\cos\theta + v[\cos\phi\cos\psi + \sin\psi\sin\phi\sin\theta] \\ + w[\sin\phi - \cos\psi + \cos\psi\sin\phi\sin\theta] \tag{3.2}$$

$$\dot{z}_E = -u\sin\theta + v\cos\theta\sin\phi + w\cos\phi\cos\theta \tag{3.3}$$

where $u, v, w$ $[m/s]$ are the velocities measured in the body-frame, as described in Section 3.2.

The propagation of Euler angles is given through the differential equations defined by the body angle rates $p, q, r$ expressed in $rad/s$ (described in Section 3.2) denoting roll, pitch and yaw rates respectively:

$$\dot{\phi} = p + \tan\theta[\sin\phi q + \cos\phi r] \tag{3.4}$$

$$\dot{\theta} = \cos\phi q - \sin\phi r \tag{3.5}$$

$$\dot{\psi} = [\sin\phi q + \cos\phi r]\frac{1}{\cos\theta} \tag{3.6}$$

Forces act at different location on the body and their location relative to the center-of-gravity (c.g.) must be defined. The cavitator pivot point, assumed to be the center of pressure is located $L_{cav}$ distance in positive $x$ direction on the body $x$-axis. The overall length of the body is $L$, hence the distance of the tail from the c.g. is $L - L_{cav}$ in negative $x$ direction. The circular edge of the tail is $R$ distance from the $x$ axis. Every point $p$, $X_p$ distance from the c.g. on the vehicle can be described in the inertial frame. The transformation between the Earth and the body frame is defined with the direction cosine matrix (DCM):

$$DCM_{B\rightarrow E}(\psi,\theta,\psi) = \begin{bmatrix} c\psi c\theta & s\psi c\theta & -s\theta \\ -s\psi c\phi + c\psi s\theta s\phi & c\psi c\phi + s\psi s\theta s\phi & c\theta s\phi \\ s\psi s\phi + c\psi s\theta c\phi & -c\psi c\phi + s\psi s\theta c\phi & c\theta c\phi \end{bmatrix} \tag{3.7}$$

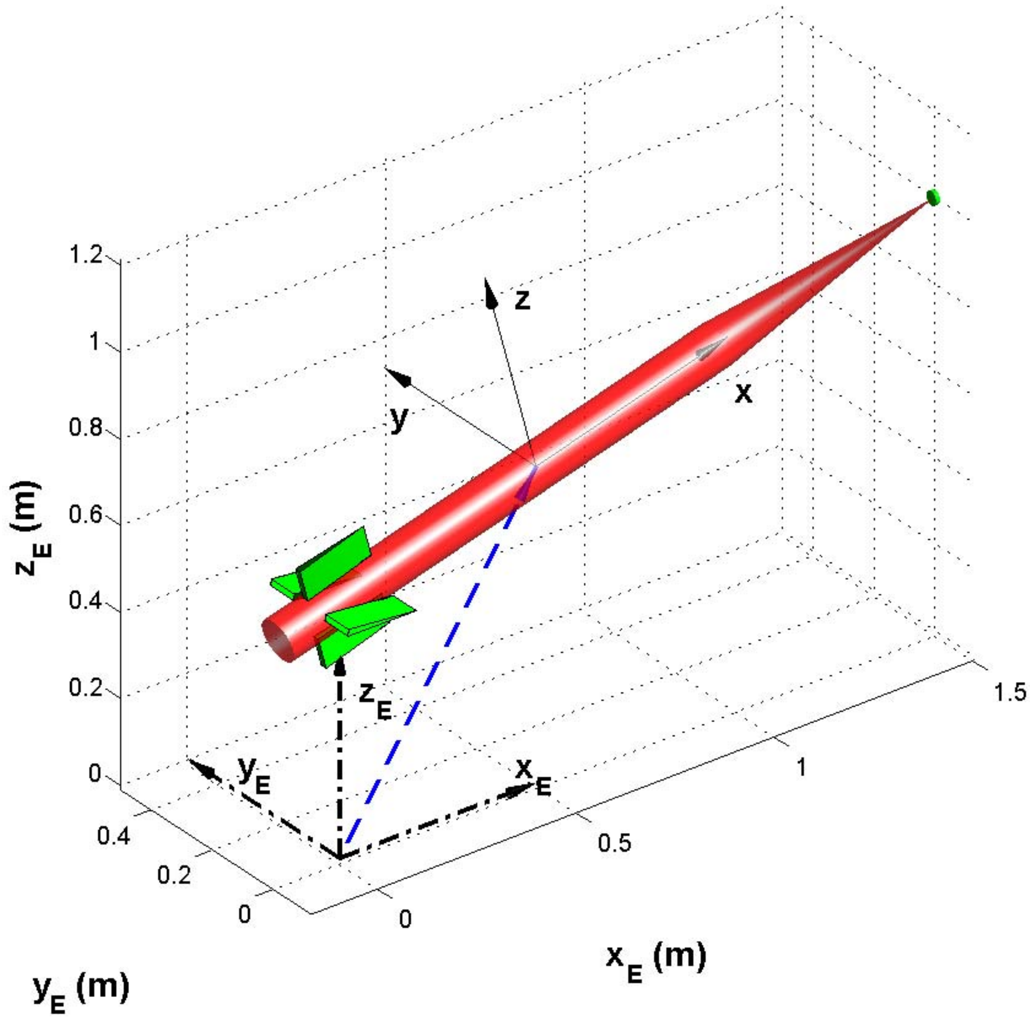


Figure 3.1: Distance between Earth centered (dash-dotted) and Body (solid) coordinate systems.

Every point $p$ on the vehicle with position $X_p$ relative to the c.g. is defined in the Earth frame as

$$X_{p,E} = X_E + DCM_{B\rightarrow E}(\psi, \theta, \psi)X_p, \tag{3.8}$$

The velocities of various points of the body are defined as:

$$V_{p,E} = V_E + DCM_{B\rightarrow E}(\psi, \theta, \psi)\omega \times X_p \tag{3.9}$$

$\omega = [p, q, r]^T$ denotes the angular rates.

### 3.1.2 Cavity Model

The cavity is a major component of the vehicle equations-of-motion. The behavior of the gas bubble surrounding the vehicle affects the immersion of the fins and can also lead to afterbody planing. The cavity is coupled with the vehicle motion through memory effect [4, 15]. This alters the cavity shape at the transom region. Due to this coupling behavior, the understanding of cavity-vehicle interaction is of great importance to vehicle stability and control.

A simple supercavity model suitable for time domain simulation and control design is presented. The model neglects several important properties of the cavity. High-fidelity models account for cavity pulsation and cavity closure with slender body theory, boundary-element methods and Reynolds-averaged Navier-Stokes equations. The simplified cavity model provides an accurate description of the time evolution of a quasi-steady cavity for control purposes.

The quasi-steady supercavitating flow parameters important to characterize are cavitation number $\sigma$, cavity Froude number $\mathcal{F}$ and ventilation coefficient $\mathcal{C}_Q$:

$$\sigma = \frac{p_\infty - p_c}{0.5\rho V^2} \tag{3.10}$$

$$\mathcal{F} = \frac{V_m}{\sqrt{g d_c}} \tag{3.11}$$

$$\mathcal{C}_Q = \frac{Q}{V d_c^2} \tag{3.12}$$

$g$ in $m/s^2$ denotes the gravitational acceleration and $\rho$ in $kg/m^3$ is the water density. $p_\infty$ and $p_c$ are the ambient and cavity pressures measured in $Pa$, respectively. The cavitator diameter is $d_c$ measured in $m$, and $V_m$ stands for vehicle velocity in $m/s$. The volumetric rate of the gas measured in $m^3/s$ ventilating the cavity is $Q$. Cavitation number expresses the tendency of cavitation to occur in a flow, hence it is a major quantity governing the cavity dimensions. The Froude number describes the importance of gravity to the flow, and helps characterize the distortion of the cavity from nominally axisymmetrical shape. The ventilation coefficient governs the time evolution of the cavity dimensions as gas is injected to the bubble to maintain the cavity even under non-ideal conditions.

Garabedian [26] provided an approximation of the maximum cavity diameter $d_{max}$ and cavity length $l_c$, which is widely accepted in the current literature to characterize the cavity shape:

$$\frac{d_{max}}{d_c} = \sqrt{\frac{C_D(\sigma, 0)}{\sigma}} \tag{3.13}$$

$$\frac{l_c}{d_c} = \sqrt{\frac{C_D(\sigma, 0)}{\sigma^2} \ln \frac{1}{\sigma}} \tag{3.14}$$

$C_D$ the drag coefficient of the cavitator with flow angle-of-attack $\alpha_c$ is estimated as:

$$C_D(\sigma, \alpha_c) = C_{D0}(1 + \sigma) \cos^2 \alpha_c \tag{3.15}$$

The drag coefficient at zero angle of attack and cavitation number is based on empirical data given in [27].

Most of prior work in time-domain simulation of vehicle dynamics use the approximations for cavity shape derived based on low-order potential flow by Münzer and Reichardt [28]:

$$R_c(L) = \frac{d_c}{2} \left[ 1 - \left( \frac{L}{L_{max}} \right)^2 \right]^{1/2.4} \tag{3.16}$$

where $R$ is the cavity radius at archlength $L$ on the cavity centerline. The distortion from nominal shape due to body acceleration and gravity is given by:

$$y_c(L) = \mp \frac{d_c}{\mathcal{F}^2} \frac{\dot{v}}{g} \left( \frac{L}{d_c} \right)^2 \tag{3.17}$$

$$z_c(L) = \frac{d_c}{\mathcal{F}^2} \frac{\dot{w} \pm g}{g} \left( \frac{L}{d_c} \right)^2 \tag{3.18}$$

where $y_c$ and $z_c$ in meters is the offset of line of centers from the body centerline axis at distance $L$ backwards from the cavitator. The above equations describe the cavity shape in a fairly precise manner in steady-state conditions, however if the vehicle is exposed to disturbances and excitation on the timescale of the delay associated with the propagation of flow from cavitator to tail, then this description becomes obsolete.

A better description is provided by Logvinovich [19], who made the following fundamental observation: “Each cross-section of the cavity expands relative to the path of the body-center almost independently of the subsequent or preceding motion of the body". The cavity model used in this thesis uses the independence principle described by Logvinovich.

Our interest in cavity parameters is limited to the neighborhood of the fins, where planing also occurs. To simplify the equations describing the cavity shape the following constants are defined:

$$\kappa_1 = \frac{2L}{d_c}\left(\frac{1.92}{\sigma} - 3\right)^{-1} - 1 \tag{3.19}$$

$$\kappa_2 = \left(1 - \left(1 - \frac{4.5\sigma}{1+\sigma}\right)\kappa_1^{\frac{40}{17}}\right)^{\frac{1}{2}} \tag{3.20}$$

Using the above expressions, the radius of the cavity measured in meters at L distance from the cavitator according to Logvinovich is:

$$R_c = \frac{d_c}{2}\left(0.82\frac{1+\sigma}{\sigma}\right)^{\frac{1}{2}}\kappa_2 \tag{3.21}$$

The cavity radius is not constant, its rate of contraction is defined at every cavity section. $\dot{R}_c$ measured in $m/s$ describes the rate of expansion or contraction of the cavity, which is important when describing the liquid-vehicle interaction:

$$\dot{R}_c = -\frac{20}{17}\left(0.82\frac{1+\sigma}{\sigma}\right)^{\frac{1}{2}} V \frac{1 - \frac{4.5\sigma}{1+\sigma}\kappa_1^{\frac{23}{17}}}{\kappa_2(\frac{1.92}{\sigma} - 3)} \tag{3.22}$$

The equations for the cavity shape presented in equation (3.21) are valid given that they are evaluated sufficiently far from the cavitator:

$$L > \frac{d_c}{2}\left(\frac{1.92}{\sigma} - 3\right) \tag{3.23}$$

but before the cavity closure. The above expression uses the assumption of the cavitator being a disk, however experimental results suggest that only the drag coefficient and cavitation number determines the cavity shape. Hence the cavity generated by a cone shaped cavitator can be approximated accurately by the equivalent disk cavitator's cavity shape. The cavity shape predicted by Logvinovich is not significantly different from the shape predicted by Münzer and Reichardt as seen on Figure 3.2. The contribution of Logvinovich describing the behavior of the vehicle surrounded by the supercavity is to realize the independence principle, the cavity centerline is solely determined by the past trajectory of the cavitator, which is only modified by buoyancy as the water is more dense than the gas

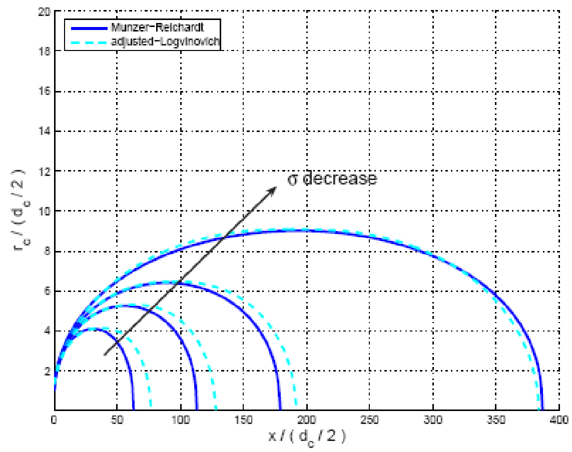


Figure 3.2: Cavity shapes varying with cavitation number $\sigma$ = 0.05, 0.03, 0.02, 0.01 (Courtesy: [4]).

pocket. As a result, disturbances on the cavity caused by motion of the cavitator propagate towards the afterbody with certain time lag, determined by the vehicle speed. The dynamic behavior of the vehicle, including fin immersion and planing, are influenced by not only instantaneous states of the vehicle but also ones under impact of memory effects.

To understand the difference between the two descriptions of cavity time evolution, assume an initial maneuver as a constant rate turn. Then suddenly the vehicle changes to straight and level flight. As seen on Figure 3.3 the two cavity descriptions are different since the Münzer-Reichardt model does not account for time delay to propagate the cavity centerline through the path of the cavitator. The Logvinovich cavity description leads to smoother cavity behavior also, since the whole bubble cannot switch from one shape to another between time instants.

The main difficulty simulating a high-speed supercavitating vehicle is it requires tracking not only current states of the vehicle but delayed states also. Moreover the cavity position has to be defined in the inertial frame, since the two coordinate frames, when the bubble section is generated and when it is in the vicinity of the vehicle tail, are different.

Using the assumption that the vehicle speed is constant over the time evolution of each cavity segment the cavity-tail offset is defined as the difference between the delayed position

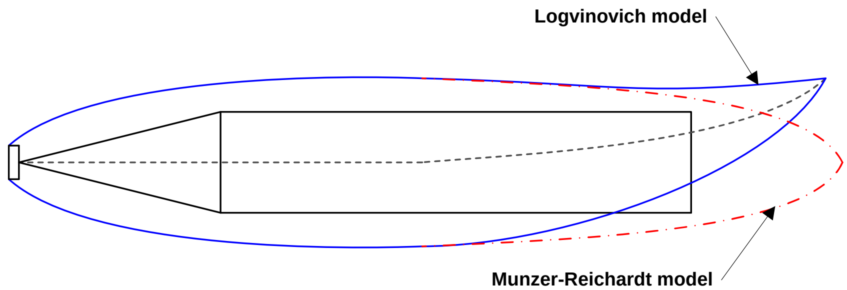


Figure 3.3: Cavity time evolution with Logvinovich and Münzer-Reichardt model.

of the cavitator affected by buoyancy:

$$X_{cav,E}(t-\tau) = X_E(t-\tau) + DCM_{B\to E}(\psi(t-\tau), \theta(t-\tau), \psi(t-\tau)) \begin{bmatrix} L_{cav} \\ 0 \\ 0 \end{bmatrix} + \begin{bmatrix} 0 \\ 0 \\ -0.5a_{buoy}\tau^2 \end{bmatrix} \tag{3.24}$$

where the empirical constant $a_{buoy}$ measured in $m/s^2$ is the effect of buoyancy. The time delay $\tau$ is defined as

$$\tau = L/V_m(t). \tag{3.25}$$

The current position of the tail

$$X_{t,E}(t) = X_E(t) + DCM_{B\to E}(\psi(t), \theta(t), \psi(t)) \begin{bmatrix} L_{cav} - L \\ 0 \\ 0 \end{bmatrix} \tag{3.26}$$

Hence the relationship for cavity-tail offset $X_c$ as seen on figure 3.4 in the body frame is:

$$X_c(t,\tau) = DCM^{-1}_{B\to E}(\psi(t), \theta(t), \psi(t))(X_{t,E}(t) - X_{cav,E}(t-\tau)) \tag{3.27}$$

The same can be done for the offset in the vicinity of the fins $X_f(t,\tau)$, which have slightly different time lag behind the cavitator. These values ($X_c(t,\tau)$ and $X_f(t,\tau)$) are assumed to contain the necessary information calculating the immersion of four fins and evaluate the distance of the vehicle tail from the liquid boundary in the planing equations.

### 3.1.3 Computation of Fin Immersion

The cavity-vehicle offset is determined by the past trajectory of the vehicle as previously discussed. The four cruciformly arranged fins operate partially in the liquid and gas phases.

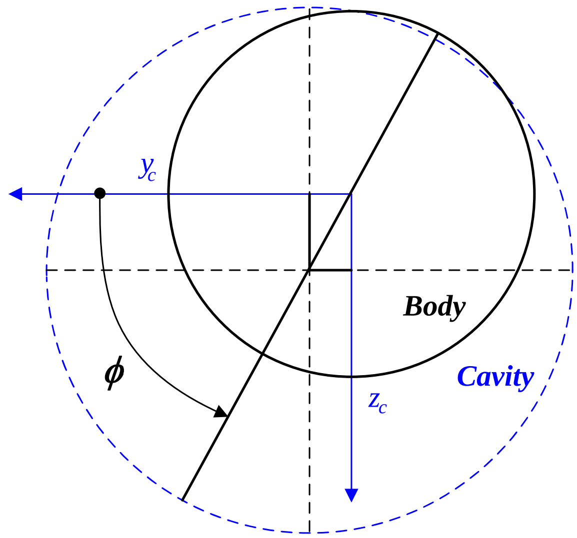


Figure 3.4: Relative position of vehicle tail and cavity centerline.

The forces and moments generated by them are dependent on the delayed position of the cavitator. Figure 3.1.3 shows how the $y_c$ and $z_c$ offset values determine the immersion of each fin. The fins are numbered following the positive direction convention starting with

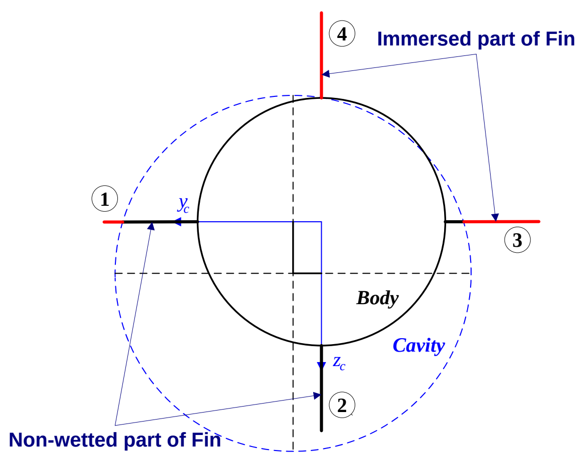


Figure 3.5: Influence of cavity vehicle offset on fin immersion.

the starboard fin at $\phi_1 = 0$ $[deg]$ and each fin is at 90 degrees increment.

$$\phi_i = (i-1) \cdot \pi/2, \ \ i = 1..4 \tag{3.28}$$

Since $X_f$ is already in body frame the equations of relative fin immersion ($I_i$) for fins $i = [1, 2, 3, 4]$ are as follows:

$$I_i(t,\tau) = \begin{cases} \left[(r_s + r_{piv}) - (y_c \cos(\phi_i) + z_c \sin(\phi_i)) - \sqrt{R_c^2 - (y_c \sin(\phi_i) + z_c \cos(\phi_i))^2}\right] / r_s \\ \quad \text{if} 0 \leq I_i \leq 1 \\ 0 \quad \text{if the above expression is negative} \\ 1 \quad \text{if the above expression is greater than 1} \end{cases} \tag{3.29}$$

where $r_s$, measured in meters, denotes the fin span, from root to tip, and $r_{piv}$ stands for the pivot point offset of root from the $x$-axis in meters.

### 3.1.4 Immersion of Afterbody

In normal operation, i.e. gentle maneuvers, the vehicle tail does not come in contact with the fluid phase, based on the design of the cavitator and the selection of the ventilation flow. During aggressive maneuvers or under the influence of large disturbances the vehicle tail can penetrate the boundary of the gas envelope and contact the fluid phase. It is advantageous in certain situations, like when the fins can no longer support the cornering force in a sharp maneuver, to use the restoring force known as planing, acting when the vehicle tail is immersed into the water. The expression for immersion depth is:

$$h(t,\tau) = \begin{cases} \sqrt{y_c^2 + z_c^2} - R_c + R & \text{if} \sqrt{y_c^2 + z_c^2} > R_c - R \\ 0 & \text{if} \sqrt{y_c^2 + z_c^2} \leq R_c - R \end{cases} \tag{3.30}$$

remember $R_c$ is the cavity half-diameter at the location of tail, while $R$ denotes the body radius. The direction of immersion ($\phi_p$) relative to the body $y$-axis, as seen on figure 3.4, is defined as:

$$\phi_p = \tan^{-1}(z_c/y_c) \tag{3.31}$$

which means, at $\phi_p = 0$ the port is going to contact the liquid first. The lateral ($y$) and longitudinal ($z$) component of the planing force is calculated based on this relationship.

## 3.2 Kinetics

Kinetics describes the vehicle motion under the action of forces. The derivatives of the vehicle states are directly related to forces or moments and compose the kinetics states. These states are: $\alpha$ $[rad]$ angle of attack, $\beta$ $[rad]$ sideslip angle, $V_m$ $[m/s]$ total vehicle speed, $p$ $[rad/s]$ roll-rate, $q$ $[rad/s]$ pitch-rate, and $r$ $[rad/s]$ yaw rate. Since control effectors generally produce changes in force or moment, these states of dynamics are the most important when analyzing the influence of control algorithms on the vehicle motion. The kinetic equations of motion, denoting the sum of $x, y$ and $z$ directional forces as $F_x, F_y, F_z$, and the moments around the c.g. $M_x, M_y, M_z$, can be briefly written as:

$$\dot{\alpha} = c_\alpha^2 \left[ \frac{F_x Q_{\alpha\beta}}{m V_m} - p t_\beta \right] + q - s_\alpha c_\alpha \tag{3.32}$$

$$\dot{q} = \frac{1}{I_{yy}} \left[ M_y + (I_{zz} - I_{xx}) r p \right] \tag{3.33}$$

$$\dot{\beta} = c_\beta^2 \left[ \frac{F_y Q_{\alpha\beta}}{m V_m} + p t_\alpha \right] - r - s_\beta c_\beta \tag{3.34}$$

$$\dot{r} = \frac{1}{I_{zz}} \left[ M_z + (I_{xx} - I_{yy}) p q \right] \tag{3.35}$$

$$\dot{V}_m = \frac{1}{m Q_{\alpha\beta}} \left[ F_x + t_\beta F_y + t_\alpha F_z \right] \tag{3.36}$$

$$\dot{p} = \frac{1}{I_{xx}} \left[ M_x + (I_{yy} - I_{zz}) q r \right] \tag{3.37}$$

$$\tag{3.38}$$

The trigonometric functions are abbreviated as follows: $\sin(\alpha)$ is denoted by $s_\alpha$, $\cos(\alpha)$ by $c_\alpha$ and $\tan(\alpha)$ by $t_\alpha$. Similarly $Q_{\alpha\beta}$ stands for $\sqrt{1 + \tan^2(\alpha) + \tan^2(\beta)}$. The vehicle configuration allows four force sources, which produce moments around the c.g. as described in Chapter 2. Three forces are always present: gravity, cavitator force and fin forces, while planing has a hybrid nature, it is switched on and off and a function of vehicle states and the time delay differential equations of the vehicle motion.

### 3.2.1 Gravity

The gravity force has substantial contribution to the equations of motion, unlike in other underwater vehicles, since the body is surrounded by gas and buoyancy is negligible. For simplicity the mass of the vehicle is assumed constant over time. This is a valid assumption since we are interested in stability and control of the vehicle for short duration maneuvers on the order of tens of seconds. The force due to gravity acts through the c.g. and it is constantly pointing in positive $z_E$ direction, towards the center of Earth.

$$F_g = mg \begin{bmatrix} -\sin\theta \\ \sin\phi \cdot \cos\theta \\ \cos\phi \cdot \cos\theta \end{bmatrix} \tag{3.39}$$

As described in Chapter 6, gravity has strong influence on the trim with respect to roll angle, assuming near level flight. Accounting for attitude relative to the Earth is important when calculating the gravity forces.

### 3.2.2 Cavitator Force Model

The cavitator is the fundamental part of the vehicle and is responsible for creating the vapor bubble around the body. Several different type of cavitators are described in the literature, for simplicity and the fact that the cavity dimensions are determined by the cavitator drag coefficient only, a simple disk cavitator is considered in this thesis. For the initial investigation it is assumed the cavitator have pitch and yaw degrees of freedom. Taking the apparent flow angles into account as seen on Figure 3.6, the cavitator forces can be computed as a function of apparent angle of attack $\alpha_{cav}$, apparent sideslip $\beta_{cav}$ and the normal velocity, perpendicular to the disk surface $V_n$.

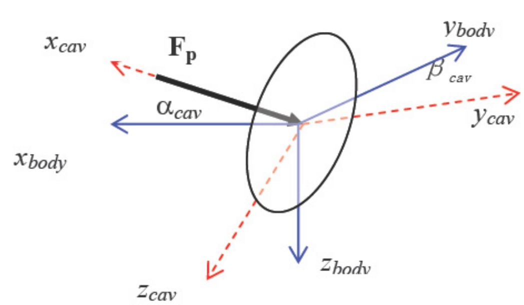


Figure 3.6: Cavitator Free-Body Diagram (Courtesy: [5]).

$$F_p = \frac{1}{2}\rho V_n^2(\pi(d_c/2)^2)C_{D0}(1+\sigma) \tag{3.40}$$

$$\alpha_{cav} = \alpha - \frac{qL_{cav}}{V_m} - \delta_{cav,pitch} \tag{3.41}$$

$$\beta_{cav} = \beta - \frac{rL_{cav}}{V_m} - \delta_{cav,yaw} \tag{3.42}$$

The components of the cavitator force in the body frame are:

$$F_{cav} = \begin{bmatrix} -F_p \cos\alpha_{cav}\cos\beta_{cav} \\ -F_p \sin\beta_{cav} \\ F_p \sin\alpha_{cav}\cos\beta_{cav} \end{bmatrix} \tag{3.43}$$

Since the moments acting about the disk cavitator's center of pressure are assumed to be zero, the moment generated about the c.g. of the cavitator is only due to the offset between the cavitator and the c.g.. Given that the cavitator lies on the body $x$ axis and the moment arm is $L_{cav}$, the moments generated by the cavitator (in body frame) are:

$$M_{cav} = \begin{bmatrix} -L_{cav} \\ 0 \\ 0 \end{bmatrix} \times F_{cav} \tag{3.44}$$

Notice, that to simplify the system equations an assumption was made that the drag coefficient $C_{D0}$ remains constant, then the perpendicular force $F_p$ at fixed velocity is only a function of apparent flow angles $\alpha_{cav}$ and $\beta_{cav}$.

### 3.2.3 Fin Force Model

The four fins are assumed to be cruciformly arranged at the vehicle aft-end. In addition to angular placement, the location of the fins on the torpedo body itself is defined by the variables $x_f$ the location of the pivot point backwards along the $x$-axis and $r_{piv}$ the pivot point offset from the body $x$-axis. Figure 3.7 shows the sign convention of the fin lift forces ($F_{z,fin}$), moments ($M_{y,fin}$), and pitch rotation for each fin. These conventions are necessary to be compatible with the lookup tables computed for a general wedge type fin. The total fin forces require special attention when expressed in the body frame due to separate coordinate frames for each fins.

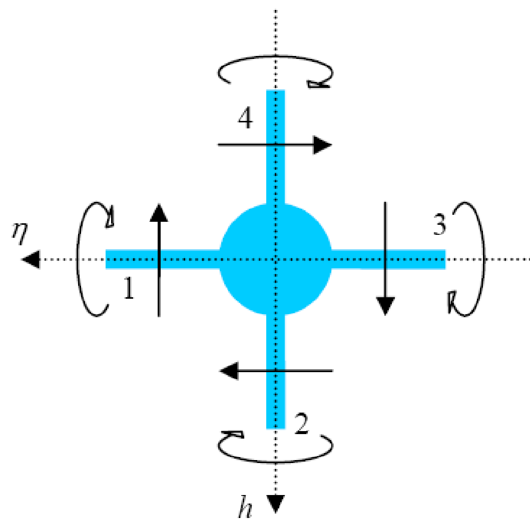


Figure 3.7: Sign conventions of fins (view from nose).

The fin forces are calculated based on a Computational Fluid Dynamics (CFD) database [15]. These forces are function of relative angle-of-attack ($\alpha_{fin}$ $[rad]$), fin sweepback ($\theta_{fin}$ $[rad]$) and relative fin immersion ($I_{fin}$ $[1]$), as shown on Figure 3.8.

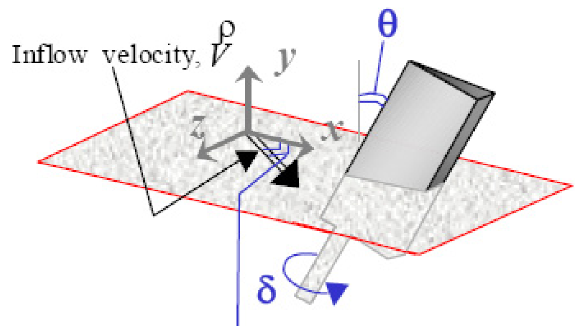


Figure 3.8: Geometry of fin forces.

The apparent sweepback angle $\theta_{fin,i}$ at the fins are:

$$\theta_{fin,i} = \theta_{fin} - \alpha \sin(\phi_i) + \beta \cos(\phi_i),\ \ i = 1..4. \tag{3.45}$$

The center of effect on the submerged portion of each fin is approximated as:

$$x_f(i) = x_{piv} + b_{fin}\frac{1 - I_i}{2}\sin(\theta_{fin,i}) \tag{3.46}$$

$$r_f(i) = r_{piv} + b_{fin}\frac{1 - I_i}{2}\cos(\theta_{fin,i}) \tag{3.47}$$

$$y_f(i) = r_f(i)\cos(\theta_{fin,i}) \tag{3.48}$$

$$z_f(i) = r_f(i)\sin(\theta_{fin,i}) \tag{3.49}$$

$$\tag{3.50}$$

The apparent flow angles are calculated as:

$$\alpha_{b,y}(i) = \alpha + \frac{qx_f(i) + py_f(i)}{V_m} \tag{3.51}$$

$$\alpha_{b,z}(i) = \beta + \frac{-rx_f(i) + pz_f(i)}{V_m} \tag{3.52}$$

and transformed to the appropriate fin reference frame:

$$\alpha_{fg,i} = \alpha_{b,y}(i)\cos(\phi_i) + \alpha_{b,z}(i)\sin(\phi_i) \tag{3.53}$$

The contribution of fin actuation angle is added to calculate the final fin flow angle:

$$\alpha_{f,i} = \alpha_{fg,i} + \delta_{fin,i}\cos(\theta_{fin,i}) \tag{3.54}$$

The force and moment coefficients are obtained from the a lookup table, which uses piece-wise linear approximation between the grid points based on the immersion, sweepback and angle of attack [1].

$$[C_{F_x,i}, C_{F_y,i}, C_{F_z,i}]^T = \mathcal{F}_F(\alpha_{f,i}, \theta_{fin,i}, I_i) \tag{3.55}$$

$$[C_{M_x,i}, C_{M_y,i}, C_{M_z,i}]^T = \mathcal{F}_M(\alpha_{f,i}, \theta_{fin,i}, I_i) \tag{3.56}$$

Numerical values of the force coefficients are presented in Figure 3.9 to better understand the behavior of the fin forces databases. It is noticeable that all graphs corresponding to constant fin immersion have a discontinuous slope. At low angles-of-attack, a small cavity forms on the low pressure side on the fins, while passing a critical value the entire fin is covered with one supercavity. The slope discontinuity on $F_z$ and the non-monotonicity on $F_x$ and $F_y$ are due to this phenomena.

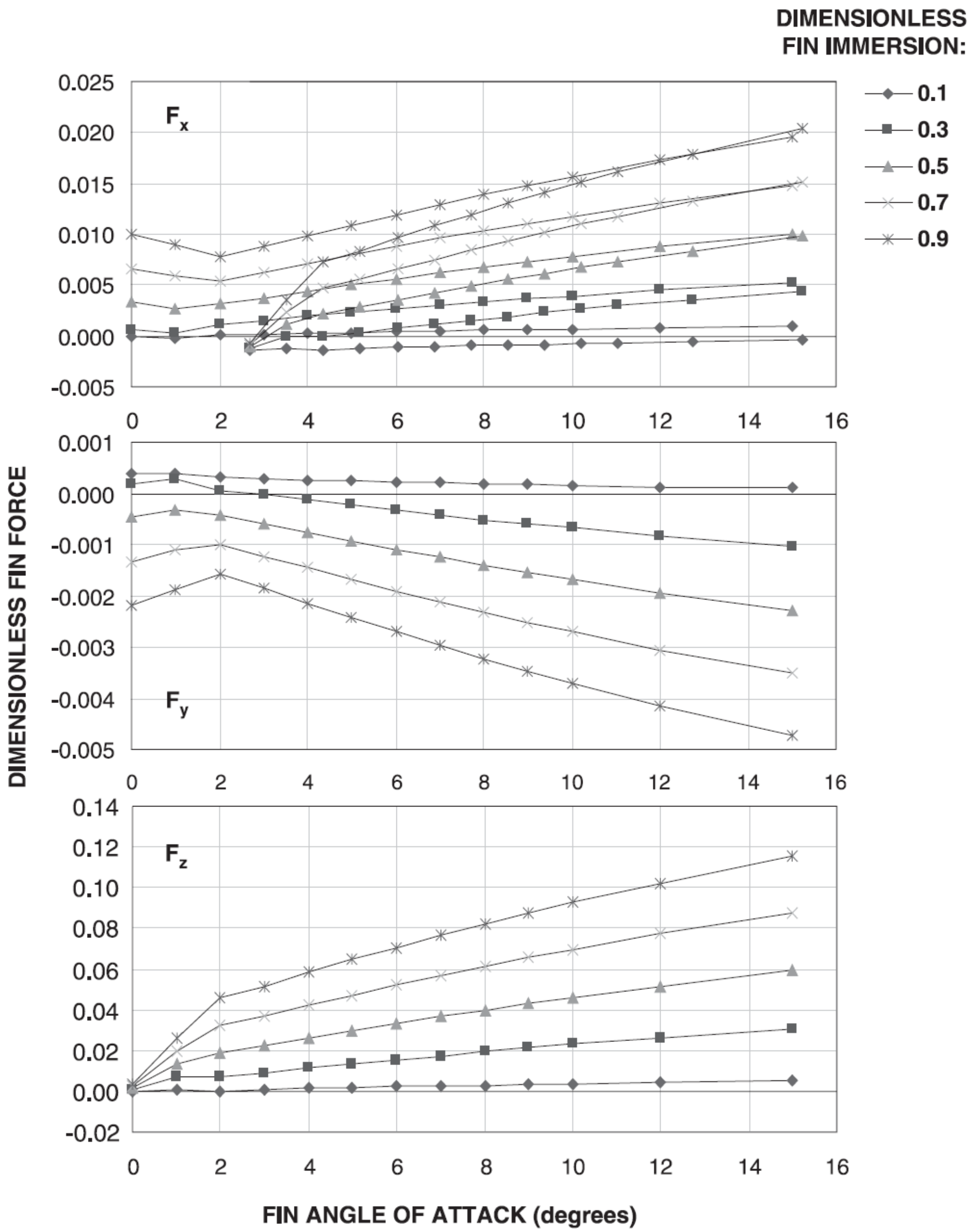


Figure 3.9: Lookup table of fin forces.

The following constant is defined to calculate the fin forces obtained in dimensionless form:

$$\bar{q} = \frac{1}{2}\rho V_m^2 \tag{3.57}$$

The objective is to determine the force and moment acting on each fin:

$$F_{fin,i} = \bar{q} r_s^2 C_{F,i}(\alpha_{fin,i}, \theta_{fin,i}, I_{fin,i}) \tag{3.58}$$

$$M_{fin,i} = \bar{q} r_s^3 C_{M,i}(\alpha_{fin,i}, \theta_{fin,i}, I_{fin,i}) \tag{3.59}$$

Each component is defined around the fins center of effect, in the coordinate system attached to the fins. Hence to obtain their contribution around the c.g. in the body coordinate frame their relative offset and deflection have to be considered.

$$F^x_{fin,body}(i) = -F^x_{fin}(i)\cos(\delta(i)) + F^z_{fin}(i)\sin(\delta(i)) \tag{3.60}$$

$$F^y_{fin,body}(i) = \cos(\phi(i))(F^y_{fin}(i)) + \sin(\phi(i))(-F^x_{fin}(i)\sin(\delta(i)) + F^y_{fin}(i)\cos(\delta)) \tag{3.61}$$

$$F^z_{fin,body}(i) = -\sin(\phi(i))(F^y_{fin}(i)) + \cos(\phi(i))(-F^x_{fin}(i)\sin(\delta(i)) + F^y_{fin}(i)\cos(\delta)) \tag{3.62}$$

$$\tag{3.63}$$

The same is true for the moments, while the forces have also contribution around the c.g. which is expressed as:

$$M^x_{fin,body}(i) = -M^x_{fin}(i)\cos(\delta(i)) + M^z_{fin}(i)\sin(\delta(i)) - F^y_{fin,body}(i) r_f(i) \tag{3.64}$$

$$\begin{aligned} M^y_{fin,body}(i) = {} & \cos(\phi(i))(M^y_{fin}(i)) + \sin(\phi(i))(-M^x_{fin}(i)\sin(\delta(i)) + M^y_{fin}(i)\cos(\delta)) \\ & + \cos(-\phi(i))(x_f(i)F_z(i)) + \sin(\phi(i))(-x_f(i)F_y(i) + r_f(i)F_x(i)) \end{aligned} \tag{3.65}$$

$$\begin{aligned} M^z_{fin,body}(i) = {} & -\sin(-\phi(i))(M^y_{fin}(i)) + \cos(\phi(i))(-M^x_{fin}(i)\sin(\delta(i)) + M^y_{fin}(i)\cos(\delta)) \\ & - \sin(\phi(i))(x_f(i)F_z(i)) + \cos(\phi(i))(-x_f(i)F_y(i) + r_f(i)F_x(i)) \end{aligned} \tag{3.66}$$

Recall, these forces and moments are functions of current vehicle states and controls as well as delayed states, since immersion is determined by the history of vehicle motion. It is assumed that only one cavity centerline position determines the immersion of all four fins to simplify the equations. The fin forces depend only on current states and past position of the nose $\left([x_{n,E}(t-\tau); y_{n,E}(t-\tau); z_{n,E}(t-\tau)]^T\right)$

### 3.2.4 Logvinovich Planing Model

Contact with the gas filled cavity bubble is called *planing*. This provides a large impulse force to direct the body back into the cavity. It can lead to oscillating motion like a fast

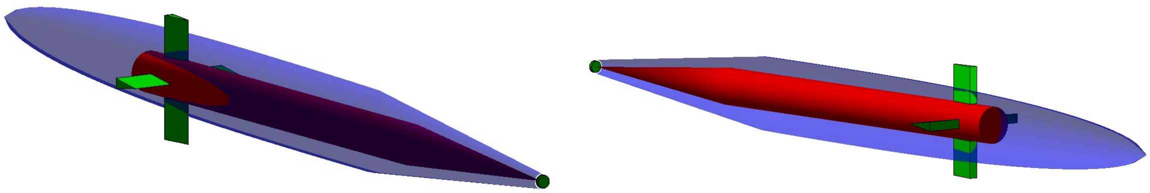

(a) Vehicle surrounded by cavity during planing. (b) Control surfaces immersion during flight.

Figure 3.10: Vehicle configuration.

boat bouncing on the top of water. There are two distinct modes: ($i$) the whole vehicle can be inside the cavity no forces are generated by planing, ($ii$) the transom can be immersed into the liquid outside of the cavity. In the later case the resulting planing force acts in the opposite direction of the immersion, determined by the immersion angle $\phi$, towards the center of the cavity as seen on Figure 3.4. To keep the equations simple, since in case of contact with the liquid all the forces act in the plane of contact, the planing equations are defined in scalar form.

The force generated by planing in the plane of immersion can be approximated by Logvinovich's method [19].

$$F_p(h, \alpha_i) = \left(1 - \left(\frac{\varepsilon}{h(t,\tau) + \varepsilon}\right)^2\right)\left(\frac{R + h(t,\tau)}{R + 2h(t,\tau)}\right)\sin(\alpha_i(t,\tau))\cos(\alpha_i(t,\tau)) \tag{3.67}$$

The associated moment acting perpendicular to the plane of immersion:

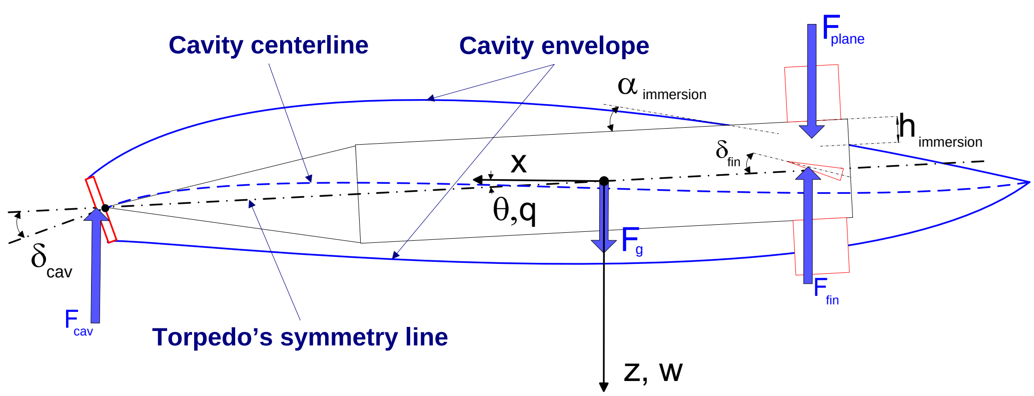


Figure 3.11: Geometry of planing forces in longitudinal plane.

$$M_p(h, \alpha_i) = \pi\rho r_c^2 u^2 \cos^2 \alpha_{plane} \frac{R + h}{R + 2h}\frac{h^2}{h + \varepsilon} \tag{3.68}$$

A friction force $F_f(h, \alpha_i)$ acting along the body $x$ direction is also taken into account.

$$F_f = 0.5\rho u^2 \cos^2 \alpha_{plane} S_w C_d \tag{3.69}$$

The unknown variables are: $h(t, \tau) = f(y_c, z_c)$, the immersion depth; $\alpha_i$ the immersion angle defined as the angle between the body's surface and the cavity bubble; $\varepsilon = R_c - R$ the median distance between the transom and the cavity; and $\tau = L/V_m$ delay, defined as the time needed for the vehicle to travel the distance between the nose and the transom of the body.

Planing depth is a discontinuous function, and can be represented as:

$$h = \begin{cases} \left|\sqrt{y_c^2 + z_c^2} + R - R_c\right| \text{ (planing)} & \text{if } \sqrt{y_c^2 + z_c^2} + R > R_c \\ 0 \text{ (no contact)} & \text{if } \sqrt{y_c^2 + z_c^2} + R < R_c \end{cases} \tag{3.70}$$

The immersion angle is also determined by the planing location, but since the current and delayed states influence its magnitude, it has to be calculated in the inertial frame:

$$\alpha_i(t) = \tan^{-1}\left(\frac{[\dot{X}_{n,E}(t-\tau) - \dot{X}_{t,E}(t)] \cdot [DCM_{BE}(t)(0, -\cos(\phi_p(t)), -\sin(\phi_p(t))]^T) + \dot{R}_c}{u(t)}\right) \tag{3.71}$$

The immersion angle is a function of three different variables. The nominal cavity has an ellipsoid shape, the cavity radius is not constant through the length of the body, its diameter is shrinking with a rate of $\dot{R}_c$ at the transom region. The cavity's shape at the tail location follows the past path of the vehicle nose ($\dot{X}_{n,E}(t-\tau)$). The vehicle tail has also relative motion when penetrating the boundary due to angle of attack and pitch rate in the immersion plane ($\dot{X}_{t,E}(t)$). The expression uses the relative speed difference of the bubble and tail, which is projected onto the unit vector $(0, -\cos(\phi_p(t)), -\sin(\phi_p(t))$ in direction of planing, and the additional velocity component of cavity contraction is added to complete the velocities in direction of contact. The expression is divided with the $x$ directional speed of the vehicle to obtain an angle.

The immersion direction $\phi_p(t)$ describes the plane in which the contact between liquid and vehicle takes place, as seen on Figure 3.4, and also determines the components of $F_p$ planing force and $M_p$ planing moment in the vehicle $y$ and $z$ coordinates. The planing force acts in the plane determined by $\phi_p$ towards the centerline of the body, while the resulting moment is perpendicular to this plane. The skin friction forces, parallel with the $x$-axis, caused by the contact with the viscous liquid phase are computed using the following set of equations [15]:

$$u_c = \sqrt{\frac{h}{\varepsilon}} \tag{3.72}$$

$$u_s = \frac{1}{d_c}\sqrt{\varepsilon h} \tag{3.73}$$

$$C_d = \frac{0.031}{\left(\frac{ul_p}{\nu}\right)^{1/7}} \tag{3.74}$$

$$\begin{aligned} S_w = {} & 2d_c\frac{\varepsilon}{\tan\alpha_i}[(1+u_c^2)\arctan u_c - u_c] \\ & + \frac{d_c^3}{16\varepsilon\tan\alpha_i}[(u_s^2-0.5)\arcsin u_s + 0.5u_s\sqrt{1-u_s^2}] \end{aligned} \tag{3.75}$$

The total resulting friction force is proportional with $S_w$ the coefficient describing the immersion geometry:

$$F_f = 0.5\rho u^2\cos^2\alpha_i S_w C_d \tag{3.76}$$

It is assumed that the moments generated by friction are negligible.

Equations 3.67-3.76 all use shallow planing approximations, assume that the vehicle's total speed ($V_m$) does not change rapidly, and the surrounding environment including the water temperature and pressure do not change. Based on the assumptions defined above, the relationship for the cavity's radius at the transom is a constant, also the expression for the contraction rate of the cavity ($\dot{R}_c$) is constant. The forces in the body frame are obtained via projection of the plane of immersion into the $x-y$ and $x-z$ planes.

$$F_{plane} = \begin{bmatrix} F_f \\ -F_p\cos\phi \\ F_p\sin\phi \end{bmatrix} \tag{3.77}$$

The resulting moments are from the change in center of effect on the tail section, and from the moment arm ($L - L_{cav}$) between the tail and the c.g.

$$M_{plane} = \begin{bmatrix} 0 \\ M_p\sin(\phi) \\ -M_p\cos(\phi) \end{bmatrix} + F_{plane} \times \begin{bmatrix} L - L_{cav} \\ 0 \\ 0 \end{bmatrix} \tag{3.78}$$

### 3.2.5 Paryshev Planing Model

Although good agreement was found between experiments and the predictions of Logvinovich planing equations [19] the Logvinovich planing equations take into account only geometric angles and immersion depth. These equations have no link to the dynamics, and do not exhibit the observed damped behavior in experiments [22]. Paryshev formulated the planning problem as an impact of a body in a cylindrical cavity [22], taking the speed and acceleration during impact into consideration. The hydrodynamic force acting per unit length under non-stationary submergence is given as:

$$f_p = \frac{\rho\pi r^2}{\varepsilon + h}\left[2\left(\frac{\varepsilon}{\varepsilon + h}V_y + V_r\right)^2 + h\left(\frac{2\varepsilon + h}{\varepsilon + h}\frac{dV_y}{dt} + 2\frac{dV_r}{dt}\right)\right] \tag{3.79}$$

where the variables are the following: $\varepsilon = R_c - R$ the nominal cavity gap, $V_y$ is relative velocity of the vehicle tail with respect to the cavity centerline, $V_r$ is the cavity radius contraction rate, $h$ is the immersion depth and $\frac{dV_y}{dt}$ is the relative acceleration of the vehicle tail, while $V_r$ is assumed constant, hence $\frac{dV_y}{dt} = 0$. Since equation 3.79 only describes the force for unit length, the equation has to be integrated over the entire wetted length of the afterbody. It is assumed that the planing depth has direct correlation with the length of immersion $l_p$.

Consider the case when the cavity is mirror symmetric to the $x$-axis and with the vehicle nose fixed at the cavitator, the body is rotated around the nose. At certain angle the tail dips into the fluid, as illustrated on Figure 3.12. Using this case as a reference, the relationship between the depth of immersion $h$ and the length of immersion $l_p$ has the following form:

$$h = L\frac{\frac{\dot{R}_c}{V}l_p - \varepsilon}{l_p - \varepsilon} - \varepsilon \tag{3.80}$$

The cavity boundary is linearly approximated with a plane tangent to the first point of immersion as seen on figure 3.12. Linearizing this equation leads to an approximation $l_p = p_0 + p_1 h$ where $p_0$ is zero since at $h = 0$ also $l_p$ is zero. Substituting $l_p = p_1 h$ into equation 3.79 and carrying out definite integral from zero till $l_p$ leads to:

$$F_p = \frac{\rho\pi R^2}{p_1}\left[\frac{2\varepsilon l_i V_y(2V_r + V_y) + p_1 l_i^2(V_y(4V_r + V_y) + \varepsilon dV_y) + p_1^2 l_i^3 dV_y}{(\varepsilon + p_1 l_i)^2} - \frac{2V_r^2\ln(\frac{\varepsilon}{\varepsilon + p_1 l_i})}{p_1}\right] \tag{3.81}$$

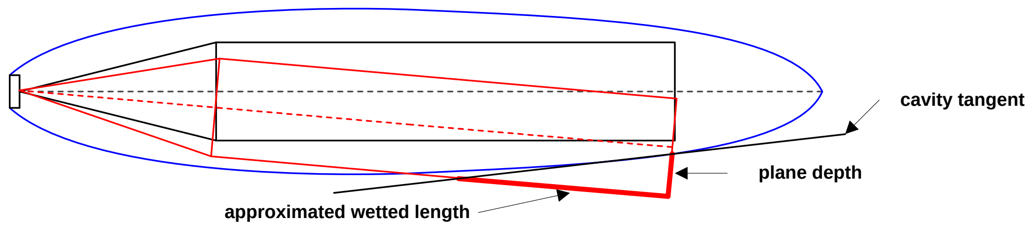


Figure 3.12: Approximation of the wetted length during planing.

Which then using equations 3.77 can be transformed to the body frame as above in the Logvinovich case. The associated moment is due to the fact that the center of effect of the planing force is not at the end of the tail but somewhere forward, hence the equations have to compensate for that. For simplicity it is assumed that the center of effect is $l_p/3$ distance forward towards the nose. This is a first guess, but likely sufficient for the purpose of comparison of the two planing descriptions, since the major part in the moment component is due to the tail-c.g. offset and the shift of center of effect is on the order of millimeters while the moment arm is about a meter in the case of the HSSV.

$$M_p = \frac{F_p p_1 h}{3} \tag{3.82}$$

An open-loop simulation with the nonlinear EOM using the two set of planing descriptions were performed using initial condition of $q = -1\ rad/s$, while all other states and controls are at their trim values around straight and level trajectory with $V_m = 77\ m/s$. The comparison between the behavior of the different planing descriptions are shown on Figures 3.13-3.14.

It is noticeable that the prediction of the two planing models are different by 150%. The Paryshev model predict larger forces (Fig.3.14) and leads to more violent contact with the liquid. The initial condition on pitch rate is high enough to cause planing at approximately 0.1 $s$. The force builds up faster, due to the acceleration component, in the Paryshev equations, indicating a lower damping coefficient. This results in slightly different dynamical behavior as comparing the time history of planing on Figure 3.14, the Logvinovich model is more gentle and leads to lower frequency limit cycles. It is beyond the scope of this thesis to further analyze the physical interpretation of these different theories, but it is advantageous to verify them before the tests of the HSSV.

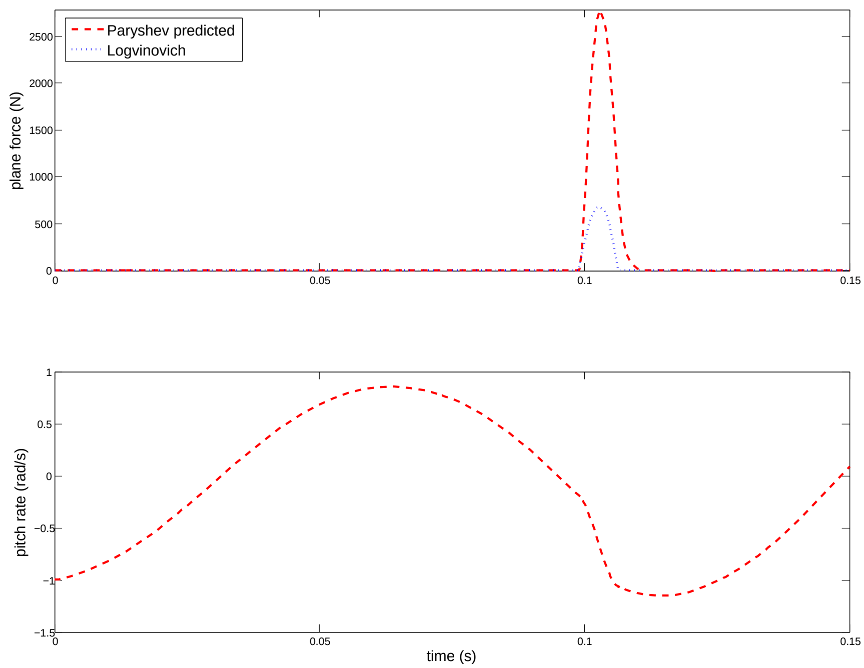


Figure 3.13: Open-loop dynamics with Logvinovich planing model (initial condition $q = -1\ rad/s$).

### 3.2.6 Equations in State Space Form

The equations of motion are written around the center of gravity (c.g.). The reference coordinate system is placed at the center of gravity with positive $x$-axis pointing in forward horizontal direction and the $y$-axis pointing to the starboard fin direction. The $z$-axis points down to the center of Earth in nominal straight and level flight (Fig.4.2).

There are 12 states composing the equations of motion including 6 states of kinetics

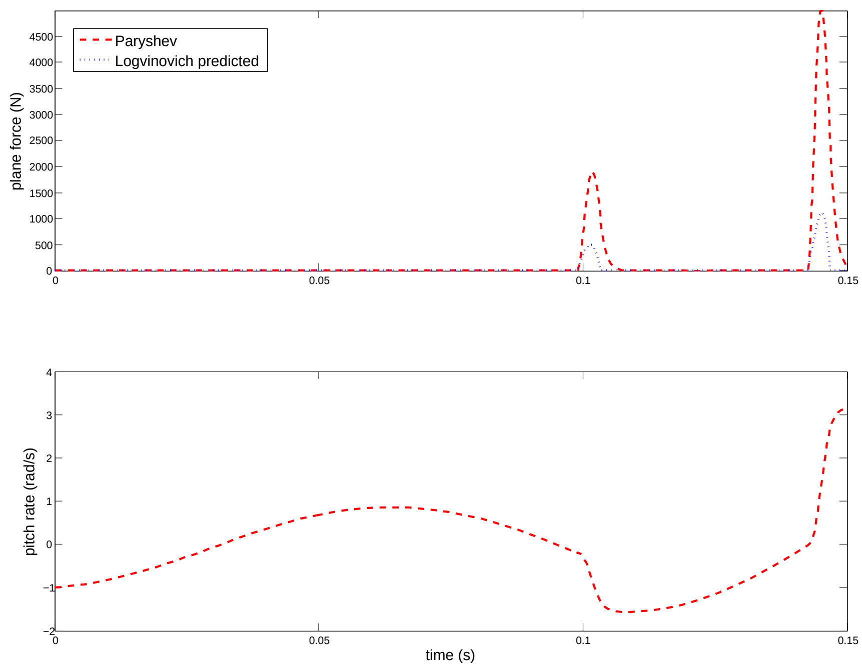


Figure 3.14: Open-loop dynamics with Paryshev planing model (initial condition $q = -1\ rad/s$).

described by Equation 3.32 and 6 states of kinematics defined in Equation 3.1.

$$\begin{bmatrix} \dot{x}_E \\ \dot{y}_E \\ \dot{z}_E \\ \dot{\psi} \\ \dot{\theta} \\ \dot{\phi} \\ \dot{\alpha} \\ \dot{\beta} \\ \dot{V}_m \\ \dot{p} \\ \dot{q} \\ \dot{r} \end{bmatrix} = [\mathbf{f}_x]_{12\times12} \begin{bmatrix} x_E \\ y_E \\ z_E \\ \psi \\ \theta \\ \phi \\ \alpha \\ \beta \\ V_m \\ p \\ q \\ r \end{bmatrix} + [\mathbf{g}_x]_{12\times6} \begin{bmatrix} \delta_{c,p} \\ \delta_{c,y} \\ \delta_{f,1} \\ \delta_{f,2} \\ \delta_{f,3} \\ \delta_{f,4} \end{bmatrix} + [\mathbf{f}_G]_{12\times3} \begin{bmatrix} \psi \\ \theta \\ \phi \end{bmatrix} + [\mathbf{f}_P]_{12\times2} \begin{bmatrix} F_P \\ M_P \end{bmatrix} \tag{3.83}$$

Where the matrices are partitioned as follows:

$$[\mathbf{f}_x]_{12\times12} = \left[\begin{array}{c|c|c|c} 0_{3\times3} & f^{1,2}_{3\times3} & f^{1,3}_{3\times3} & 0_{3\times3} \\ \hline 0_{3\times3} & f^{2,2}_{3\times3} & 0_{3\times3} & f^{2,4}_{3\times3} \\ \hline 0_{3\times3} & 0_{3\times3} & f^{3,3}_{3\times3} & f^{3,4}_{3\times3} \\ \hline 0_{3\times3} & 0_{3\times3} & 0_{3\times3} & f^{4,4}_{3\times3} \end{array}\right] \tag{3.84}$$

responsible for the dynamics. The inputs enter via a non affine matrix function:

$$[\mathbf{g}_{x,u}]_{12\times6} = \left[\begin{array}{c} 0_{6\times6} \\ \hline g^2_{6\times6} \end{array}\right] \tag{3.85}$$

While the constant gravity has projection onto the body axes through the matrix function:

$$[\mathbf{f}_G]_{12\times3} = \left[\begin{array}{c} 0_{6\times3} \\ \hline f^2_{3\times3} \\ \hline 0_{3\times3} \end{array}\right] \tag{3.86}$$

The influence of the states on the complex nonlinear function of planing is written conveniently as:

$$[\mathbf{g}_P]_{12\times2} = \left[\begin{array}{c} 0_{6\times2} \\ \hline f^2_{3\times2} \\ 0_{1\times2} \\ \hline f^2_{2\times2} \end{array}\right] \tag{3.87}$$

The six kinetics states $\alpha$ angle-of-attack, $\beta$ sideslip angle, $V_m$ velocity, $p$ roll rate, $q$ pitch rate and $r$ yaw rate all influence the states of kinematics: position coordinates $x_e; y_e; z_e$ and attitude angles $\phi; \theta; \psi$. But the opposite is not true since in equation 3.84 the lower off-diagonal terms are zero. The coupling enters only via the gravity and planing equations. Hence it is possible to separate the two sets of equations with only a few coupling terms.

The first and most important control objective is to provide stability augmentation for the vehicle, while an upper level controller operating on the closed inner-loop can then provide trajectory tracking. Hence, the focus of obtaining a control oriented model is to isolate the kinematics from the kinetics. Leading to two smaller subproblems, both sets of equations have only six states. An inner loop is closed on the kinetics, while treating the closed inner loop as a single entity an outer loop can provide trajectory tracking, using the kinematics equations. Since the gravity vector is constant, it can be handled as an offset of trim value on the control inputs to eliminate its effect on the dynamics. While one way of handling the planing force is to assume it is an outside measured disturbance on the dynamics, with given input direction $[\mathbf{g}_P]$.

For further details on the equations of motion of the HSSV vehicle , the reader is referred to [4, 15], where similar mathematical models are developed by other authors from different point of view, for different purposes, like trajectory optimization or characterizing the optimal configuration of the vehicle.

Using the expressions above for describing the behavior of the system, the kinetics equations can be written in compact form for the aim of the inner-loop control design.

$$\begin{aligned}
\dot{\alpha} = c_\alpha^2 \Bigg\{ & \left\{ \bar{q} \left[ C_{cav} \sin\alpha_{cav} \cos\beta_{cav} + r_s^2(-C_{1,z} + C_{2,y} + C_{3,z} - C_{4,y}) \right] + F_{z,p} + F_{z,g} \right\} \frac{Q_{\alpha\beta}}{mV_m} \\
& - pt_\beta \Bigg\} + q - s_\alpha c_\alpha \Bigg\{ \left\{ \bar{q} \left[ -C_{cav} \cos\alpha_{cav} \cos\beta_{cav} + r_s^2(-C_{1,x} - C_{2,x} - C_{3,x} - C_{4,x}) \right] \right. \\
& \left. + F_{x,p} + F_{x,g} \right\} \frac{Q_{\alpha\beta}}{mV_m} + rt_\beta \Bigg\}
\end{aligned} \tag{3.88}$$

$$\begin{aligned}
\dot{\beta} = c_\beta^2 \Bigg\{ & \left\{ \bar{q} \left[ C_{cav} \sin\beta_{cav} + r_s^2(C_{1,y} + C_{2,z} - C_{3,y} - C_{4,z}) \right] + F_{y,p} + F_{y,g} \right\} \frac{Q_{\alpha\beta}}{mV_m} \\
& + pt_\alpha \Bigg\} - r - s_\beta c_\beta \Bigg\{ \left\{ \bar{q} \left[ -C_{cav} \cos\alpha_{cav} \cos\beta_{cav} + r_s^2(-C_{1,x} - C_{2,x} - C_{3,x} - C_{4,x}) \right] \right. \\
& \left. + F_{x,p} + F_{x,g} \right\} \frac{Q_{\alpha\beta}}{mV_m} - qt_\alpha \Bigg\}
\end{aligned} \tag{3.89}$$

$$\begin{aligned}
\dot{V}_m = & \frac{1}{mQ_{\alpha\beta}} [(F_{x,p} + F_{x,g} + t_\alpha(F_{y,p} + F_{y,g}) + t_\beta(F_{z,p} + F_{z,g}))] \\
& + \frac{\bar{q}}{mQ_{\alpha\beta}} \{ -C_{cav} \left( \cos\alpha_{cav} \cos\beta_{cav} + t_\beta \sin\beta_{cav} - t_\alpha \sin\alpha_{cav} \cos\beta_{cav} \right) + \\
& + r_s^2 [ -C_{1,x} - C_{2,x} - C_{3,x} - C_{4,x} + t_\beta(C_{1,y} + C_{2,z} - C_{3,y} - C_{4,z}) \\
& + t_\alpha(-C_{1,z} + C_{2,y} + C_{3,z} - C_{4,y}) ] \}
\end{aligned} \tag{3.90}$$

$$\dot{p} = \frac{\bar{q} r_s^2}{I_{xx}} \{ -C_{1,z} l_1 - C_{2,z} l_2 - C_{3,z} l_3 - C_{4,y} l_4 + r_s(-C_{5,x} - C_{6,x} - C_{7,x} - C_{8,x}) \} \tag{3.91}$$

$$\dot{q} = \frac{1}{I_{yy}} \left\{ M_{y,p} + F_{z,p} l_t + \bar{q} \left[ -C_{cav} \sin\alpha_{cav} \cos\beta_{cav} l_{cav} + r_s^2 \left( (-C_{1,z} + C_{2,y} + C_{3,z} - C_{4,y}) \, l_f - \right. \right. \right.$$
$$\left. \left. \left. -C_{2,x} l_2 + C_{4,x} l_4 + r_s (C_{5,y} + C_{6,z} - C_{7,y} - C_{8,z}) \right) \right] + (I_{zz} - I_{xx}) rp \right\} \tag{3.92}$$

$$\dot{r} = \frac{1}{I_{zz}} \left\{ M_{z,p} - F_{y,p} l_t + \bar{q} \left[ C_{cav} \sin\beta_{cav} l_{cav} + r_s^2 \left( (-C_{1,y} - C_{2,z} + C_{3,y} + C_{4,z}) \, l_f + \right. \right. \right.$$
$$\left. \left. \left. + C_{1,x} l_1 - C_{3,x} l_3 + r_s (-C_{5,z} + C_{6,y} + C_{7,z} - C_{8,y}) \right) \right] + (I_{xx} - I_{yy}) pq \right\} \tag{3.93}$$

All the equations above use the conventions $\cos(\alpha) = c_\alpha$ and similar for all trigonometric functions, $\bar{q} = 0.5 \rho V_m^2$, $C_{cav} = C_{D0}(1 + \sigma)$, $Q_{\alpha\beta} = \sqrt{1 + \tan^2(\alpha) + \tan^2(\beta)}$ and the fin force and moment coefficients, obtained from lookup tables, are denoted by $C_{n,c}$ n denoting the number of fin and c is the coordinate direction. Note that the relationship between aerodynamic angles and velocities in the body frame is given as:

$$\tan(\alpha) = \frac{w}{u}; \;\; \tan(\beta) = \frac{v}{u}; \;\; V_m = \sqrt{u^2 + v^2 + w^2} \tag{3.94}$$

### 3.2.7 Uncertainties in System Parameters

The physical characteristics of the vehicle under investigation [1] are described in Table 3.1. Although it is assumed that all the system parameters are measured accurately it is natural to assume there is uncertainty associated with them. Most importantly, the forces generated by the fins have uncertainty associated with them, due to the hysteresis effect of cavity formation and collapse around the fins. As described in several publications [18] a base cavity is always present on the fins, since ventilation gas from the cavity around the body can help maintaining the cavity on the fins. A large supercavity forms around each fin as the angle of attack increases on them. When the angle of attack is decreasing the supercavity is still present on the fin even at lower angle of attack when it was formed, providing lower lift compared with non supercavitating mode. This phenomena lacks predictability, no analytical or experimental method can describe quantitatively the hysteresis, hence it is assumed there is only one force curve with a range of uncertainty associated with it. Other uncertainties are the vehicle mass and inertia properties. Due to the fuel consumption mass and inertia change along the duration of the flight. Important source of uncertainty is related to the description of the cavity, since most equations use simplifications or derived based on experimental data. It is natural to assume uncertainty on cavity dimensions. It

Table 3.1: System parameters for simulation model [1]

| Parameter | Description | Value and Units |
|---|---|---|
| $g$ | Gravitational acceleration | $9.81\frac{m}{s^2}$ |
| $m$ | Weight, | $22kg$ |
| $I_{xx}$ | Inertia around x-axis, | $0.0261kgm^2$ |
| $I_{yy,zz}$ | Inertia around y,z-axis, | $5.1847kgm^2$ |
| $d_c$ | Cavitator diameter | $0.0381m$ |
| $R$ | Vehicle radius | $0.0508m$ |
| $R_{piv}$ | pivot point radius | $0.9R$ |
| $L$ | Length | $2.066m$ |
| $L_{cav}$ | Cavitator c.g. offset | $1.1223\ m$ |
| $x_f$ | Fin pivot c.g. offset | $0.85L - x_c$ |
| $r_s$ | Fin length | $0.07m$ |
| $a_{buoy}$ | Buoyancy | $8.29m/s^2$ |
| $\alpha_s$ | Fin sweepback angle | $15deg$ |
| $\sigma$ | Cavitation number | 0.029 |
| $C_{x0}$ | Lift coefficient | 0.805 |
| $V_{m,i}$ | Nominal Velocity | $77\frac{m}{s}$ |
| $\nu_w$ | kinematic viscosity | $1.4 \cdot 10^{-6}$ |
| $T$ | Nominal Thrust | $3092\ N$ |

becomes clear analyzing the sensitivity of the system to changes in vehicle parameters, that even a slight uncertainty in the cavitation number, cavitator radius or any other parameter determining the cavity shape has strong influence on the vehicle dynamics. For these reasons a simplified model of the vehicle is developed, where the behavior of the motion can be analyzed in a lower complexity longitudinal model.

# Chapter 4

# Longitudinal Equations-of-Motion of the Supercavitating Vehicle

The following Chapter focuses on gaining physical insight into the behavior of High-Speed Supercavitating Vehicles (HSSV) to help theoretical developments in modeling and control design. A simplified model of longitudinal dynamics is developed here to serve as a platform for control design described in Chapter 5. Since the system dynamics is highly complex, it is essential to understand the most important properties before addressing the control problem on the full vehicle dynamics. Special emphasis is made here to understand the behavior of the cavity governed delay differential equations.

## 4.1 Motivation

This thesis focuses on control challenges associated with the supercavitating vehicle. In most engineering applications, where the objective is to develop a reliable mathematical model of the plant of interest, the underlying physics is very well understood. Fields like flight control and control of ground vehicles have almost 100 years of information available and their historic development is well documented in numerous publications. Research on supercavitation dates back only a few decades, when mostly the hydrodynamic properties of the cavity were studied [6, 29], only limited effort was made to address the dynamics of supercavitating vehicles.

The coupling between the gas cavity and the vehicle dynamics was first investigated in [1], using a simple 1-DOF mathematical model to show interesting behavior, including bifurcations and chaos. A more realistic 2-DOF supercavitating vehicle model describing the longitudinal motion is presented in this chapter. This model can help better understand the basic characteristics of a supercavitating vehicle and serves as an intermediate step towards the understanding the 6-DOF dynamics. An experimental platform is also developed at the University of Minnesota's Saint Anthony Falls Laboratory as seen on Figure 4.1. The test bed can support valuable information on the cavity-vehicle interaction. The actively controlled hydrodynamic surfaces allow closed loop stabilization and tracking control experiments serving as an important validation tool for the mathematical model developed in this chapter.

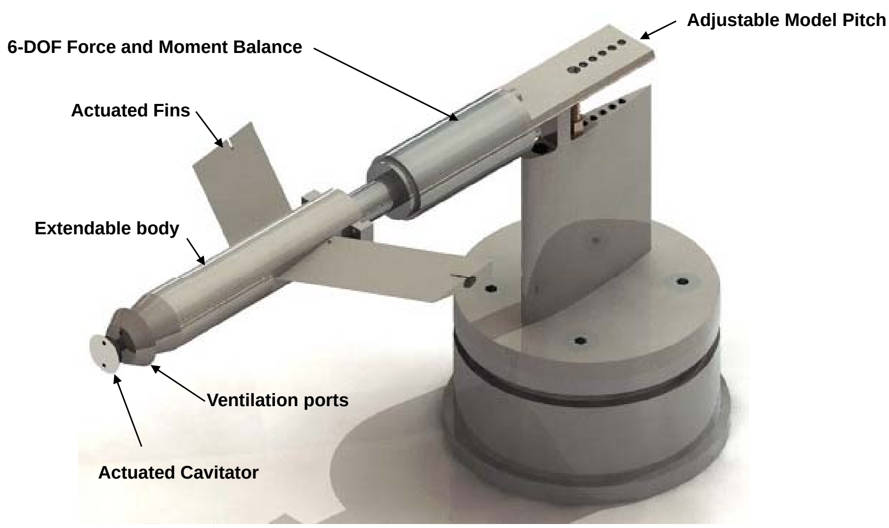


Figure 4.1: Water tunnel experimental test bed on supercavitation

The first part of the chapter (Section 4.2) describes a simplified pitch-plane model of a HSSV. This model is a refined version of the model described in [30], which was motivated by the papers of [16] and [31]. The model includes delay-dependent interaction between the vehicle and cavity wall, pitch-angle-dependent terms, and the Logvinovich planing model described in Chapter 3.

Simulation results of the simplified open-loop system are compared with the full nonlinear simulation. The sensitivity of the system with respect to various physical parameters are highlighted to help guide the designer of the control system. Chapter 5 using the longitudinal mathematical model of the supercavitating vehicle describes the systematic design of a dynamic-inversion-based inner-loop control architecture.

## 4.2 Mathematical Model

Several mathematical descriptions of supercavitating vehicles are available in the literature, ranging from a vertical directional one degree-of-freedom (DOF) model [31], a simplified 2-DOF longitudinal description [16], to a high fidelity 6-DOF model [1]. A broader overview on the characteristics of these models can be found in [32] where another 2-DOF model from [30] is described.

Delay-dependent behavior of the cavity with memory effect influencing planing was developed in [33], however the derivation neglected the control forces' pitch angle dependence. Given a single control surface an additional force to support the vehicle requires constant nonzero pitch angle of the vehicle. This is apparent since trimming the vehicle around straight level flight requires nonzero angle of attack on the fins and cavitator, to generate the required force and moment balance. Hence, a relationship between the pitch angle, moments and forces need to be developed.

For simplicity, the equations of motion are written around the center of gravity (c.g.) and small angle approximations are used to eliminate trigonometric nonlinearities. The small angle assumption is valid since we anticipate angles less than 0.2 $rad$. Variable definition and coordinate directions are shown in Figure 4.2.

The geometry of the model is intended to capture the main characteristics of the test vehicle described in chapter 2. The body consists of a cylindrical and a conical section, with the length of the latter half of the former. The reference coordinate system is placed at the center of gravity with positive $x$-axis pointing in forward horizontal direction and the $z$-axis pointing to the center of Earth. The pitch angle is denoted by $\theta$ $(rad)$, pitch rate $q$ $(rad/s)$, the vertical position $z$ $(m)$ and vertical velocity is $w$ $(m/s)$. $\delta_c$ $(rad)$ is the cavitator angle with respect to the $x$ body axis, and $\delta_f$ $(rad)$ the fin angle of attack in the body coordinates. In general, there are four forces acting on the body, the cavitator and fins forces, gravity, and planing which is not always present.

The body length is denoted by $L$ $(m)$ and its radius by $R$ $(m)$. The body has uniform density $\rho_b = \rho m$ $(kg/m^3)$, with relative density $m$ compared with water $(\rho)$, from which the mass and inertia can be calculated, neglecting the cavitator and fins contribution. Hence, the vehicle mass $(M)$, moment of inertia around the y axis $(I_{yy})$ and center of gravity location from the nose $(x_{cg})$ are given as:

$$M = \frac{7}{9}(m\rho\pi)R^2L \tag{4.1}$$

$$I_{yy} = \frac{11}{60}R^4L\pi\rho m + \frac{1933}{45360}R^2L^3\pi\rho m \tag{4.2}$$

$$x_{cg} = \frac{17}{28}L \tag{4.3}$$

If the full vehicle body is inside the cavity, hydrodynamic forces only act on the cavitator

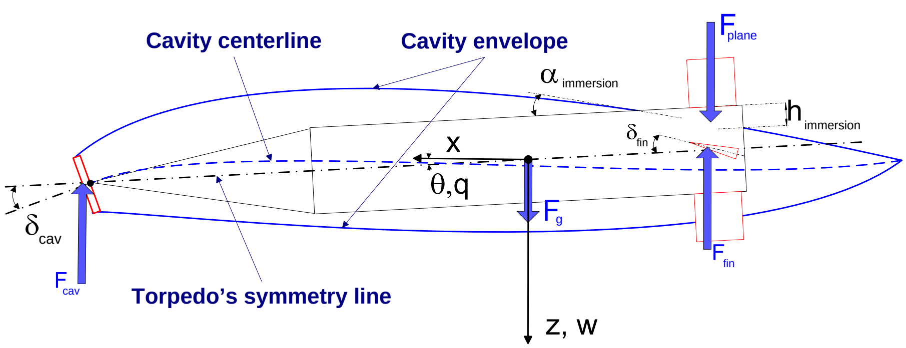


Figure 4.2: Variables in the longitudinal plane

and the fins. The cavitator drag coefficient is modeled as $C_x = C_{x_0}(1+\sigma)$ where $\sigma$ is the cavitation number and $C_{x_0} = 0.82$ [19]. The resulting lift on the cavitator using small angle approximations is:

$$F_{cav} = \frac{1}{2}\pi\rho R_n^2 V^2 C_x \alpha_c = C_l \alpha_c \tag{4.4}$$

where $R_n$ $(m)$ is the cavitator radius, $\rho$ the water density, $V$ $(m/s)$ the vehicle's horizontal speed, and $\alpha_c$ is the cavitator angle of attack.

The force acting on the fins located at the tail is further simplified from Equation 3.60. It is assumed that like in the case of the simplified cavitator force model, the fin force is proportional to fin angle-of-attack, and the relative location of the cavity does not change the fins lift coefficient:

$$F_{fin} = nC_l\alpha_f \tag{4.5}$$

$n$ represents the fins effectiveness in providing lift as a function of angle of attack ($\alpha_f$) relative to the cavitator. Note that in the longitudinal plane, the two horizontal fins are assumed to move in unison. Only small angle deflections with maximum value of 0.2 $rad$ are considered. The following simplifying assumptions are valid through out this Chapter: the horizontal velocity ($V$), water density ($\rho$) and cavitation number ($\sigma$) are assumed constant.

The force and moment equations around the c.g. using the conventions shown in Figure 4.2 are written as:

$$M\dot{w} = F_{cav} + F_{fin} + F_g + F_p \tag{4.6}$$

$$I_{yy}\dot{q} = -(F_{cav}L_c + F_{fin}L_f + F_pL_f) \tag{4.7}$$

where $L_c = 17/28L$ and $L_f = -11/28L$ are the respective moment arms of the cavitator and fin forces. The planing force is assumed to act at $-L_f$ distance from the c.g.

The force components as function of vehicle states are:

$$F_{cav} = \frac{1}{2}\pi\rho R_n^2 V^2 C_l(\frac{w}{V} - \frac{qL_c}{V} + \theta + \delta_c) \tag{4.8}$$

$$F_{fin} = -\frac{1}{2}\pi\rho R_n^2 V^2 C_l n(\frac{w}{V} - \frac{qL_f}{V} + \theta + \delta_f) \tag{4.9}$$

$$F_g = \frac{7}{9}\rho m\pi R^2 Lg \tag{4.10}$$

The clear benefit of representing the system in the form of equations 4.6 and 4.7 is that the system is linear, no trigonometric functions or other nonlinearities are complicating the understanding of the system behavior, with the exception of the planing force.

The planing force $F_p$, needs further consideration. The expression for cavity tail interaction can be simplified from equations in chapter 3 since the vehicle motion is constrained to the longitudinal plane.

The planing force is present when the vehicle transom interacts with the cavity wall, leading to a force similar to that sustained by powerboats bouncing on the top of the water. In the case of the longitudinal dynamics of the HSSV, the free fluid surface which is the circular cavity wall created by the cavitator, reduces to two points, one down in positive $z$ direction from the vehicle tail, and another one in negative direction.

The Logvinovich [19] and Paryshev [21] planing equations presented in the previous chapter also apply to the current vehicle configuration. These analytical results relate the immersion depth $h$ $(m)$ and the distance from the axis of symmetry to the narrowest part of the spray sheet, generated by the displaced fluid.

The pressure force on the body is calculated from the energy of the spray sheet. If the diameter of the cavity at the planing location is denoted by $R_c$, and assuming small cavity gap $((R_c - R) << R_c)$ and small immersion angles, around the nominal straight and level flight condition the planing force approximated by Logvinovich can be written as:

$$F_p = -\rho R^2 \pi V^2 \left(1 - \frac{R'}{h' - R'}\right)^2 \left(\frac{1 + h'}{1 + 2h'}\right) \alpha_p \tag{4.11}$$

The variable $R'$ denotes the normalized difference between the cavity and body diameter $(R' = (R_c - R)/R)$.

The variables $h'$ the normalized immersion depth and $\alpha_p$ $(rad)$ the immersion angle, capture the switched, nonlinear behavior of the dynamics. From Figure 4.2, the planing depth is determined by the cavity shape (as a function of the cavitator trajectory), vehicle position, and orientation. The position of the vehicle transom, where planing occurs, is a function of the vehicle position, rotation, and vehicle radius at the transom.

The cavity boundary is located at $R_c$ distance from its centerline, which is determined by the vehicle nose path through the water. At the transom, the centerline is at $z_n(t - \tau)$ with the nose position of $z_n(t) = z(t) - L_c\theta(t)$. The cavity radius at the planing location is assumed to be constant. Hence, the immersion depth is the difference between the nose and the transom position, plus the nominal cavity-bubble gap.

$$h' = \begin{cases} \frac{1}{R}[z(t) + \theta L_f + R - z_n(t - \tau) - R_c] & \text{if} \quad z_n(t - \tau) + R_c < z(t) + \theta L_f + R \\ 0 & \quad\;\; \text{(inside cavity)} \\ \frac{1}{R}[z_n(t - \tau) - R_c - z(t) - \theta L_f + R] & \text{if} \quad z_n(t - \tau) - R_c > z(t) + \theta L_f + R \end{cases} \tag{4.12}$$

Following the same reasoning, the immersion angle can be calculated based on the knowledge of the delayed vertical speed of the vehicle nose $(\dot{z}_n(t) = w(t) - V\theta(t) - L_c q(t))$ and current pitch angle plus the contraction rate of the cavity bubble $(\dot{R}_c)$:

$$\alpha_p = \begin{cases} \theta - \frac{\dot{z}_n(t-\tau) + \dot{R}_c}{V} & \textit{bottom contact} \\ 0 & \textit{inside cavity} \\ \theta - \frac{\dot{z}_n(t-\tau) - \dot{R}_c}{V} & \textit{top contact} \end{cases} \tag{4.13}$$

It is important to note that, based on equation (4.12) the system is described by three sets of equations corresponding to three possible modes, one with linear and the other two with nonlinear delay dependent terms. The vehicle dynamics are continuous on the switching surface between different modes, since the nonlinear planing force is zero on the boundary. It is important to notice that while the model has been significantly simplified and the baseline dynamics is linear, the model accurately represents the memory effect related to planing.

Using equations 3.21 for cavity shape, supplemented by the basic kinematic equations for position and pitch angle:

$$\dot{\theta} = q, \quad \dot{z} = w - V\theta \tag{4.14}$$

the system states $z, \theta, w$ and $q$ can be written in state space form as:

$$\begin{bmatrix} \dot{z} \\ \dot{\theta} \\ \dot{w} \\ \dot{q} \end{bmatrix} = A \begin{bmatrix} z \\ \theta \\ w \\ q \end{bmatrix} + B \begin{bmatrix} \delta_e \\ \delta_c \end{bmatrix} + F_{\text{grav}} + F_{\text{plane}}(t, \tau) \tag{4.15}$$

where $A$ and $B$ represent the linear part, $F_{grav}$ is a constant term and $F_{plane}$ corresponds to the nonlinear relationship associated with planing. The specific values of the system matrices are as follows:

$$A = \begin{bmatrix} 0 & -V & 1 & 0 \\ 0 & 0 & 0 & 1 \\ 0 & \frac{(C_1-C_2)}{M} & \frac{(C_1-C_2)}{(MV)} & \frac{(-C_1L_c+C2L_f)}{(MV)} \\ 0 & \frac{(-C_1L_c+C_2L_f)}{I_{yy}} & \frac{(-C_1L_c+C_2L_f)}{(I_{yy}V)} & \frac{(C_1L_c^2-C_2L_f^2)}{(I_{yy}V)} \end{bmatrix} \tag{4.16}$$

$$B = \begin{bmatrix} 0 & 0 \\ 0 & 0 \\ \frac{C_1}{M} & \frac{C_2}{M} \\ \frac{-C_1}{I_{yy}}L_c & \frac{C_2}{I_{yy}}L_f \end{bmatrix} \tag{4.17}$$

$$F_{\text{grav}} = \begin{bmatrix} 0 \\ 0 \\ g \\ 0 \end{bmatrix} \tag{4.18}$$

$$F_{\text{plane}} = \begin{bmatrix} 0 \\ 0 \\ \frac{C_p}{M} \\ -\frac{C_p}{I_{yy}}L_f \end{bmatrix} \left(1 - \frac{R'}{h'(t,\tau) - R'}\right)^2 \left(\frac{1 + h'(t,\tau)}{1 + 2h'(t,\tau)}\right) \alpha_p(t,\tau) \tag{4.19}$$

The constant terms $C_1, C_2, C_p$ are defined to simplify the presentation. Their specific values are:

$$C_1 = \frac{1}{2}\pi\rho R_n^2 V^2 C_x,\ C_2 = \frac{1}{2}\pi\rho R_n^2 V^2 C_x n,\ C_p = \pi\rho R^2 V^2 \tag{4.20}$$

The system parameters are based on the benchmark HSSV [1] presented in Chapter 3. The set of parameters used in the longitudinal model are presented in Table 4.2.

## 4.3 Open Loop Analysis

The HSSV model described above aims to provide a simplified description of the complex system equations described in Chapter 3. Since several simplifications were made, it is essential to analyze the behavior of the two different dynamics. Open-loop simulations of the simplified model are compared with the complex 6-DOF model on Figure 4.3.

Table 4.1: System parameters for longitudinal simulation model [2]

| Parameter | Description | Value and Units |
|---|---|---|
| $g$ | Gravitational acceleration | 9.81 $\frac{m}{s^2}$ |
| $m$ | Density ratio, $\frac{\rho_m}{\rho}$ | 2 |
| $n$ | Fin effectiveness | 0.5 |
| $R_n$ | Cavitator radius | 0.0191 $m$ |
| $R$ | Vehicle radius | 0.0508 $m$ |
| $L$ | Length | 1.80 $m$ |
| $V$ | Velocity | 75 $\frac{m}{s}$ |
| $\sigma$ | Cavitation number | 0.03 |
| $C_{x0}$ | Lift coefficient | 0.82 |

The dynamic evolution of the two models are compared for a 1 $rad/s$ initial pitch rate disturbance as shown on Figure 4.3. Slight difference between the two open loop dynamics can be observed. Planing has higher influence on the complex model, but both the time constant and the magnitude of planing force are similar in the two models. The damping coefficient observed in the simplified model is slightly lower. The simplified model is a reasonably accurate approximation of the complex dynamics, based on which important characteristics of cavity vehicle interaction can be studied.

After initial studies, a few key parameters were identified which require the most attention during the analysis of the vehicle behavior. It is expected that the c.g. location shifts during the flight as propellant is used. The propellant tank is in the tail section which will result in a shift of c.g. in forward direction which is analyzed on Figure 4.4(b). As shown the change in dynamic behavior is noticeable but not dramatic. The dynamics due to lower destabilizing moment arm of the cavitator tends to be more stable. The time constant is lower and the peak planing force is decreased. It is a reasonable performance criteria for the nominal controller to be robust for 5% change in c.g. location.

The effect of uncertainty in the fin force coefficient is analyzed on Figure 4.5(a). 5% decrease in fin force coefficient leads to minimal change in dynamics as observed. The dynamic behavior changes only slightly towards faster modes, with lower damping provided

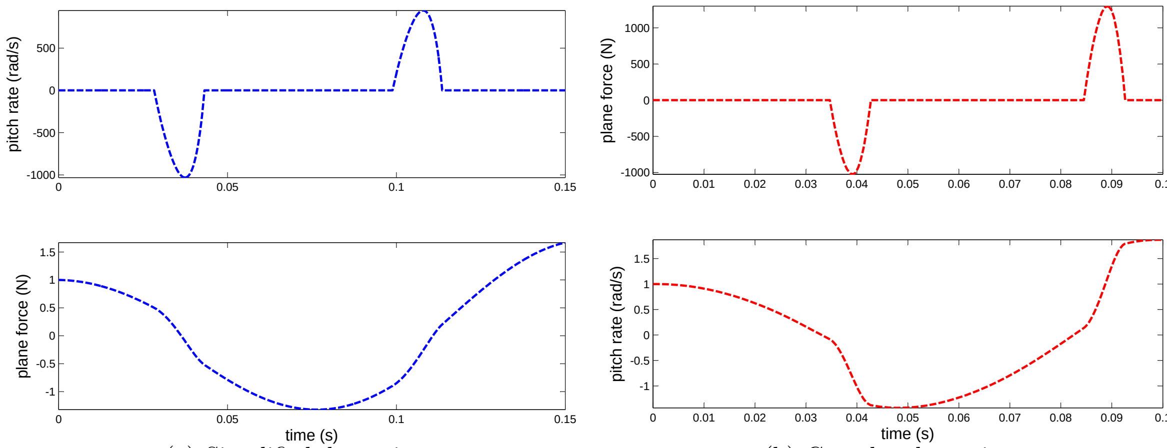


(a) Simplified dynamics. (b) Complex dynamics.

Figure 4.3: Open-loop analysis of the simplified and full longitudinal dynamics, initial condition $q = 1rad/s$

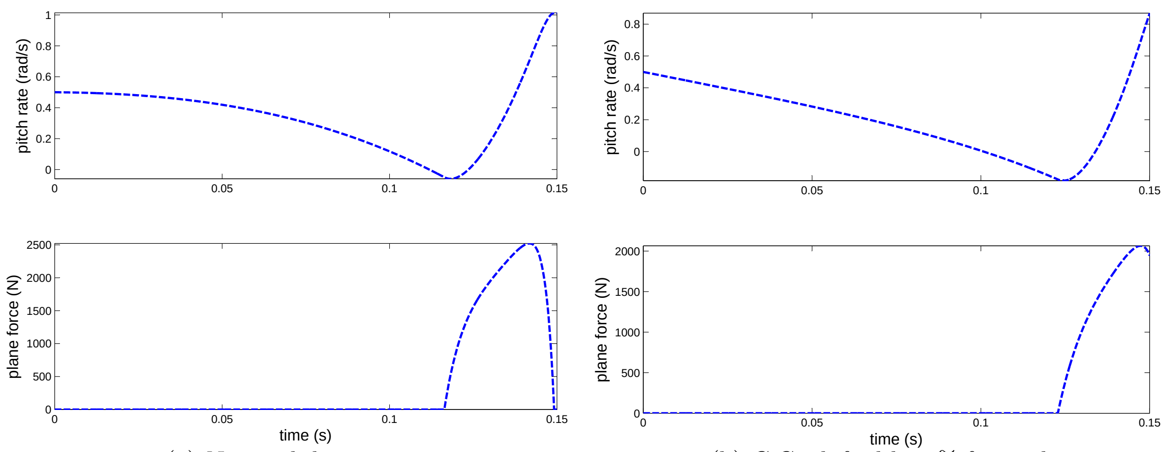


(a) Nominal dynamics. (b) C.G. shifted by 5% forward.

Figure 4.4: Open-loop comparison of the simplified longitudinal dynamics for uncertainty, initial condition $q = 0.5rad/s$

by the decreased stabilizing moment of the fins.

The most sensitive property is the cavitation number. Increasing it by 5% drastically alters the motion as shown on Figure 4.5(b), since change in cavitation number changes the cavity diameter at the tail section, leading to planing with higher frequency. This indicates that cavitation number and cavitation parameters should be measured accurately to predict the vehicle behavior in a precise manner.

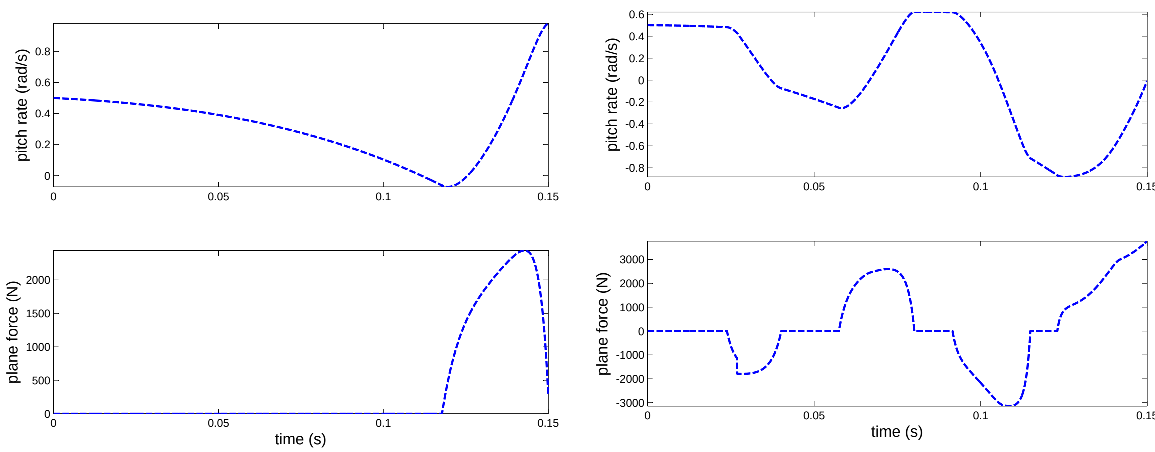


(a) Fin force coefficient increased by 5%. (b) Cavitation number increased by 5%.

Figure 4.5: Open-loop comparison of the simplified longitudinal dynamics for uncertainty, initial condition $q = 0.5 rad/s$

# Chapter 5

# Longitudinal Control of the Supercavitating Vehicle

A dynamic inversion based control technique is proposed to handle the switched, time-delay dependent behavior of the longitudinal axis HSSV model described in Chapter 4. This approach not only demonstrates a feasible way of augmenting vehicle stability, but also provides a theoretical framework for system analysis, from controllability point of view. The dynamic inversion controller is used to control the fast dynamics of the vehicle. This represents the inner-loop control.

A higher level outer-loop controller is added to guarantee trajectory tracking objectives for the vehicle model. Two outer-loop control schemes are compared for guidance level tasks, a pole-placement trajectory tracking controller with vertical position and pitch-angle-tracking objectives is compared with a receding horizon control (RHC) based design, where position and angle tracking, planing avoidance, and actuator saturation are formulated as performance objectives. Various aspects of disturbance characteristics and actuator dynamics are investigated and analyzed.

The chapter focuses on control of delay dependency of the system governing equations and addresses planing avoidance as a performance objective. Linear control methods previously proposed [12, 13] did not take into account the large deviations from the nominal equations of motion, hence stability and performance were not guaranteed when the vehicle was planing. Nonlinear methods proposed by [16, 33] guarantee stability during planing, using the control surfaces to attenuate the large forces caused by planing, but did not take into account actuator position and rate limits, which restricts the operation envelope of the vehicle. It is seen that planing avoidance as a performance objective can significantly expand the operation envelope of the HSSV. The increased performance comes at the expense of slightly degraded position tracking performance, while planing with undesirably high acceleration happens seldom if ever.

The challenges facing the control designer are highlighted with respect to the actuator and sensor requirements, modeling issues, vehicle configuration, robustness and performance. Conclusions and guidelines towards the control of the full six degrees-of-freedom vehicle model, emphasizing the most important design criteria are highlighted.

## 5.1 Theoretical aspects of controller design

The state space longitudinal axis supercavitating vehicle equations in eq. (4.15) represent a bimodal switched system. The system is described with continuous and discrete states. The equations of motion have two distinct dynamical modes depending on the state dependent switching condition. Several characteristics of this model are of interest: (i) in the first mode, the system dynamics are linear (inside cavity), and in the second mode they are nonlinear (planing) input affine, though the control inputs affect the dynamics linearly in both modes, (ii) the switching condition does not depend on the control inputs, and (iii) the switching hyperplane depends on the delayed output variable $z_n(t - \tau)$.

A switched, hybrid control strategy was developed in [32] for this type of system. Properties (i) and (ii) allow for feedback linearization in both modes. This is performed via a coordinate system with suitable geometric structure for the problem. It was shown in [32] that this design results in linear dynamics in both modes ensuring continuous dynamics on the switching hypersurface. Since the latter depends on delayed state variables, controllability has to be analyzed, and a controller has to be designed that ensures stability and tracking performance.

The proposed approach relies on the assumption that the delay in the equations of motion can be eliminated by applying a suitable feedback. The resulting controllability analysis and control design can then be performed for bimodal linear time invariant (LTI) systems.

### 5.1.1 Feedback linearization

Since the concept of relative degree plays a central role in this approach, its definition for nonlinear, time delay and LTI systems are presented.

Given a nonlinear input affine system:

$$\dot{x} = f(x) + \sum_{i=1}^{m} g_i(x) u_i, \quad x \in \mathcal{X}, \quad u \in \mathcal{U} \tag{5.1}$$

$$y_j = h_j(x), \quad y_j \in \mathcal{Y}, \quad j = 1, \ldots, p, \tag{5.2}$$

**Definition 5.1** (Lie Derivative of a Function). *Given a smooth vector field $X\colon M \mapsto TM$ and a smooth function $h\colon M \mapsto \mathbb{R}$ the Lie derivative of $h$ with respect to the vector field $X$ is a new function $L_x h:\ M \mapsto \mathbb{R}$ given by*

$$L_x h(p) = X(h)(p) \tag{5.3}$$

*The Lie derivative of a function $h$ with respect to a vector field $X$ is the rate of change of $h$ in the direction of $X$.*

**Definition 5.2** (Vector relative degree [34]). *The system has a vector relative degree $r = [r_1, \ldots, r_p]$, $r_i \geq 0, \forall i$, if at a point $x_0$*
*(i) $L_{g_j} L_f^k h_i(x) = 0, \ldots j = 1, \ldots, m, k < r_{i-1}$,*
*(ii) The matrix*

$$\mathcal{A}_{IA} = \begin{bmatrix} L_{g_1} L_f^{r_1 - 1} h_1(x), & \ldots, & L_{g_1} L_f^{r_1 - 1} h_1(x) \\ \vdots, & & \\ L_{g_m} L_f^{r_p - 1} h_p(x), & \ldots, & L_{g_m} L_f^{r_p - 1} h_p(x) \end{bmatrix} \tag{5.4}$$

*has rank $p$ at $x_0$.*

For linear time invariant (LTI) systems given by $(A, B, C)$, we have that $Lg_j L_f^{r_i - 1} h_i(x) = c_i A^{r_i - 1} b_j$ and if $p = m$ then the vector relative degree is defined if $rank \mathcal{A}_{LTI} = n$ where $n$ is the state dimension.

The concept of relative degree can be extended to time delay systems, too. Usually this is defined for a discrete time equivalent of the continuous time systems by introducing the discrete time shift operator $\Delta$ as $\Delta x_t = x_{t-\tau}$ with $\tau$ denoting the given time delay.

The time delay system is given now by $(A(\Delta), B(\Delta), C(\Delta))$, i.e. the matrices depend on the delay operator. This implies that the coefficients are elements of the polynomial ring $\mathcal{R}[\Delta]$. The relative degree is defined similarly to the LTI case as follows.

**Definition 5.3.** *Given the single input - single output linear time delay system* $(A(\Delta), b(\Delta), c(\Delta))$. *It has relative degree* $r > 0$ *if* $cA^k b = 0, \quad k = 0, \ldots, r-1$ *and* $cA^r b \neq 0$. *It has pure relative degree* $r$ *if in addition* $cA^r b$ *is an invertible element of* $\mathcal{R}[\Delta]$.

This definition has an obvious extension to the multivariable case. It requires the matrix $\mathcal{A}_{TD}$ is invertible over $\mathcal{R}^{p\times p}[\Delta]$. New state variables for equation (4.15) are selected for analysis and control design:

$$\begin{bmatrix} \bar{x}_1(t) \\ \bar{x}_2(t) \\ \bar{x}_3(t) \\ \bar{x}_4(t) \end{bmatrix} = \begin{bmatrix} z_n(t) \\ -V\theta(t) + w_n(t) \\ \theta(t) \\ q(t) \end{bmatrix} \tag{5.5}$$

The matrix used for this coordinate transformation is:

$$T_c = \begin{bmatrix} c_1 \\ c_1 A \\ c_2 \\ c_2 A \end{bmatrix} = \begin{bmatrix} 1 & -L_c & 0 & 0 \\ 0 & -V & 1 & -L_c \\ 0 & 1 & 0 & 0 \\ 0 & 0 & 0 & 1 \end{bmatrix} \tag{5.6}$$

The state space equations in the new coordinate system are:

$$\dot{\bar{x}} = \begin{cases} A_c\bar{x}(t) + B_c u(t) + \bar{F}_g & \text{if } \bar{c}(\delta)\bar{x}(t) \leq 0, \\ A_c\bar{x}(t) + \bar{F}_p(t, x, \delta) + B_c u(t) + \bar{F}_g & \text{if } \bar{c}(\delta)\bar{x}(t) \geq 0, \end{cases} \tag{5.7}$$

where

$$A_c = \begin{bmatrix} 0 & 1 & 0 & 0 \\ -\alpha_{110} & -\alpha_{111} & -\alpha_{120} & -\alpha_{121} \\ 0 & 0 & 0 & 1 \\ -\alpha_{210} & -\alpha_{211} & -\alpha_{220} & -\alpha_{221}, \end{bmatrix} B_c = \begin{bmatrix} 0 \\ c_1 AB \\ 0 \\ c_2 AB \end{bmatrix} \tag{5.8}$$

The difference between $F_{grav}$ and $\bar{F}_{grav}$ is that $\bar{F}_{grav} = T_c F_{grav} + K_1$ where $K_1$ is a constant associated with the shift in the origin of the coordinate system. Similarly $\bar{F}_{plane} = T_c F_{plane}$.

The inputs enter linearly in the state equations in both modes, and it is assumed that all states can be measured. This allows us to select two outputs defined as $y_1 = \bar{x}_1$ and $y_2 = \bar{x}_3$, such that the vector relative degree is well defined in both modes, and in addition, they are identical, i.e. by defining:

$$C_c = \begin{bmatrix} 1 & 0 & 0 & 0 \\ 0 & 0 & 1 & 0 \end{bmatrix} \tag{5.9}$$

The relative degree for the modes are:

$$r_1^2 = 2, \quad r_2^1 = 2, \quad r_1^2 + r_2^1 = n = 4 \quad \textit{Mode 1} \tag{5.10}$$

$$r_1^2 = 2, \quad r_2^2 = 2, \quad r_1^2 + r_2^2 = n = 4 \quad \textit{Mode 2} \tag{5.11}$$

$$\tag{5.12}$$

The consequence of this property is that one can apply state feedback in both modes to eliminate the time delay in Mode 1 and the nonlinearity (exact feedback linearization) in Mode 2 [35]. This feedback is given by [32]:

$$u_{flc} = \begin{cases} M_1^{-1}(\dot{y}_{12,ref}(t) - F_\alpha \bar{x}(t) - \bar{F}_g + v_I(t)) & \text{if } c(\delta)\bar{x}(t) \leq 0, \\ M_1^{-1}(\dot{y}_{12,ref}(t) - F_\alpha \bar{x}(t) - \bar{F}_g - \bar{F}_p(x,\delta) + v_{II}(t)) & \text{if } c(\delta)\bar{x}(t) \geq 0, \end{cases} \tag{5.13}$$

where $M_1 = (CAB)$, $y_{12,ref} = [y_1, y_2]_{ref}^T$. The feedback gain $F_\alpha$ is defined by the controllability invariants $\alpha_{ijk}$ of the linear part of the system (Equation (5.8)). The structure of the designed feedback system is shown in Figure 5.1.

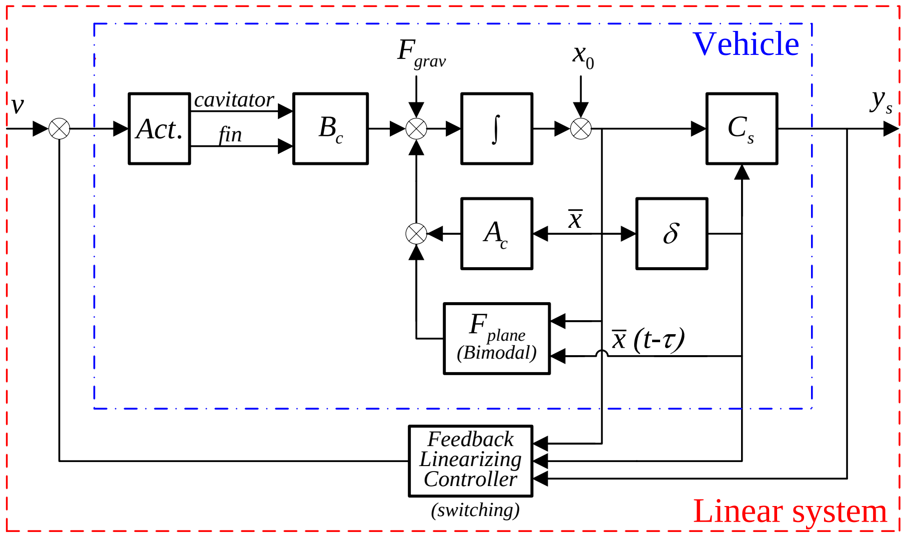


Figure 5.1: Control architecture for supercavitating vehicle model

The feedback linearized closed-loop has the following form in both modes:

$$\dot{\bar{x}} = \begin{bmatrix} 0 & 1 & 0 & 0 \\ 0 & 0 & 0 & 0 \\ 0 & 0 & 0 & 1 \\ 0 & 0 & 0 & 0 \end{bmatrix} \bar{x} + \begin{bmatrix} 0 & 0 \\ 1 & 0 \\ 0 & 0 \\ 0 & 1 \end{bmatrix} \begin{bmatrix} v_1 \\ v_2 \end{bmatrix} \tag{5.14}$$

The switching condition is given by the sign of $y_s = c(\delta)\bar{x}$.

### 5.1.2 Controllability analysis of the bimodal system

The controllability of the linearized, bimodal dynamics needs to be analyzed and a tracking controller designed. Results on controllability of single input single LTI systems with single switching surface and relative degrees $r = r_1 = r_2 = 1$ has been published by [36].

The problem is reduced to analyzing the dynamics of the system on the switching surface in [36]. This is given by the zero dynamics derived with respect to the "switching output" $y_s$. It was shown that the zero dynamics have to be controllable when using positive $y_s$ in one mode (negative $y_s$ in the second mode, respectively). It was assumed that the system is both left and right invertible and the dynamics is continuous on the switching surface, i.e. $A_1x + b_1u = A_2x + b_2u$.

Since the relative degree $r = 1$, under the above assumptions, the zero dynamics can be written as:

$$\dot{\eta}(t) = H\eta + \begin{cases} g_1 y_s(t) & \text{if } y_s(t) \leq 0, \\ g_2 y_s(t) & \text{if } y_s(t) \geq 0, \end{cases} \tag{5.15}$$

with $\eta \in \mathbb{R}^{n-1}$.

It can be proved that the problem (5.15) is equivalent to the following (sign constrained) switching problem with systems $(H, g_1)$ and $(H, -g_2)$ with a nonnegative input $u$, see [35]. The same results can be obtained using the following reasoning: in the unconstrained input case to compute the reachability set the following Lie-algebra of the vector spaces $H\eta + g_1 u$ and $H\eta - g_2 u$, i.e., the Lie-algebra generated by $H\eta + [g_1 \ \ -g_2][u \ u]^T$, needs to be defined. Denote this set by $\mathcal{R}(H, [g_1, -g_2])$. Thus a necessary condition of controllability is that $\mathcal{R}(H, [g_1, \ -g_2]) = \mathbb{R}^n$, i.e., the pair $(H, [g_1, -g_2])$ has to be controllable. This is a Kalman - like rank condition. Since one can use only sign constrained inputs, this imposes an additional condition on $H$. A sufficient condition is that if $H$ has an even number of eigenvalues with zero real parts, then the zero dynamics is controllable with nonnegative inputs. More results on controllability with nonnegative inputs can be found in [37,38].

This result is extended for our application as follows. Consider the MISO system with $B \in \mathbb{R}^{n \times m}$ and $y_s = Cx$. Also consider the case, when there is a direction $p \in ImB$ such that the system is left and right invertible corresponding to the direction $p$. Using the notation $B = [\ p \ \bar{B}]$, one has the system:

$$\dot{x} = Ax + pu_p + \bar{B}\bar{u}, \quad y_s = Cx. \tag{5.16}$$

Let us denote by $\mathcal{V}^*$ the largest $(A, p)$ - invariant subspace in $\mathcal{C} = kerC$ and by $\mathcal{W}_*$ the smallest $(C, A)$ invariant subspace over $Imp$. It follows that system has the following decomposition induced by a choice of basis in $\mathcal{V}^*$ and $\mathcal{W}_*$:

$$\dot{\xi} = A_{11}\xi + \gamma v \tag{5.17}$$

$$u_p = \frac{1}{\gamma}(-A_{12}\eta - \bar{B}_{21}\bar{u} + v) \tag{5.18}$$

$$\dot{\eta} = A_{22}\eta + \bar{B}_{22}\bar{u} + Gy_s, \tag{5.19}$$

Since $r = 1$, $\xi = y_s$, equation (5.19) describes the dynamics of the system on $\mathcal{C}$. Rewrite the equation of this zero dynamics as

$$\dot{\eta} = P\eta + Q\bar{u} + Ry_s. \tag{5.20}$$

assuming that $Q$ is monic.

**Proposition 5.1.** *If the pair $(P, Q)$ is controllable, then $\eta$ is controllable "without" using $y_s$, e.g. by applying $\bar{u} = Q^{\#}(-Ry_s + w)$, where $^{\#}$ denotes the pseudo-inverse. If the pair $(P, Q)$ is not controllable, then the conditions of controllability with unconstrained $\bar{u}$ but nonnegative $y_s$ is the following.*

1. *The pair $(P, [Q\,R])$ has to be controllable.*

2. *Consider the decomposition induced by the reachability subspace $\mathcal{R}(P, Q)$,*

$$\dot{\eta}_1 = \quad P_{11}\eta_1 + P_{12}\eta_2 + Q_1\bar{u} + R_1y_s \tag{5.21}$$

$$\dot{\eta}_2 = \qquad P_{22}\eta_2 + R_2y_s, \tag{5.22}$$

*where $R_2 \neq 0$. Then $P_{22}$ has no real eigenvalues.*

**Remark 5.1.** *The first condition is a Kalman-rank condition. The second one can be given in some alternative forms using e.g. results from [37, 38].*

For the high speed supercavitating vehicle model, this result has to be applied to a time delay system. The following approach is taken.

Since only one delay time is present in the switching condition, it is possible to discretize the system with extended state space by including the delayed state variable. Since feedback linearization has been already applied, it is possible to use a backward difference scheme defined for LTI systems that preserves the geometry needed to analyze the zero dynamics. The resulting discrete time state equations are:

$$x(t+1) = A_d x(t) + B_d v(t), \quad y_s = C_d x(t) \tag{5.23}$$

where

$$A_d = \begin{bmatrix} 1 & T & 0 & 0 & 0 \\ 0 & 1 & 0 & 0 & 0 \\ 0 & 0 & 1 & T & 0 \\ 0 & 0 & 0 & 1 & 0 \\ 1 & 0 & 0 & 0 & 0 \end{bmatrix}, \quad B_d = \begin{bmatrix} 0 & 0 \\ \beta_{21}T & \beta_{22}T \\ 0 & 0 \\ \beta_{41}T & \beta_{42}T \\ 0 & 0 \end{bmatrix}, \quad C_d = [1, 0, v, 0, -1] \tag{5.24}$$

where $T$ denoted the sample time.

The next step is to find the relative degrees by selecting one of the inputs, say $v_1$ first. They are identically $r = 2$ for both modes since the feedback linearization and state transform resulted in the same linear canonic form in both modes.

To obtain the zero dynamics one has to construct a state transform matrix $T_{cd}$ from the row vectors spanning the orthogonal complement of $\mathcal{V}^*$ and $imB_{d1}$ where $imB_{d1}$ is the first column of $B_d$.

It can be shown that $\mathcal{V}^{*\perp} = span\{c_s, c_s A_d\}$ and that the remaining three rows of $T_{cd}$ is selected from $ImB_1^{\perp}$ resulting in the transform:

$$T_{cd} = \begin{bmatrix} & & c_s & & \\ & & c_s A & & \\ 1 & 0 & 0 & 0 & 0 \\ 0 & 0 & 1 & 0 & 0 \\ 0 & \beta_{41}T & 0 & -\beta_{21}T & 0 \end{bmatrix} \tag{5.25}$$

Using this state transform $[\xi^T(t), \eta^T(t)]^T = T_{cd}x(t)$ and that $\mathcal{V}^*$ is $(A_d, B_{d1})$ invariant, the following decomposition is obtained:

$$\xi(t+1) = \begin{bmatrix} 0 & a_{12} \\ 0 & a_{22} \end{bmatrix} \xi(t) + \begin{bmatrix} 0 \\ b_{21} \end{bmatrix} v_1(t) + \begin{bmatrix} 0 \\ e_{22} \end{bmatrix} v_2(t) \tag{5.26}$$

$$y_s = \begin{bmatrix} 1 & 0 \end{bmatrix} \xi(t) \quad \textit{switching condition} \tag{5.27}$$

$$\eta(t+1) = P\eta(t) + R\xi(t) + Qv_2(t), \tag{5.28}$$

where

$$P = \begin{bmatrix} p_{11} & p_{12} & p_{13} \\ 0 & p_{22} & p_{23} \\ 0 & 0 & p_{33} \end{bmatrix}, \quad R = \begin{bmatrix} 0 & r_{12} \\ 0 & r_{22} \\ 0 & 0 \end{bmatrix}, \quad Q = \begin{bmatrix} 0 \\ 0 \\ q_{31} \end{bmatrix}. \tag{5.29}$$

The zero dynamics are described by the last equation. (The same approach can be repeated when selecting the second column of $B_d$.) Using Proposition 1, it can be seen that due to their special structure, the $(P, Q)$, pair is controllable. This implies that the dynamic inversion controller with switching and pole placement for tracking error stability can be applied to control the bimodal system.

## 5.2 Outer loop control strategy

A single, linear outer-loop controller can guarantee stability and achieve the desired tracking properties with feedback linearization, since the system behaves the same regardless of the interior switching state. A variety of linear design approaches can be used for stability and control [39–42]. The ability of the controller to directly handle constraints could provide significant benefits if planing is restricted. Hence, a simple pole placement controller is compared with receding-horizon control approach which allows for actuator and state constraints.

The inner loop dynamics after feedback linearization, using the new canonical coordinates are:

$$\begin{bmatrix} \dot{x}_1 \\ \dot{x}_2 \\ \dot{x}_3 \\ \dot{x}_4 \end{bmatrix} = \begin{bmatrix} 0 & 1 & 0 & 0 \\ 0 & 0 & 0 & 0 \\ 0 & 0 & 0 & 1 \\ 0 & 0 & 0 & 0 \end{bmatrix} \begin{bmatrix} x_1 \\ x_2 \\ x_3 \\ x_4 \end{bmatrix} + B_c \begin{bmatrix} \Delta\delta_f \\ \Delta\delta_c \end{bmatrix} \tag{5.30}$$

where $\Delta\delta_{f,c}$ denotes the additional deflection of the fins and cavitator commanded by the higher level controller. This system is nilpotent, because all eigenvalues of $A$ are zero. There is no cross coupling between the first two states (vertical position and speed), and the other states (vehicle angle and angle rate). Hence, they can be controlled independently by the two control inputs.

### 5.2.1 Multivariable Pole Placement for Tracking

An easy and tractable control design approach for linear systems is pole placement. The performance objective is to track desired state commands with no restrictions on the maximum actuator deflections, since the tracking signals have minor contribution on the actuator deflections compared with the action due to planing. With the assumption of full state feedback, this can be done fairly simply. The inversion based controller has the form:

$$\begin{bmatrix} u_1(t) \\ u_2(t) \end{bmatrix} = (CAB)^{-1}(-[\alpha_u] \begin{bmatrix} x_1(t) \\ x_2(t) \end{bmatrix} - [\alpha_l] \begin{bmatrix} x_3(t) \\ x_4(t) \end{bmatrix} - [G_c] - [P_c(t,\tau)]) + \begin{bmatrix} \Delta\delta_f \\ \Delta\delta_c \end{bmatrix} \tag{5.31}$$

Where the $\alpha_{u,l}$ coefficients are the elements of the $A_c$ matrix (Equation (5.8)) and $\Delta\delta_{f,c}$ are the signals responsible for reference tracking.

$$[\alpha_u] = \begin{bmatrix} -\alpha_{110} & -\alpha_{111} \\ -\alpha_{210} & -\alpha_{211} \end{bmatrix}; \quad [\alpha_l] = \begin{bmatrix} -\alpha_{120} & -\alpha_{121} \\ -\alpha_{220} & -\alpha_{221} \end{bmatrix} \tag{5.32}$$

The reference tracking part of the controller responsible for pole locations:

$$\begin{aligned} \begin{bmatrix} \Delta\delta_f \\ \Delta\delta_c \end{bmatrix} = (CAB)^{-1} \Bigg\{ & \begin{bmatrix} -\bar{\alpha}_{110} & -\bar{\alpha}_{111} \\ 0 & 0 \end{bmatrix} \begin{bmatrix} x_1(t) - x_{1,ref}(t) \\ x_2(t) - x_{2,ref}(t) \end{bmatrix} + \\ & + \begin{bmatrix} 0 & 0 \\ -\bar{\alpha}_{220} & -\bar{\alpha}_{221} \end{bmatrix} \begin{bmatrix} x_3(t) - x_{3,ref}(t) \\ x_4(t) - x_{4,ref}(t) \end{bmatrix} + \begin{bmatrix} \dot{x}_{1,ref} \\ \dot{x}_{3,ref} \end{bmatrix} \Bigg\} \end{aligned} \tag{5.33}$$

The feedback linearized closed loop has the following form in all modes:

$$A_{cl} = A_c - B_c F_{inv} + B_c F_{ctr} = \begin{bmatrix} 0 & 1 & 0 & 0 \\ -\bar{\alpha}_{110} & -\bar{\alpha}_{111} & 0 & 0 \\ 0 & 0 & 0 & 1 \\ 0 & 0 & -\bar{\alpha}_{220} & -\bar{\alpha}_{221} \end{bmatrix} \tag{5.34}$$

The closed-loop system is stable for a given set of $\bar{\alpha}$ coefficients.

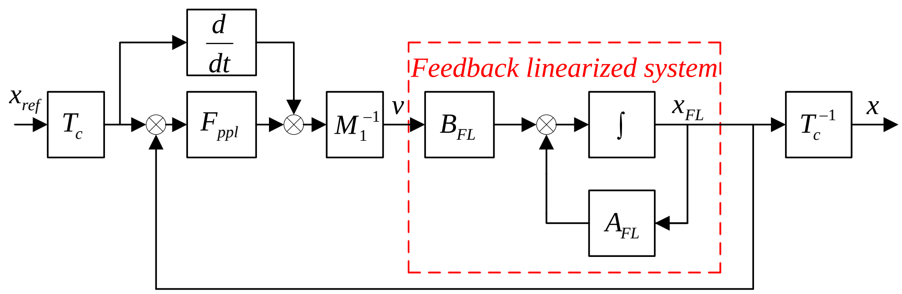


Figure 5.2: Control architecture for supercavitating vehicle model

The tracking part of the controller is responsible for the location of the poles. The eigenvalues of the system are:

$$\lambda_{1,2} = -0.5\bar{\alpha}_{221} \pm 0.5\sqrt{(-\bar{\alpha}_{221})^2 - 4\bar{\alpha}_{220}} \tag{5.35}$$

$$\lambda_{3,4} = -0.5\bar{\alpha}_{121} \pm 0.5\sqrt{(-\bar{\alpha}_{121})^2 - 4\bar{\alpha}_{120}}$$

The poles can be freely adjusted in the stable region, while the driving factor for actuator deflections remains planing cancelation. Hence, the only limiting factor for setting the pole locations is the actuator bandwidth.

The structure of the feedback controller is shown in Figure 5.1. The inner-loop controller feedback linearizes the system, and the outer-loop controller handles reference tracking. It is possible to track both position and angle commands with consistent position, velocity, angle and angle rate reference signals. The designed pole placement controller also operates on the transformed canonic coordinates. The special structure of the feedback linearized system allows the vehicle position and angle to be controlled independently.

### 5.2.2 Outer-Loop RHC control

This section describes the design of an outer-loop controller using Receding Horizon Control (RHC). The previous section focused on the inner-loop control with a simple pole-placement controller to achieve reference tracking properties. In addition to the performance specifications, the reference tracking control should avoid actuator saturation and immersion into the fluid, preventing the inner loop to command unrealistically high deflections to cancel out the forces generated by planing. Predicting planing may provide beneficial information which can broaden the stable operation envelope of the vehicle, enabling more aggressive reference trajectories, at the expense of slightly degraded tracking performance.

A popular way to avoid saturations on the actuators is to use prediction based control methods (Receding Horizon Control or Model Predictive Control). The proposed control scheme is shown in Figure 5.3.

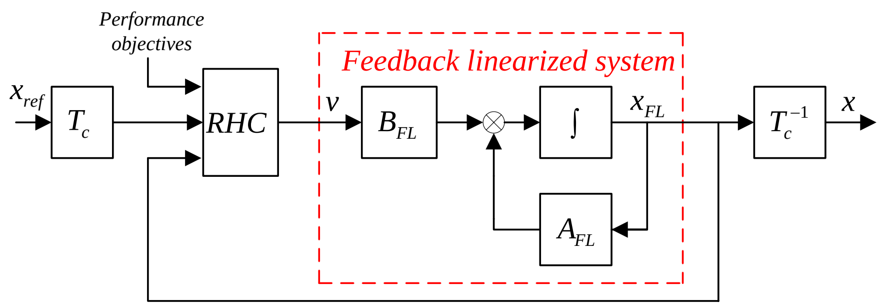


Figure 5.3: The RHC control loop structure

The controller structure differs from the controller discussed in [32], as the outer-loop uses RHC technique (equation 5.36).

$$\begin{bmatrix} u_1(t) \\ u_2(t) \end{bmatrix} = (CAB)^{-1}\left(-[\alpha_u]\begin{bmatrix} x_1(t) \\ x_2(t) \end{bmatrix} - [\alpha_l]\begin{bmatrix} x_3(t) \\ x_4(t) \end{bmatrix} - [G_c] - [P_c(t,\tau)] - \begin{bmatrix} v_{1,RHC}(t) \\ v_{2,RHC}(t) \end{bmatrix}\right) \tag{5.36}$$

The standard linear RHC problem and solution using quadratic programming is well known [43] and reliable software tools are available for controller design [44]. The discrete time controller is obtained in a receding horizon fashion using model-based predictions by solving a finite time constrained optimization problem:

$$\min_{\Delta u(k|k),\ldots,\Delta u(m+k-1|k),\varepsilon} \left\{ \sum_{i=0}^{p-1} \left( \sum_{j=1}^{n_y} \left| w_{i+1,j}^{y} (y_j(k+i+1|k) - r_j(k+i+1)) \right|^2 + \right.\right.$$
$$\left.\left. + \sum_{j=1}^{n_u} \left| w_{i,j}^{\Delta u} \Delta u_j(k+i|k) \right|^2 + \sum_{j=1}^{n_u} \left| w_{i,j}^{u} (u_j(k+i|k) - u_{j,des}(k+i)) \right|^2 \right) + \rho_\varepsilon \varepsilon^2 \right\} \tag{5.37}$$

where $\Delta u$ denotes the input increments, $(k+i|k)$ indicates the value for time $k+i$ using the available information at $k$. The tracking is achieved by minimizing the error between

$y(k+i|k)$ the predicted output and the reference $(r(k+i))$. The actuator usage and input rates are also weighted in the cost function with $w_{i,j}$ coefficients. The constraints on inputs, input rates, or outputs can be implemented as soft constraints:

$$u_{j,min}(i) - \varepsilon V^u_{j,min}(i) \leq u_j(k+i|k) \leq u_{j,max}(i) + \varepsilon V^u_{j,max}(i) \tag{5.38}$$

where $\varepsilon$ is the slack variable relaxed with weight $V_j^u$, which is heavily penalized in the cost function with $\rho_\varepsilon$. Normally input constraints are implemented as hard constraints while output constraints are softened to ensure feasibility when large disturbances are expected. The prediction $(n_y)$ and control horizons $(n_u)$ have large impacts on the solution and computational requirements. In general the prediction does not exactly match the system response. Hence, the best solution is often obtained by a suitable finite prediction horizon, while the decision variable (the control signal), is changed over a shorter horizon, and then held constant through the end of the prediction horizon.

The special structure of the inner-loop controller requires only a single linear RHC controller for the feedback linearized system described by Equation 5.14. The objectives are reference tracking and planing avoidance. One of the main assumptions is constant horizontal speed, hence the delay is assumed constant. The delay in the simulation is $1.8\ m/(75\ m/s) = 0.024\ s$ which is included in the discrete time system model used for predictions in the RHC controller. The extended state-space system includes the delayed position of the nose in addition to the states described in Equation 5.39. The sampling time of the RHC controller is set to $0.008\ s$, three unit delays are required to express the desired state.

$$\begin{bmatrix} x_1(t) \\ x_2(t) \\ x_3(t) \\ x_4(t) \\ x_5(t) \\ x_6(t) \\ x_7(t) \end{bmatrix} = \begin{bmatrix} z(t) \\ -V\theta(t) + w(t) \\ \theta(t) \\ q(t) \\ z(t-\tau) \\ z(t-2\tau) \\ z(t-3\tau) \end{bmatrix} \tag{5.39}$$

The system matrices used for prediction are derived from the continuous time model using backward difference approximation [45]. This preserves the simple geometry of the equations, including the relative degree, and the dynamics are easier tractable, than with the simple zero-order hold equivalence transformation.

$$A_d = \begin{bmatrix} 1 & T & 0 & 0 & 0 & 0 & 0 \\ 0 & 1 & 0 & 0 & 0 & 0 & 0 \\ 0 & 0 & 1 & T & 0 & 0 & 0 \\ 0 & 0 & 0 & 1 & 0 & 0 & 0 \\ 1 & 0 & 0 & 0 & 0 & 0 & 0 \\ 0 & 0 & 0 & 0 & 1 & 0 & 0 \\ 0 & 0 & 0 & 0 & 0 & 1 & 0 \end{bmatrix}, \quad B_d = \begin{bmatrix} 0 & 0 \\ \beta_{21}T & \beta_{22}T \\ 0 & 0 \\ \beta_{41}T & \beta_{42}T \\ 0 & 0 \\ 0 & 0 \\ 0 & 0 \end{bmatrix}, \tag{5.40}$$

$T$ denotes the sample time in $A_d$ and $B_d$. The seventh state ($x_7$) represents the delayed position of the nose. The planing condition is expressed using $x_7$ with the relation described in Equation 4.12:

$$R - R_c \leq C_p x_d \leq R_c - R, \; C_p = [1, 0, L, 0, 0, 0, -1] \tag{5.41}$$

This additional output can be used in the control predictions to constrain planing, causing the inner-loop to generate smaller control deflections.

Direct constraint fulfilment cannot be guaranteed because the two controllers act parallel (Figure 5.1) and only the RHC signals are constrained. This is only sufficient for a limited maneuver range. Usually as soon as the RHC command reaches its maximum value, the body hits the cavity wall or the tracking performance becomes poor. The wall impact results in oscillations and increased control deflections, while the drag on the hull also increases.

## 5.3 Control of a Supercavitating Vehicle Model

Simulations are performed in the Matlab/Simulink environment, and parameter dependencies are analyzed for comparison with a basic setup. The reference trajectory is an obstacle avoidance maneuver: the horizontal speed is constant $75 m/s$ while the vehicle moves down 2 $m$ and returns to continue its straight path within 1.2 seconds, as seen in Figure 5.4. The initial trajectory is composed by four arcs approximated by B-splines to provide continuous, easily numerically differentiable functions. The additional reference signals are derived using further assumptions. The vertical position change ($\dot{z}(t)$) is caused by the vertical speed of the vehicle ($w(t)$) plus the longitudinal speed component's projection to the vertical plane ($-V\theta(t)$). Earlier results [16] suggested that $w$ is closely related to planing, hence it is desired to be kept small.

$$w_{ref}(t) = 0, \quad \theta_{ref}(t) = \frac{-1}{V}\dot{z}_{ref}(t) \tag{5.42}$$

The pitch rate reference ($q_{ref}(t)$) can be calculated as $\dot{\theta}_{ref}(t)$. It is assumed that the environment (static pressure and water density) remains constant during the maneuver. A 200 $rad/s$ first order actuator model is included in the simulation, which was not considered in the control design. In addition to the model mismatch, the system is also affected by random disturbance, which is based on measurements derived from water tunnel experiments done in UMN St. Anthony Falls Laboratory [46]. The cavity wall disturbance is modeled as white noise passed through a 150 $Hz$ second order low-pass filter (Equation 5.43). The cavity disturbance has maximum 10% magnitude of the nominal cavity gap. This disturbance by nature does not show up in all simulations, if the transom is far enough from the cavity walls, it has no effect on the vehicle. But if the transom is close to the cavity surface and immersion occurs, the immersion depth will be determined not only by the vehicle states but also by the noisy cavity radius which has a randomly varying component. A non-smooth cavity represents a challenge as the cavity wall is the switching surface of the controller.

$$G_n = \frac{0.1}{55.93}(Rc - R)\frac{10^6}{s^2 + 2000 + 10^6} \tag{5.43}$$

### 5.3.1 Pole Placement simulation results

The performance specifications are to track trajectory reference commands while minimizing limit cycle oscillations. Reference tracking has a lower priority compared with oscillation attenuation. The following controller gains were selected:$-\bar{\alpha}_{110} = -40000; -\bar{\alpha}_{111} = -400; -\bar{\alpha}_{220} = -90000; -\bar{\alpha}_{221} = -600$. With which the resulting eigenvalues are $-300; -300; -200; -200$ (Equation 5.35).

The contribution from the tracking part of the controller with these high gains is still

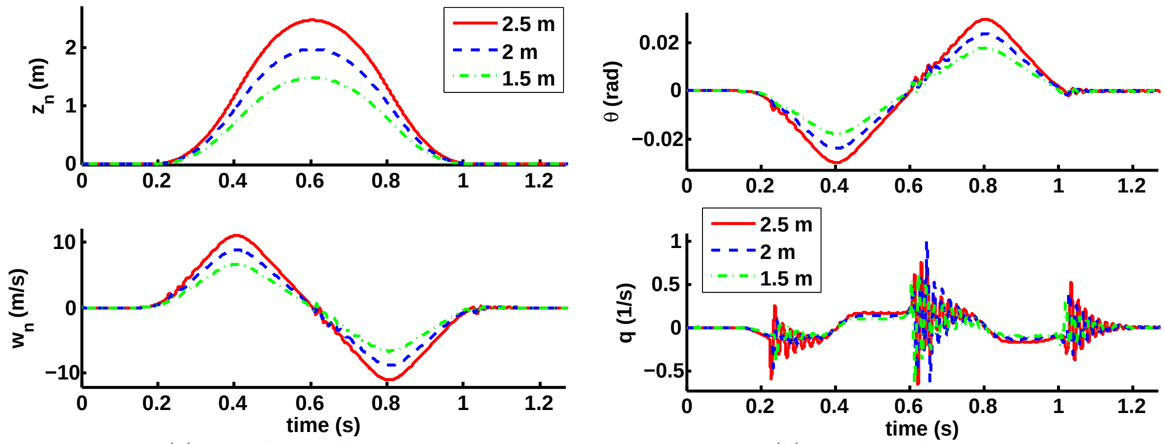


(a) Translational states.    (b) Rotational states.

Figure 5.4: Tracking different amplitude maneuvers with pole placement controller.

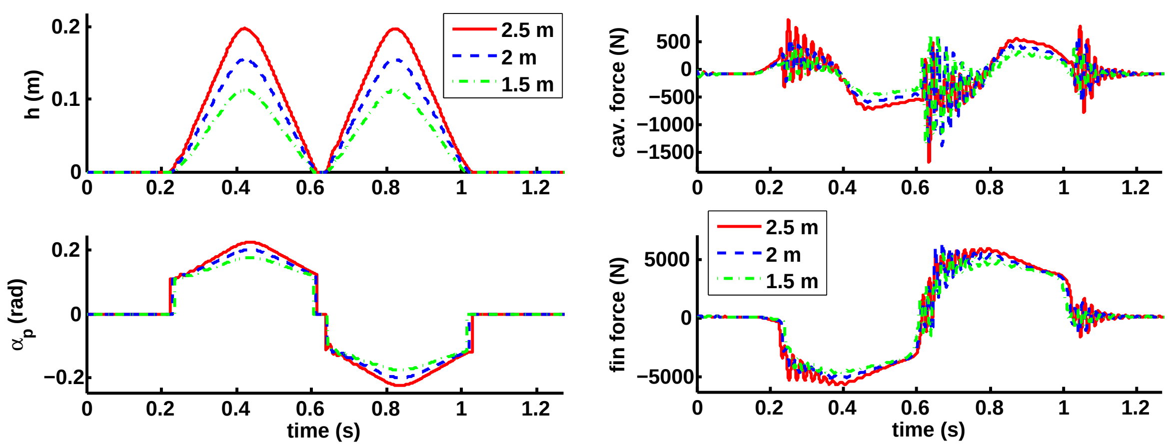


(a) Variables describing planing.    (b) Actuator deflections.

Figure 5.5: Tracking different amplitude maneuvers with pole placement controller.

negligible compared with the inversion based contribution to compensate the effect of planing.

Three maneuvers with $1.5, 2$ and $2.5$ $m$ amplitudes are compared in Figures 5.4 and 5.5. The tracking performance of the closed-loop system is very good, considering the high disturbance level, though the planing depth ($h$) is significant. Large oscillations are present when the transom steps over from one mode to another. The planing depth has a clear relationship with the sharpness of the maneuver (Figure 5.5). These sharp maneuvers require large actuator deflections, and create significant drag. Increased thrust would be required to maintain constant longitudinal speed. Including this additional control objective

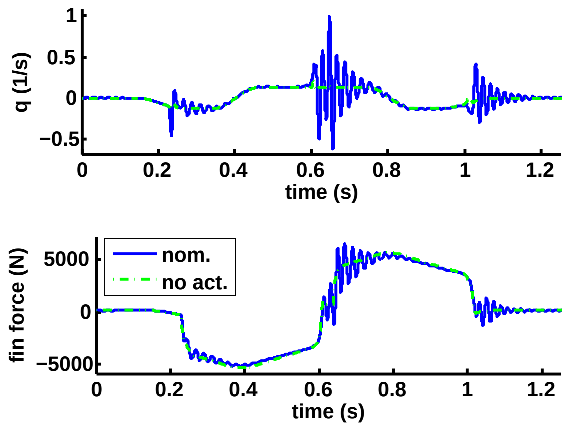


Figure 5.6: Role of the actuator model with pole placement controller

is undesirable, since thrust is not a control variable.

Accurate knowledge of the delay in the cavity shape description plays an important role in the performance. The vehicle tracks the reference signal well given accurate information of the delay. Imprecise knowledge of the delay results in oscillations and the system becomes unstable at approximate $15 - 20\%$ error. Simulations with 2.4 $ms$ variation in the delay lead to poor performance with oscillations and intensive actuator usage.

The original controller was designed without an actuator model. The effect of a first order actuator, shown on Figure 5.6, with 30Hz bandwidth is considered through the simulations. Significantly slower actuators were not able to stabilize the system, while faster actuators achieved better performance. The case when the actuator is treated as unity (Figure 5.6) clearly results in better performance than the one with the first order actuator model, since only small oscillations occur. All other results presented have the actuator model included.

Sensitivity to cavity wall disturbances is investigated by varying the magnitude and frequency content of the disturbance. The maximum planing depth remains the same if the disturbance magnitude increase by a factor of 5 to 0.5 times the cavity gap, but the actuator deflections are slightly more aggressive. The responses have larger spikes and has longer settling times. Changing the second order disturbance filter to a first or third order filter with the same bandwidth has a small effect on the response. Hence the pole placement design is relatively insensitive to the smoothness of the cavity wall disturbance, because of the high planing depth.

The vehicle has noticeably different dynamical behavior for long excursion maneuver, which do not require high pitch rate motion, (Figure 5.10). The reference maneuver is a 4 $s$ down-up maneuver with amplitude 20 $m$, and as suggested in [16] with the reference on normal velocity ($w_{ref}(t)$) set to zero. The maneuver can be executed without planing, because the disturbances on cavity shape fade away noticeably faster than the maneuver changes. The cavity bubble is in quasi-steady state during the maneuver.

### 5.3.2 RHC simulation results

The continuous-time feedback linearization controller is implemented in the inner-loop while the discrete RHC controller is running at 0.008 $s$ sampling time as an outer-loop (Figure 5.3). The predictive controller has a six step prediction horizon, which is sufficiently longer than the delay in the cavity description. The best results are achieved with a three step long control horizon, which allows sufficient freedom for the control solutions but is less sensitive to uncertainties in the predictions. Constraints are chosen corresponding to the physical limitations of the vehicle. The maximum actuator deflections are set to $\pm 0.2$ $rad$ and the maximum deflection rates are $\pm 100$ $rad/s$.

The maximum deflection is meant to constrain the maximum achievable force, while its angle value is less important, since the size of the fins are currently under investigation. The maximum vertical speed is 28.75 $m/s$ and the maximum pitch angle is set to 0.25 $rad$ to ensure the validity of small angle approximations. Structural loads are closely related to maximum pitch rate which is constrained to $\pm 10$ $rad/s$. Drag reduction and smooth motion with extending the operation envelope of the vehicle can be achieved with planing-free flight, while the control surface deflections are also lower. The maximum transom deviation from the cavity centerline is constrained to 1 $cm$, which is smaller than the nominal cavity gap (1.39 $cm$) required to guarantee planing avoidance in the presence of disturbances.

The optimization problem weights differently the input and output variables. The input weight is set to 100 on both inputs, and the input rate weight set to 50. These weights can be interpreted with the knowledge of the output-error weights. The high position error weight (25000) indicates that position tracking received the highest priority, while

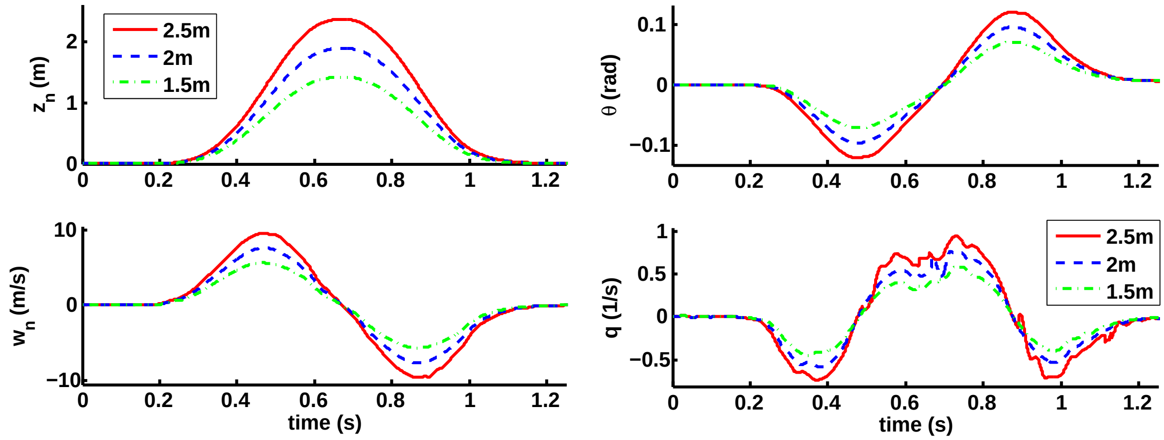


(a) Translational states.

(b) Rotational states.

Figure 5.7: Tracking different amplitude maneuvers with predictive controller.

the lower velocity error weight (1000), angle error weight (100) and angle rate error weight (2500) ensure that tracking of these variables have lower impact on the optimization. These slightly penalized variables improve stability with oscillation damping. The planing depth is not weighted high (1000). It is important to note that the output variable constraints are implemented as soft constraints, and planing depth constraint violations generate 10 times higher slack variable than other outputs. The slack variable weight is chosen to be $2.5 \times 10^9$. The actuator model $G_{act} = \frac{200}{s+200}$, and the disturbance model $G_n = \frac{0.1}{55.93}(Rc - R)\frac{10^6}{s^2+2000+10^6}$ are the same as before.

The same 1.2 $s$ reference trajectory on $z(t), w(t), \theta(t)$ and $q(t)$ is used. The results with the basic setup for $1.5, 2,$ and 2.5 $m$ amplitude maneuvers are shown in Figures 5.7 and 5.8.

The RHC reference tracking performance is less precise (Figure 5.10) than the pole placement controller, particularly on the signals with lower weights. The tradeoff is that planing occurs only for short periods with low depth (Figure 5.8). Tracking is achieved with low actuator deflections, without oscillations. As the trajectory becomes more aggressive, planing occurs more frequently. This requires increased actuator usage, though the maximum planing depth, unlike in the pole placement case, is not increase with the trajectory amplitude. The overall control effort is significantly smaller than the pole placement design though at the expense of the state trajectories, especially the angle rate, being less smooth.

Uncertainty in delay time induces significant performance degradation because the

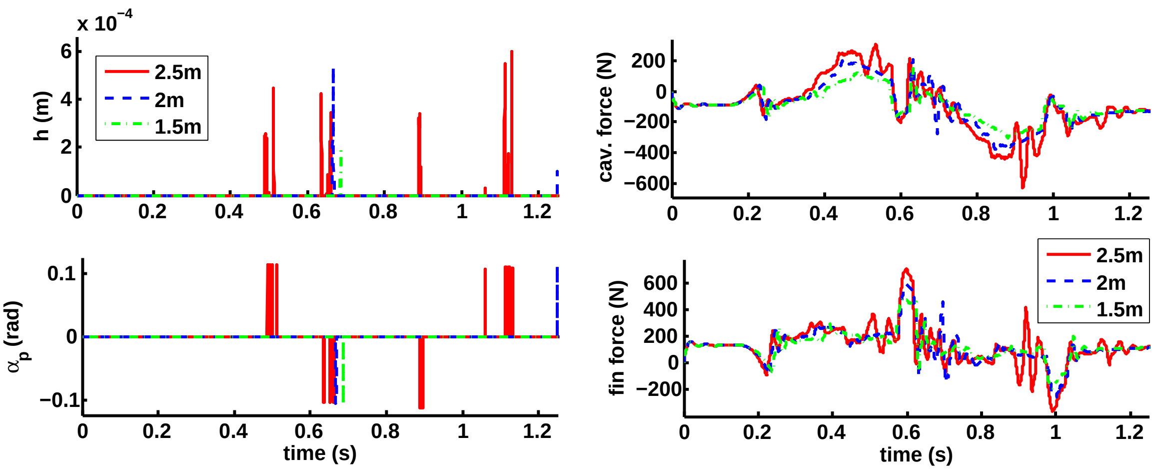


(a) Variables describing planing. (b) Actuator deflections.

Figure 5.8: Tracking different amplitude maneuvers with predictive controller.

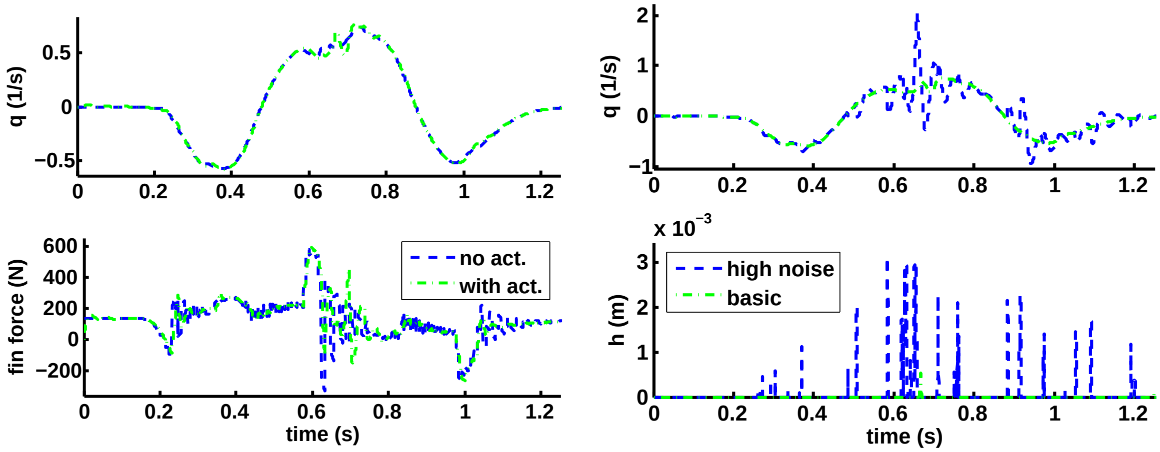


(a) Role of the actuator model. (b) Role of disturbance magnitude.

Figure 5.9: Sensitivity of RHC tracking performance.

bounds on constraining the maximum transom deviation from the cavity centerline are very tight. Uncertainty in the delay of 24 $ms$ leads to oscillatory behavior, and larger control deflections are commanded due to the consequent uncertainty in the planing location. The closed-loop system becomes unstable around $10-15\%$ $(24-36\ ms)$ error in delay time.

The impact on tracking performance due to the addition of actuators, which are not addressed in the controller design, is shown in Figure 5.9. As one would expect, the performance is better if the actuator is perfect. Planing occurs for a very short time when

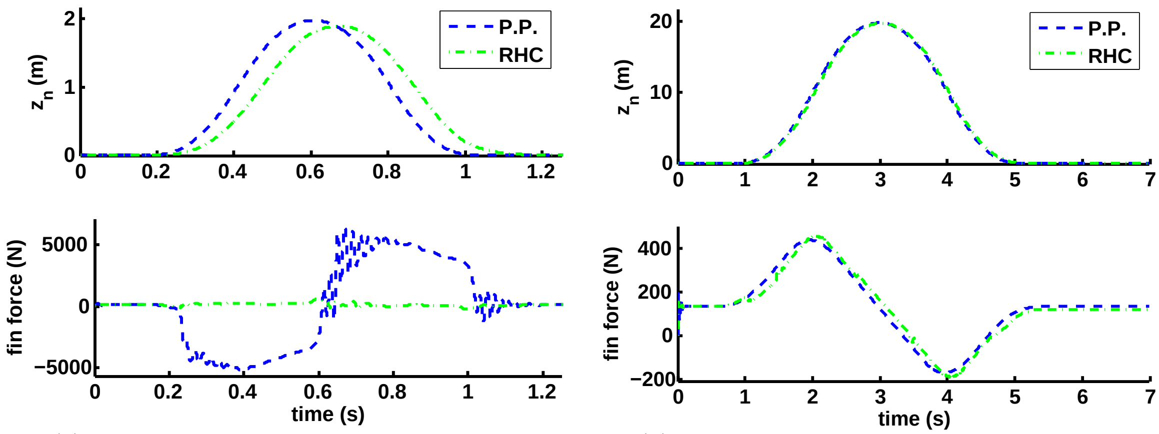


(a) Short maneuver with 2 $m$ depth change.

(b) Short maneuver with 20 $m$ depth change.

Figure 5.10: Comparison of pole placement and predictive controller.

actuators are included in the simulation. Assuming perfect actuators provide reduced oscillations, at the expense of high-rate control signals, what can significantly influence the cavity stability [18].

The disturbance magnitude has a strong influence on the performance. A comparison with a disturbance magnitude of 0.1 and 0.5 cavity gap is shown in Figure 5.9. As the disturbance magnitude increases, planing occurs more frequently and the immersion depth increases. This leads to larger control deflections and fast angle rate responses. The position tracking performance is not significantly affected by the disturbance level.

The bandwidth of the cavity disturbance model also influences the closed-loop performance. Although limited information is available about the cavity wall smoothness, it is natural to assume that it is not perfect. The selected disturbance magnitude is $0.1(R_c - R)$ passed through a 1000 $rad/s$ low-pass filter. The nominal simulation uses a second order filter $G_{nom}(s) = \frac{0.1}{K_{nf}}(Rc - R)\frac{10^6}{s^2+2000+10^6}$ which is normalized to provide approximately maximum $0.1(Rc - R)$ magnitude signals. Two other disturbance filters are studied: a normalized first order $(K_1\frac{1000}{s+1000})$ and a third order one $(K_3\frac{10^9}{s^3+3000s^2+3\cdot 10^6 s+10^9})$, they are comparable in point of all their poles are at 1000 $rad/s$ and the maximum magnitude of the cavity disturbance is held constant. The closed-loop response with third-order disturbance filter planes longer, also causing larger angle rates. Hence, it indicates the importance of correct characterization of the cavity wall disturbance.

Longer maneuvers with higher amplitude excursions $(4\ s, 20\ m)$ are also considered

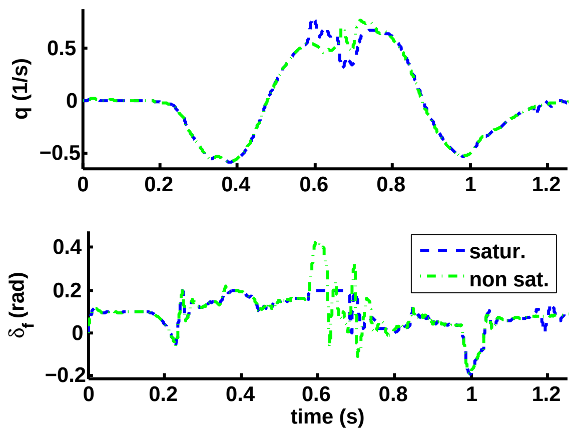


Figure 5.11: Tracking with hard actuator constraints using predictive controller (2m maneuver)

with the RHC design (Figure 5.10). As expected from the pole placement results, planing does not occur with the receding horizon approach. The state and control trajectories are very similar to the pole placement case. Figure 5.10 also shows the importance of planing avoidance, since the pole-placement controller commands unrealistically high actuator deflections in the short maneuver when planing occurs.

A simulation is performed with only a position reference signal, while all the other states are desired to be zero, to analyze how the constraints restrict the motion of the vehicle. Slight degradation in the position tracking performance is observed. The actuator deflection and all the vehicle state trajectories are very close to the original reference case. Hence, as was expected, planing avoidance represents a very tight constraint on the system.

The RHC scheme was implemented on the plant to aid in avoiding actuator saturations. As indicated in Figure 5.1, the control loop has two independent components. Therefore, direct constraint fulfilment is not possible. The controller performance is analyzed with hard actuator constraints on cavitator and fin deflections set to 0.2 $rad$ in Figure 5.11. Note that the fin deflection command increases to 0.4 $rad$ at 0.55 $s$ but it is not allowed. The plant remains stable with slightly degraded performance, while the system with pole placement controller [32] becomes unstable with same conditions at this maneuver. However, if the trajectory becomes more aggressive, the tracking performance and/or the stability of the system become poor with hard actuator limitations using the RHC controller.

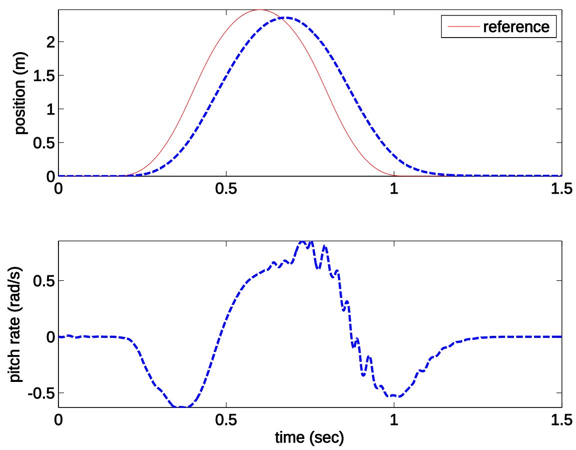


(a) position and pitch rate.

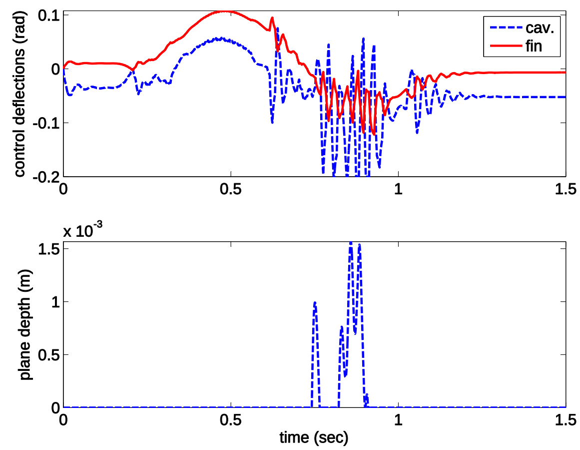


(b) control deflections and plane depth.

Figure 5.12: 2.5 $m$ maneuver with no uncertainty.

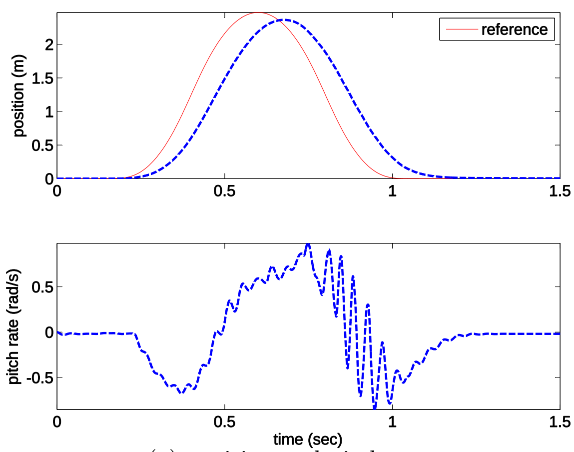


(a) position and pitch rate.

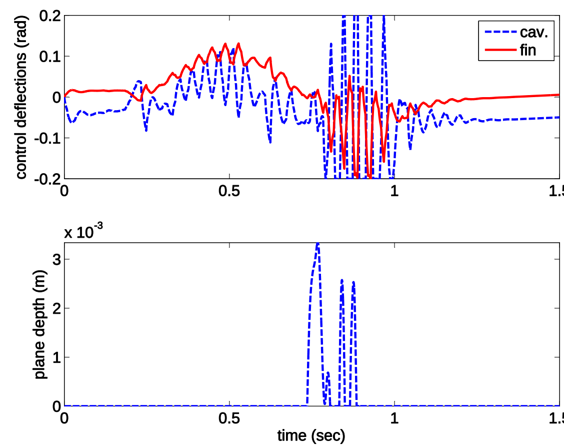


(b) control deflections and plane depth.

Figure 5.13: 2.5 $m$ maneuver with 5% shift in c.g. location.

The effect of uncertainty on the closed loop stability and tracking performance is analyzed to further understand the most important characteristics of the vehicle behavior. A maneuver with 2.5 $m$ amplitude is performed as seen on Figure 5.12, it is a fairly aggressive maneuver, as the tail is in contact with the fluid even when one of the control objectives is to avoid planing. As seen on figure 5.13, where the nominal controller is implemented on a vehicle model which has the c.g. shifted forward by 5%, the tracking performance is not influenced significantly, but the workload of the controller is significantly increased, with more oscillations in pitch rate, while planing is also slightly deeper.

A 5% change in cavitation number drastically changes the cavity-vehicle clearance. No

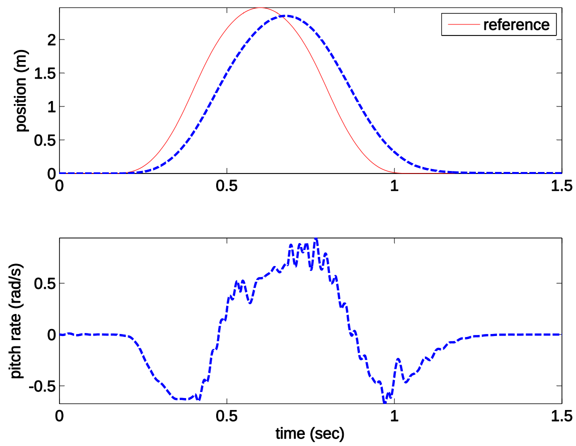

(a) position and pitch rate.

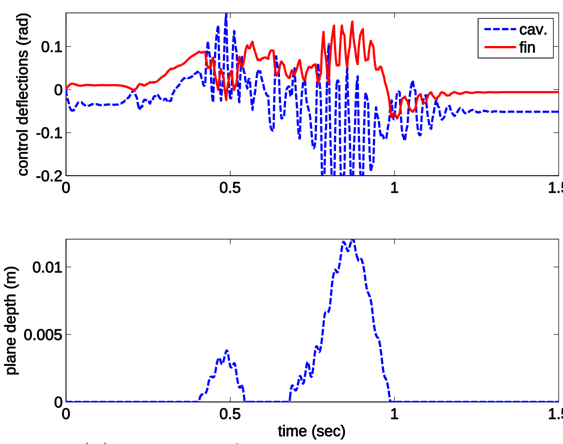

(b) control deflections and plane depth.

Figure 5.14: 2.5 $m$ maneuver with 5% change in cavitation number.

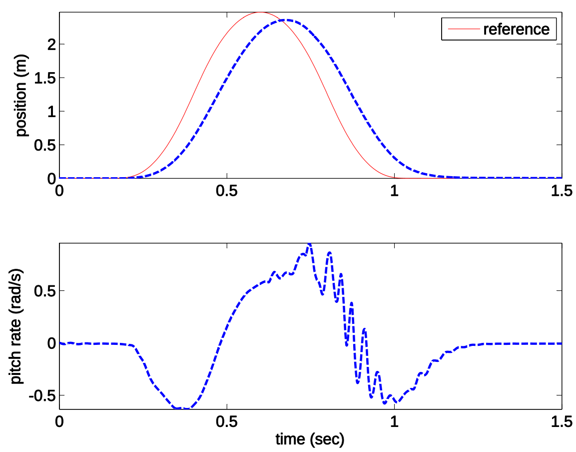

(a) position and pitch rate.

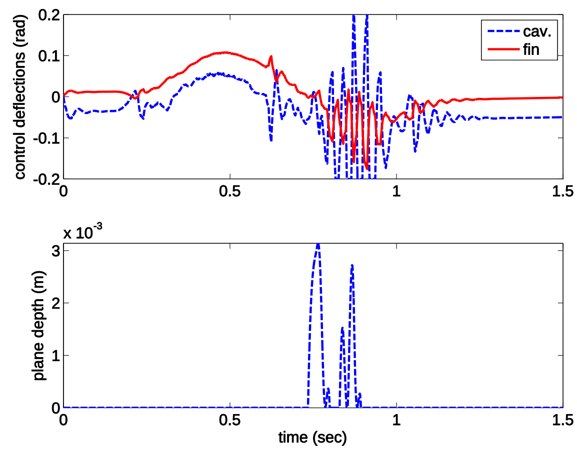

(b) control deflections and plane depth.

Figure 5.15: 2.5 $m$ maneuver with 5% increase in fin force coefficient.

change is observed as long as the vehicle is inside the cavity. When the tail hits the water, strong oscillations are induced which significantly impact the controls, but the trajectory tracking still performs excellent. Only slight differences can be observed between the nominal behavior and when the fin lift coefficient has 5% uncertainty on them, hence this kind of model mismatch poses relatively the easies task for the controller, which can also predicted based on the open loop analysis of the model is Chapter 4.

## 5.4 Conclusion

Two outer loop control strategies are implemented with a dynamic inversion controller for the HSSV. The main objective of the pole- placement design is to stabilize the vehicle and provide precise trajectory tracking commands, while the actuator deflections are not constrained. Stabilization and tracking are successfully demonstrated, and with selection of reference signals, planing was avoided in sufficiently large maneuvers. The pole-placement controller was insensitive to cavity disturbances, though the performance is strongly affected by the delay time. For certain cases, the pole-placement controller led to significant immersion into the fluid requiring high actuator deflections which resulted in increased drag on the hull and fins.

With the receding horizon approach, planing avoidance was successfully incorporated into the performance objectives at the expense of reduced tracking precision and higher sensitivity to cavity disturbances and delay information. The smaller immersion depth and actuator deflections led to significantly lower drag in all maneuvers. Although the approach relies heavily on the precision of the vehicle mathematical model, its beneficial properties make it a reasonable method for further development.

The analysis of the system behavior, and its sensitivity to the cavity parameters indicate that successful development of the HSSV system will require increased collaboration between fluid and control researchers. As an intermediate step, the control design challenges including delayed state dependency, nonlinearities, and switching with disturbed switching surface were analyzed. An extensive comparison was made between a classical linear outer-loop controller and the receding horizon controller. The objective of planing avoidance was solved, for a limited operating range. Important aspects of the reference maneuvers were analyzed and sensitivity properties (a vulnerable point of dynamic inversion) were studied with respect to different cavity disturbances and uncertainties.

# Chapter 6

# Linearized Parameter Dependent Model of the Supercavitating Vehicle

Modeling and control using Linear Parameter Varying (LPV) systems provides an intermediate step between linear and nonlinear theory. LPV techniques offer a systematic design methodology to address control of highly coupled, nonlinear uncertain dynamic systems. The benefits of this approach include guaranteed global stability and robust performance, and real-time implementation of these controllers is similar to that of existing gain-scheduled controllers. LPV control techniques have been applied successfully to a number of advanced, high performance aircraft, missiles, flexible structures and road vehicles [47].

Many finite dimensional systems can be well characterized with LPV systems, where the most dominant underlying dynamics is understood while the state-space description involves other variables, called *exogenous*, which have the certain properties:

- the dynamic evolutionary rules for the exogenous variables behavior is not understood, or is too complicated to be modeled;
- the values of the exogenous variables affect (in a known manner) the evolutionary rules which govern the dynamics of the state variables;

- the values of the exogenous variables change with time, but are measurable in real-time using sensors

These requirements are often met in most aerospace application, hence LPV control gained popularity recently [47]. Further benefit is that almost all design features and experience with linear robust control can be directly translated to the design process, where performance, noise and uncertainties can be treated the same way as in the $\mathcal{H}_\infty$ framework, not like in many nonlinear approaches where precise knowledge of the plant is inevitable, while the desired response is hard to tune.

The complex dynamical behavior of the supercavitating vehicle is largely due to the gas cavity surrounding the hull. This represents a serious challenge for the control designer since the vehicle, including the control surfaces, has to operate under the impact of two fundamentally different media, liquid and gas. The highly nonlinear vehicle dynamics often lead researchers to make simplifying assumptions [31]. The most common assumption is to analyze only the linearized dynamics of the supercavitating vehicle at a specific operating condition. Several researchers have applied conventional control design approaches to this situation [1, 15]. Unfortunately these results could only provide quantitative measures around a specific operating point and are not valid throughout the entire vehicle flight envelope. Hence applying traditional linear control methodology to supercavitating vehicles could limit the potential advantages exploiting supercavitation. Another simplifying assumption is made by researchers is to restrict the motion only to the vertical plane where the motion is symmetric. Successful results were published pointing out the importance of applying nonlinear control design for supercavitating vehicles [2, 16], but these results are limited to longitudinal motion and omit many important dynamical properties of the vehicle. The present chapter focuses on modeling the vehicle dynamics with Linear Parameter Varying (LPV) model, which is a more general class of systems than the Linear Time Invariant (LTI) models widely used in present control methods. The nonlinear behavior of the vehicle can be better captured with an LPV model but design experience with LTI systems accounting for robustness and performance can be directly carried over from robust control to provide solid platform for trajectory tracking guidance level controllers discussed in Chapter 7.

## 6.1 LPV and Quasi-LPV systems

Linear Parameter Varying (LPV) systems are linear systems whose describing matrices depend on a time varying parameter such that both the parameter and its rate of variation are known to be contained in pre-specified sets.

In this case, if $\rho(t)$ denotes the exogenous variable vector, and $x(t)$ denotes the modeled state, then the state equations for the system have the form

$$\dot{x}(t) = f(x(t), \rho(t), u(t)), \quad y(t) = h(x(t), \rho(t), u(t)) \tag{6.1}$$

where $u(t)$ is the input (control). The entire trajectory $\rho$ is not known, though the value of $\rho(t)$ is measured at time $t$, and hence may be used in any control strategy.

If in Equation 6.1 $f$ and $h$ are linear in the pair $[x, u]$, then the system appears as

$$\dot{x}(t) = A(\rho(t))x(t) + B(\rho(t))u(t), \quad y(t) = C(\rho(t))x(t) + D(\rho(t))u(t) \tag{6.2}$$

and is called *linear parameter-varying.*

LPV models assume that the parameter (and possibly its rate of variation), although not known a priori, is on-line measurable. Hence the actual parameter value can be used as an extra information to describe, and possibly control, the system. When using an LPV model to describe the system, a natural choice is to use a similar LPV structure for control design. It is important to stress the distinction between time-varying systems and LPV systems, since the model description is assumed to be known a priori in time varying systems over the whole time interval $[0, \infty)$, while in LPV systems the model is assumed to be known at time instant $t$ only over interval $[0, t]$.

Extensive research has focused on LPV systems over the last fifteen years developing analysis and synthesis techniques for modeling and controlling systems described with the LPV framework [48–50]. Reference [51] building on the previous work by [52] introduced Parameter Dependent Lyapunov Functions (PDLF) to address quadratic stability and induced $L_2$-norm level performance for LPV systems, involving bounding the rate of variations of the scheduling parameters.

LPV systems in general can be formally defined as ( [51]):

**Definition 6.1** (Linear Parameter Varying (LPV) Systems.)**.** *Given a compact subset $P \subset \mathbb{R}^s$, the parameter variation set $\mathcal{F}_p$ denotes the set of all piecewise continuous functions* *mapping $\mathbb{R}^+$ (time) into $\rho$ with a finite number of discontinuities in any interval. And given continuous functions: $A : \mathbb{R}^s \rightarrow \mathbb{R}^{n \times n}$, $B : \mathbb{R}^s \rightarrow \mathbb{R}^{n \times n_u}$, $C : \mathbb{R}^s \rightarrow \mathbb{R}^{n_y \times n}$, and $D : \mathbb{R}^s \rightarrow \mathbb{R}^{n_y \times n_u}$.*

*An n-th order linear parameter-varying system is defined as:*

$$\begin{bmatrix} \dot{x}(t) \\ y(t) \end{bmatrix} = \begin{bmatrix} A(\rho(t)) & B(\rho(t)) \\ C(\rho(t)) & D(\rho(t)) \end{bmatrix} \begin{bmatrix} x(t) \\ u(t) \end{bmatrix} \tag{6.3}$$

*where $\rho \in \mathcal{F}_p$.*

A general characteristics of a LPV systems is the $A(\rho), B(\rho), C(\rho)$, and $D(\rho)$ matrices are generally nonlinear functions of the scheduling vector, while the state $(x)$ and control input vector $u(t)$ enter linearly.

Quasi-LPV systems are a subclass of LPV systems, when any of the scheduling variables is also a state of the system. It is possible then to partition the state vector of the nonlinear system into scheduling states $(z)$ and non scheduling states $(w)$, thus $x(t) = [z(t)\ w(t)]^T$. Treating the scheduling parameter independent introduces conservativeness, since the LPV plant can exhibit behavior which is is not possible for the real system. With the added conservativeness the same modeling and control techniques can be applied to q-LPV systems.

The selection of adequate scheduling variables that capture the nonlinearities of the system are not always obvious, since the transformation of nonlinear systems to LPV is not unique, it is the task of the designer to select the most beneficial description.

## 6.2 Analysis of LPV Systems

Stability analysis for LTI systems is very well known. An LTI system is stable if the system dynamics matrix A is Hurwitz. Since LPV systems are not LTI, checking eigenvalues of A of an LPV system at each frozen point of the scheduling variable is not sufficient to analyze the stability of a LPV system. For stability analysis for an LPV system, parameter dependent stability has to be guaranteed: The system in Equation 6.3 is said to be quadratically stable if there exists a symmetric positive definite matrix $X = X^T > 0$ solution for:

$$A^T(\rho)X + XA(\rho) < 0 \tag{6.4}$$

for all $\rho \in \mathcal{P}$ for any parameter trajectory $\rho(\cdot) \in \mathcal{F}_P$.

## 6.3 Mathematical Model

As described in [49, 53] three techniques are available to obtain an LPV model from a nonlinear system:

- Cast the nonlinear model as a quasi-LPV system via Jacobian linearizations. Generally, the linearizations are carried out at a number of critical operating points, trim values representative of the flight envelope. The resultant set of linearized systems are thus parameterized by the variables describing the operating points. The complete state space data is generated by interpolating between the selected equilibrium points. If the states of the linearized system retain the same meaning for all operating points, the Jacobian Linearization approach results in an LPV model which is a first order approximation of the nonlinear system. On the other hand it is the most widespread technique, and it has a sounded theoretical and practical base.

- Another way of arriving at a parameter varying system is as follows: often we have a nonlinear system whose behavior depends on complicated system dynamics that we do not understand or to complex to model. However, the effects of this complicated dynamics on the system could be simplified by treating them as a set of exogenous variables affecting the state space description of a nonlinear system in a known manner. We can get a collection of plant models by evaluating the nonlinear system at discrete values of the exogenous variable. By treating this collection of plants as functions of the exogenous variables, we have a parameter-varying description of the nonlinear system.

  For a certain class of nonlinear systems, a quasi-LPV model can be obtained through exact state transformation. The non-scheduling states definition is changed to account for the nonlinear terms of the equations. The LPV model is evaluated at certain equilibrium points. The State Transformation method results in an "exact" LPV model, which theoretically will be equal to the nonlinear model. But in this approach, it is assumed that there exist equilibrium functions for the non-scheduling states, $w$, and the control inputs, $u$. Unfortunately this is not always the case. Both of these approaches, Jacobian and State Transformation, must be evaluated at different equilibrium points points of the flight envelope. The complete state-space description is obtained by interpolating between these selected equilibrium points whenever the flight condition is at a different equilibrium point. Thus, as in any interpolation method an error is introduced in the model.

For the same class of nonlinear systems aforementioned the Function Substitution approach obtains an LPV model around a unique trim point by decomposing the nonlinear functions. The decomposition is performed by posing it as a parameter optimization problem. The resulting linear functions are then substituted in lieu of the nonlinear terms in the initial system. This method has the advantage of providing an LPV model around a unique equilibrium point. This means that in cases with reduced trim regions there will be no impact on the model since only one trim point is needed to obtain a quasi-LPV model. The disadvantage of this method is a lack of theory. It is not yet known how the selection of trim point around which the model is obtained affects the LPV control synthesis. Transforming the possible parameter dependent uncertainties can also become problematic.

- Suppose we perform system identification of a time-varying system in terms of measurable quantities from the system and designate these quantities as parameters. Effectively, we are re-parameterizing the time-varying system into parameter-varying by covering time-dependence with parameter dependence.

Unfortunately, there is no theoretical rule which approach to use when describing a certain system. Most often experimental investigation would be necessary to evaluate the "best" LPV modeling approach, especially since the LPV model almost always serves as a basis for LPV control synthesis.

### 6.3.1 Jacobian Linearisation

This is the most comonly used method to linearize nonlinear systems. It can be used to create an LPV or a family of LPV models with respect to a set of equilibrium points that represent the flight envelope of interest. There is a downside due to the first order approximation used to obtain the linear system and to the interpolations between the equilibrium points. The first order approximation is only acceptable within small deviation of the trim point. This could lead to divergent behavior, with respect to the nonlinear model, for large control inputs. The result is an approximation to the dynamics of the nonlinear plant around a set of equilibrium points. It is generally impossible to capture the transient behavior of the nonlinear plant by this method. Reference [54] shows how to account for the essential features of the transient response for a particular type of nonlinear system.

Assume the nonlinear system has the following form:

$$\dot{z} = f_1(z(t), w(t), u(t), p(t)) = A_{11}(\rho(t))z(t) + A_{12}(\rho(t))w(t) + B_1(\rho(t))u(t) + E_1(\rho(t))p(t) \tag{6.5}$$

$$\dot{w} = f_2(z(t), w(t), u(t), p(t)) = A_{11}(\rho(t))z(t) + A_{22}(\rho(t))w(t) + B_2(\rho(t))u(t) + E_2(\rho(t))p(t) \tag{6.6}$$

The state vector is defined by $x(t) = [z(t)\ w(t)]^T$, the control inputs by $u(t)$, and the scheduling vector is given as $\rho(t) = [z(t)\ p(t)]^T \in F_p$, where $p(t)$ is a vector formed by exogenous scheduling parameters. For notational purposes the dependence on time and the dependency of the matrices $A, B, E$ on $\rho$ is dropped from now on, unless otherwise stated.

It is desirable to linearize the system with respect to the equilibrium point $\rho_{eq} = (z_{eq}, p_{eq})$. Applying small disturbance theory (references [24] and [55]) and using a first order approximation

$$x = x_{eq} + \delta_x \tag{6.7}$$

$$\dot{x} = \dot{x}_{eq} + \dot{\delta}_x \tag{6.8}$$

Via Taylor's expansion,

$$\begin{aligned}\dot{z} = f_1(z_{eq}, w_{eq}, u_{eq}, p_{eq}) + \left[\frac{\partial A_1 1}{\partial z} z + A_1 1 + \frac{\partial A_2 1}{\partial z} w + \frac{\partial B_1}{\partial z} u + \frac{\partial E_1}{\partial z} p\right]\Bigg|_{eq} \delta_z \\ + [A_{12}]\Bigg|_{eq} \delta_w + [B_1]\Bigg|_{eq} \delta_u + \left[\frac{\partial A_1 1}{\partial p} z + \frac{\partial A_1 2}{\partial p} w + \frac{\partial B_1}{\partial z} u + \frac{\partial E_1}{\partial p} p + E_1\right]\Bigg|_{eq} \delta_p\end{aligned} \tag{6.9}$$

The first term on the right hand side is zero, since by definition the derivative is zero at equilibrium. The higher order terms are dropped if the area of interest is restricted to be within a sufficiently small neighborhood of the equilibrium point. Thus, performing a similar differentiation on $\dot{w}$, the Jacobian model becomes:

$$\begin{bmatrix} \dot{\delta}_z \\ \dot{\delta}_w \end{bmatrix} = \begin{bmatrix} a_{11} & a_{12} \\ a_{21} & a_{22} \end{bmatrix} \Bigg|_{eq} \begin{bmatrix} \delta_z \\ \delta_w \end{bmatrix} + \begin{bmatrix} b_1 \\ b_2 \end{bmatrix} \Bigg|_{eq} [\delta_u] + \begin{bmatrix} e_1 \\ e_2 \end{bmatrix} \Bigg|_{eq} [\delta_p] \tag{6.10}$$

evaluated at $eq = [z_{eq},\ _{p_{eq}}]$, and where the matrix terms are give by:

$$a_{11} = \partial A_{11} \partial z z + A_1 1 + \frac{\partial A_2 1}{\partial z} w + \frac{\partial B_1}{\partial z} u + \frac{\partial E_1}{\partial z} p \tag{6.11}$$

$$a_{12} = A_1 2 \tag{6.12}$$

$$a_{21} = \partial A_{21} \partial z z + A_2 1 + \frac{\partial A_2 2}{\partial z} w + \frac{\partial B_2}{\partial z} u + \frac{\partial E_2}{\partial z} p \tag{6.13}$$

$$a_{22} = A_2 2 \tag{6.14}$$

$$b_1 = B_1 \tag{6.15}$$

$$b_2 = B_2 \tag{6.16}$$

$$e_1 = \partial A_{11} \partial p z + \frac{\partial A_1 2}{\partial p} w + \frac{\partial B_1}{\partial p} u + \frac{\partial E_1}{\partial p} p + E_1 \tag{6.17}$$

$$e_2 = \partial A_{21} \partial p z + \frac{\partial A_2 2}{\partial p} w + \frac{\partial B_2}{\partial p} u + \frac{\partial E_2}{\partial p} p + E_2 \tag{6.18}$$

$$\tag{6.19}$$

To find the quasi-LPV model the above state-space model is evaluated at different points of the flight envelope. The equilibrium values for the non-scheduling states, $w_{eq}$ and the control inputs $u_{eq}$ are found by substituting in 6.5 and 6.6 the desired equilibrium point $(z_{eq}, p_{eq})$ and setting the rates to zero. Thus, we are effectively parameterizing the model in terms of the scheduling variables of choice, $\rho = [z\ p]^T$.

Notice that in general a family of Jacobian linearizations cannot capture the nonlinear behavior of the plant, only the time evolution of the scheduling parameter captures the nonlinear nature of the problem. Also it is not straightforward to deduce without prior experience which parameters and/or states capture the plant's nonlinearities. In general, to reduce the problem size the fewest number of scheduling parameters should be selected, but then it is not clear how to handle the values which are varying with the operating point but not included in the scheduling vector. For example in the case of an aircraft longitudinal dynamics, where the forward speed $V$, the angle-of-attack $\alpha$, flight path angle $\gamma$, pitch rate $q$ and altitude $h$ are all states of the motion. It is not straight forward if the designer wants to use $\alpha$ and $V$ or $\alpha$,$V$ and $h$ for scheduling. Also it is a question, how to handle $h$ if omitted from the scheduling vector, which values to use for trim and linearization.

### 6.3.2 State Transformation

It was shown for a class of nonlinear systems described in [56] that using a nonlinear state transformation, the nonlinear dynamics can be brought to quasi-LPV form. The class of nonlinear systems considered is described as:

$$\begin{bmatrix} \dot{z} \\ \dot{w} \end{bmatrix} = \begin{bmatrix} k_1(z) \\ k_2(z) \end{bmatrix} + \begin{bmatrix} A_{11}(z) & A_{12}(z) \\ A_{21}(z) & A_{22}(z) \end{bmatrix} \begin{bmatrix} z \\ w \end{bmatrix} + \begin{bmatrix} B_1(z) \\ B_2(z) \end{bmatrix} u \tag{6.20}$$

where $z \in \mathbb{R}^{n_z}$, $w \in \mathbb{R}^{n_w}$ and $u \in \mathbb{R}^{n_u}$. It can be seen that if $n_u = n_z$, then 6.20 can be rearranged into quasi-LPV form whose state space model is a function of $z$ only. Where it is assumed that that $z$ can be measured real-time. Assume that there exist continuously

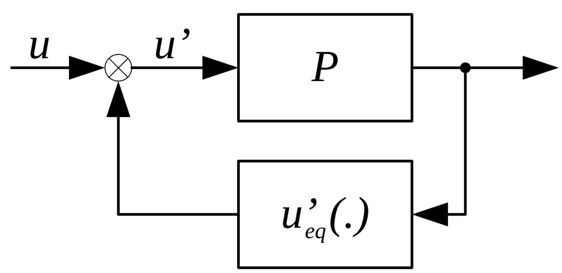


Figure 6.1: Schematics of quasi-LPV transformation.

differentiable functions $w_{eq}(z)$ and $u_{eq}(z)$ such that for every z

$$\begin{bmatrix} 0 \\ 0 \end{bmatrix} = \begin{bmatrix} k_1(z) \\ k_2(z) \end{bmatrix} + \begin{bmatrix} A_{11}(z) & A_{12}(z) \\ A_{21}(z) & A_{22}(z) \end{bmatrix} \begin{bmatrix} z \\ w_{eq}(z) \end{bmatrix} + \begin{bmatrix} B_1(z) \\ B_2(z) \end{bmatrix} u_{eq}(z) \tag{6.21}$$

In other words, we have a family of equilibrium states parameterized by the controlled output $z$. Subtracting 6.21 from 6.20 results in:

$$\begin{bmatrix} \dot{z} \\ \dot{w} \end{bmatrix} = \begin{bmatrix} 0 & A_{12}(z) \\ 0 & A_{22}(z) \end{bmatrix} \begin{bmatrix} z \\ w - w_{eq}(z) \end{bmatrix} + \begin{bmatrix} B_1(z) \\ B_2(z) \end{bmatrix} (u - u_{eq}(z)) \tag{6.22}$$

As

$$\dot{w}_{eq}(z) = \frac{dw_{eq}}{dt} = \frac{\partial w_{eq}}{\partial z} \dot{z} \tag{6.23}$$

Which leads to the following quasi-LPV plant description, assuming $z$ as an exogenous parameter:

$$\begin{aligned} \begin{bmatrix} \dot{z} \\ \dot{w} - \dot{w}_{eq}(z) \end{bmatrix} &= \begin{bmatrix} 0 & A_{12}(z) \\ 0 & A_{22}(z) - \frac{\partial w_{eq}}{\partial z} A_{12}(z) \end{bmatrix} \begin{bmatrix} z \\ w - w_{eq}(z) \end{bmatrix} \\ &+ \begin{bmatrix} B_1(z) \\ B_2(z) - \frac{\partial w_{eq}}{\partial z} B_1(z) \end{bmatrix} (u - u_{eq}(z)) \end{aligned} \tag{6.24}$$

The state space model 6.24 can be seen as a result of a linearizing feedback loop, as seen on Figure 6.1. This linearizing feedback loop could lead to a closed loop system with poor robustness properties, since the control synthesis can provide robustness with respect to the quasi-LPV system input not at the actual real plant input, where the uncertainty has real physical meaning. This is due to the fact that the feedback loop essentially cancels part of the system dynamics. The feedback loop can be eliminated by pre-compensating the inputs of the nonlinear plant with integrators before transforming to quasi-LPV form as described in [56]. A common problem with this approach, when the plant's dynamics is not linear in the plant input the method can not be applied to the system. The method requires further consideration to be applicable for the HSSV, since the inputs act on the system via non-affine lookup tables.

### 6.3.3 Function Substitution

A third approach was proposed in reference [53] for LPV systems with nonlinearities in the control input (recall from Section 6.1 that the LPV system must be linear in the pair [states, control inputs]). In reference [53] a transformation of the nonlinear input parameter was performed to obtain a linear input. The system was then casted into an LPV model where the real input was computed through a scheduled inverse of the nonlinear input. Notice that this approach offers obvious advantages for modeling the HSSV since non-affine equations of motions can be handled and only one trim point has to be obtained.

Assume a nonlinear system with a nonlinear control input

$$\begin{bmatrix} \dot{z} \\ \dot{w} \end{bmatrix} = \begin{bmatrix} k_1(\rho) \\ k_2(\rho) \end{bmatrix} + \begin{bmatrix} A_{11}(\rho) & A_{12}(\rho) \\ A_{21}(\rho) & A_{22}(\rho) \end{bmatrix} \begin{bmatrix} z \\ w \end{bmatrix} + \begin{bmatrix} B_1(\rho) \\ B_2(\rho) \end{bmatrix} \begin{bmatrix} \tilde{u}(\rho, \delta) \end{bmatrix} \tag{6.25}$$

where $z \in \mathbb{R}^{n_z}$ is the scheduling-state vector, $w \in \mathbb{R}^{n_w}$ the non-scheduling states, $\tilde{u} : \mathbb{R}^{n_z \times n_p \times n_\delta} \to \mathbb{R}^{n_\delta}$ is the control input vector, invertible with respect to $\delta$, the nonlinear input. The matrices $A,\ B$ are well-defined functions with no singularities. The scheduling parameters vector is $\rho = [z\ p]^T \in \mathcal{F}_\mathcal{P}$ and $u \in \mathbb{R}^{n_\delta}$

$$\tilde{u}(z, p, \tilde{v}(z, p, u)) = u \tag{6.26}$$

The term $\tilde{u}(z, p, \delta)$ enters the equations in a linear fashion. Therefore it is possible to treat $u$ as the input of the nonlinear system (6.38) and rewrite it as

$$\begin{bmatrix} \dot{z} \\ \dot{w} \end{bmatrix} = \begin{bmatrix} k_1(\rho) \\ k_2(\rho) \end{bmatrix} + \begin{bmatrix} A_{11}(\rho) & A_{12}(\rho) \\ A_{21}(\rho) & A_{22}(\rho) \end{bmatrix} \begin{bmatrix} z \\ w \end{bmatrix} + \begin{bmatrix} B_1(\rho) \\ B_2(\rho) \end{bmatrix} \begin{bmatrix} u \end{bmatrix} \tag{6.27}$$

The nonlinear system 6.27, is ready to be modeled via the LPV form . It is important to note that the actual input $\delta$ is calculated via a scheduled inverse of $\tilde{u}$, namely

$$\delta(t) = \tilde{v}(z(t), p(t), u(t)) \tag{6.28}$$

For simplicity assume there are no exogenous scheduling variables, $\rho = z \in \mathbb{R}^{n_z}$, which means the model will be quasi-LPV. Define functions of the following form

$$\eta_z = z - z_{trim} \tag{6.29}$$

$$\eta_w = w - w_{trim} \tag{6.30}$$

$$\eta_u = u - u_{trim} \tag{6.31}$$

$$\tag{6.32}$$

where $z_{trim}$ is a chosen trim condition. $w_{trim}$ and $u_{trim}$ the correspond to trim values for the non-scheduling states and inputs. Substituting the above relations into Equation 6.27

and rearranging the terms

$$\begin{bmatrix} \dot{\eta}_z - \dot{z}_{trim} \\ \dot{\eta}_w - \dot{w}_{trim} \end{bmatrix} = \begin{bmatrix} A_{11}(\eta_z + \dot{z}_{trim}) & A_{12}(\eta_z + \dot{z}_{trim}) \\ A_{21}(\eta_z + \dot{z}_{trim}) & A_{22}(\eta_z + \dot{z}_{trim}) \end{bmatrix} \begin{bmatrix} \eta_z \\ \eta_w \end{bmatrix} + \begin{bmatrix} B_1(\eta_z + \dot{z}_{trim}) \\ B_2(\eta_z + \dot{z}_{trim}) \end{bmatrix} [\eta_u] + \mathcal{F}(\eta_z, w_{trim}, u_{trim}) \tag{6.33}$$

where

$$\mathcal{F}(\eta_z, w_{trim}, u_{trim}) = \begin{bmatrix} A_{11}(\eta_z + \dot{z}_{trim}) & A_{12}(\eta_z + \dot{z}_{trim}) \\ A_{21}(\eta_z + \dot{z}_{trim}) & A_{22}(\eta_z + \dot{z}_{trim}) \end{bmatrix} \begin{bmatrix} z_{trim} \\ w_{trim} \end{bmatrix} + \begin{bmatrix} B_1(\eta_z + \dot{z}_{trim}) \\ B_2(\eta_z + \dot{z}_{trim}) \end{bmatrix} [u_{trim}] + \begin{bmatrix} k_1(\eta_z + \dot{z}_{trim}) \\ k_2(\eta_z + \dot{z}_{trim}) \end{bmatrix} \tag{6.34}$$

The objective is to decompose $\mathcal{F}(\eta_z, w_{trim}, u_{trim})$ into functions linear in $\eta_z \in \mathbb{R}^{n_z}$ and substitute the result back into Equation 6.33.

$$\mathcal{F}(\eta_z, w_{trim}, u_{trim}) = f_1(z)\eta_{z1} + f_2(z)\eta_{z2} + ... + f_n(z)\eta_{zn} \tag{6.35}$$

The decomposition can be posed as an optimization problem

$$\begin{gathered} \min \epsilon \\ \text{subject to} \\ \mathcal{F}(\eta_z, w_{trim}, u_{trim}) = f_1(z)\eta_{z1} + f_2(z)\eta_{z2} + ... + f_n(z)\eta_{zn} \\ \|f_i(z) - f_{i_{trim}}\| \leq \Gamma \|f_{i_{trim}}\| + \epsilon \text{ for } i = 1, 2, ..., n \end{gathered} \tag{6.36}$$

$\mathcal{F}$ corresponds to Equation 6.34 at a fixed trim condition, and $\Gamma$, a measure of the change in the derivative, are both known parameters. The objective is to minimize $\epsilon$, variations in $f_i(z)$, over all possible $\eta_z$. The unknown functions, $f_i(x)$, will be used to obtain the desired decomposition once evaluated at the chosen trim position. This can be solved via a linear program, see reference [48].

Rewrite the solution from the decomposition, Equation 6.35, as follows

$$\mathcal{F}(\eta_z, w_{trim}, u_{trim}) = \begin{bmatrix} f_1(z) & 0 \\ f_2(z) & 0 \end{bmatrix} \begin{bmatrix} \eta_z \\ \eta_w \end{bmatrix} \tag{6.37}$$

The quasi-LPV model is obtained by substituting into Equation 6.33

$$\begin{bmatrix} \dot{z} \\ \dot{w} \end{bmatrix} = \begin{bmatrix} A_{11}(z) + f_1(z) & A_{12}(z) \\ A_{21}(z) + f_2(z) & A_{22}(z) \end{bmatrix} \begin{bmatrix} z - z_{trim} \\ w - w_{trim} \end{bmatrix} + \begin{bmatrix} B_1(z) \\ B_2(z) \end{bmatrix} \begin{bmatrix} u - u_{trim} \end{bmatrix} \tag{6.38}$$

where $z_{trim}, w_{trim}$, and $u_{trim}$, the previously chosen trim condition, are fixed. The inputs used in the LPV description are called synthetic inputs, since their physical interpretation is related to the actual fin commands via the scheduled inverse function. A possible way of using this approach for modeling the HSSV, including its non-affine characteristics, is to select the synthetic inputs as forces and moments exerted on the body at the location of the fins, and the actual fin command are obtained via a scheduled inverse function. The remaining part of the dynamics can be represented as a pure LPV system.

This method, similar to the state transformation, results in an exact LPV model, obtained around one equilibrium point. The disadvantage is a lack of theory, it is not yet known how to select the best equilibrium point. How the point, around which the model is obtained, affects the LPV control synthesis.

## 6.4 6-DOF Equations of Motion in LPV Form

Jacobian linearization of the nonlinear vehicle mathematical model is important for linear analysis of the vehicle dynamics. The Jacobian linearization serves as a basis for the LPV model since this method can be applied straight forward to the HSSV problem .The parameter dependent plant is defined via interpolation of LTI plants obtained with Jacobian linearization at the specified grid points. The linearized models are describing only the six states composing the vehicle kinetics since the focus of the thesis, the inner loop control algorithm, has to stabilize and provide tracking for these states. Two cavitator and four fin control inputs are used. To incorporate the planing force into the description, which is coupled with the kinematics, planing is assumed to act as an outside measured disturbance, which is obtained from an estimator. Hence we are looking for a system description in a form of:

$$\begin{bmatrix} \dot{\delta}_\alpha \\ \dot{\delta}_\beta \\ \dot{\delta}_{V_m} \\ \dot{\delta}_p \\ \dot{\delta}_q \\ \dot{\delta}_r \end{bmatrix} = A(\rho) \begin{bmatrix} \delta_\alpha \\ \delta_\beta \\ \delta_{V_m} \\ \delta_p \\ \delta_q \\ \delta_r \end{bmatrix} + B(\rho) \begin{bmatrix} \dot{\delta}_{c1} \\ \dot{\delta}_{c2} \\ \dot{\delta}_{f1} \\ \dot{\delta}_{f2} \\ \dot{\delta}_{f3} \\ \dot{\delta}_{f4} \end{bmatrix} + P(\rho) \begin{bmatrix} F_{p,x} \\ F_{p,y} \\ F_{p,z} \\ M_{p,y} \\ M_{p,z} \end{bmatrix} \tag{6.39}$$

With assuming full state measurement:

$$y = C \begin{bmatrix} \delta_\alpha \\ \delta_\beta \\ \delta_{V_m} \\ \delta_p \\ \delta_q \\ \delta_r \end{bmatrix} ; \quad C = I_{6\times 6} \tag{6.40}$$

### 6.4.1 Trim of Equations of Motion

The trim points need to be determined to linearize the model at equilibrium points. Trimming the vehicle introduces several difficulties, since the delayed position of the cavitator is part of the dynamics. The equations have to be trimmed around fixed trajectories instead of only frozen operating points. The fin forces and moments are available in lookup-table form, hence no analytical method can be used to obtain the system coefficients. Moreover a unique solution is not guaranteed since the six control variables (two-degrees of freedom cavitator and four independent fins) can generate force and moment balance in different configurations for the same flight condition, if minimal drag is not considered as a performance object.

For initial investigation a two dimensional grid of trim points is selected. A natural choice would be to parameterize the plants with angle-of-attack ($\alpha$) and sideslip angle ($\beta$) while enforcing the remaining states ($V_m, p, q, r$) to be zero, and the position and orientation coordinates to be constant. A limitation of this realization is it would lead to non-uniform planing depth and fin immersion values among the grid points, since the cavity offset ($y_c, z_c$) at the tail is closely correlated with $\alpha$ and $\beta$. Consider for these conditions two sets of models, one obtained at $\beta = 0$ *deg* while $\alpha$ ranges between $\pm 1.5$ *deg*, the vehicle is always far away from planing. The other model set is at $\beta = 1.5$ *deg* allowing $\alpha$ to be between $\pm 1.5$ *deg*. This set have planing and non-planing models. Close to $\alpha = 0$ with $\beta = 1.5$ *deg* the vehicle is away from planing, while the models where $\alpha > 1$ are influenced by planing. The control surfaces are not able to achieve equilibrium at the boundary of the range at $\alpha = \beta = 1.5$ *deg*, since the planing force grows rapidly as the tail is outside of the cavity.

An alternative is to parameterize the system in a polar coordinate system with combined parameters

$$\mathcal{P}_1 = \sqrt{\alpha^2 + \beta^2} \tag{6.41}$$

and the second scheduling variable

$$\mathcal{P}_2 = \tan^{-1}(\beta/\alpha) \tag{6.42}$$

as seen on Figure 6.2. For this coordinate system in the direction of $\mathcal{P}_1$ the cavity offset is changing in direction of planing, while $\mathcal{P}_2$ parameterizes the angle between the vehicle axes and the cavity bubble's centerline. This coordinate system provides a more uniform parameter grid than parameterizing the vehicle with angles only. Moreover the fin immersion changes smoother along $\mathcal{P}_1$ and $\mathcal{P}_2$ then along $\alpha$ and $\beta$.

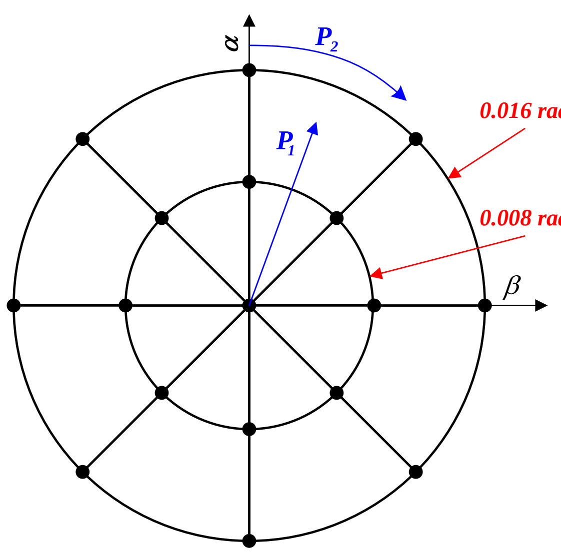


Figure 6.2: Trim and linearization points of the flight envelope, each dot representing one equilibrium point.

The following equations hold for the delayed position of the cavitator, assuming the velocity vector $V_m$ is parallel with the Earth $x_E$ axis, for maneuvers with constant $\alpha,\ \beta,\ q$

and $r$ and zero $p$:

$$y_{0,n} = -(V_m \sin(\beta)/r \sin(r\tau) + V_m \cos(\beta)/r(\cos(r\tau) - 1)) - L_{cav} \sin(r\tau); \tag{6.43}$$

$$z_{0,n} = -(V_m \sin(\alpha)/q \sin(q\tau) - V_m \cos(\alpha)/q(\cos(q\tau) - 1)) + L_{cav} \sin(q\tau) - 0.5 a_{buoy}\tau^2; \tag{6.44}$$

This can be derived from the kinematic equations. The location of the transom is:

$$y_{0,t} = \beta(L - Lcav) \tag{6.45}$$

$$z_{0,t} = \alpha(L - Lcav) \tag{6.46}$$

Hence the vehicle-tail cavity-centerline offset is the difference of the two.

$$y_{0,c} = y_{0,t} - y_{0,n} \tag{6.47}$$

$$z_{0,c} = z_{0,t} - z_{0,n} \tag{6.48}$$

This indicates that with zero $p, q$ and $r$ there is a one-to-one match between cavity offset $(y_c, z_c)$ and aerodynamic angles $\alpha$ and $\beta$. This means that the fin immersions and planing force are also constant at constant $\alpha$ and $\beta$.

It is also important to notice the numerical complexity involved in determining the trim values at steady-state operating points. As stated above finding the equilibrium trim condition is not unique, since two forces $(F_y, F_z)$ and three moments $M_x, M_y, M_z$ have to be balanced with six control inputs. To resolve the undetermined problem, finding the trim point, drag reduction is added to the performance objectives in the optimization task. The equations of motion described in Chapter 3 are implemented in MATLAB's SIMULINK environment. The nonlinear dynamical equations are simulated with variable step size using third order Bogacki-Shampine integration method to achieve the required numerical precision. The trim is calculated with MATLAB's sequential quadratic programming algorithm applied to the SIMULINK representation of the vehicle.

The vehicle model used to obtain the trim differs from the full vehicle model in the description of the cavity, which is assumed to be fixed, according to the trim condition, based on the hypothetical previous flight path of the vehicle nose as described by Equation 6.43. An additional constraint is enforced to help better numerically conditioning the optimization task, making use of the symmetry in solutions of opposite sign sideslip angles.

It is easy to understand that trimming at $\beta$ or at the opposite of it at $-\beta$ comply with certain symmetry properties. Namely if $[\delta_{c,p}, \delta_{c,y}, \delta_{f,1}, \delta_{f,2}, \delta_{f,3}, \delta_{f,4}]^T$ is a trim solution for $\alpha, \beta, p, q, r$ then $\delta_{c,p}, -\delta_{c,y}, -\delta_{f,3}, -\delta_{f,2}, -\delta_{f,1}, -\delta_{f,4}$ is a trim for $\alpha, -\beta, -p, q, -r$. The trim is searched parallel in two symmetric cases to improve the numerical conditioning of the problem and to ensure that symmetry is conserved in the solutions.

With vehicle configuration described in Table 3.1 planing occurs at 0.029 $m$ cavity-tail offset, which corresponds to approximately 0.95 $deg$ sideslip angle, 0.85 $deg$ positive or 1.04 $deg$ negative angle-of-attack, due to buoyancy, or somewhere between these values at arbitrary aerodynamic angles. The reason for avoiding planing in the trim equations is, that planing creates very large forces even at low planing depths, hence the control surfaces might not be able to achieve trim. For this reason trim and linearization is calculated around $\mathcal{P}_1 = [0; 0.46; 0.92]$ $deg$ and at $\mathcal{P}_2 = [0; 45; 90; 135; 180; 225; 270; 315; 360]$ $deg$ values. This composes a $3 \times 9$ grid as shown on Figure 6.2, where each dot corresponds to a linearization point. The planing condition has strong correlation with aerodynamic angles $(\alpha, \beta)$ in steady state flight. Hence, as stated above the outer linearization points are close to planing, explore sufficiently the operating envelope.

Using system parameters listed in Table 3.1 the obtained trim conditions are shown on Figure 6.3 and Figure 6.5. It can be seen that even with sparse grid like one parameter

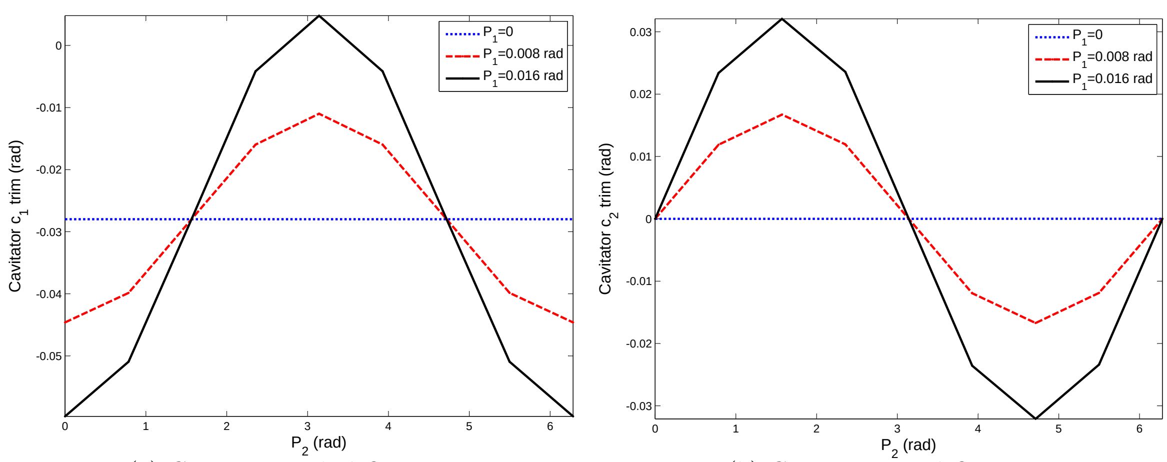


(a) Cavitator pitch deflections.

(b) Cavitator yaw deflections.

Figure 6.3: Cavitator inputs to achieve trim at various parameter values $(\mathcal{P}_1, \mathcal{P}_2)$.

point in $\mathcal{P}_2$ direction at every $\pi/4$ provides a reasonable value of the required trim deflection on the control surfaces (Fig.6.4). Since the port and starboard fins have same trim values

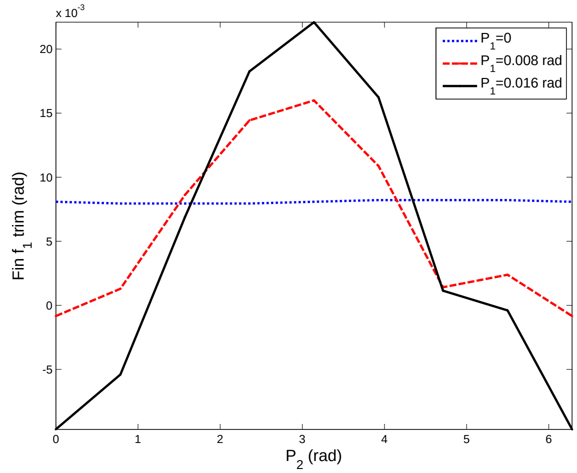


Figure 6.4: Starboard fin deflections to achieve trim at various parameter values $(\mathcal{P}_1, \mathcal{P}_2)$.

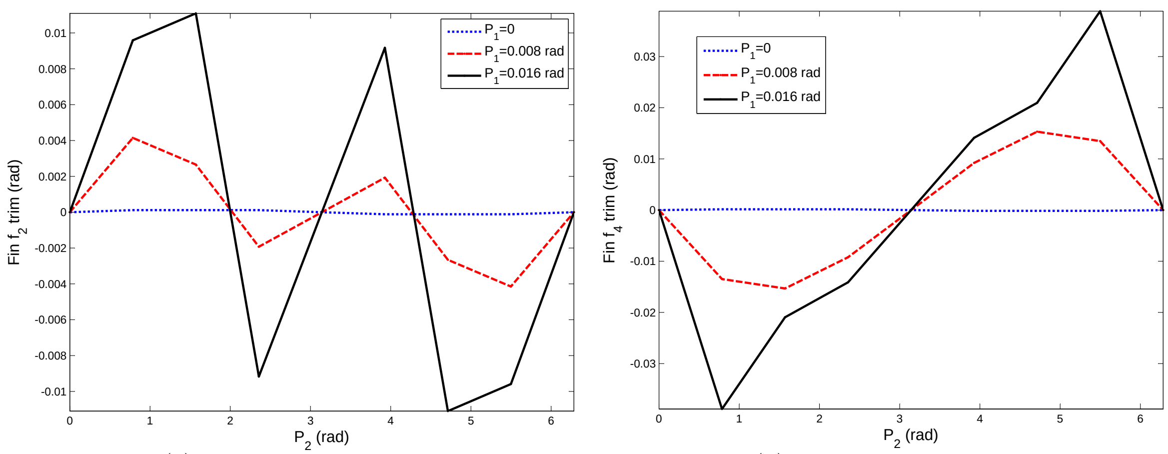


(a) Lower fin deflections. (b) Upper fin deflections.

Figure 6.5: Fin inputs to achieve trim at various parameter values $(\mathcal{P}_1, \mathcal{P}_2)$.

at opposite $\mathcal{P}_2$ parameters $(\delta_1(\mathcal{P}_1, \mathcal{P}_2) = \delta_3(\mathcal{P}_1, 2\pi - \mathcal{P}_2))$, only the starboard trim values are presented here (Fig.6.4). The down $(f_2)$ and upper $(f_4)$ fins are both presented on Figure 6.5. It is important to notice that the upper fin has a pure periodic behavior between 0 to $2\pi$, though the lower fin due to slope discontinuity at low angles of attack in the force curve (Figure 3.9) has non monotonic behavior between $\mathcal{P}_2 = 0 - \pi$. Notice that the upper fin which has lower immersion, due to buoyancy acting on the bubble, requires significantly larger defections for trim. This results in significant nonlinear coupling on the control effectiveness input function.

### 6.4.2 Linear Parameter Varying Description of the Vehicle

The linearizations are carried out numerically using the trim values obtained at given parameter values of $(\mathcal{P}_1, \mathcal{P}_2)$. The trim routine implemented in MATLAB uses the algorithm developed in [57].

To solve for the state matrix $A$, the input $u$ is set to the specified trim value and the states are perturbed about the operating point. For the $B$, $C$, and $D$ matrices, the states are set to the operating point, and the input is perturbed. These perturbations are used to determine the rate of change in the state derivatives and outputs.

The numerical algorithms on which the algorithm is based assume that the system nonlinearities are differentiable. This means they can be represented by a Taylor series expansion. The derivative of a function $f(x)$ at a point $x_0$ can be estimated by computing a finite central difference:

$$\frac{df}{dx} = \lim_{\delta \to 0} \frac{f(x_0 + \delta) - f(x_0 - \delta)}{2\delta} \tag{6.49}$$

provided that the derivative at $x_0$ exists. $\delta$ represents the perturbation level in the above expression. Complete accuracy would require the perturbation to be infinitesimal and the number of significant digits in the function evaluations to be infinite.

In theory, any error incurred in using Equation 6.49 is an indication of the curvature of the nonlinearity. If the nonlinear function can be represented by a Taylor-series expansion, the accuracy of (6.49) depends on how dominant the constant, linear, and quadratic terms are in relation to the higher order terms of the expansion. The expression in Equation 6.49 yields an exact result only for quadratic functions. Errors arise due to the truncation of the higher order terms present in the Taylor series expansion. Such errors are thus called truncation error. Since truncation error increases with perturbation size, the obvious remedy would seem to be to use the smallest perturbation possible. However small perturbation increase the risk of having lower precision due to finite representation of numbers in computer programs.

In case of the HSSV, the polytopic LPV description, assumes linear interpolation between the previously specified grid points. This is a valid assumption if the plants do not change significantly between neighboring points.

It is assumed that the planing force only acts as an outside disturbance for the initial investigation. Considering planing would require additional states, related to the cavity vehicle-tail offset. Due to the nature of the switched planing force, these states would be uncontrollable when the tail is not in contact with the water. Hence, to avoid this problem related to realization theory, planing is not included in the system dynamics, instead the plant has 11 inputs: the six control deflections and the three forces and two moments generated by planing. It is assumed that planing does not generate moment around the $x$-axis $M_{x,p} = 0$. The plant outputs are the six states: $\alpha, \beta, V_m, p, q$ and $r$ as described by Equation 6.39.

The LPV description of the vehicle is obtained with numerical linearization carried out at the obtained trim conditions on the nonlinear vehicle equations-of-motion. The change in system dynamics along the two parameters are shown on Figures 6.6 and 6.7. Figure 6.6 represents the open-loop transfer function gains from cavitator inputs $(\delta_{c,p}, \delta_{c,y})$ to body rates $(p, q, r)$. Notice that when $\mathcal{P}_1 = 0$, denoted with blue, $\alpha = \beta = 0$ and the cavitator pitch has no contribution to roll and yaw channel, and cavitator yaw has no influence on pitch. Then as $\mathcal{P}_1$ increases and $\beta$ is non-zero the cross coupling introduces higher gains in these channels. As the magnitude of $\alpha$ and $\beta$ increases, represented by colors changing from blue to red and to green, the magnitude of the response is also getting larger. The bandwidth on cavitator pitch to pitch rate and yaw to yaw rate does not change significantly, while the other coupled modes have wide dynamic range, indicating the importance of cross-coupling in the equations-of-motion. Notice the wide range of steady state gains and the unstable behavior of certain models with larger aerodynamic angles (Figure 6.8).

The system responses for the different fin inputs exhibits rich dynamical complexity. Since the cavitator is always fully enveloped with water, the variation in system gains on Figure 6.6 only a function of the changes in system dynamics. Analyzing the responses on Figure 6.7 we note that changes in fin immersion, caused by steady cavity offset, alter the dynamics $(A(\rho))$ and also the input matrix $B(\rho)$. This change in the fin effectiveness leads to two orders of magnitude variation in steady state gain and an order of magnitude difference in system bandwidth poses a fundamentally challenging problem for the control

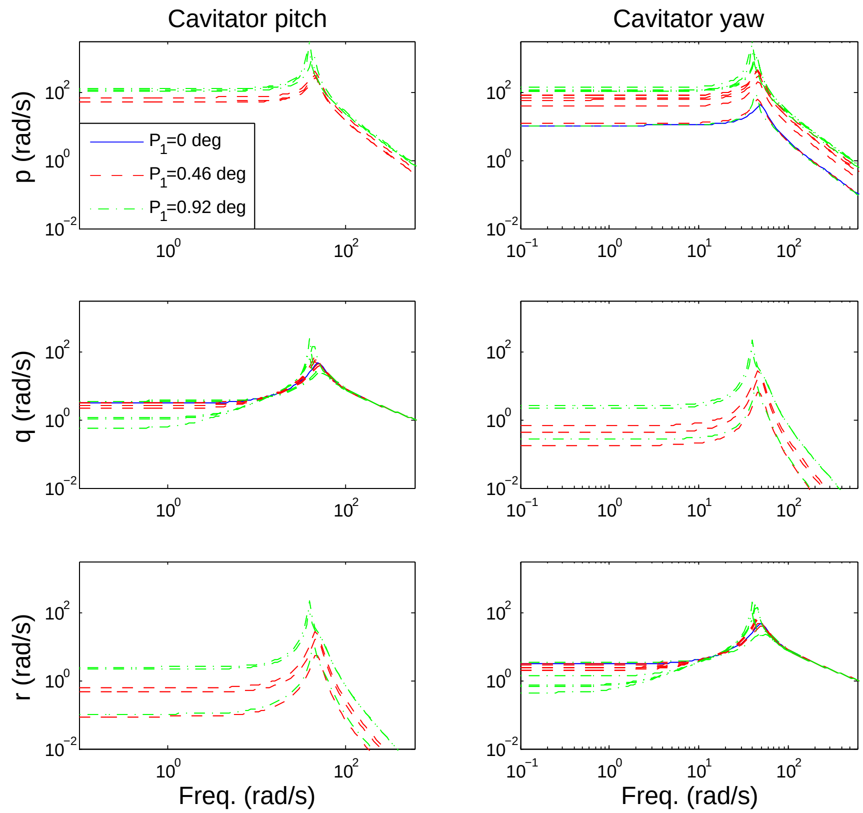


Figure 6.6: Range of frequency responses of linearized models from cavitator inputs.

design.

It is important to notice the vehicle's non-minimum phase behavior of pitch and yaw rate from fin inputs as shown on Figure 6.8. As described by several authors [58], non-minimum phase response fundamentally limits the performance, pitch and yaw rate disturbance attenuation and tracking is fundamentally limited to poor performance. To avoid this problem, it is important to keep the option of pitch and yaw actuation of the cavitator possible, which provide enough control authority for the controller to eliminate the slow response caused by non-minimum phase behavior.

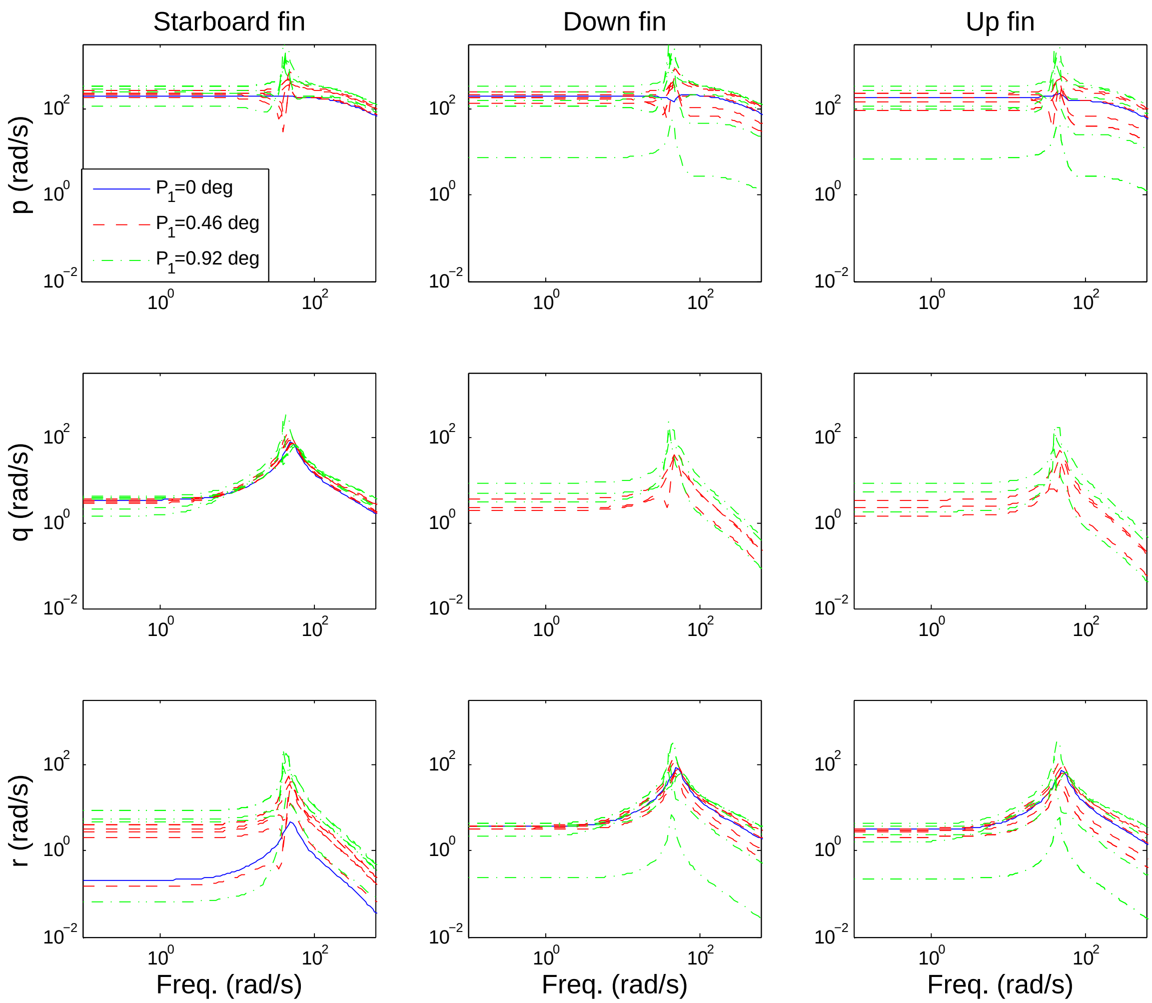


Figure 6.7: Range of frequency responses of linearized models from fin inputs.

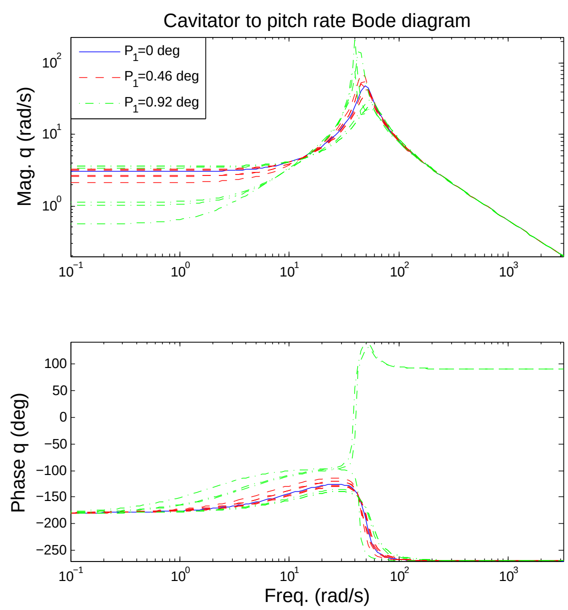

(a) Cavitator pitch to $q$.

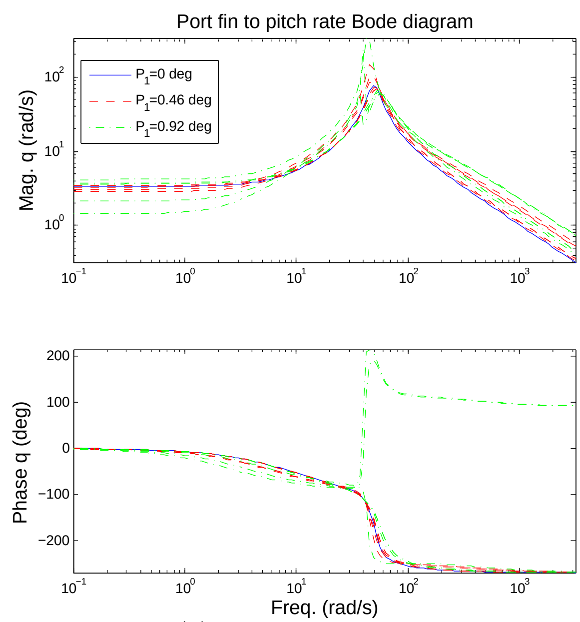

(b) Starboard fin to $q$.

Figure 6.8: Pitch rate response from Cavitator and Fin inputs.

# Chapter 7

# Linear Parameter Varying Control of the Supercavitating Vehicle

A systematic approach to parameter-dependent control synthesis of a candidate High-Speed Supercavitation Vehicle (HSSV) is presented. The aim of the design is to provide robust reference tracking properties in a large flight envelope, while directly accounting for the interaction of liquid and gas phases with the vehicle.

## 7.1 Control design

As previously discussed the HSSV model is highly nonlinear and the LPV description covers almost the entire operating envelope of the vehicle. Designing a feedback controller for the system is challenging since only a few methods, like nonlinear dynamic inversion [34], sliding-mode control [59] and a few others are available to handle nonlinear plants in a systematic manner. One common method applied to systems with widely varying nonlinear dynamics is gain-scheduling. Gain-scheduling control uses controllers obtained with linear design methods around operating points and the compensator gains are interpolated between the design points using the measured or computed scheduling variables. Despite the lack of theoretical guarantees, gain scheduling is widely used in industry, several commercial and military aircraft use gain scheduled stability augmentation system [60]. Gain scheduled controllers come with no guarantee on their global behavior, even when they have excellent local properties. Stability, robustness and performance guarantees of the gain scheduled controller cannot be set a priori. The rate of variation of the parameter in linear design is assumed to be zero, hence stability, robustness and performance cannot be guaranteed not just between but at the design points themselves. An additional consideration for gain scheduling is dynamic feedback. It is straight forward to use static compensators and schedule the gains according to the current parameter values, but in the case of dynamical compensators the initialization of controllers is a problem. If all the controllers at all design points are calculated in parallel, the few around the current parameter value are in the closed-loop, while the others in open-loop leading to high computational load. The other way is when the parameter enters a new parameter region off-line controllers are initialized, likely from zero initial condition, which leads to undesired transients in the controller response.

The most important design guidelines in the synthesis of gain scheduled controllers are: 1) the scheduling variables should vary slowly, and 2) the scheduling variables should capture the important nonlinearities of the system. These guidelines are simply emphasizing the fact that while the design is based on LTI plants, the stability margin is proportional with frozen point stability, the actual system is nonlinear, since the stability margin is inversely proportional to the rate of change of the scheduling variables [61]. For these reasons certifying a gain scheduled control system requires extensive testing and simulations.

An alternative way of designing controllers for systems with highly coupled nonlinear dynamics is nonlinear dynamic inversion (NDI), as discussed in Chapter 5. The main advantage of this method is that the designer does not have to decide on how to interpolate the controller gains, this is done directly [60]. Again the important problem is the resulting controller does not come with robustness guarantees and in general it is hard to incorporate robustness into the design. Hence the clearance of control laws will face challenges before implementation.

Significant progress was made in the last fifteen years on development of systematic control synthesis techniques for robust gain scheduled controllers [50]. With certain assumptions on the plant description and on the implementation of the control algorithm, linear parameter varying (LPV) control technique can guarantee a systematic procedure to design a robust parameter dependent controller. The designer does not have to decide how to interpolate the controller gains, since the parameter dependent controller is a single entity and robust stability is guaranteed a priori as described in the next section.

## 7.2 LPV Control design

LPV techniques offer a systematic design methodology to address control of highly coupled, nonlinear uncertain dynamic systems. The benefits of this approach include guaranteed global stability and robust performance, and a formal structure of the controller that leads itself to real-time implementation. LPV control is based on the $\mathcal{H}_\infty$-robust control framework. Frequency dependent weighting functions are used to translate traditional linear robustness and performance specifications into the LPV design framework. Two conceptually different approaches exist for synthesizing robust gain scheduled controllers for LPV systems: the single and parameter dependent Lyapunov function approach [51] and the linear fractional transformation (LFT) approach [62].

### 7.2.1 Analysis of Parameter-Dependent Systems

General properties used in the analysis of LPV systems, and the synthesis are presented.

**Definition 7.1** (Parameter-Dependent Stability [51]). *Assume that the parameter $\rho \in \mathbb{R}^p$, the parameter rate $\dot{\rho}$ is bounded by $\bar{\nu}_i$ and $\underline{\nu}_i$, and a matrix function $A$ denoted as $A(\rho, \dot{\rho})$; then the function $A$ is parametrically-dependent stable over $\rho$ if there exists a continuously differentiable symmetric matrix function $P$: $\mathbb{R}^p \to \mathbb{R}^{n\times n}$ such that $P(\rho) > 0$ and*

$$A^T(\rho,\dot{\rho})P(\rho) + P(\rho)A^T(\rho,\dot{\rho}) + \sum_{i=1}^{m}(\dot{\rho}_i \frac{\partial P}{\partial \rho_i}) < 0 \ \forall \rho_i \in F_p \ i = 1, 2, ..., m. \qquad (7.1)$$

*where $n$ is the dimension of $A$ and $m$ is the number of parameters.*

Given LPV system $G_\rho$, the system is stable over all allowed parameter variations $\rho$ when $P$ is positive definite function of parameters $\rho$ and a solution of Equation 7.1.

Using parameter-dependent stability property as a starting point for analysis, parameter dependent synthesis techniques can be derived. More specifically, a synthesis problem can be posed which ask if there exists a linear parameter-dependent controller, such that the closed loop system composed of an LPV plant in feedback connection with LPV controller satisfies condition 7.1. However, the stabilization problem, seeking for parameter dependent controller $G_K(\rho)$ is not sufficient in most cases. We are interested in guaranteeing robust performance in addition to stability of the closed loop, as in the standard $\mathcal{H}_\infty$ control framework [63].

The performance measurement of an LPV system from disturbances to errors in terms of norm values is defined with an induced $\mathcal{L}_2$-norm as follows:

**Definition 7.2** (Induced $\mathcal{L}_2$-Norm of an LPV system)**.** *Given a quadratically stable LPV system $G_\rho$, for zero initial conditions, define*

$$\|G_\rho\|_{L_2 \leftarrow L_2} := \sup_{\rho \in P} \sup_{\|d\|_2 \neq 0, d \in L_2} \frac{\|e\|_2}{\|d\|_2} \tag{7.2}$$

$\|G_\rho\|_{\mathcal{L}_2 \leftarrow \mathcal{L}_2}$ represents the largest disturbance to error (in the $L_2 \leftarrow L_2$ sense) over the set of all causal linear operators described by $G_\rho$.

**Lemma 7.1** (Quadratic Performance)**.** *Given $G_\rho$ and the scalar $\gamma > 0$ , if there exists $X \in \mathbb{R}^{n_x \times n_x}$,$X = X^T > 0$ such that for all $\rho \in P$*

$$\begin{bmatrix} A^T(\rho)X + XA(\rho) & XB(\rho) & \gamma^{-1}C^T(\rho) \\ B^T(\rho)X & -I & \gamma^{-1}D^T(\rho) \\ \gamma^{-1}C(\rho) & \gamma^{-1}D(\rho) & -I \end{bmatrix} < 0 \tag{7.3}$$

*then, $(i)$ the function $A$ is quadratically stable over $P$, and $(ii)$ there exists a $\beta < \gamma$ such that $\|G_\rho\|_{L_2 \leftarrow L_2} \leq \beta$*

Note that the affine matrix inequality can be rewritten into the more familiar Ricatti inequality via Schur complements:

$$\begin{aligned} & A^T(\rho)X + XA(\rho) + \gamma^{-2}C^T(\rho)C(\rho)(XB(\rho) + \gamma^{-2}C^T(\rho)D(\rho)) \\ & (I - \gamma^{-2}D^T(\rho)D(\rho))^{-1}(B^T(\rho)X + \gamma^{-2}D^T(\rho)C(\rho)) < 0 \end{aligned} \tag{7.4}$$

### 7.2.2 Synthesis of Parameter-Dependent Control

The analysis test for stability and performance in addition to the measurement of $\mathcal{L}_2$-norm of the system is defined. $G_\rho$ can be regarded as a closed-loop system of a parameter dependent plant with a parameter dependent controller. The following section describes the closed loop synthesis problem and state the output feedback synthesis solution for a given open-loop plant.

Consider a generalized open-loop interconnection for synthesizing a parameter dependent controller. The interconnection is composed in general of LPV plant $G_\rho$, sensor models, actuator models, noise and uncertainty weighting functions and ideal reference models with weighting functions on performance outputs. Note that these system components can be LPV models.

The system matrices of the generalized open-loop system are written as follows:

$$\begin{bmatrix} \dot{x}(t) \\ e(t) \\ y(t) \end{bmatrix} = \begin{bmatrix} A(\rho) & B_1(\rho) & B_2(\rho) \\ C_1(\rho) & D_{11}(\rho) & D_{12}(\rho) \\ C_2(\rho) & D_{21}(\rho) & D_{22}(\rho) \end{bmatrix} \begin{bmatrix} x(t) \\ d(t) \\ u(t) \end{bmatrix} \tag{7.5}$$

Where the system is partitioned as follows: inputs to $B_1(\rho)$ are the disturbance input effects on the states, $B_2(\rho)$ are the control inputs effect on the states, output of $C_1(\rho)$ are the errors to be minimized, and $C_2(\rho)$ are the output measurements provided to the controller. Figure 7.1 provides an illustrative example. The disturbances are denoted by $[\Delta, d, c, n]$, the control input is $[u]$, while the outputs addressed in the performance objectives are $[W_\Delta, e, p, z]$ and the measurements provided for the controller are $[d, r, y]$. Notice that unstructured uncertainty is included via the $\Delta$, $W_\Delta$ input-output. Where $\Delta$ denotes the uncertainty input entering the system in the control input channels.

Without loss of generality, we can assume there is no direct input from from control signal $u$ to measurement $y$. When $D_{22}(\rho) \neq 0$, the system can be converted into a new LPV system with $D_{22}(\rho) = 0$ using a possibly parameter dependent coordinate transformation [52]. Assume, $D_{12}(\rho)$ is full column and $D_{21}(\rho)$ is full row rank over the parameter space $\mathcal{P}$, then the $D(\rho)$ matrix can be rewritten in Equation 7.6, using QR decomposition and the input-output norm preserving transformation.

$$\begin{bmatrix} \dot{x}(t) \\ e_1(t) \\ e_2(t) \\ y(t) \end{bmatrix} = \begin{bmatrix} A(\rho) & B_{11}(\rho) & B_{12}(\rho) & B_2(\rho) \\ C_{11}(\rho) & D_{1111}(\rho) & D_{1112}(\rho) & 0 \\ C_{12}(\rho) & D_{1121}(\rho) & D_{1122}(\rho) & I_{n_u} \\ C_2(\rho) & 0 & I_{n_d2} & 0 \end{bmatrix} \begin{bmatrix} x(t) \\ d_1(t) \\ d_2(t) \\ u(t) \end{bmatrix} \tag{7.6}$$

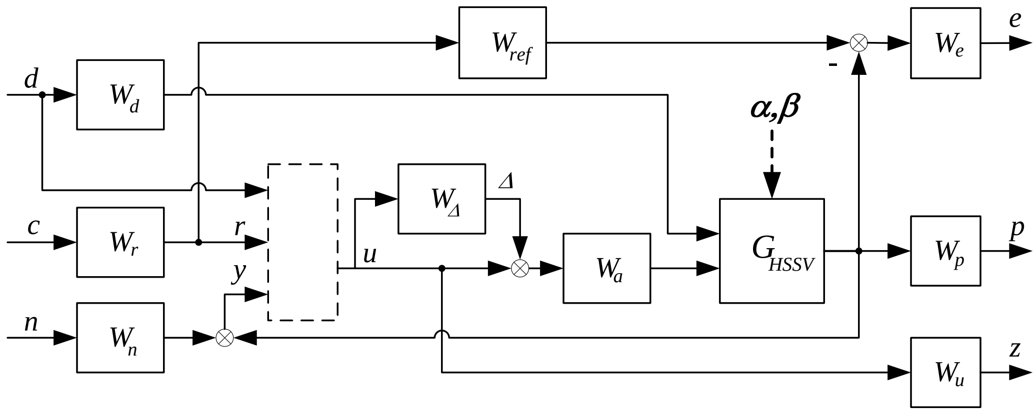


Figure 7.1: General weighted control synthesis interconnection.

In Equation 7.6 the symbols stand for: state $x(t) \in \mathbb{R}^n$, errors $e_1(t) \in \mathbb{R}^{n_{e1}}$,$e_2(t) \in \mathbb{R}^{n_{e2}}$, disturbances $d_1(t) \in \mathbb{R}^{n_{d1}}$,$d_2(t) \in \mathbb{R}^{n_{d2}}$, control signal $u(t) \in \mathbb{R}^{n_u}$, and measurements $y(t) \in \mathbb{R}^{n_y}$.

The class of finite dimensional parameter-dependent controllers, which depend on their parameters and their derivatives, is given by $G_K(\rho, \dot{\rho})$:

$$\begin{bmatrix} \dot{x}_K(t) \\ u(t) \end{bmatrix} = \begin{bmatrix} A_K(\rho, \dot{\rho}) & B_K(\rho, \dot{\rho}) \\ C_K(\rho, \dot{\rho}) & D_K(\rho, \dot{\rho}) \end{bmatrix} \begin{bmatrix} x_K(t) \\ y(t) \end{bmatrix} \tag{7.7}$$

Using the above controller $G_K(\rho)$ and the generalized open loop plant $G_\rho$ in Equation 7.6, the generalized closed-loop LPV system can be written as follows.

$$\begin{bmatrix} \dot{x}_{cl}(t) \\ e(t) \end{bmatrix} = \begin{bmatrix} A_{cl}(\rho, \dot{\rho}) & B_{cl}(\rho, \dot{\rho}) \\ C_{cl}(\rho, \dot{\rho}) & D_{cl}(\rho, \dot{\rho}) \end{bmatrix} \begin{bmatrix} x_{cl}(t) \\ d(t) \end{bmatrix} \tag{7.8}$$

where

$$A_{cl}(\rho,\dot{\rho}) = \begin{bmatrix} A(\rho) + B_2(\rho)D_K(\rho,\dot{\rho})C_2(\rho) & B_2(\rho)C_K(\rho,\dot{\rho}) \\ B_K(\rho,\dot{\rho})C_2(\rho) & A_K(\rho,\dot{\rho}) \end{bmatrix},$$

$$B_{cl}(\rho,\dot{\rho}) = \begin{bmatrix} B_{11}(\rho) & B_{12}(\rho) + B_2(\rho)D_K(\rho,\dot{\rho}) \\ 0 & B_K(\rho,\dot{\rho}) \end{bmatrix},$$

$$C_{cl}(\rho,\dot{\rho}) = \begin{bmatrix} C_{11}(\rho) & 0 \\ C_{12}(\rho) + D_K(\rho,\dot{\rho})C_2(\rho) & C_K(\rho,\dot{\rho}) \end{bmatrix},$$

$$D_{cl}(\rho,\dot{\rho}) = \begin{bmatrix} D_{1111}(\rho) & D_{1112}(\rho) \\ D_{1121}(\rho) & D_{1122}(\rho) + D_K(\rho,\dot{\rho}) \end{bmatrix}. \tag{7.9}$$

The parameter-dependent $\gamma$ performance problem is defined next. Given a parameter-dependent plant, the problem is to determine if there exists a parameter-dependent controller which achieves $\gamma$-performance level of the closed loop system.

**Definition 7.3** (Parameter-dependent $\gamma$ performance problem [51])**.** *Given LPV system $G_\rho$ and a performance level $\gamma > 0$. The parameter-dependent $\gamma$ performance problem is solvable if there exists an integer $m > 0$, a function $W(\rho) \in \mathcal{C}_1$ and a continuous matrix functions $A_K(\rho), B_K(\rho), C_K(\rho), D_K(\rho)$ such that $W(\rho) > 0$ and*

$$\begin{bmatrix} A_{cl}^T(\rho,\dot{\rho})W(\rho) + W(\rho)A_{cl}(\rho,\dot{\rho}) + \sum_{i=1}^{m}(\underline{\overline{\nu}}_i \frac{\partial W}{\partial \rho_i}) & W(\rho)B_{cl}(\rho,\dot{\rho}) & \gamma^{-1}C_{cl}^T(\rho,\dot{\rho}) \\ B_{cl}^T(\rho,\dot{\rho})W(\rho) & -I_{n_d} & \gamma^{-1}D_{cl}^T(\rho,\dot{\rho}) \\ \gamma^{-1}C_{cl}(\rho,\dot{\rho}) & \gamma^{-1}D_{cl}(\rho,\dot{\rho}) & -I_{n_e} \end{bmatrix} < 0 \tag{7.10}$$

*for all $\rho \in \mathcal{P}$ and parameter rate $\dot{\rho}$ is bounded by $\overline{\nu}$ upper and $\underline{\nu}$ lower rate bounds. Where the matrices $A_{cl}, B_{cl}, C_{cl}, D_{cl}$ are defined in Equation 7.8.*

This problem is a generalization of the standard sub-optimal $\mathcal{H}_\infty$ optimal control problem [39].

**Theorem 7.1** (Solution for parameter dependent input/output feedback controller)**.** *Given an LPV system $G_\rho$, defined in Equation 7.6 with bounded parameter rates. A parameter dependent feedback controller $G_K(\rho)$ can be constructed by solving the following optimization problem:*

$$\min_{X,Y:\mathcal{P}\to\mathcal{S}^{n\times n}} \gamma \tag{7.11}$$

*subject to*

$$\begin{bmatrix} \hat{A}(\rho)X(\rho)+X(\rho)\hat{A}^T(\rho)-\sum_{i=1}^m \underline{\overline{\nu}}_i \frac{\partial X}{\partial p_i} B_2(\rho)B_2^T(\rho) & X(\rho)C_{11}^T & \gamma^{-1}\hat{B}(\rho) \\ C_{11}(\rho)X(\rho) & -I_{n_{e1}} & \gamma^{-1}D_{111\cdot}(\rho) \\ \gamma^{-1}\hat{B}^T(\rho) & \gamma^{-1}D_{111\cdot}^T(\rho) & -I_{n_d} \end{bmatrix} < 0, \tag{7.12}$$

$$\begin{bmatrix} \tilde{A}^T(\rho)Y(\rho)+Y(\rho)\tilde{A}+\sum_{i=1}^m \underline{\overline{\nu}}_i \frac{\partial Y}{\partial p_i} - C_2^T(\rho)C_2(\rho) & Y(\rho)B_{11}(\rho) & \gamma^{-1}\tilde{C}^T(\rho) \\ B_{11}^T(\rho)Y(\rho) & -I_{n_{d1}} & \gamma^{-1}D_{11\cdot 1}^T(\rho) \\ \gamma^{-1}\tilde{C}(\rho) & \gamma^{-1}D_{11\cdot 1}(\rho) & -I_{n_e} \end{bmatrix} < 0, \tag{7.13}$$

$\underline{\overline{\nu}}_i$ *denoting all possible combination of upper and lower rate bounds on parameter* $\rho$

$$\begin{bmatrix} X(\rho) & -\gamma^{-1}I_n \\ -\gamma^{-1}I_n & Y(\rho) \end{bmatrix} < 0. \tag{7.14}$$

$$X(\rho) > 0,\ Y(\rho) > 0 \tag{7.15}$$

Omitting the matrices dependence on $\rho$ the variables in Equations 7.12-7.13 are defined as

$$\begin{aligned} \hat{A} &= A - B_2C_{12} & \tilde{A} &= A - B_{12}C_2 \\ \hat{B} &= B_1 - B_2D_{112\cdot} & \tilde{C} &= C_1 - D_{11\cdot 2}C_2 \end{aligned} \tag{7.16}$$

For convenience of notation, the $D$ matrix is partitioned as follows.

$$\begin{bmatrix} D_{111\cdot} \\ D_{112\cdot} \end{bmatrix} = \left[\begin{array}{cc} D_{1111} & D_{1112} \\ \hline D_{1121} & D_{1122} \end{array}\right] \tag{7.17}$$

$$\begin{bmatrix} D_{11\cdot 1} & D_{11\cdot 2} \end{bmatrix} = \left[\begin{array}{c|c} D_{1111} & D_{1112} \\ D_{1121} & D_{1122} \end{array}\right] \tag{7.18}$$

The parameter dependent controller $G_K(\rho)$ as described in Equation 7.7 can be constructed from the solutions $X(\rho)$ and $Y(\rho)$. The system matrices, $A_K(\rho), B_K(\rho), C_K(\rho)$ and $D_K(\rho)$ are written as follows.

$$A_K(\rho,\dot{\rho}) = \bar{A} + B_2 F + Q^{-1} Y L C_2 - \gamma^{-2} Q^{-1} M \tag{7.19}$$

$$B_K(\rho,\dot{\rho}) = -Q^{-1} Y L \tag{7.20}$$

$$C_K(\rho,\dot{\rho}) = F \tag{7.21}$$

$$D_K(\rho,\dot{\rho}) = \Omega \tag{7.22}$$

where $Q = Y - \gamma^{-2} X^{-1} > 0$ uniformly on $\mathcal{P}$, the proof [51] uses the variable transformation $v = u - \Omega(\rho) y$ and $F, L, M$ and $\Omega$ are defined as follows. For convenience, the dependence on $\rho$ and $\dot{\rho}$ is omitted.

$$F = -(D_{12}^T D_h D_{12})^{-1} (B_2^T X^{-1} + D_{12}^T D_h \bar{C}_1) \tag{7.23}$$

$$L = -(Y^{-1} \underline{C_2}^T + \bar{B}_1 D_t D_{21}^T)(D_{21} D_t D_{21}^T)^{-1} \tag{7.24}$$

$$\Omega = -D_{1122} - D_{1121} (\gamma^2 I_{n_{d1}} - D_{1111}^T D_{1111})^{-1} D_{1111}^T D_{1112} \tag{7.25}$$

$$\begin{aligned} M =& H(\rho,\dot{\rho}) + F^T \left[ B_2^T X^{-1} + D_{12} (\bar{C}_1 + D_{12} F) \right] + \left[ \gamma^2 Q (-Q^{-1} Y L D_{21} - \bar{B}_1) + F^T D_{12}^T \bar{D}_{11} \right] \\ & \gamma^{-2} D_t \left[ \bar{B}_1^T X^{-1} + \bar{D}_{11}^T (\bar{C}_{11} + D_{12} F) \right] \end{aligned} \tag{7.26}$$

with the following definitions,

$$\begin{aligned} H = - \Bigg[ & X^{-1} A_F + A_F^T X^{-1} + \sum_{i=1}^{m} \frac{\dot{\rho}_i \partial X^{-1}}{\partial \rho_i} + C_F^T C_F \\ & + (X^{-1} \bar{B}_1 + C_F^T D_{11}) \gamma^{-2} D_t (\bar{B}_1^T X^{-1} + \bar{D}_{11}^T C_F) \Bigg] \end{aligned}$$

$$\begin{aligned} \bar{A} &= A + B_2 \Omega C_2 & \bar{B} &= B_1 + B_2 \Omega D_{21} \\ \bar{C}_1 &= C_1 + D_{12} \Omega C_2 & \bar{D}_{11} &= D_{11} + D_{12} \Omega D_{21} \\ D_h &= \left( I_{n_e} - \gamma^{-2} \bar{D}_{11} \bar{D}_{11}^T \right)^{-1} & D_t &= \left( I_{n_d} - \gamma^{-2} \bar{D}_{11}^T \bar{D}_{11} \right)^{-1} \\ \underline{B}_2 &= B_2 + \gamma^{-2} \bar{B}_1 \bar{D}_{11} D_h D_{12} & \underline{C}_2 &= C_2 + \gamma^{-2} D_{21} D_t \bar{D}_{11}^T \bar{C}_1 \\ A_F &= \bar{A} + B_2 F & C_F &= \bar{C}_1 + D_{12} F \end{aligned}$$

The closed-loop system with $G_K(\rho)$ in Equation 7.7 satisfies $\gamma$-performance described in Theorem 7.1. The Linear Matrix Inequality (LMI) constraints of the optimization problem in Equations 7.12 and 7.13 represent a problem with infinite number of constraints assuming continuous parameter variations. To make the problem computationally tractable, the solution is obtained over a finite set of parameter points composing an $n$ dimensional grid. This is a conservative step which is necessary to calculate the solution. The obtained solution of $X(\rho)$ and $Y(\rho)$ is then evaluated on a finer grid to ensure the performance between the grid points. Also the arbitrary $X(\rho)$ and $Y(\rho)$ functions are represented by a finite set of continuously differentiable basis functions.

$$X(\rho) = \sum_{i=1}^{N_{xb}} f_i(\rho) X_i, \quad Y(\rho) = \sum_{i=1}^{N_{yb}} g_i(\rho) Y_i \tag{7.27}$$

Where $f_i(\rho)$ and $g_i(\rho)$ are basis functions and $N_{xb}, N_{yb}$ are the order of basis functions for $X$ and $Y$ respectively.

There is no analytical way to find the best basis functions for the LPV solution. Choosing basis functions in Equation 7.27 is an ad-hoc method [48]. Using the heuristic rule that the basis function match the parameter-dependence in the plant seems to produce the best results [53]. Several authors suggested methods for basis function selection for LPV synthesis. A set of cubic splines is suggested as a linear basis function set by Wood and Papageorgiou [54] and Legendre polynomials is suggested for control of the planar ducted fan by Primbs. Power series is used in the control of the short period motion of the F-16 by Lee [64]. Becker performed a comparison on basis functions matched with the parameter dependence against one linear set of basis functions and the $\mathcal{L}_2$ norm performance was better with matched basis [52]. Still, only guidelines and trial and error methods exists for selecting the basis functions.

The computational time for synthesizing an LPV controller is dependent on the number of LMI constraints and the number of decision variables of $X(\rho)$ and $Y(\rho)$ in the optimization problem 7.11. The total number of LMIs is dependent on the grid points of each parameter and the number of scheduling variables. When the number of scheduling parameters is $m$ and the total number of grid points is $n_{gp}$, the total number of LMIs is $n_{gp}(2 \cdot 2^m + 3)$. Since the computational time is assumed to be proportional to the number of LMIs, the computational time increases at an exponential growth rate with respect to the number of parameter $m$. When the state order of the generalized open-loop interconnection is $n_s$, and the orders of basis functions described in Equation 7.27 are $N_{xb}$ and $N_{yb}$, and the number of decision parameter is $(N_{xb}+N_{yb})\frac{n_s(n_s+1)}{2}$, the total computational time of LPV control synthesis may be proportional to:

$$n_{gp}(2 \cdot 2^m + 3)(N_{xb}+N_{yb})\frac{n_s(n_s+1)}{2}. \tag{7.28}$$

Therefore, computational time is a limiting factor in LPV synthesis, when a high order state LPV system and a large number of scheduling parameters are considered. A possibility to reduce the computation time of LPV synthesis is discussed next.

### 7.2.3 Blending of LPV Controllers

Since the controller synthesis problem poses a difficult, resource intensive task even for present day computers, it is essential to break down the complex LMI optimization into several subproblems, which can be solved independently. A method of synthesizing LPV controllers for smaller regions of the operating envelope and then blending them together is described by Lee [64]. Partitioning the parameter set may allow to handle plant dynamics experiencing drastic variations at boundaries, between well defined regions. For example, the variation of dynamics of the HSSV on the boundary of non-planing and planing region is dramatic, since the new source the planing force drastically alters the dynamical behavior, even more sudden than a supersonic vehicle transitioning from subsonic to supersonic speed, where the aerodynamic coefficients of the airplane transition during the transonic part of the flight. The need to model the plant and the weighted interconnection with high order models, with the clear need to use higher order basis functions and dense grid on the entire parameter space, may lead to prohibitive computational cost. It is also noticed, that for a wider region of parameters, higher order basis functions are more suitable, hence partitioning the parameter set allows for richer class of variables, in effect introducing piecewise bases [64].

Consider the parameter set $\mathcal{P}$ as the union of finite number of overlapping compact subsets $\mathcal{P}^0, \mathcal{P}^1, ..., \mathcal{P}^n$. Denote the (nonempty) interior of their intersection by

$$\mathcal{P}_\cap := (\mathcal{P}^0 \cap \mathcal{P}^1 \cap, ..., \cap \mathcal{P}^n) \neq 0 \tag{7.29}$$

Moreover, assume that the complementary sets

$$\mathcal{P}^0 \setminus \mathcal{P}_\cap, ..., \mathcal{P}^n \setminus \mathcal{P}_\cap \tag{7.30}$$

are disjoint.

The blended input/output feedback case for the problem described in Section 7.2 can be defined. Here, each LPV controller is individually designed for each parameter spaces $\mathcal{P}_i$ defined above for a given performance level $\gamma_i$. Using Theorem 7.2, individual LPV controllers are blended for intersection parameter space $\mathcal{P}_\cap$ and the blended controller can achieve $\gamma$ performance level.

Extending results of Section 7.2 using scalar interpolation or "blending" functions $b_i(\rho) \in \mathcal{C}^1(\mathbb{R}^s \to \mathbb{R})$ that satisfy the boundary condition

$$b_i(\rho) = \begin{cases} 0 & \rho \in \mathcal{P}_i \setminus \mathcal{P}_\cap \\ 1 & \rho \in \mathcal{P} \setminus \mathcal{P}_i \end{cases} \tag{7.31}$$

For the intersection region,

$$\sum_{i=1}^{n} b_i(\rho) = 1, \quad 0 \leq b_i(\rho) \leq 1, \ \rho \in \mathcal{P}_\cap \tag{7.32}$$

Where $b_i(\rho)$ is a monotonic function.

**Theorem 7.2.** *Given the open-loop LPV system in Equation 7.6, parameter sets satisfying Equations 7.29-7.30, and blending functions $b_{xj}(\rho)$ and $b_{yj}(\rho)$ satisfying Equations 7.31-7.32. Suppose there exist $\gamma_j \in \mathcal{R}$, positive definite matrix functions $X_j(\rho)$ and $Y_j(\rho)$ that satisfy Equations 7.12 and 7.13. There exist positive definite matrix functions $X(\rho)$ and $Y(\rho)$*

$$X(\rho) = \sum_{j=1}^{n} b_{xj}(\rho) X_j(\rho), \rho \in \mathcal{P}_\cap \tag{7.33}$$

$$Y(\rho) = \sum_{j=1}^{n} b_{yj}(\rho) Y_j(\rho), \rho \in \mathcal{P}_\cap \tag{7.34}$$

*such that $X$ and $Y$ defined in Equations 7.33 and 7.34 satisfies equations 7.12 and 7.13 on the entire parameter subspace $\mathcal{P}_\cap$ with*

$$\sum_{i=1}^{m}\left(\underline{\overline{\nu}}_i \sum_{j=1}^{n} X_j(\rho)\frac{\partial b_{xi}(\rho)}{\partial \rho_i}\right) > 0 \tag{7.35}$$

$$\sum_{i=1}^{m}\left(\underline{\overline{\nu}}_i \sum_{j=1}^{n} Y_j(\rho)\frac{\partial b_{yi}(\rho)}{\partial \rho_i}\right) > 0 \tag{7.36}$$

*$\underline{\overline{\nu}}_i$ denoting all possible combination of upper and lower rate bounds on parameter $\rho$, where*

$$\frac{\partial X}{\partial \rho_k} = \sum_{j=1}^{m} b_j(\rho)\frac{\partial X_j}{\partial \rho_k} + \frac{\partial b_j}{\partial \rho_k}X_j(\rho) \tag{7.37}$$

$$\frac{\partial Y}{\partial \rho_k} = \sum_{j=1}^{m} b_j(\rho)\frac{\partial Y_j}{\partial \rho_k} + \frac{\partial b_j}{\partial \rho_k}Y_j(\rho) \tag{7.38}$$

*Achieving performance level*

$$\gamma = \max(\gamma_1, ..., \gamma_n) \tag{7.39}$$

*where $m$ is the number of scheduling parameters and $n$ is the number of parameter subspaces $\mathcal{P}_i$. The blended controller is constructed as described above, using piecewise functions of $X(\rho)$ and $Y(\rho)$ as defined in Equations 7.33-7.33 and substituted into Equations 7.19-7.22 describing the controller. It is guaranteed that the overall performance does not exceed the maximum $\gamma_i$ performance level achieved over the subsets.*

The method is illustrated in Section 7.3, where it is applied to the control synthesis of the HSSV vehicle.

### 7.2.4 Avoiding Fast Controller Dynamics

The issue of "fast" controller dynamics is discussed in this section. A method proposed by Lee [64] use pole-placement ideas to avoid certain numerical difficulties associated with high frequency controller dynamics. It has been observed that output feedback controllers formed using Theorem 7.7 can unnecessarily possess very fast modes (i.e., the controller matrix $A_k$ can have very large stable eigenvalues), especially if the matrix in 7.12 is nearly singular. This can render the implementation of such controller on a digital computer virtually impossible, because of the potential of aliasing.

Fortunately, LMI-based tools developed by Chilali and Gahinet [65] for $\mathcal{H}_\infty$ control with pole-placement can be readily adapted to the LPV framework. The problem considered here is to constrain the (negative) real part of the eigenvalues of $A_K$; a more general treatment of $\mathcal{H}_\infty$ control with pole-placement can be found in [65]. We will use the following lemma to characterize a constraint on the closed loop "poles".

**Lemma 7.2.** *Let $A \in \mathbb{R}^{n\times n}$ and $\eta > 0$. There exists a positive-definite matrix $P \in \mathbb{R}_+^{n\times n}$ such that*

$$2\eta P + A^T P + PA > 0 \tag{7.40}$$

*if and only if $Re(\gamma) > -\eta$ for every eigenvalue $\gamma$ of $A$.*

**Proof**: Observe that the eigenvalue condition is met if and only if the matrix $-(\eta I_n + A)$ is Hurwitz. This, in turn, is equivalent to the existence of a positive definite matrix $P$ that satisfies the Lyapunov inequality

$$-(\eta I_n + A)^T P - P(\eta I_n + A) < 0 \tag{7.41}$$

which is equivalent to 7.40. The following generalization of Lemma 7.2 in the special case $D_{ed} = 0$ modifies the LMI (7.10) so that the LPV controller that solves the output feedback $\gamma$-performance problem does not introduce fast dynamics into the closed-loop system (as measured by the closed loop "poles"). Although the result strictly applies only in the case of constant parameter trajectories (indeed, only LTI systems can be said to have poles), we believe that the numerical robustness introduced also provides sufficient protection against aliasing for parameter variations at modest rates.

**Theorem 7.3.** *Given a scalar function $\eta \in \mathcal{C}(\mathbb{R}^s \mapsto \mathbb{R}_+)$ and the LPV plant $G_\rho$ in Equation 7.6, assume $D_{ed}(\rho) = 0$ for all $\rho \in \mathcal{P}$. Suppose there exist $X \in \mathcal{C}^1$ and $Y \in \mathcal{C}^1$ satisfying 7.12,7.13 and*

$$\begin{bmatrix} Y(\rho) & I_n \\ I_n & X(\rho) \end{bmatrix} + \frac{1}{2\eta(\rho)}\left(\Phi(\rho) + \Phi^T(\rho)\right) > 0 \tag{7.42}$$

*at all $(\rho, \dot{\rho})$ for which $\rho \in \mathcal{P}$ and $\dot{\rho} \in \underline{\overline{\nu}}(\rho)$, where omitting the dependence on $\rho$*

$$\Phi = \begin{bmatrix} \hat{A}Y - \gamma B_2 B_2^T & B_2 C_2 + B_{12} C_2 \\ -\gamma^{-1}\left(C_{11}^T C_{11} Y + (XB_{11})B_{11}^T\right) & XA - \gamma C_2^T C_2 \end{bmatrix} \tag{7.43}$$

*Then the output-feedback $\gamma$-performance problem is solvable with order $n$ and, for all $\rho \in \mathcal{P}, Re(\gamma) > -\eta(\rho)$ for every eigenvalue $\lambda$ of $A_{cl}(\rho)$, where $A_{cl}$ is given by Equations 7.7 and the other formulae for controller synthesis.*

The proof of the procedure can be found in [64]. It should be noted, that the procedure is most effective if the fast poles are well-damped, since their imaginary part (if any) are not constrained. Finally, the controller poles are influenced only indirectly via closed-loop eigenvalues.

## 7.3 LPV Control Synthesis Applied to the HSSV

Two approaches are proposed to synthesize pitch, roll and yaw reference tracking controllers for the supercavitating vehicle using rate-bounded LPV synthesis techniques described in Section 7.2. The vehicle as described by Equations 3.88-3.93 has six states and six inputs and after investigation of the coupling between the kinematics and kinetics equations, an LPV description of the form of Equation 6.39 is proposed to serve as a model for control design. The LPV description has 11 inputs, including the 6 actuators and 5 measured disturbances, accounting for the effect of planing. Two scheduling parameters are used to describe the change in dynamics throughout the operating envelope. They are parameterizing the plant at $\mathcal{P}_1 = \sqrt{\alpha^2 + \beta^2}$ and $\mathcal{P}_2 = \tan^{-1}(\beta/\alpha)$. These parameters are presented on a $3 \times 9$ grid, as seen on Figure 6.2, where the parameters range as $\mathcal{P}_1 = [0; 0.46; 0.92]$ *deg* and $\mathcal{P}_2 = [0; 45; 90; 135; 180; 225; 270; 315; 360]$ *deg*. As observed in Chapter 6, there is a one-to-one correspondence between aerodynamic angles $\alpha, \beta$ and cavity offset parameters $z_c, y_c$, at trim conditions with zero angular rates. Hence it is possible to schedule the plant with the corresponding cavity offset values also. The final vehicle will have restrictions on actuation rate, hence six first order actuator models are augmented with the plant for control design.

It is assumed that a high level trajectory planing algorithm provides position and/or heading angle reference commands to an autopilot. To allow this, the vehicle has to follow three dimensional trajectories. The autopilot, due to the high complexity of vehicle dynamics, does not command deflections directly. Rather it provides low-level roll, pitch and yaw rate commands for the stability augmentation control system. The low-level control system commands the actuator deflections of the hydrodynamic surfaces. The objective of the inner-loop is to provide good tracking on $p_{ref}, q_{ref}$ and $r_{ref}$ and disturbance rejection properties throughout the operating envelope, while minimizing the effect of planing. Note, that the LPV equations-of-motion are obtained around zero flight-path angle with steady-state approximation of the cavity dynamics, hence the control algorithm has to be robust to unmodeled dynamics, even in the presence of measurement noise.

It is assumed that a real-time measurement of the scheduling parameter is available to the LPV controller. The LPV controllers, similarly to LTI $\mathcal{H}_\infty$ regulators, are designed to minimize command-tracking errors and disturbance responses, in the $\mathcal{L}_2 \to \mathcal{L}_2$ sense, associated with a weighted interconnection structure.

The conventional way to synthesize inner-loop controllers for aircrafts and missiles is to break the coupled lateral and longitudinal motion of the vehicle and synthesize controllers for the decoupled dynamics [55]. This decoupled problem formulation results in smaller subproblems, which can be handled with conventional control synthesis techniques. A drawback of the approach is it neglects the coupling between the lateral and longitudinal modes. This is often a valid assumption for moderate angles-of-attack on airplanes and missiles. However, in the case of the supercavitating vehicle these coupling terms are significant, as seen on the frequency domain responses shown in Figure 6.6-6.7, and largely due to the behavior of the cavity. Synthesizing fully coupled controllers poses a more difficult task for the control designer, since interactions have to be handled in a higher dimensional problem, which is often less transparent.

To provide an overall picture of synthesizing controllers for the HSSV vehicle, two scenarios are considered *i*) a decoupled, longitudinal-, lateral-directional controller consisting of three different loops for pitch, yaw and roll tracking, and *ii*) a coupled controller design, which treats the full 6-DOF control problem as a single entity. These two approaches are compared in the following.

Two different maneuvering types, skid-to-turn and bank-to-turn, are considered. The former takes advantage of all control actuators, while the later reduces the usage of cavitator yaw actuation which is a potential requirement by vehicle design. The closed-loop requirements for the augmented vehicle are:

- maintaining stability in the presence of modeling error over operation range specified by $\sqrt{\alpha^2 + \beta^2} < 1 \ deg$,
- track pitch-, and yaw-rate reference signals with maximum value on their commands of 1 $rad/s$, with less than 0.2 $sec$ time constant, less than 10% overshoot and no more than 1% steady state error within the operation range,
- track roll-rate reference commands less than 8 $rad/s$, with less than 0.075 $sec$ time constant, less than 10% overshoot and no more than 1% steady state error within the operation range,
- decoupled pitch, yaw and roll response during skid-to-turn maneuvers with zero steady state roll-rate and less than 0.1 $rad/s$ maximum roll-rate,
- decoupled pitch, yaw and roll response during bank-to-turn maneuvers with zero steady state yaw-rate and less than 0.1 $rad/s$ maximum yaw-rate,
- stability for disturbances exceeding the nominal operating envelope of $\alpha, \beta, p, q, r$ by 50%,
- maximum actuator commands should not exceed 15 $deg$ for more than 0.1 $s$ for tasks specified above, with 15 $deg$ actuator deflection limits
- maintaining stability over operation range previously specified, with ±5% uncertainty in c.g. location,±5% uncertainty in fin span,
- maintaining stability during steady planing, when commands are high enough tracking is guaranteed with constant immersion into the liquid.

It should be noted that the difference between pitch/yaw rate and roll rate requirements is due to the nature of bank-to-turn maneuvering. Since the inertia around the $x$-axis is approximately 200 times smaller than around the $y$ or $z$-axis, higher bandwidth control can be achieved on roll rate, hence the controller task is easier, with lower interaction between channels, if the bandwidth requirements are separated. The rise time for roll rate is constrained by the actuators used on the vehicle, which are assumed to be first order models with 30 $Hz$ bandwidth. An additional requirement of control command attenuation at high frequencies is often expected in case of vehicles with flexible modes, since high order excitation from control can interact with the structure. This requirement is not directly enforced here, since no information is available on the flexible modes of the body.

The inner-loop control architecture is shown on Figure 7.2, the inputs to the vehicle are control commands from an LPV controller scheduled on $\alpha, \beta$ or $z_c, y_c$ measured parameters, combined with trim values obtained from a lookup-table scheduled with bank angle $\phi$. Scheduling the trim with additional parameters does not provide additional benefit, since we expect trajectories with moderate flightpath angle, while in the case of non-steady state conditions trim with $\alpha$ and $\beta$ introduces hidden feedback loops as described in [50], which reduce the performance of the overall control system. The LPV controller receives measurements of the states including $\alpha, \beta, p, q, r$ and estimates of the planing forces and moments $F_{p,y}, F_{p,z}, M_{p,y}, M_{p,z}$, with the objective to follow the reference commands $(p_{ref}, q_{ref}, r_{ref})$.

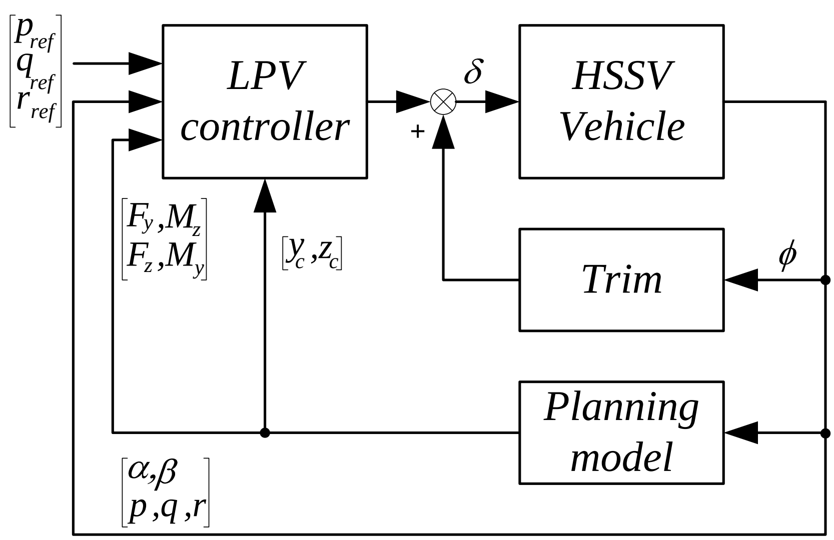


Figure 7.2: Control interconnection structure.

### 7.3.1 Decoupled LPV Design

For simplicity the synthesis of the decoupled controller is presented first. It should be noted, that the design parameters, i.e. weighting functions, used in the controller synthesis are tuned for both the coupled and decoupled cases simultaneously. Since there is clear physical correspondence between the inputs, outputs and system dynamics of the coupled and decoupled systems, the assumption of using the same weighting functions during synthesis of the two controllers provides a fair comparison between the two designs.

The pitch loop operates on the longitudinal dynamics, using $\alpha$ and $q$ for feedback, while the planing force $F_z$ and the corresponding moment $M_y$ enters the longitudinal controller as measured disturbances. The longitudinal dynamics $G_{long}(\alpha)$ are parameterized with $\alpha$ given the assumption of zeros sideslip-angle ($\beta = 0$). The model has 3 states with three inputs and two outputs, in addition to the two disturbance input channels of planing. Notice, that since the longitudinal motion is symmetric, it is assumed that the port and starboard fins have exactly the opposite effect, due to the sign convention in rotation direction. The LPV controller is parameterized as a function of $\alpha$, hence the longitudinal axis controller will schedule as a function of $\alpha$ as seen on Figure 7.3.

The problem is formulated as a model matching problem in the LPV framework. We desire the pitch loop to respond for reference command $r$ like an ideal reference model, denoted by $W_{ref}$, and the difference between this desired response and the true plant is penalized via the weight $W_e$. The disturbance input $d$ represents the planing force and moment inputs to the plant, and are available to the controller. $d$ is filtered through $W_d$ to obtain the specific characteristics of planing disturbances. The measurements of $\alpha$ and $q$ fed-back to the controller are corrupted by noise or modeling error $n$ via weight $W_n$, for which the closed-loop should be robust. Low angle-of-attack ($\alpha$), which is closely related to avoiding planing, is ensured by keeping $p$ small in frequencies described by $W_p$. Input and actuator modeling errors, actuator rate and magnitude constraints are accounted for in the controller design via the $u$ to $w$ input/output pair, representing an input multiplicative uncertainty structure. The measurements available to the controller are: $W_d, r$ and the $\alpha, q$ measurements corrupted by noise $W_n$, while the controller outputs ($c$) are the three actuator commands: cavitator pitch ($\delta_{c,p}$), port ($\delta_{f,1}$) and starboard ($\delta_{f,3}$) fin deflections.

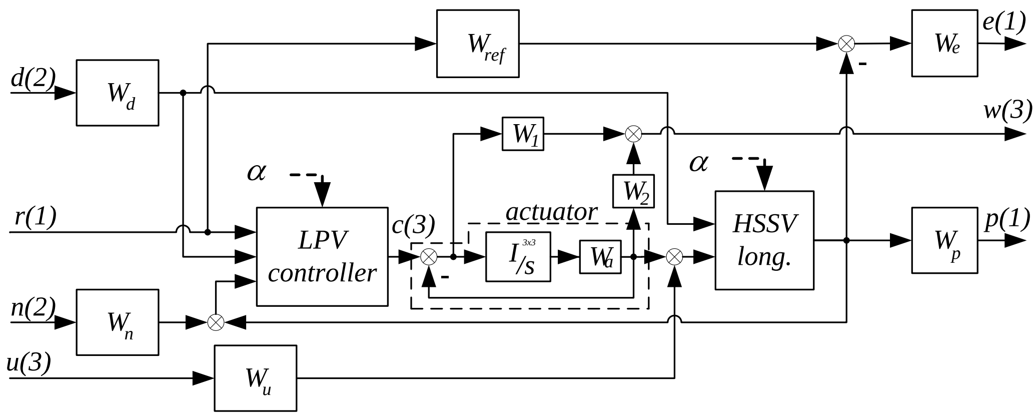


Figure 7.3: Weighted LPV control synthesis interconnection for pitch tracking.

Yaw rate tracking is approached in a similar manner, using the same weighted interconnection as shown in Figure 7.3, only the yaw rate controller is scheduled with $\beta$. Feedback of measurements $r, F_{p,y}$ and $M_{p,z}$, are used. The plant and the controller are scheduled on $\beta$ and the mirror symmetry is lost as the plant leaves the longitudinal plane. Hence in addition to providing cavitator yaw control command ($\delta_{c,p}$) the controller also outputs the lower $\delta_{f,2}$ and upper $\delta_{f,4}$ fin deflections.

Preliminary results [16] suggest that the planing behavior is oscillatory with approximately 15 $Hz$ frequency in the uncontrolled mode. The actuator bandwidth has to be high to cope with the planing effect. The actuators are assumed to have 30 $Hz$ bandwidth which is represented as a first order transfer function:

$$G_{act} = \frac{W_a}{s + W_a};\ W_a = 200. \tag{7.44}$$

The realization as shown in Figure 7.3 allows both actuator rate and magnitude to be penalized via $W_1$ and $W_2$ weights respectively. Moreover, the controller objective to minimize the gain between $u$ to $w$ can be interpreted as incorporating input multiplicative uncertainty to the plant input. The uncertainty weight is represented by the transfer function from input channel $c$ to performance output $w$:

$$G_{cw} = \frac{sW_1 + W_aW_2}{s + W_a} \tag{7.45}$$

This realization of the uncertainty model has less freedom than an arbitrary weighting function. Since we desire a low state order, due to computational complexity, it is sufficient for our purposes. The $W_1$ and $W_2$ weights are selected as

$$W_1 = \begin{bmatrix} 2 & 0 & 0 \\ 0 & 3 & 0 \\ 0 & 0 & 3 \end{bmatrix} \tag{7.46}$$

$$W_2 = \begin{bmatrix} 0.2 & 0 & 0 \\ 0 & 0.3 & 0 \\ 0 & 0 & 0.3 \end{bmatrix} \tag{7.47}$$

These weights ensure that actuator rates are penalized with a magnitude higher cost than the actuator deflections and the overall uncertainty weight transfer function from $c$ to $w$ has a frequency response as shown in Figure 7.4. This corresponds to 20% uncertainty on

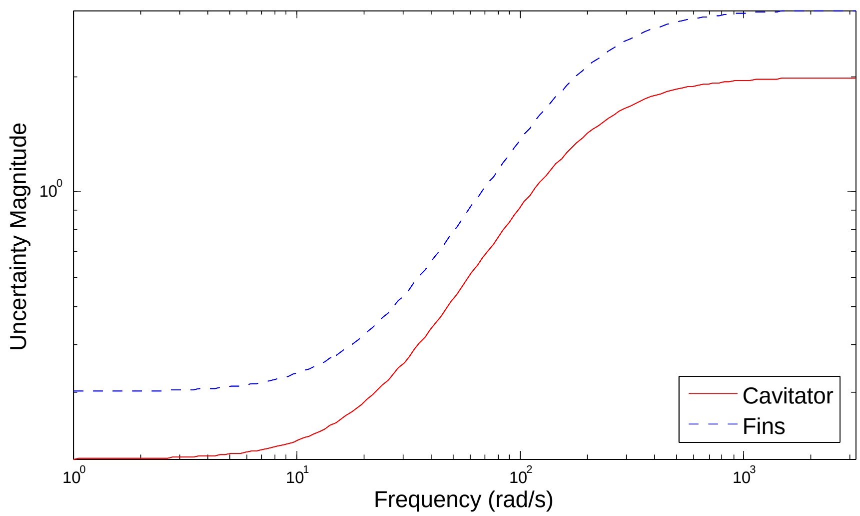


Figure 7.4: Weighted interconnection of the control problem

cavitator and 30% uncertainty on fin inputs at low frequencies, while their uncertainties exceed 100% at frequencies higher than 100 $rad/s$. It is important to notice, that fins have higher uncertainty associated with them due to the cavity hysteresis effect described in Chapter 3.

Planing force $F_{p,z}$ and moment $M_{p,y}$ are entering the model and available for the controller via the low pass filter $W_d$ which is responsible for scaling the influence of planing with its expected value.

$$W_d = \begin{bmatrix} 1000\frac{100}{s+100} & 0 \\ 0 & 1000\frac{100}{s+100} \end{bmatrix}. \tag{7.48}$$

This description corresponds to the observation that planing disturbances can have high frequency content up to approximately 15 $Hz$. It is important to point out in $\mathcal{H}_\infty$/LPV control design, that the inputs and outputs of the plant have to be normalized to avoid ill-posed problems. Since the objective of the $\mathcal{H}_\infty$/LPV problem formulation is to achieve robust performance, which is guaranteed if $\gamma$ described in Equation 7.10 is less than one. However, if the inputs and outputs of the weighted interconnection are not scaled properly the optimization can be biassed towards undesired properties. To illustrate the problem given the present example, assume the design achieved $\gamma = 1$, hence the gain between $d$, the planing input to $p$, angle-of-attack output has to be less than one. If the input/output channels are not normalized for 1 $N$ planing force it is guaranteed that $\alpha$ does not exceed 1 $rad$. This is clearly not the performance we want to achieve. Assuming planing force has expected value of 1000 $N$, and approximately the moment arm of planing force is 1 $m$, then input $d$ has to be scaled up as described by $W_d$ to address the effect of planing on the plant behavior. The same can be done for $u$ which is the associated with the uncertainty on the actuators. Assume the actuators have deflection limits of $\pm 0.3$ $rad$, $W_u$ is selected to have 10% uncertainty on each actuator channel.

$$W_u = \begin{bmatrix} 0.03 & 0 & 0 \\ 0 & 0.03 & 0 \\ 0 & 0 & 0.03 \end{bmatrix} \tag{7.49}$$

The pitch rate reference input ($r$) is not normalized, since the maximum reference commands are expected to be $\pm 1$ $rad/s$.

At the present stage no characteristics are available on the quality of measurements available for feedback, though it is expected that the sensors will have noise component. For this reason, $W_n$ is selected as

$$W_n = \begin{bmatrix} 0.002 & 0 \\ 0 & 0.02 \end{bmatrix} \tag{7.50}$$

which represents biassed assumptions, with low noise component on $\alpha$ channel and relatively corrupted measurement of pitch rate.

Handling qualities specified previously are addressed in the design with the reference model $W_{ref}$, which is a second order weighting function. A first order ideal model would not be sufficient for our purpose, since the derivative of the ideal model has to be continuous for step changes in reference commands. The way the plant is augmented with the actuator model, the controller optimization problem would be infeasible with first order reference model.

$$W_{ref} = \frac{25^2}{s^2 + 50s + 25^2} \tag{7.51}$$

This ideal model corresponds to rise time of 0.2 $s$ and has no overshoot due to damping coefficient of 1, while the second order behavior allows sufficiently smooth reference following response.

Precise tracking is guaranteed by the appropriate selection of weight $W_e$. It is desired to keep the mismatch between the reference model and the vehicle response small at low frequencies, resulting in low steady-state error. The limited actuator bandwidth, the possibility of lightly damped flexible body modes and the high frequency model uncertainty dictates the controller should roll-off at high frequencies, hence the performance requirement should decrease below 1 around the loop-bandwidth.

$$W_e^q = 35\frac{400}{s^2 + 40s + 400} \tag{7.52}$$

We will help ensure good model tracking in the range of $0 - 20\ rad/sec$ with little or no steady state error and allow sufficient freedom for the performance to degrade at high frequency. As described in Chapter 3, instantaneous changes in $\alpha$ do not necessarily lead to planing due to the lag between the cavitator-tail distance. Therefore an additional performance requirement, penalizing $\alpha$ at low frequency, is added to the performance requirement.

$$W_p = 6\frac{250}{s + 250} \tag{7.53}$$

Since $\alpha$ is expected to be less than 0.016 $rad$, the weight has to account for the low magnitude of the signal. The low frequency weight is higher than 1, but it is sufficiently low not to bias the overall problem towards only minimizing $\alpha$.

The parameter dependent weighting functions can also be used in the LPV synthesis. This provides additional flexibility for the control designer and allows engineering insight to be included in the problem formulation. For example, tracking performance and robustness can be traded off at different parameter ranges. Near $\alpha = 0$ the model has higher fidelity, hence the uncertainty description is allowed to have lower values with providing freedom to define higher tracking performance. The opposite is true at high-angles of attack, where lower performance would be accepted in exchange for increased robustness. However, since no information is available on the fidelity of system parameters, and the advantages of parameter dependent performance criteria were not exploited, only parameter independent weight are used here.

The behavior of the yaw dynamics is very similar to the pitch channel, hence the same weighted interconnection is used to formulate the yaw-rate tracking problem (Figure 7.3). Since only minor differences can be observed between the two problem, the same set of weights are used in here. The differences between the pitch- and yaw-rate controller synthesis are in the system dynamics $G_{yaw}$ is different from $G_{pitch}$. The yaw dynamics have 3 states and scheduled with sideslip angle ($\beta$), assuming $\alpha = 0$. Inputs are cavitator yaw $\delta_{c,y}$, lower $\delta_{f,2}$ and upper $\delta_{f,4}$ fin deflections. Measurements available for feedback are sideslip-angle $\beta$ and yaw-rate $r$, plus the two disturbance input channels of planing $(F_{p,y}, M_{p,z})$. Notice, that since the yaw motion is non-symmetric, the lower and upper fin have different effectiveness, due to the difference in their immersion. The LPV controller obtained during the design is scheduled on $\beta$ like the plant.

A single $\mathcal{H}_\infty$ controller is sufficient to provide roll rate reference tracking with roll rate measurement across the flight envelope. Since the roll actuators have much higher control authority due to low inertia around the x-axis. Here the plant $G_{roll}$ is LTI, obtained at $\alpha = \beta = 0$ corresponding to the middle of the parameter range. And has four inputs, one output and a single state. The performance objective is good reference tracking via minimizing the error between the plant output and the response of the ideal model $W_{ref}$. Robustness against unmodelled dynamics and uncertainty in actuator modeling are addressed in the synthesis by the transfer function from $u$ to $w$ as shown on Figure 7.5. The effect of sensor noise, weighted across frequencies via $W_n$ is desired to be low in the closed loop.

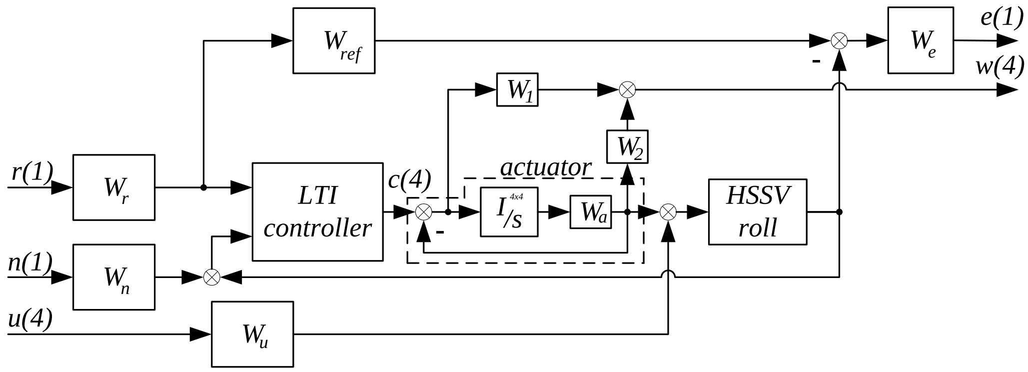


Figure 7.5: Weighted $\mathcal{H}_\infty$ control synthesis interconnection for roll tracking.

As seen in Figure 7.5, the roll-rate tracking problem has similar set of weighting functions as the pitch and yaw rate control problems.

Command tracking is achieved in the roll-rate problem via minimizing the error vector ($e$) over the range of frequencies as described by $W_e$ weighting function.

$$W_e^p = 10\frac{200}{s+200} \tag{7.54}$$

Which by definition, ensures less than 10% steady state error but due to the integral action in the plant it is essentially zero. Moreover, $W_e$ guarantees sufficient command tracking in the frequency range of $0-50\ rad/s$. The ideal model has higher bandwidth than the pitch and yaw loop, to separate their frequency ranges, eliminating the possible interference between roll and pitch/yaw rate loops. In case bank-to-turn maneuvering is desired, the roll commands have to be executed fast to allow sufficient time to execute the the pitch maneuvers, composing the major part of the trajectory.

$$W_{ref} = \frac{50^2}{s^2+100s+50^2} \tag{7.55}$$

Similarly to the pitch and yaw reference model, the ideal roll response exhibits a second order behavior, with sufficiently high damping coefficient to eliminate overshoot. Since the expected roll-rate commands have higher magnitude, on the order of $8-10\ rad/s$ meaning 1.5 rotation in one second, an input weight

$$W_r = 8 \tag{7.56}$$

is used to scale the reference input. The noise component on the roll rate measurement is assumed to be equal to noise on pitch and yaw rate channels.

$$W_n = 0.02 \tag{7.57}$$

Similarly the $W_u, W_1, W_2$ weights associated with the uncertainties are kept at the same values as in the previous design, with the difference that the roll control uses four fins for control.

$$W_u = \begin{bmatrix} 0.03 & 0 & 0 & 0 \\ 0 & 0.03 & 0 & 0 \\ 0 & 0 & 0.03 & 0 \\ 0 & 0 & 0 & 0.03 \end{bmatrix} \tag{7.58}$$

$$W_1 = \begin{bmatrix} 3 & 0 & 0 & 0 \\ 0 & 3 & 0 & 0 \\ 0 & 0 & 3 & 0 \\ 0 & 0 & 0 & 3 \end{bmatrix} \tag{7.59}$$

$$W_2 = \begin{bmatrix} 0.3 & 0 & 0 & 0 \\ 0 & 0.3 & 0 & 0 \\ 0 & 0 & 0.3 & 0 \\ 0 & 0 & 0 & 0.3 \end{bmatrix} \tag{7.60}$$

Leading to the similar level of uncertainty as in the pitch/yaw axis.

### 7.3.2 Coupled LPV Design

The second approach provides a more sophisticated way of handling the strongly coupled vehicle dynamics by treating the pitch, roll and yaw dynamics as a single entity. As illustrated in Figure 7.6, the integrated approach combines measurement of $\alpha, \beta, p, q$ and $r$ with the estimates of $F_{p,y}, F_{p,z}, M_{p,y}$ and $M_{p,z}$ planing forces and moments, to synthesize a LPV controller scheduled with $\mathcal{P}_1$ and $\mathcal{P}_2$. The scheduling parameters are functions of $\alpha$ and $\beta$ aerodynamic angles, or alternatively the cavity offset values $y_c$ and $z_c$ corresponding to $\alpha_{trim}$ and $\beta_{trim}$ angles. It is assumed that these signals are available in real-time for scheduling the controller.

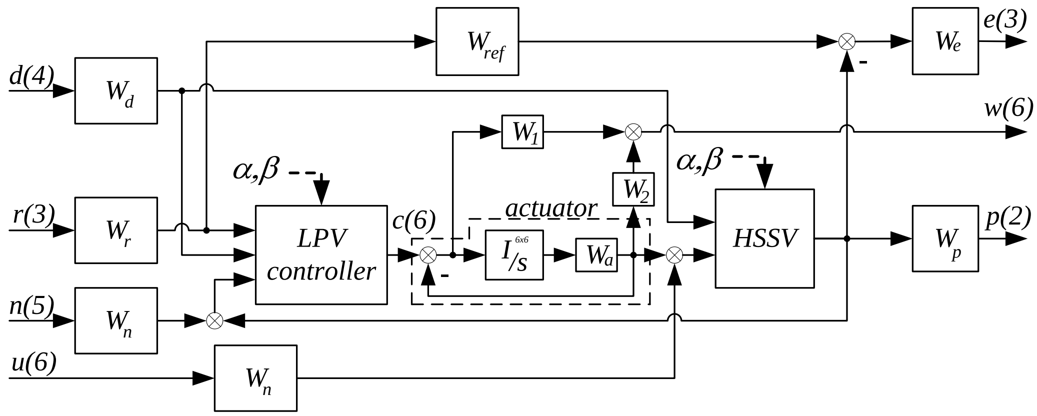


Figure 7.6: Weighted interconnection of the coupled control problem

The system interconnection shown in Fig. 7.6 provides the robust parameter dependent controller synthesis architecture proposed for the trajectory tracking problem. Model mismatches are accounted for as weighted unmodeled LTI dynamics and disturbances are modeled as exogenous signals, in the same way as presented in the decoupled synthesis. The same control design objectives, stated above, are required achieving decoupled responses on all channels throughout the operating envelope, with sufficient speed of response and robustness.

The vehicle model $G_\rho$ has six states, five of them are measurable $\alpha, \beta, p, q, r$. The velocity $V_m$ is omitted since the linearized models only account for deviation from trim and velocity tracking using thrust for control is not included in the present formulation. Six inputs, two cavitator and four fins are available for control. The controller, similar to the plant, is scheduled with $\mathcal{P}_1$ and $\mathcal{P}_2$, associated with $\alpha$ and $\beta$ as described in Equations 6.41-6.42.

The weights used in the system interconnection on Figure 7.6 are derived from the weights presented in Section 7.3.1. The weights are tuned for the coupled and for the decoupled problem at the same time, to provide a comparison of the two scenarios.

The weights associated with the influence of planing forces and moments, modeled as measured disturbances, are denoted with $W_d$. They represents the expectation of maximum planing forces $F_y, F_z$ and moments $M_y, M_z$ during nominal maneuvers.

$$W_d = I_{4\times4}\left(1000\frac{100}{s+100}\right) \tag{7.61}$$

Noise characteristics are captured with $W_n$ in the $\alpha, \beta$ and $p, q, r$ channels. Since the LPV plant is scheduled with $\mathcal{P}_1$ and $\mathcal{P}_2$, the control is very sensitive to $\alpha$ and $\beta$ measurements, hence only a small amount of noise is assumed on these two channels. $W_n$ is diagonal with weights:

$$W_n = \begin{bmatrix} 0.002 I_{2\times 2} & 0 \\ 0 & 0.02 I_{3\times 3} \end{bmatrix} \tag{7.62}$$

Model matching is achieved via the same "ideal" model as described previously to achieve smooth behavior with adequate speed of response for steering commands.

$$W_{ref} = \begin{bmatrix} \frac{50^2}{s^2+100s+50^2} & 0 \\ 0 & \frac{25^2}{s^2+50s+25^2} I_{2\times 2} \end{bmatrix} \tag{7.63}$$

Multiplicative input uncertainty is included in the design to provide robustness against improper knowledge of fin and cavitator forces. The uncertainty model is augmented with the actuator model to reduce the problem size as seen on Figure 7.6. $W_1$ is a diagonal matrix with equal channels on the two cavitators and on the four fins:

$$W_1 = \begin{bmatrix} 2 I_{2\times 2} & 0 \\ 0 & 3 I_{4\times 4} \end{bmatrix} \tag{7.64}$$

while $W_1$ penalizes high actuator rate, $W_2$ weights actuator deflections in the control optimization:

$$W_2 = \begin{bmatrix} 0.2 I_{2\times 2} & 0 \\ 0 & 0.3 I_{3\times 3} \end{bmatrix} \tag{7.65}$$

The combined output of $W_1 + W_2$ acts as a filter which represents higher than 100% model uncertainty above the actuator bandwidth, while it has significantly lower $20-30\%$ uncertainty in the low frequency range, below 10 $rad/s$ (see Fig 7.4).

To address actuation limitations the plant is augmented with actuator models on all six control input channels with actuator model implemented as an integrator in a feedback loop, with both rate and position information available in the control synthesis:

$$G_{act} = \frac{200}{s+200} I_{6\times 6}. \tag{7.66}$$

The main control objective, to keep the error between the plant output $p, q, r$ and the desired response $W_{ref}$ low, is weighted across frequency with:

$$W_e = \begin{bmatrix} 10\frac{200}{s+200} & 0 \\ 0 & 35\frac{400}{s^2+40s+400}I_{2\times 2} \end{bmatrix} \tag{7.67}$$

function. Providing a tradeoff between good steady state tracking with degraded performance at frequencies higher than 50 $rad/s$ on roll response and 25 $rad/s$ on pitch and yaw channel. Roll response due to low inertia and high control authority is separated in frequency from pitch and yaw, to provide decoupling for bank-to-turn maneuvers.

Not only the turning rate response is important during maneuvering but it is desired to have low aerodynamic angles, to stay inside of the cavity bubble where the parameter dependent plant description is valid. The objective of low $\alpha$ and $\beta$ are also addressed in the setup of the LPV problem, similar to the decoupled problems, with weights of:

$$W_p = \begin{bmatrix} 6\frac{250}{s+250} & 0 \\ 0 & 6\frac{250}{s+250} \end{bmatrix} \tag{7.68}$$

The weights are optimized with linear point design first, at all operating points in the polytope model. The present method does not benefit from parameter dependent performance weights, all design points use the same constant filters only the plant itself is parameter varying.

The rate-bounded LPV control design directly accounts for the rate of variation of the scheduled parameters. To be able to obtain a solution for the infinite dimensional problem described in Section 7.2, the rate-bounded LPV design is approximated by a fixed set of basis functions and solved using LMI optimization. The solution of rate-bounded synthesis is based on parameter dependent scalings of $X$ and $Y$. There is no restriction on these variables, hence the solution can be chosen from any matrix functions, provided a finite number of basis functions can be selected to represent the optimum solution. The basis functions used for the coupled control synthesis case are:

$$X(\rho) = X_0 + \mathcal{P}_1 X_1 + \mathcal{P}_2 X_2 \tag{7.69}$$

$$Y(\rho) = Y_0 + \mathcal{P}_1 Y_1 + \mathcal{P}_2 Y_2 \tag{7.70}$$

This represents that dependence on both parameters enters in a linear manner. In the decoupled case, $X$ and $Y$ have second order basis,

$$X(\rho) = X_0 + \rho X_1 + \rho^2 X_2 \tag{7.71}$$

in the lateral case parameterized with $\rho = \alpha$ and in the longitudinal control solution parameterized with $\rho = \beta$.

Currently there is no systematic way to select the basis functions. Engineering insight can lead to selection of basis functions which result in an LPV controller performing good [51]. Our experience led us to select basis functions that correspond to physical parameters that directly effect the dynamic response of the plant. This is another reason why it is important to use scheduling parameters $\mathcal{P}_1$ and $\mathcal{P}_2$ instead of $\alpha$ and $\beta$ in the coupled control synthesis.

Two pairs of rate-bounded LPV controllers are synthesized for the decoupled and coupled control problem. The first formulates the standard rate-bounded controller. The second, using the solution of the first synthesis adds another constraint to the problem. As described by Equation 7.41 the closed loop poles can be constrained in the solution with an additional LMI. The $\mathcal{L}_2$ norm achieved by the rate-bounded solution is relaxed by 5% and the solution is recalculated with an objective of reducing the poles of the $A_{cl}(\rho)$ matrix over the parameter space, to eliminate high frequency poles often experienced in $\mathcal{H}_\infty$/LPV control design.

After adjusting the design weights at extremes of the operating envelope covering $\mathcal{P}_1 = [0...1]$ *deg* and $\mathcal{P}_2 = [0...180]$ *deg* to guarantee linear robust performance at all design points, the LPV synthesis is done on a polytope model covering 24 points where the range of plants are described in the Section 6.4.2.

First pointwise $\mathcal{H}_\infty$ designs led to performance values of $\gamma = 0.7824 - 0.7926$ in the pitch rate, $\gamma = 0.7903 - 0.7944$ in the yaw rate and $\gamma = 0.3$ in roll rate controllers. The coupled controller synthesis have $\gamma = 0.7926 - 0.7959$ values corresponding to close correlation between the coupled and the decoupled controller synthesis on the plant. These $\gamma$ values mean the controller in the closed loop achieve robust performance ($\gamma \leq 1$) even with significant uncertainties on the input channels. The results also provide a good comparison for the $\mathcal{L}_2$ gain achieved during the LPV synthesis.

### 7.3.3 Blending Method for the HSSV Control

Control synthesis for the fully coupled case is performed in two steps, first local LPV controllers are synthesized on subspaces which are blended together in the second step. The blending method described in Section 7.2.3 is used in the LPV control synthesis for the coupled case, due to computational complexity of solving the LMIs over the entire grid in one step. The problem size of the optimization prohibited the calculation of the optimal solution on grids larger than $3 \times 5$ points. Since the grid has $3 \times 9$ points the parameter set is divided into 9 overlapping regions of size $3 \times 3$, where the optimization can be executed more efficiently.

The polytope LPV plant composed of 24 linear plants, as shown on Figure 6.2, is divided into 8 subregions using 9 LTI plants each as illustrated in Figure 7.7. The first blending region $\mathcal{B}_1$ is highlighted with horizontal pattern, the second region $\mathcal{B}_2$ is with vertical pattern. The blending solution is obtained over the intersection of $\mathcal{B}_i$ and $\mathcal{B}_{i+1}$. Using 9 blending regions defined as:

$$\mathcal{B}_i := \mathcal{P}_1 \in [0; 0.016\ rad];\ \mathcal{P}_2 \in [(i-1)\pi/8; (i+1)\pi/8];\quad i = 1...9 \tag{7.72}$$

The entire polytope model is covered with regions defined by Equation 7.72, every plant is contained in exactly two regions, excluding the middle point ($\mathcal{P}_1 = 0$) which is included in all regions. The controllers at each point of the parameter space are a blend of the two (different) solutions that were obtained for the corresponding regions ($\mathcal{B}_i$) LPV solution $X_i(\rho)$ and $Y_i(\rho)$ at the given parameter point ($\mathcal{P}_1, \mathcal{P}_2$). The blending function used for obtaining the solution for the complete parameter space uses linear interpolation of the neighboring points to obtain the solution.

$$b_i = \begin{cases} 1 - |\frac{8}{2\pi}\mathcal{P}_2 - i| & \text{if} \frac{8}{2\pi}\mathcal{P}_2 - i > 1 \quad (i = 1...9) \\ 0 & \text{if} \frac{8}{2\pi}\mathcal{P}_2 - i \leq 1 \quad (i = 1...9) \end{cases} \tag{7.73}$$

Function $b_i$ takes value 1 when $\mathcal{P}_2 = i\frac{2\pi}{8}$ and decreases to zero as $\mathcal{P}_2$ approaches $(i-1)\frac{2\pi}{8}$ and $(i+1)\frac{2\pi}{8}$, meaning the weight of the solution in the center of the region is 1 and the weight goes to zero as the solution is calculated on the boundary of the region.

It is proven in [64] that blending the solutions of overlapping regions $\mathcal{B} = \mathcal{B}_1 \cup \mathcal{B}_2 ... \cup \mathcal{B}_n$

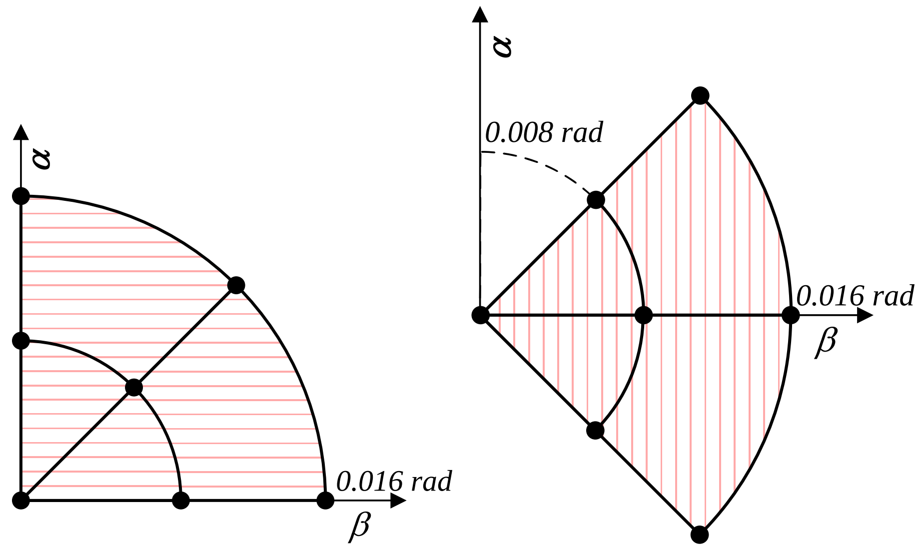


Figure 7.7: First and second blending regions of the LPV control synthesis.

preserves the achieved robust stability with performance level $\gamma_{\cup}$ over the entire parameter range.

The solutions for $X(\rho)$ and similarly for $Y(\rho)$ for the entire parameter space excluding the midpoint are obtained:

$$X(\rho) = \sum_{i=1}^{9} b_i(\rho) X_i(\rho); \quad 0 \leq \mathcal{P}_2 < 2\pi, 0 < \mathcal{P}_1 \leq 0.016 \tag{7.74}$$

$$Y(\rho) = \sum_{i=1}^{9} b_i(\rho) Y_i(\rho); \quad 0 \leq \mathcal{P}_2 < 2\pi, 0 < \mathcal{P}_1 \leq 0.016 \tag{7.75}$$

Which satisfies the equations 7.12-7.14 in the entire parameter range $\mathcal{P}$, and achieves performance level $\gamma = \max_{i=1...n} \gamma_i$.

The center point ($\mathcal{P}_1 = 0$; $\mathcal{P}_2 = [0...2\pi]$) needs further consideration. This point represents a singularity of the solution space since the plant does not change along $\mathcal{P}_2$ when $\mathcal{P}_1 = 0$. To resolve this problem, the solution for this point is calculated over the 8 different regions. Remember the parameter space is divided into 8 regions, but it is covered with 9 overlapping subsets to guarantee the solution at the boundaries ($\mathcal{P}_2 = 0, 2\pi$) also. The solution for $X(0, \mathcal{P}_2)$ and similarly for $Y(0, \mathcal{P}_2)$ is obtained as an average of all blending regions:

$$X(0,\mathcal{P}_2) = \frac{1}{8}\sum_{i=1}^{8} 0.25X_i(0,(i-1)\frac{2\pi}{8}) + 0.5X_i(0,i\frac{2\pi}{8}) + 0.25X_i(0,(i+1)\frac{2\pi}{8}); \quad 0 \le \mathcal{P}_2 < 2\pi \tag{7.76}$$

Equation 7.76 ensures that the solution is continuous as the parameter vector crosses the $(0,0)$ point and all solutions over the entire parameter space are well defined.

## 7.4 Controller Synthesis Results

The value of $\gamma$ ranges between 0.7926 and 0.7959 in the coupled synthesis for the pointwise $\mathcal{H}_\infty$ control designs. The coupled LPV synthesis on the blending regions with rate bounds of $\frac{\partial \mathcal{P}_1}{\partial t} = \pm 5\ deg/s$; $\frac{\partial \mathcal{P}_2}{\partial t} = \pm 225\ deg/s$ leads to a maximum $\mathcal{L}_2$ gain slightly higher $0.795-0.798$. This is a consequence of using finite number of basis functions to characterize the LPV synthesis solution and the fact that nonzero rate bounds lead to higher induced $\mathcal{L}_2$ norm during the synthesis. Rate bound on $\mathcal{P}_1$ is selected based on the expectation that the pitch and yaw rate reference tracking have 0.2 second rise time, corresponding to reaching 1 $deg$ aerodynamic angle, the boundary of the operation envelope, in 0.2 $s$. The rate bound on $\mathcal{P}_2$ has less clear physical interpretation. It is associated with the special structure of the scheduling variables. $\mathcal{P}_2$ can vary very fast in case $\mathcal{P}_1$ is close to zero. $\mathcal{P}_2$ changing 180 $deg$ with $\mathcal{P}_1$ going from one extreme to zero and back would take 0.4 $s$. Since this scenario has low probability, the bound is relaxed with 50% to 225 $deg/s$ to avoid balancing the LPV synthesis towards optimizing the performance for fast variations on $\mathcal{P}_2$.

During the synthesis using blended regions a uniform performance level of $\gamma = 0.805$ is specified for each sub-region. It is a relaxation of the optimal LPV control problem, based on the performance level of individual regions, to avoid high frequency poles often experienced in optimal $\mathcal{H}_\infty$ solutions. The global solution over all regions have the same guaranteed performance level of $\gamma_\cup = 0.805$ as the subregions guaranteed by Theorem 7.2.

The coupled LPV synthesis is done on a grid composed of 24 linearized models, the obtained controller is a continuous function of $\rho$. However, the controller implemented in the simulation model uses linear interpolation of controller calculated at grid points to reduce the computational complexity of the algorithm. The interpolation points, shown in

Figure 7.8, are chosen to be a refined grid of the original parameter points, composed of $5\times16$ parameter points. This refined grid ensures that the interpolation is done in a smooth way, to reduce the conservativeness introduced by representing the controller at only discrete points of the parameter space. The controllers at the refined grid points are calculated based on the blended control solution and linearized models obtained at these operating points. Checking the performance of the LPV controller at these interpolation points can ensure that the original grid is sufficiently smooth and the approximations introduced during the synthesis do not affect the obtained solution significantly.

A similar approach to the coupled design is taken of obtaining decoupled controllers scheduled on $\alpha$ and $\beta$. The control loops are implemented as interpolated controllers among grid points on the parameter space, both the longitudinal and the lateral controller are calculated at 9 points equally spaced on $\alpha = [-0.016, 0.016]$ and $\beta = [-0.016, 0.016]$ respectively.

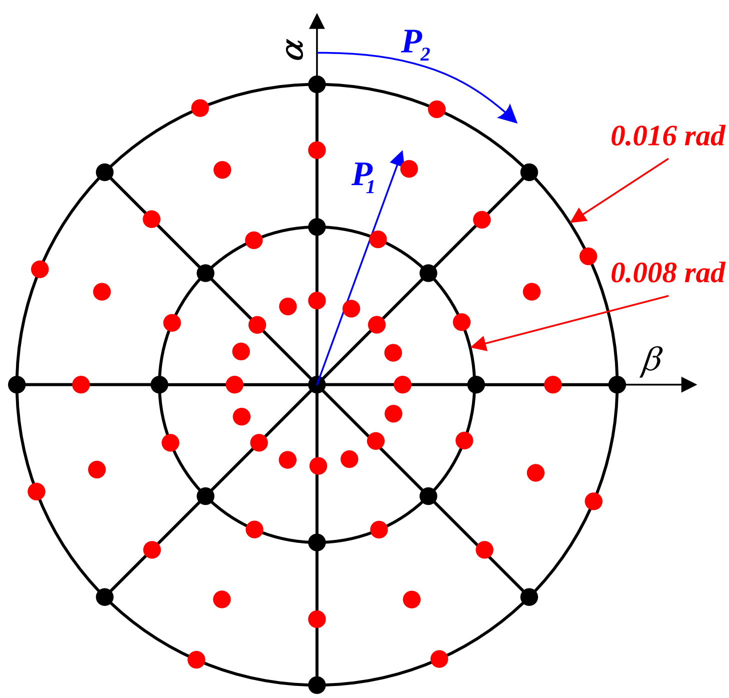


Figure 7.8: Grid points for controller blending.

Consider the robustness analysis of the LPV controller evaluated at 9 points on the boundary of the operating envelope ($\mathcal{P}_1 = 0.016\ rad, \mathcal{P}_2 = 0...\pi$). Multivariable input and output sensitivity and complementary sensitivity are calculated for all cases as shown in Figure 7.9 (decoupled) and Figure 7.10 (coupled design) using frozen parameter values of the LPV controllers.

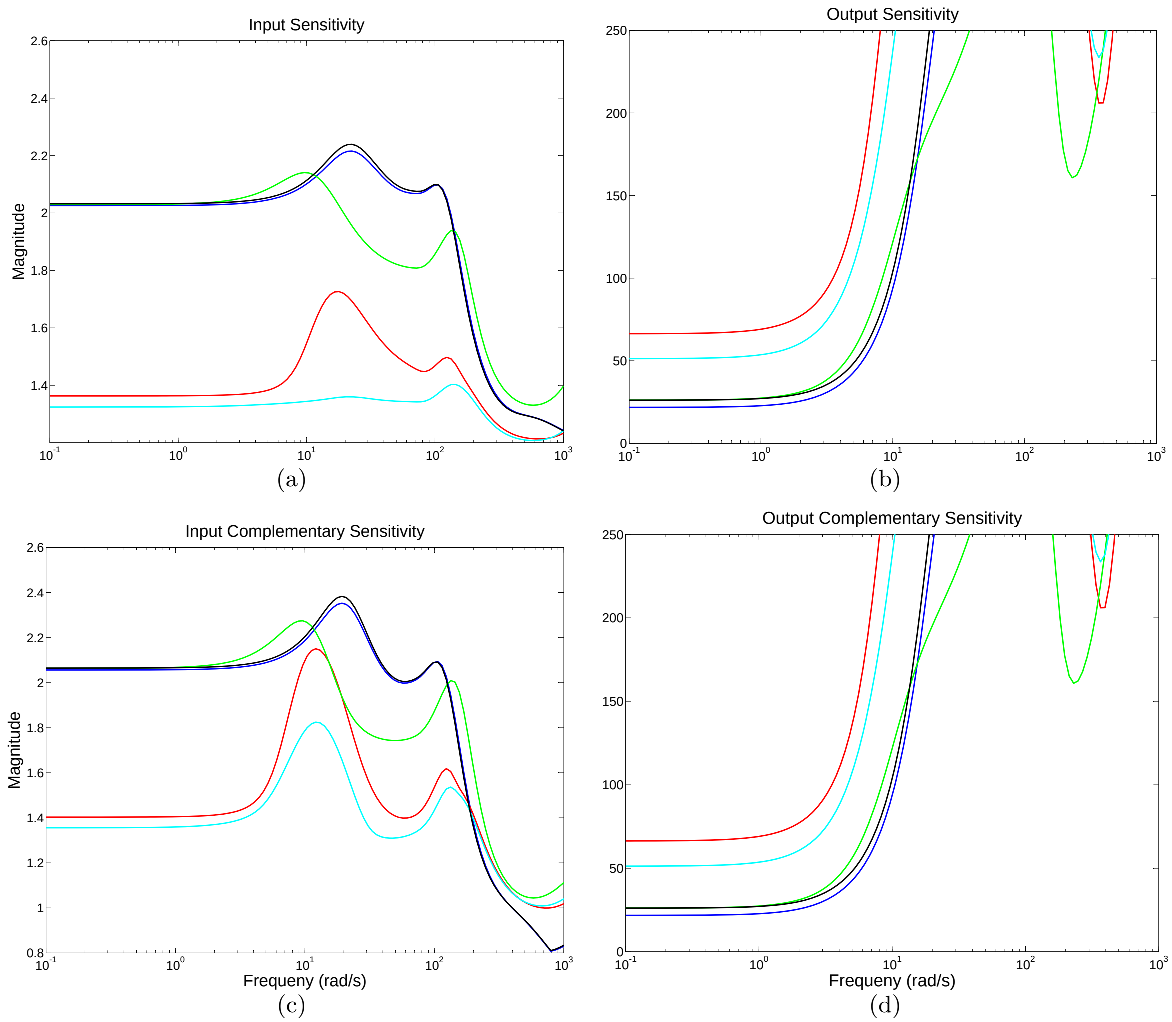


Figure 7.9: Sensitivity/complementary sensitivity LPV decoupled design.

The input sensitivity and complementary sensitivity plots of the decoupled design have peaks of approximately 2.4 which indicate robustness to 40% full block uncertainty on the input channel, while the sensitivity and complementary sensitivity functions on the output have values on the order of 50 indicating very poor robustness of the design to output multiplicative uncertainty. Notice the high variation of gains at low frequency. This implies the performance objectives are not equally distributed among the selected operating points. The design points close to pure $\alpha$ and pure $\beta$ parameters have better performance but indicate high sensitivity to sensor noise.

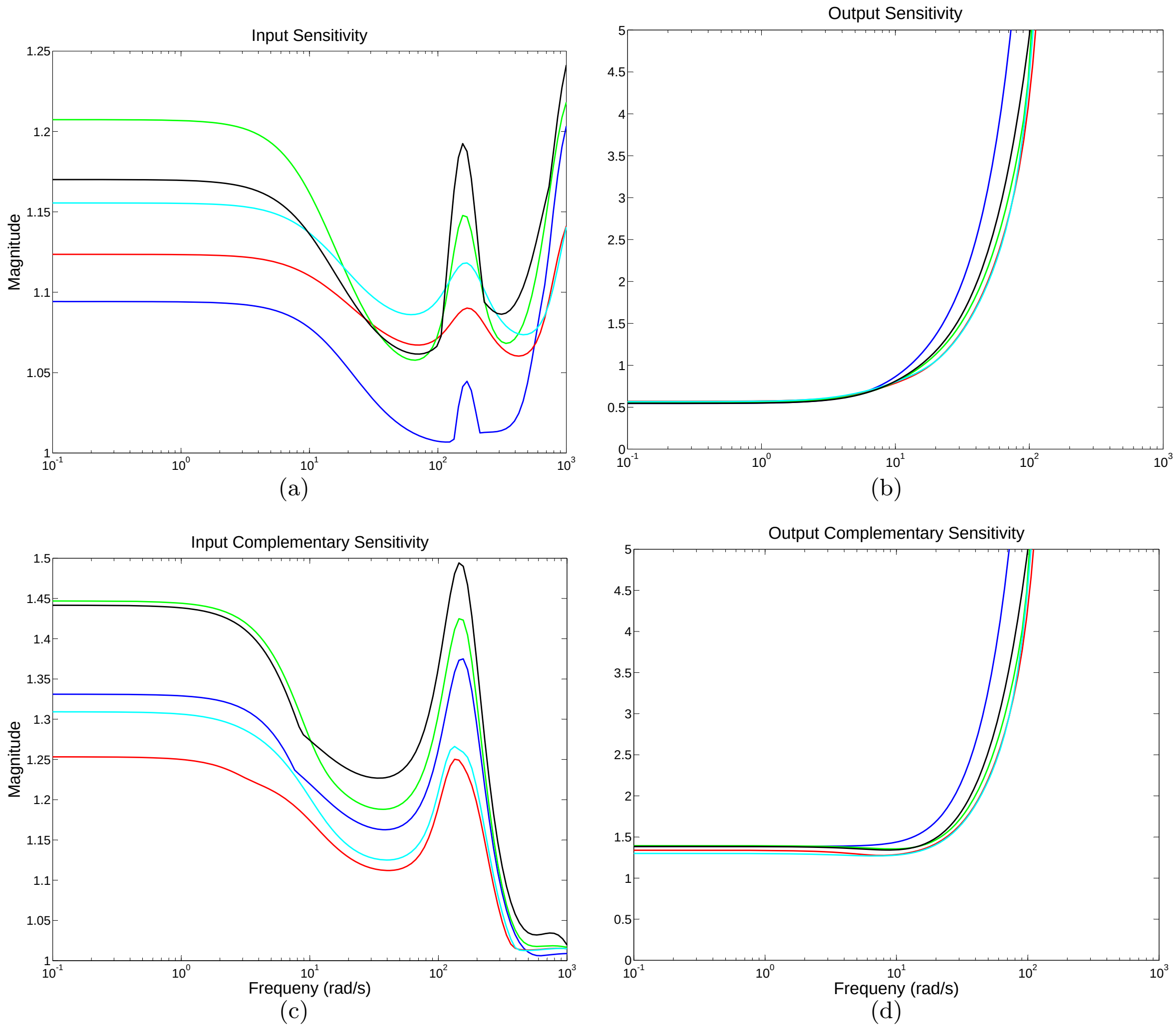


Figure 7.10: Sensitivity/complementary sensitivity LPV coupled design.

The coupled designs have excellent input sensitivity and complementary sensitivity, and are robust up to 70% full block uncertainty on the input channels. The output sensitivity/complementary sensitivity unlike in the decoupled case have also excellent robustness up to 20 $rad/s$ until where it can tolerate the same 70% full block uncertainty, but the output sensitivity degrades at high frequency, since that objective was not directly addressed in the control design. Based on these results it is expected that the coupled design have better performance tolerating uncertainty on input and output channels.

To gain further insight of the performance of the controllers, closed-loop Bode magnitudes at the same frozen parameter values as described earlier are shown on Figures 7.11-7.16.

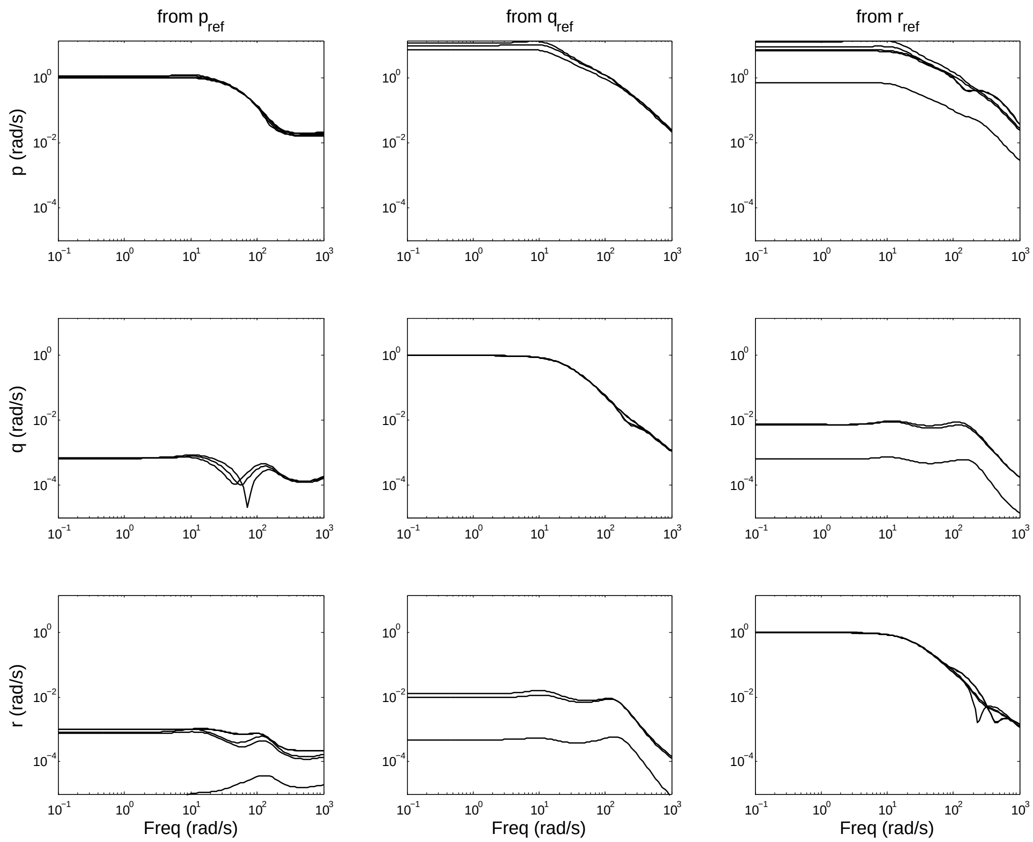


Figure 7.11: Magnitude frequency response of decoupled LPV controller at $\mathcal{P}_1 = 0.016\ rad$.

The performance difference between the two control approaches can be seen when comparing Figures 7.11 and 7.12. The control objectives of command tracking are executed very well in both cases, only slight degradation of roll tracking can be observed on the decoupled case. However, the difference between the two designs can be clearly seen in the coupling terms. Notice the high gain of $q_{ref}$ and $r_{ref}$ to $p$ transfer function on Figure 7.11. The coupled LPV controller (Fig. 7.12) has two orders of magnitude lower coupling. It is also important to notice that the coupled LPV design achieves higher bandwidth in both 3 tracking channels.

The sensitivity of the closed loop from reference commands to angle-of-attack ($\alpha$)

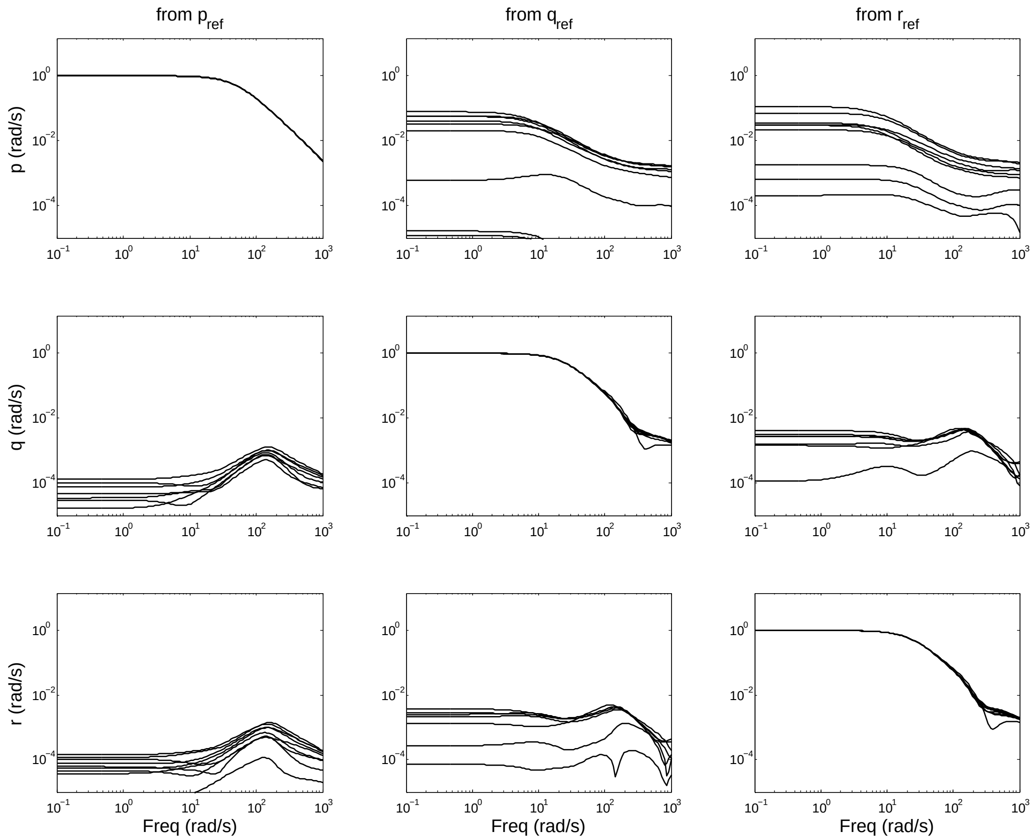


Figure 7.12: Magnitude frequency response of coupled LPV controller at $\mathcal{P}_1 = 0.016\ rad$.

response have lower magnitude and less variation in gain using the decoupled design (Fig.7.13). This is due to the fact that the coupled design (Fig.7.14) have to take into account performance objectives, mostly related to roll damping, while the longitudinal (decoupled) controller only tracks pitch-rate ($q$) and minimizes $\alpha$. Similarly, for reference commands the coupled controller outputs $\delta_1$ and $\delta_3$ have more variation in steady state gains, since the controller has information about $\alpha$ and $\beta$ at the same time, unlike in the decoupled case.

The disturbance input attenuation, caused by afterbody planing, is compared on Figures 7.15 and 7.16. Compared with the open loop (denoted by dashed line) both designs achieve considerable attenuation on all channels. The only exception is the high sensitivity of roll response of the decoupled design, due to similar reasons mentioned in the tracking performance. It is also interesting to note the high sensitivity of roll response to noise

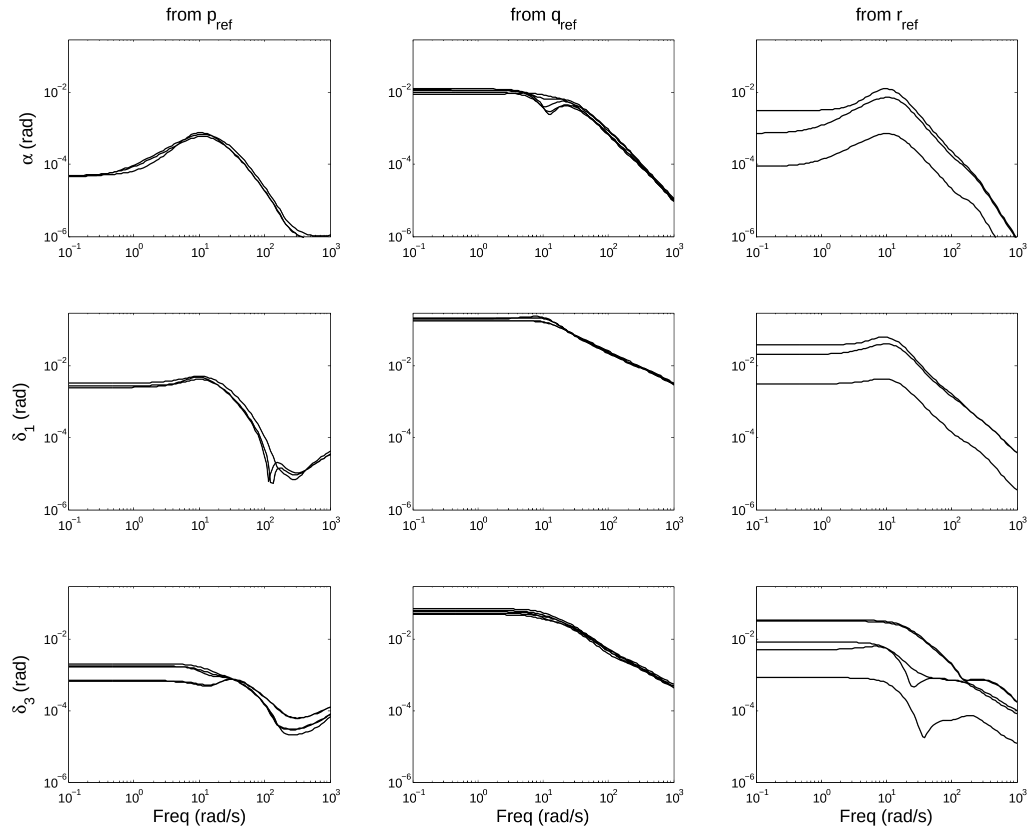


Figure 7.13: Magnitude frequency response of decoupled LPV controller at $\mathcal{P}_1 = 0.016\ rad$.

input on the $\alpha$ channel using the decoupled control. This objective, due to the lack of cross-coupling, is not emphasized in the problem setup of the decoupled LPV formulation.

### 7.4.1 Simulation Results

The coupled and decoupled LPV controllers are integrated into the nonlinear HSSV simulation model. In addition to the nonlinear equations of motion with dimension described in Table 3.1, deflection and deflection rate limits on the actuators are included and the measurement signals are corrupted by noise. It is also assumed that the planing forces and moments can be approximated online using the vehicle states. The LPV controllers are gain scheduled with parameters $\mathcal{P}_1, \mathcal{P}_2$ in the coupled case and with $\alpha$ and $\beta$ in the decoupled case. The control trim inputs, based on the trim map obtained in Chapter 6 added to the LPV control inputs are scheduled as a function of $\phi$ the bank angle of the vehicle.

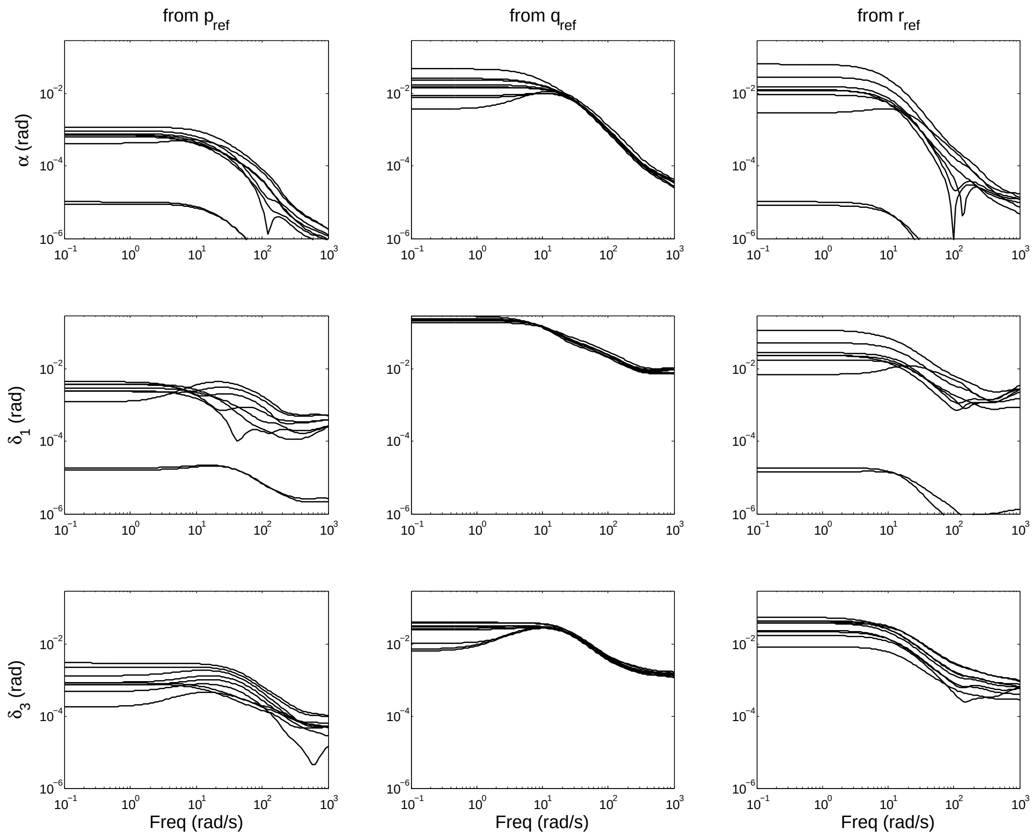


Figure 7.14: Magnitude frequency response of coupled LPV controller at $\mathcal{P}_1 = 0.016\ rad$.

Using the trim scheduling variable is necessary to compensate against the effect of gravity, since the kinetics does not account for orientation relative to the Earth. Additional trim scheduling on $\theta, \alpha$ or $\beta$ is omitted since they do not improve the controller performance. They introduce so-called hidden feedback loops [61] leading to undesired coupling between the dynamics and the trim lookup-tables.

#### 7.4.1.1 Initial Response

Large disturbing forces and moments, caused by interaction with the liquid and variation in the surrounding environment are expected during the flight of the vehicle. The first and most important step in analyzing the vehicle-controller interaction is to investigate the region of attraction. The set of initial points from where the controller can steer the vehicle back to straight and level flight are explored in the following.

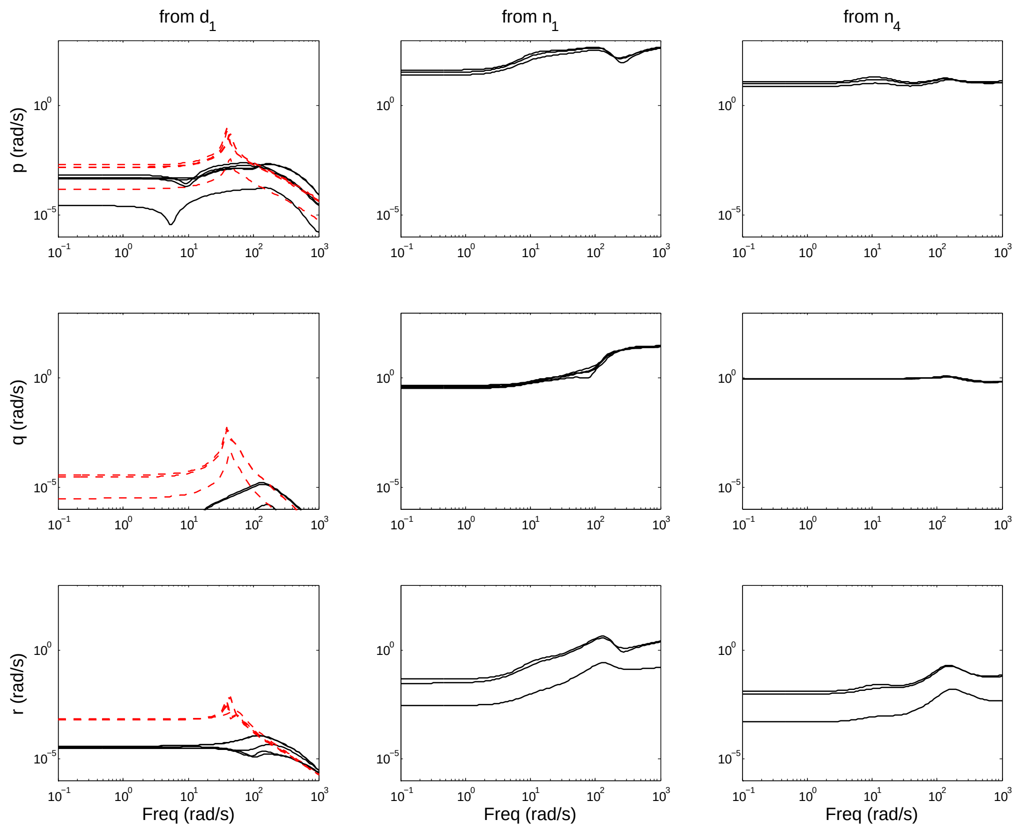


Figure 7.15: Magnitude frequency response of decoupled LPV controller at $\mathcal{P}_1 = 0.016\ rad$.

The controllers behavior for initial disturbances is investigated first. Figure 7.17 shows the response of the vehicle angular rates to initial conditions: $p_i = 10\ rad/s$, $q_i = 3\ rad/s$, $r_i = 3\ rad/s$. This corresponds to an initial disturbance strong enough to force the vehicle into planing before the the control can achieve steady-state. Recall, the performance objective is to track 1 $rad/s$ commands on pitch and yaw channel, hence this initial condition represents a challenge for the controller. The coupled LPV controller drives the system towards the desired condition of $p, q, r = 0\ rad/s$ with a higher initial rate. It also able to provide a well damped response as shown on Figure 7.17. On the other hand, due to strong coupling, the plant regulated by the decoupled LPV controller experiences large roll rates and requires significant time to return to equilibrium. The angle-of-attack response shown on Figure 7.18 reaches steady state after significant time, when using the decoupled controller. The coupled LPV regulates both $\alpha$ and $\beta$ efficiently, even when the initial

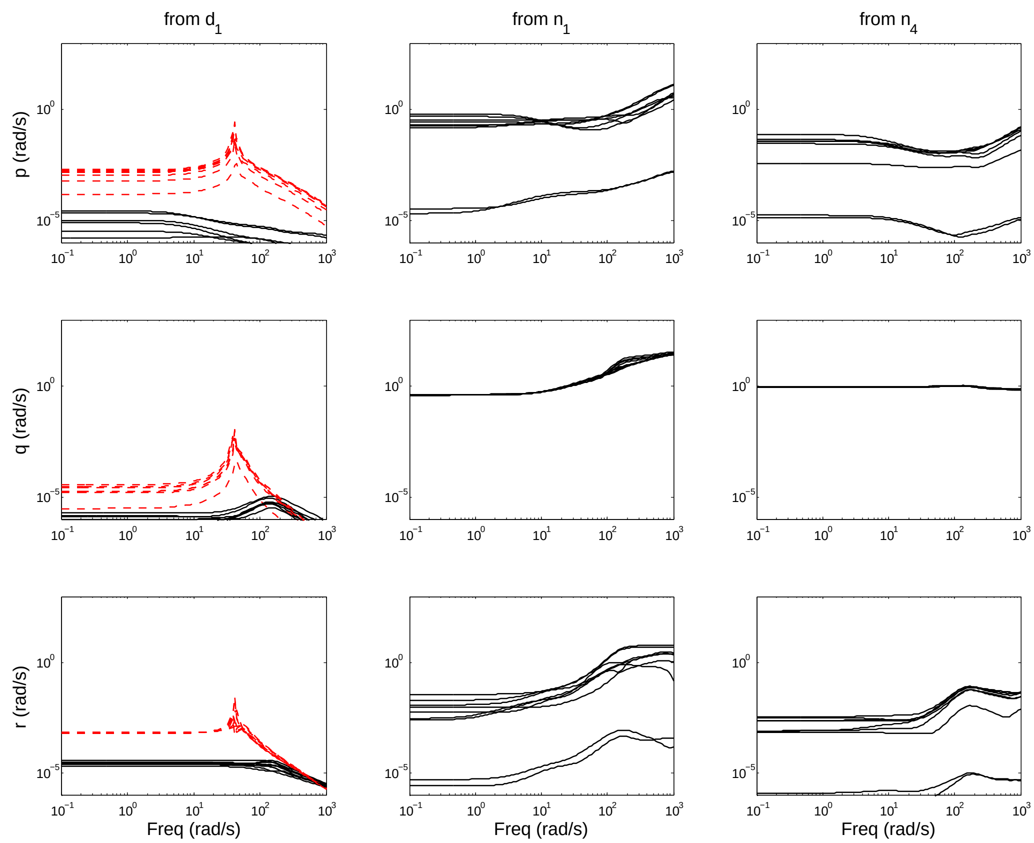


Figure 7.16: Magnitude frequency response of coupled LPV controller at $\mathcal{P}_1 = 0.016\ rad$.

conditions are nearly at the limit of performance. It is important to note that the vehicle with the decoupled controller rapidly looses speed due to intensive motion. The comparison of control deflections on Figure 7.19 shows that the initial disturbance is high enough to saturate the control actuators. Nevertheless, the coupled LPV controller recovers faster from saturation and with higher bandwidth it achieves the control goals significantly faster. Figure 7.20 shows the system parameters related to planing. It can be seen on the relation of cavity offset ($y_c$ vs. $z_c$) that the coupled design keeps the system in a narrow range of $\phi_p$ cavity offset angle, even though high roll rates would drive the system towards more variation in $\phi_p$ as experienced with the decoupled design. Planing only occurs for short duration with the coupled control design, while the decoupled case has 3 short contact with the liquid surface.

Note that the simulation uses the Logvinovich planing model. As seen on the bottom

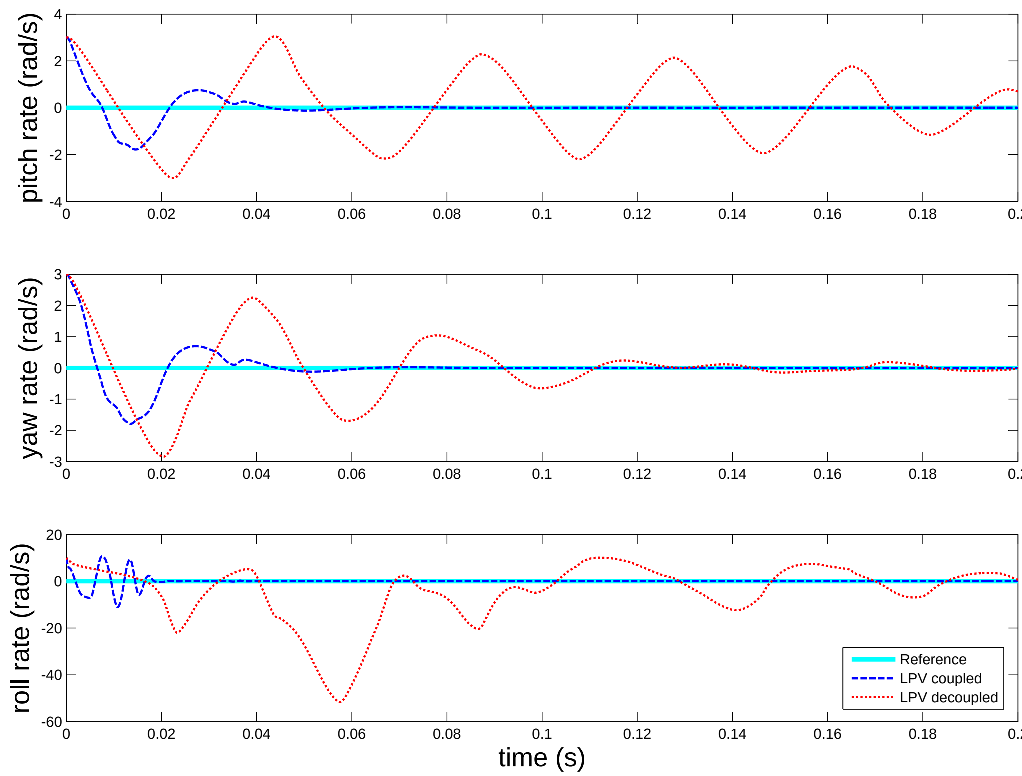


Figure 7.17: Simulation of angular rates for initial condition $p = 10\ rad/s, q = 3\ rad/s, r = 3\ rad/s$.

plots of Figure 7.20, the acceleration in the initial phase exceeds 10 $g$ and in the order of 5 $g$ in the later part of the simulation, which indicates the range of expected accelerations during operation.

#### 7.4.1.2 Limits of Envelope with Different Scheduling Variables

The limits of possible maneuvers is another important aspect when analyzing the nonlinear plant in closed-loop with the LPV controller. The mathematical model used for control synthesis uses steady-state approximation, while the nonlinear model captures the transient behavior between operating points, hence it is important to analyze the controller in nonlinear simulations. It is assumed that testing corner cases of the operating envelope ensures that performance is maintained inside the whole region.

As described in Chapter 6 the LPV system is parameterized with $\alpha$ and $\beta$ measurements,

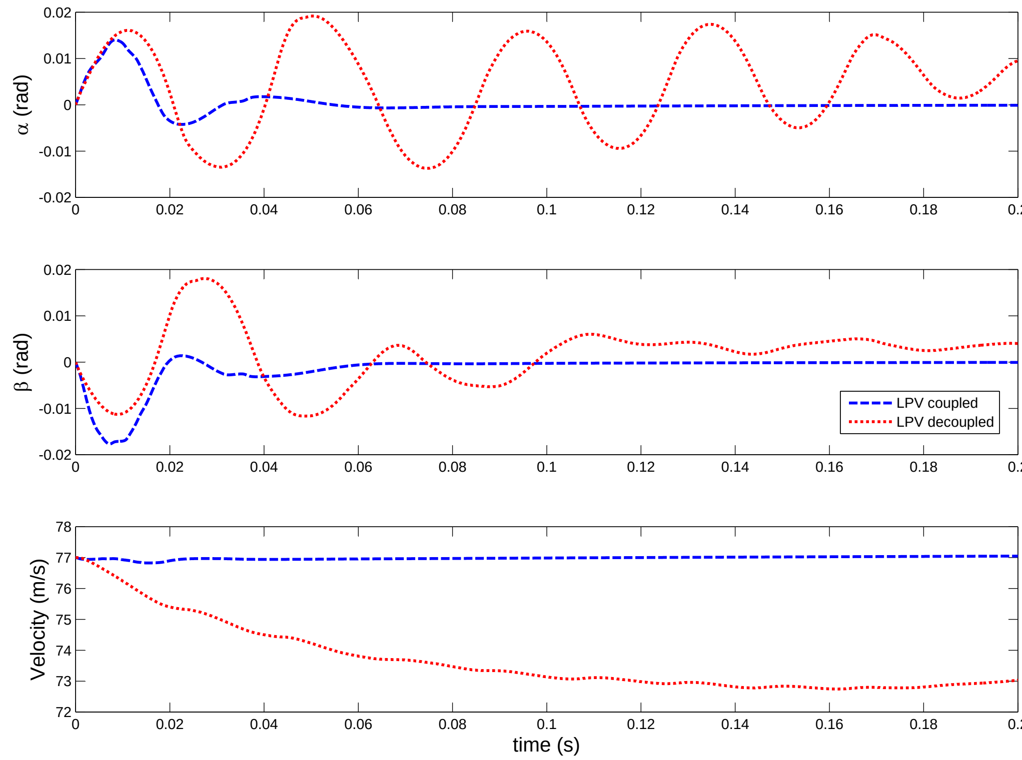


Figure 7.18: Simulation of aerodynamic angles for initial condition $p = 10\ rad/s, q = 3\ rad/s, r = 3\ rad/s$.

but for each $\alpha, \beta$ pair there is a unique cavity offset value $(y_c, z_c)$. Since the one-to-one correspondence between cavity offset and aerodynamic angles only valid for steady state conditions, it is possible to parameterize the LPV controller with cavity offset, which leads to different closed-loop response. It is possible to use the cavity offset value, measured online, to calculate the corresponding steady-state aerodynamic angles and schedule the controller without changing the problem setup.

The limits of the operating envelope are explored in Figure 7.21 where a maneuver with 1 $rad/s$ pitch/yaw rate commands are performed. The reference commands as shown on Figure 7.22 are pitch rate doublet with $\sqrt{0.5}\ rad/s$ and yaw rate doublet using the same magnitude command with 0.6 $s$ offset. This maneuver requires change in yaw rate while maintaining pitch rate at high value, and the opposite maintaining yaw rate while changing pitch rate from one extreme point of the operating envelope to another. The points of the trajectory where $q_{ref}^2 + r_{ref}^2 = 1\ rad/s$ corresponds to operation during steady

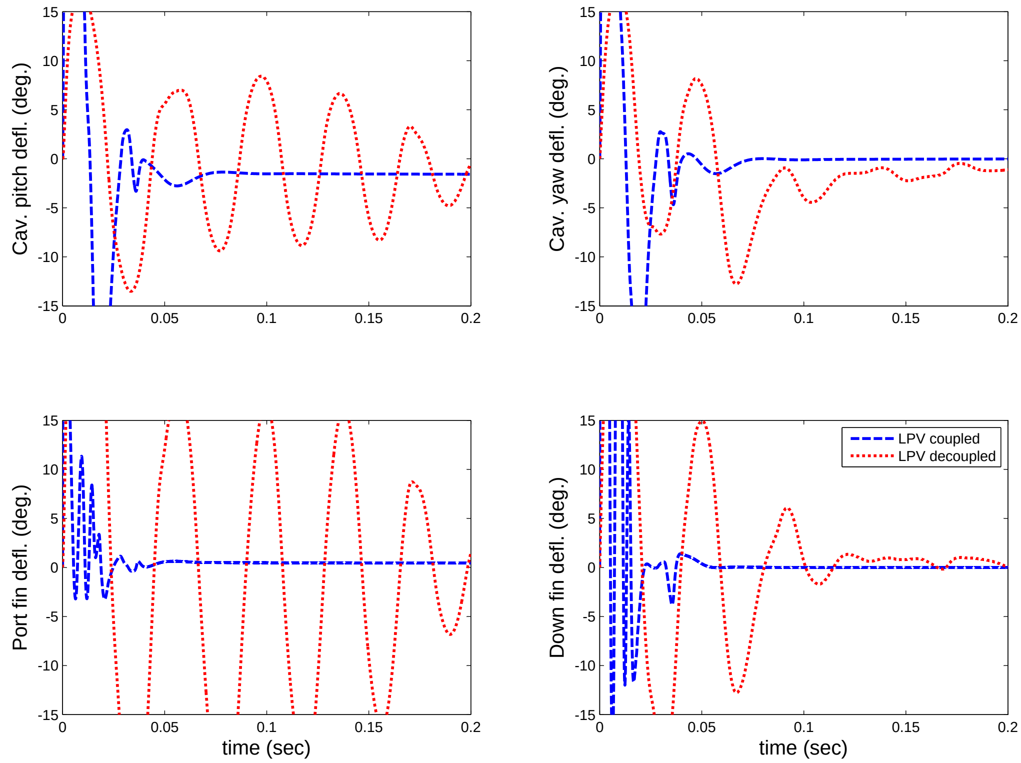


Figure 7.19: Simulation of angular control deflections for initial condition $p = 10\ rad/s, q = 3\ rad/s, r = 3\ rad/s$.

planing. The resulting trajectory has 40 $m$ depth change and a 4 $m$ amplitude sinusoid in lateral direction within 2 $s$, while bank angle reaches 30 $deg$. It is important to mention, that the decoupled LPV controller is not able to follow the trajectory, it looses stability at approximately 1.1 $sec$.

Despite the large maneuver with significant bank angle and planing during longer periods, the tracking response of the coupled LPV controller is excellent (Fig. 7.22). Only minor deviation from the reference response is observed during contact with the liquid, resulting in large disturbance forces. The roll rate during most of the maneuver is below 0.05 $rad/s$ which is considered excellent.

The conventional way of scheduling the LPV controller with $\rho(\alpha, \beta)$ is compared with scheduling using the cavity offset $\rho(y_c, z_c)$ using the maneuver exploring the limits of envelope. It is under investigation if the final vehicle will have sensors measuring the cavity

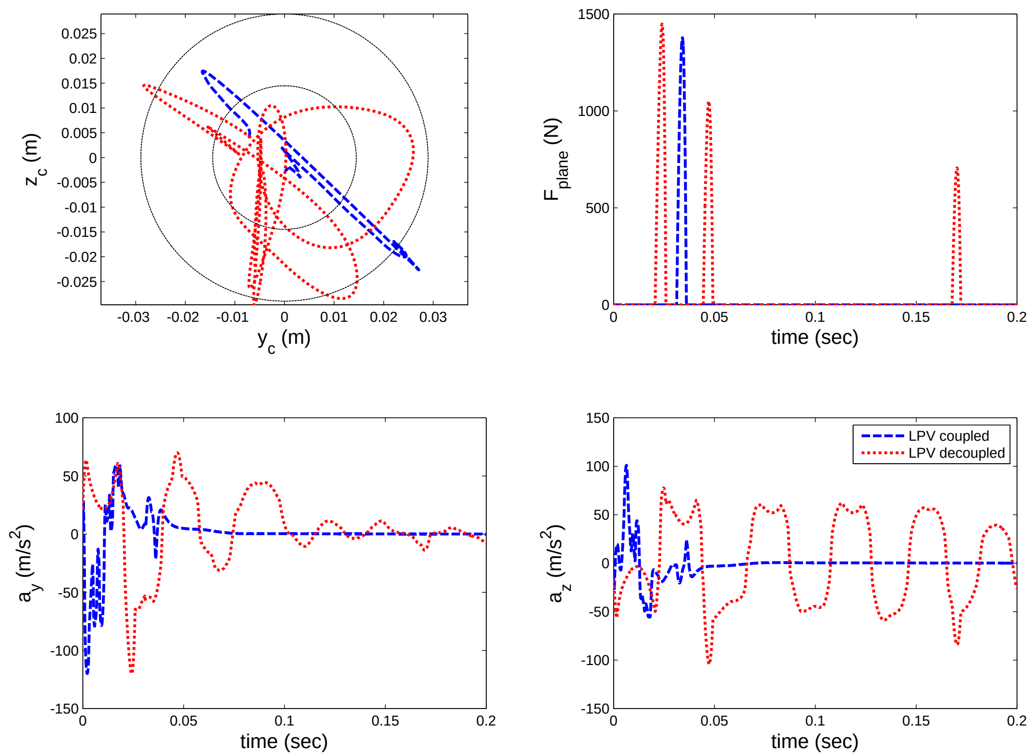


Figure 7.20: Simulation of cavity parameters for initial condition $p = 10\ rad/s, q = 3\ rad/s, r = 3\ rad/s$.

parameters, but it is possible, hence scheduling with $\rho(y_c, z_c)$ is a feasible option. Using the controller scheduled with $\rho(y_c, z_c)$ provides slightly better tracking with fewer spikes as shown on Figure 7.22. The aerodynamic angles shown on Figure 7.23 indicate that the vehicle is on the limit of performance, as the $\mathcal{P}_1$ parameter exceeds 0.016 $rad$ for short time. It is also interesting to note that the maneuver leads to loss of speed, indicating that sharp maneuvers with intensive actuator usage create more drag than straight flight. This is an interesting trade-off between cavitator drag which decreases as the cavitator is deflected and fin drag which increases as fins are used for control.

The deflection of control actuators are shown on Figure 7.24. It can be clearly seen that the cavitator reaches its deflection limit of 15 $deg$ using both designs for short time to balance the effect of planing. It is interesting to see that the controller scheduled with cavity offset parameters have more fin usage with slightly higher deflections. Figure 7.25 compares the system parameters related to planing using the two different scheduling vector. It is seen

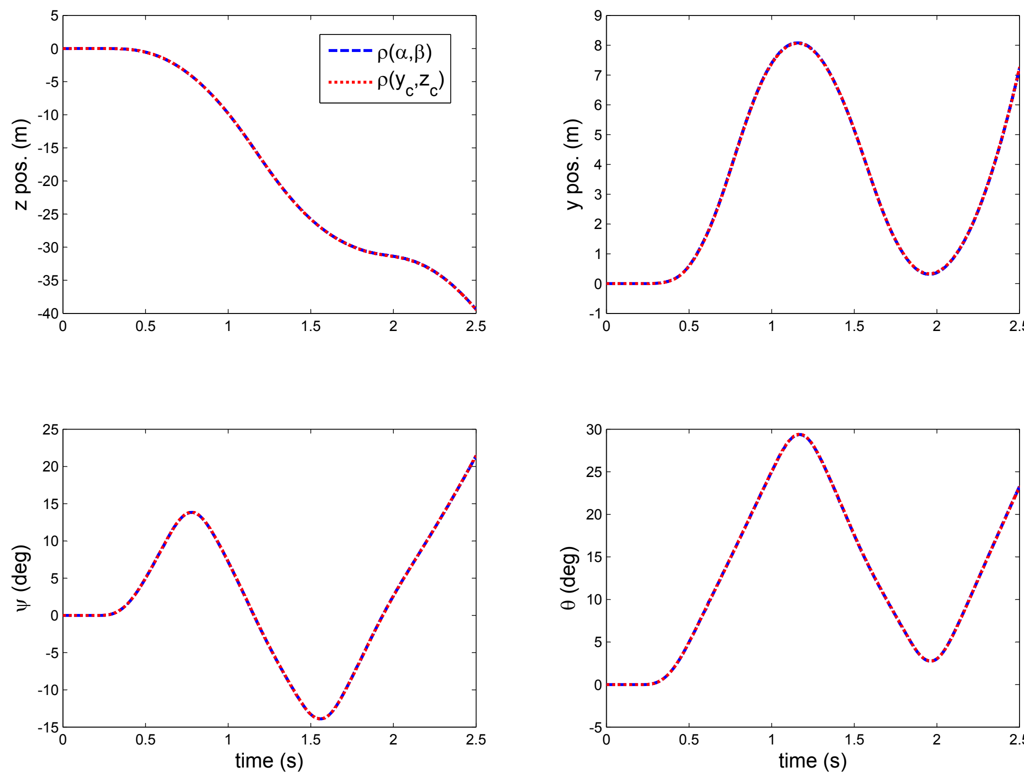


Figure 7.21: Exploring the operating envelope of the vehicle, simulation of position and orientation of the vehicle.

based on the relation of cavity offset ($y_c$ vs. $z_c$) that the operating envelope is sufficiently explored by the maneuver. The main difference between the two scheduling methods is obvious based on the plot of planing forces (Fig. 7.25). Scheduling with cavity offset leads to 450 $N$ peak force while parameterizing the controller with aerodynamics angles have 600 $N$ peak. As seen on the lower two Figures of 7.25 the acceleration during the maneuver has 6 $g$ in both $y$ and $z$ direction which indicates that maneuvers with sustained 8.5 $g$ can be achieved.

#### 7.4.1.3 Maneuvering Type

The guidance level control algorithm has the freedom to select the maneuvering type. Conventional airplanes use *bank-to-turn* maneuvering, where 3-D trajectories are tracked with coordinated roll and subsequent pitch maneuvers. The aerodynamic lift on the wings is

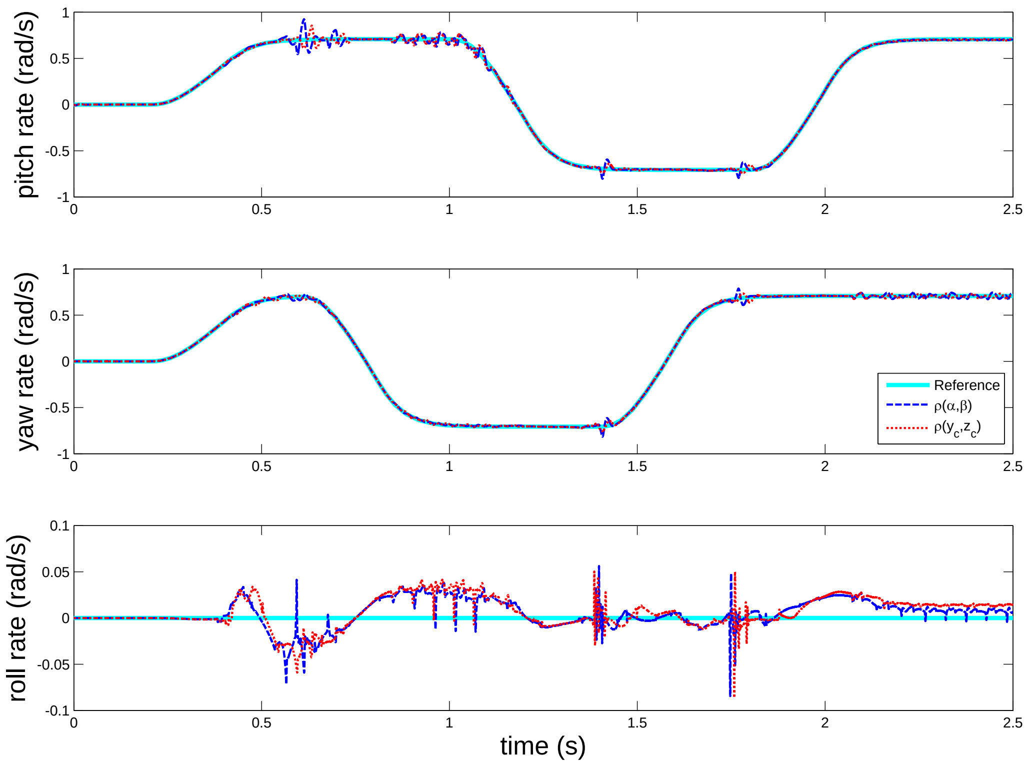


Figure 7.22: Exploring the operating envelope of the vehicle, simulation of angular rates of the vehicle.

used to counteract the centripetal force caused by turning. On the other hand missiles use *skid-to-turn* maneuvering, since lift force is generated by four (left, right, up and down) equivalent control surfaces. This approach allows more agility, since no coordination between roll and pitch is required to achieve yaw motion. Skid-to-turn maneuvering with the supercavitating vehicle is possible if the cavitator has both pitch and yaw degrees of freedom. The bank-to-turn maneuvering is presented here also, since due to mechanical complexity the cavitator yaw actuation might be omitted.

A benchmark maneuver, to further investigate the performance of the control approach, is defined which sufficiently explores the operating envelope of the vehicle. Several results suggested to use bank-to-turn maneuvering for guidance [1], which is essential if the cavitator has only pitch actuation. Recall, the yaw dynamics with only fin control has non minimum phase response and no sufficient performance can be guaranteed for tracking. In contrast if the cavitator is able to provide independent $y$ and $z$ directional control forces a

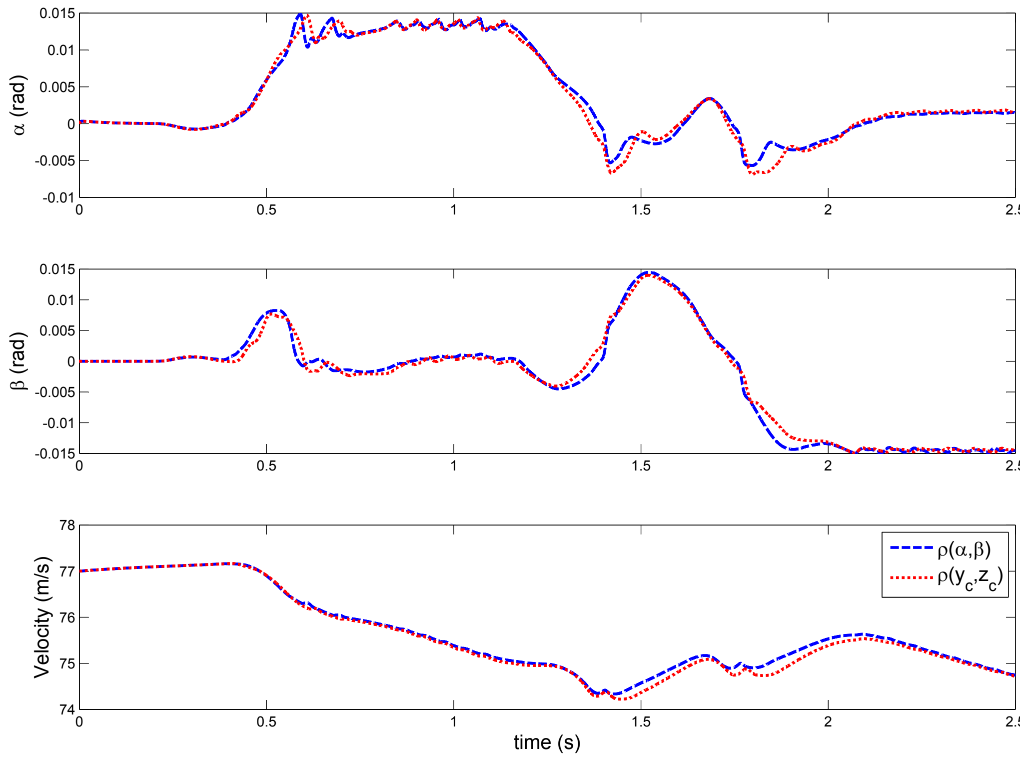


Figure 7.23: Exploring the operating envelope of the vehicle, simulation of aerodynamic angles of the vehicle.

skid to turn maneuver could be more advantageous since it does not require sequential roll and yaw maneuvers. To compare the bank-to-turn and skid-to-turn maneuvers the same trajectory is flown by the two different approaches and compared in the following.

As seen on Figure 7.26, the maneuver consists of a 45 $deg$ roll then a pitch doublet with amplitude $\sqrt{0.5}$ $rad/sec$ then 90 $deg$ roll in the opposite direction followed by an opposite directional pitch doublet, then the vehicle returns back with 45 $deg$ roll to straight and level. The vehicle initial conditions are $p, q, r = 0$ $rad/sec$ and $\alpha = 0$ $rad$, $\beta = 0$ $rad$.

Figure 7.27 demonstrates excellent tracking performance of pitch and roll commands using the coupled LPV approach, while degraded performance is observed using the decoupled LPV controller on roll tracking. As expected from the bank-to-turn maneuver the sideslip angles are small (Fig.7.28), especially using the decoupled controller, where the yaw rate tracking loop does not consider any other objectives, only to keep $\beta$ low and track the reference command $r_{ref}$ which is constant zero. Figure 7.29 compares the control

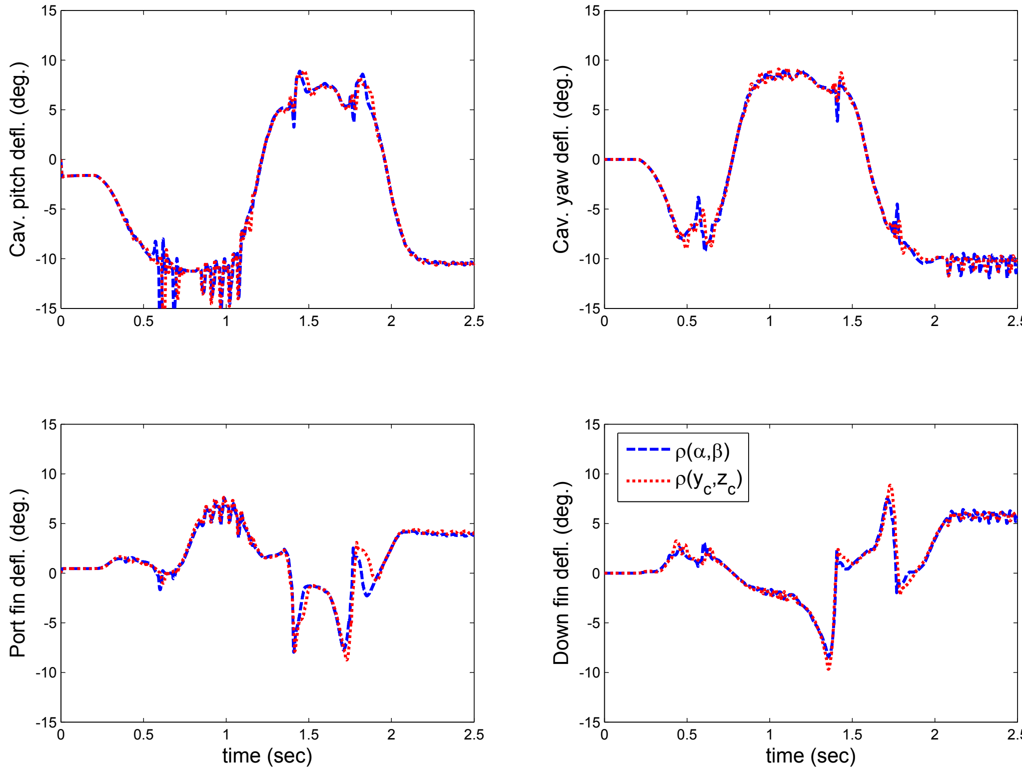


Figure 7.24: Exploring the operating envelope of the vehicle, simulation of control deflections of the vehicle.

deflections of the two design. The commands in the two cases are nearly identical, when the roll tracking performance is good. When the roll rate tracking becomes challenging, the coupled LPV controller provides the additional effort to keep the error low at 0.3 $s$ and 1.5 $s$ on Figure 7.29, while the decoupled regulator does not. Cavity vehicle offset parameters are shown in Figure 7.30 along with the accelerations. It is noticeable, that the coupled controller has wider range of cavity offset values, it possibly reaches planing at lower reference commands indicating smaller operating envelope. The lateral directional acceleration $a_y$ is also lower in the decoupled case, as expected from the lower yaw rates.

The trajectory shown in Figure 7.26 using bank-to-turn maneuver can be flown with skid-to-turn maneuver as shown in Figure 7.31. The maneuver does not use roll, instead it is executed with combined pitching and yawing motion.

The tracking performance of the pitch-rate and roll-rate commands required for the

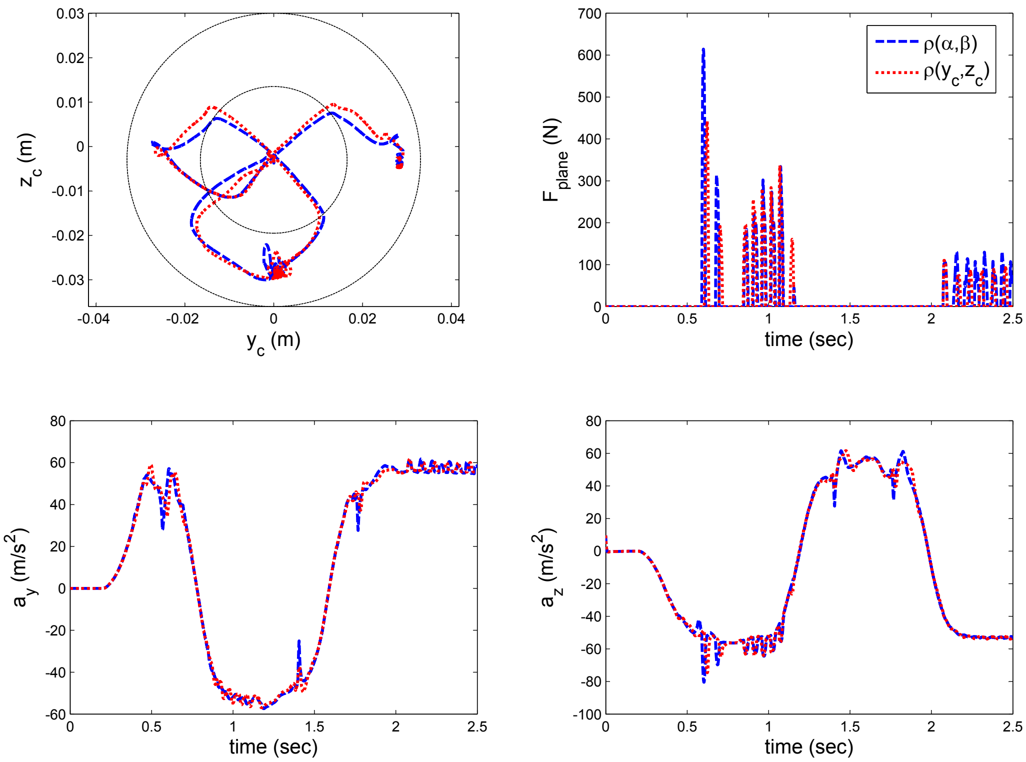


Figure 7.25: Exploring the operating envelope of the vehicle, simulation of cavity parameters of the vehicle.

trajectory are tracked very well, only minor degradation is seen in Figure 7.32 at 1.6 $s$ when the coupled LPV has a slight oscillation. The roll rate tracking of the decoupled controller is poor, mostly due to the lack of cross coupling. It is interesting to notice, that the coupled controller has the slight performance degradation when the roll rate error of the decoupled control is the highest. This indicates, that the coupled LPV controller has the slight perturbation on pitch- and yaw-rate tracking due to the high demand on roll-rate response at 1.6 $s$.

Figure 7.33 shows the response of the aerodynamic angles in the skid-to-turn maneuver. Comparing the peak values of this approach with the bank-to-turn maneuver indicates, that skid-to-turn maneuvers have larger aerodynamic angles. This indicates that the bank-to-turn maneuvering might be more advantageous to ensure more robustness by keeping the vehicle dynamics in the center of the operating envelope. On the other hand, the required control action on the actuators are lower, as seen on Figure 7.34, using skid-to-

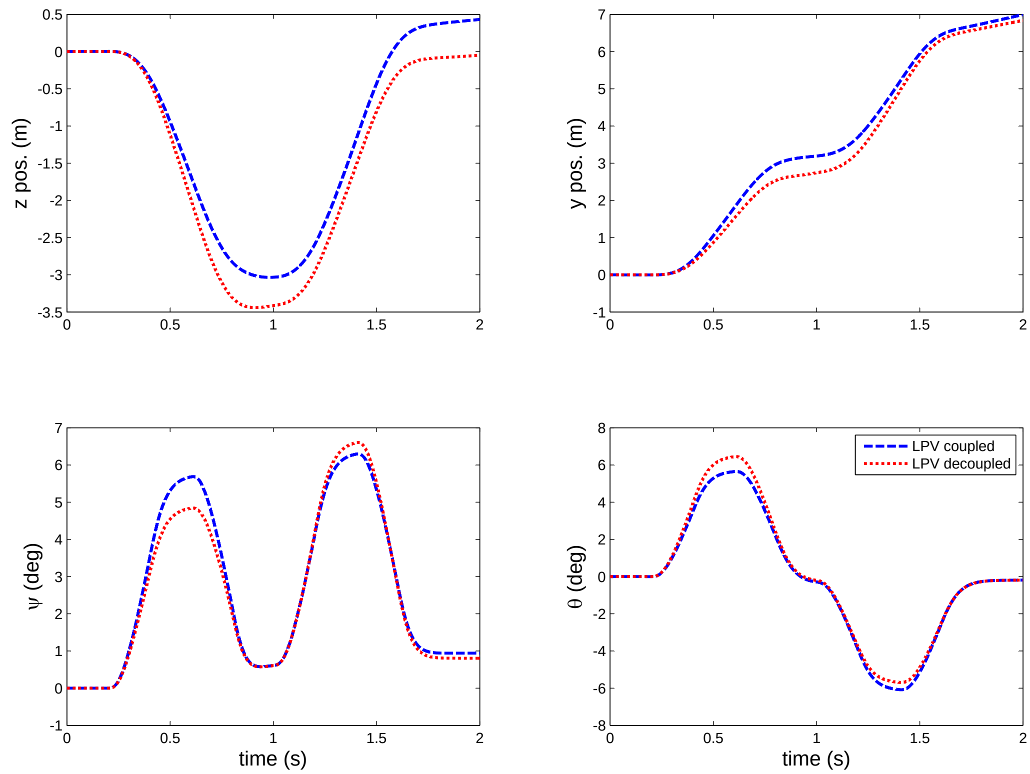


Figure 7.26: Bank-to-turn maneuver, simulation of position and orientation of the vehicle.

turn maneuvering. Mostly since the effort is distributed among all actuators, not like in the bank-to-turn maneuver when only cavitator pitch and port-starboard fins are used. The main problem of using decoupled LPV controller for skid-to-turn maneuvers can be well understood based on the property shown on Figure 7.35. The observation of low cavity vehicle offset when using the decoupled LPV controller no longer holds for skid-to-turn maneuvers, hence the longitudinal and lateral models based on which the controller was synthesized are no longer valid.

#### 7.4.1.4 Effect of Uncertainty

The mathematical model used for control synthesis and the real system on which the controller is implemented are different. Several simplifications are required to keep size of the control synthesis problem tractable. Moreover properties of the model including mass, moment of inertia and dimensions are only approximate values. The control forces provided

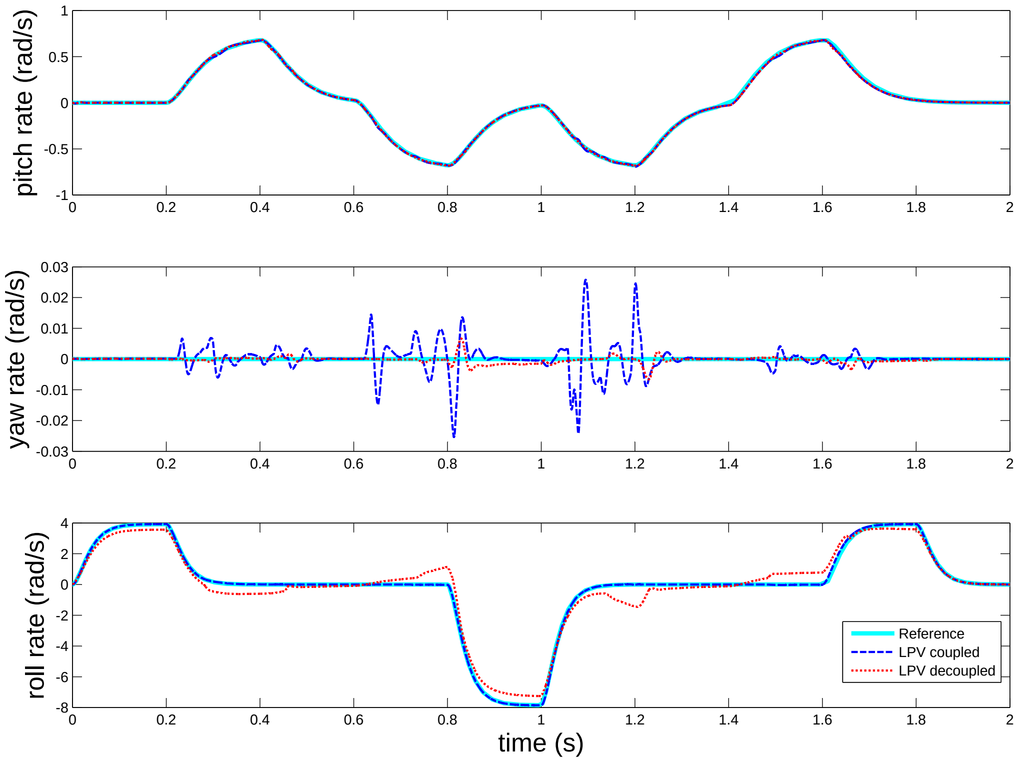


Figure 7.27: Bank-to-turn maneuver, simulation of angular rates of the vehicle.

by actuators have uncertainty associated with them due to partial cavity on the fins and disturbances entering from the water. The controller performance have to be guaranteed even in the presence of these imperfections.

The effect of uncertainty is analyzed in Figure 7.36. The bank-to-turn maneuver with pitch rate doublet of 0.5 $rad/s$ is simulated with the nominal system using the coupled LPV controller. The same controller is used to simulate the system with parameters changed via a 5% backward shift in the c.g. location and 5% lower fin span. Both of these changes represent a challenging task, since the shift in c.g. location makes the vehicle less stable, while reducing the span of the fins leads to lower control authority and lower system damping.

The tracking tasks are handled well by both coupled and decoupled controllers on the uncertain system. The previously experienced poor roll-rate tracking is even more dominant in the uncertain case using the decoupled controller. While tracking of yaw rate requires more effort from the coupled LPV controller on the uncertain plant.

As expected, keeping the aerodynamic angles small is more challenging in the presence

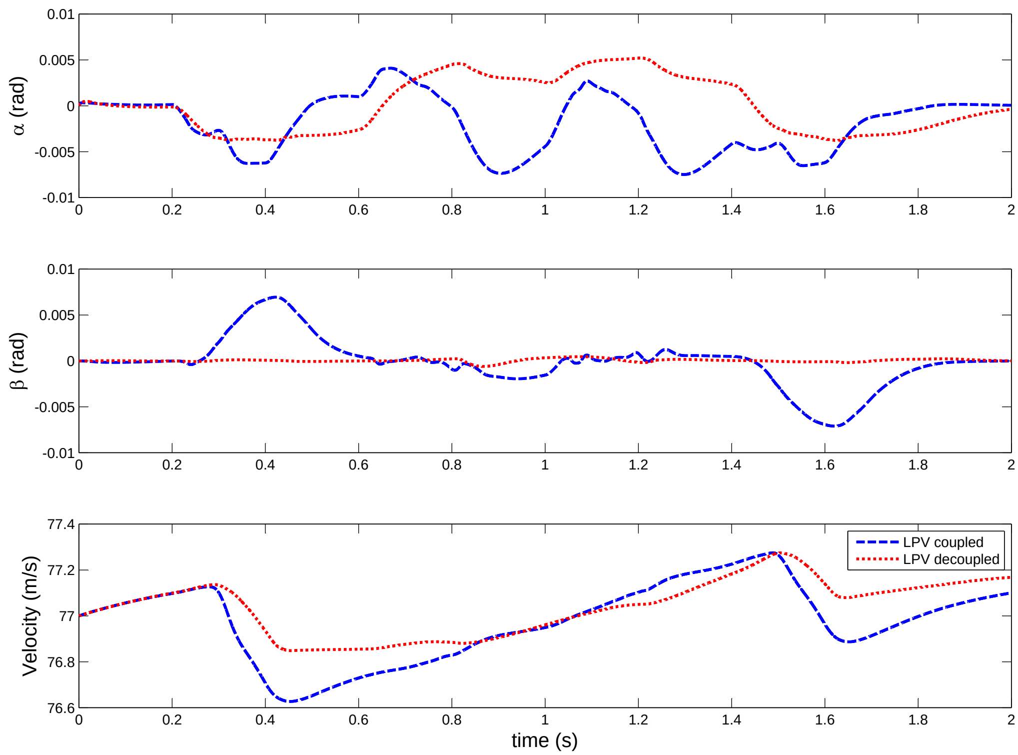


Figure 7.28: Bank-to-turn maneuver, simulation of aerodynamic angles of the vehicle.

of model mismatch, hence the uncertain system has 50% higher peak values on $\alpha$ and $\beta$ as shown on Figure 7.37. The change in control deflection is noticeable on both cavitator and fin inputs, (see Fig. 7.38). Since the cavitator has longer moment arm, lower deflections are required. The fins have to support the same force with lower surface area, hence their deflections increase. As shown on Figure 7.39 the cavity-vehicle offset increases significantly using the coupled LPV controller. The decoupled controller does not have this trend, hence it might be a better alternative if uncertainties of this type are expected during the flight.

#### 7.4.1.5 Planing Description

Two different planing descriptions are given in Chapter 3. It was identified, that the planing model have significant impact on the open-loop vehicle dynamics. Since no experimental results are available on the fidelity of these descriptions both of them are valid candidates to represent the planing behavior.

To analyze the difference between the two planing models in closed-loop, a simulation

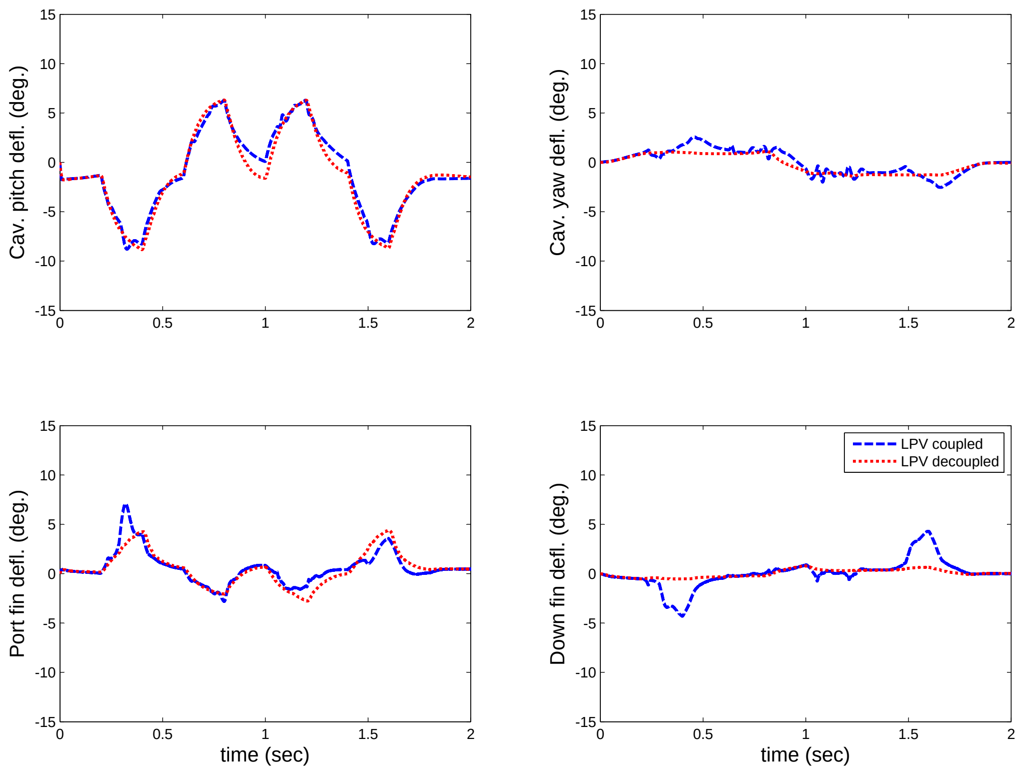


Figure 7.29: Bank-to-turn maneuver, simulation of control deflections of the vehicle.

using the Logvinovich planing model is compared with the Paryshev model on the maneuver designed to explore the operating envelope using the coupled LPV controller.

The tracking performance of pitch rate and roll rate are noticeably influenced by the Paryshev planing model, (see Fig. 7.40). Spikes with magnitude larger than 0.1 $rad/s$ are observed in the system response, indicating the importance of planing model. Further analysis of the difference between the two behavior indicate, that the degraded performance of angular rate tracking does not influence the aerodynamic angles (Fig. 7.40). The control deflections around 1 $s$ and after 2 $s$ have larger oscillatory peaks using the Paryshev model. It indicates that it requires less control effort to compensate the effect of planing using the Logvinovich description. In contrary, the magnitude of maximum planing force associated with the Logvinovich planing force description is higher than the Paryshev force as shown on Figure 7.43. This is an interesting results since, based on the previous results, the forces using the Paryshev model were expected to be higher.

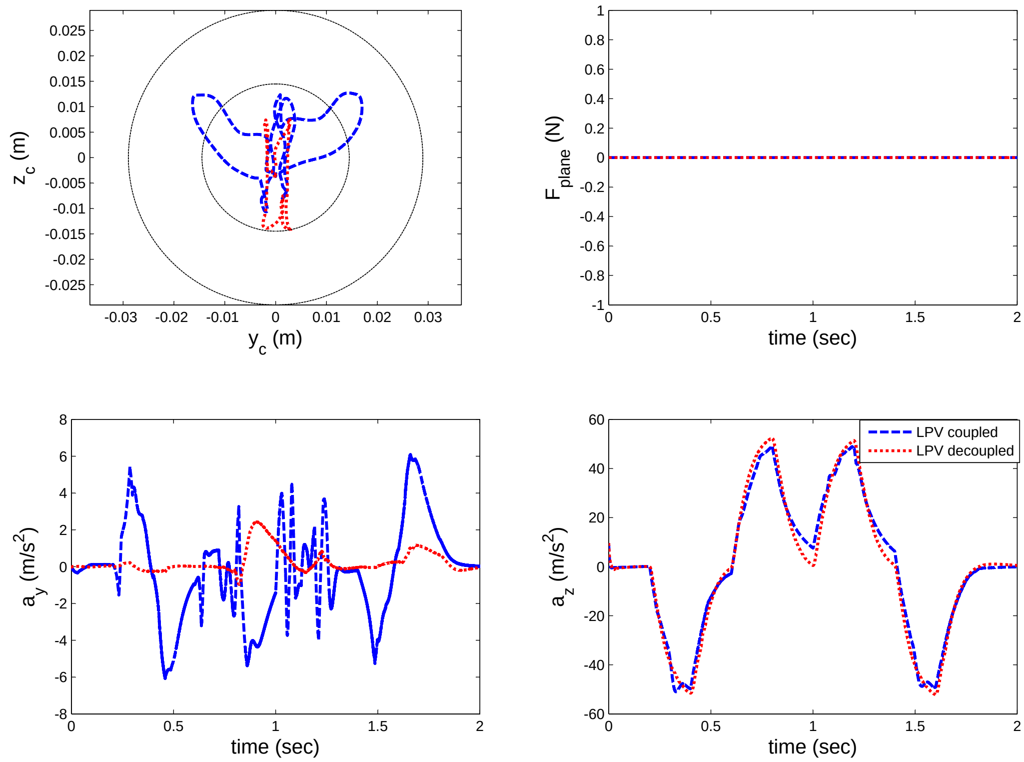


Figure 7.30: Bank-to-turn maneuver, simulation of cavity parameters of the vehicle.

The reason can be identified with further analysis. A short segment of the trajectory is shown on Figure 7.44, where the spikes on the response can be clearly identified as the control algorithm's response to the measured disturbance of planing. In the Logvinovich case, the force builds up slower, hence the control action input by the LPV controller is more gentle. To be able to account for the different planing description in the LPV synthesis the weighting prefilter $W_d$ must be tuned, hence it is important to identify the planing characteristics before scheduling underwater tests of the vehicle. Alternatively, the controller should be designed to be insensitive to the planing model since it is a large unknown.

## 7.5 Conclusion

This Chapter corresponds to design of LPV controllers and their analysis applied to complex, highly coupled systems including the HSSV. A method of blending LPV controllers

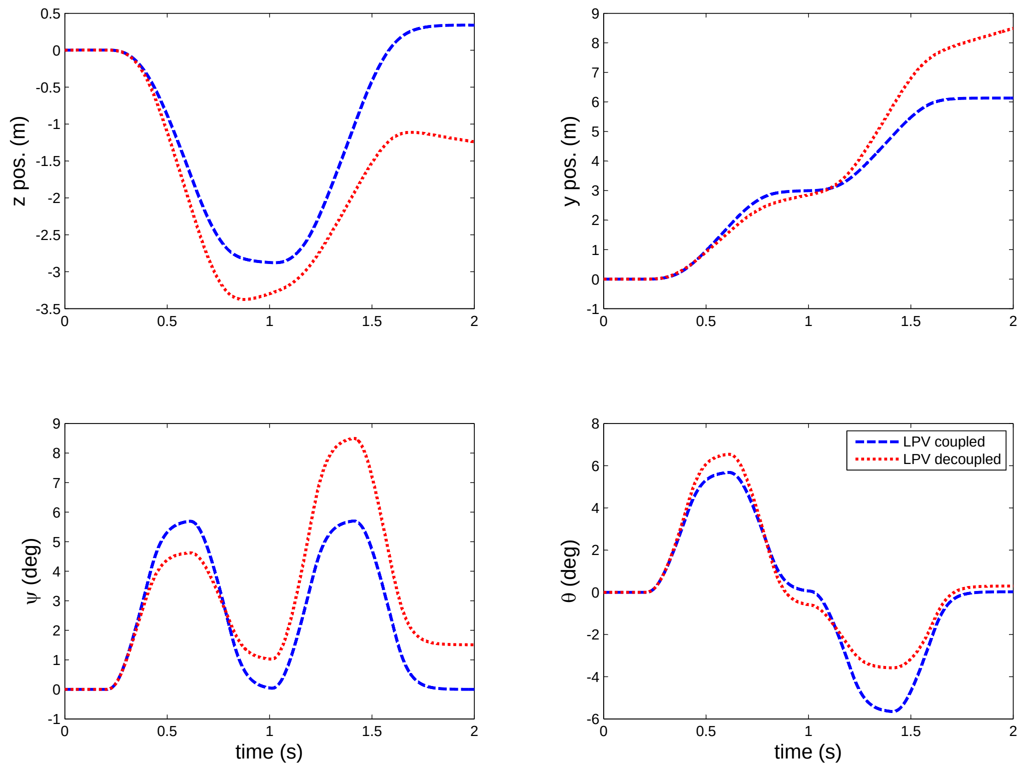


Figure 7.31: Skid-to-turn maneuver, simulation of position and orientation of the vehicle.

synthesized for smaller subspaces and simulation results presenting the benefits of the proposed control method are presented. Simulation results for inner loop control of the HSSV with two different LPV controllers using the rate-bounded synthesis method are compared. The results suggest that the benefits of using parameter-varying control even at the expense of computationally more intensive design makes the present method more appealing for controlling the future supercavitation vehicle. Several questions needs further analysis. The planing description strongly influence the vehicle behavior, hence it is important to determine the right approach to represent this force. Another interesting question, remains unsolved, is to optimize the vehicle configuration, including fins and vehicle/cavity dimensions for the mission. Lower drag can be achieved with smaller fins at the expense of lower maneuverability. Also, the vehicle length and radius are strongly coupled with the tendency of planing to occur, hence a lower diameter cavitator with larger fins might be a better solution to reduce the overall drag.

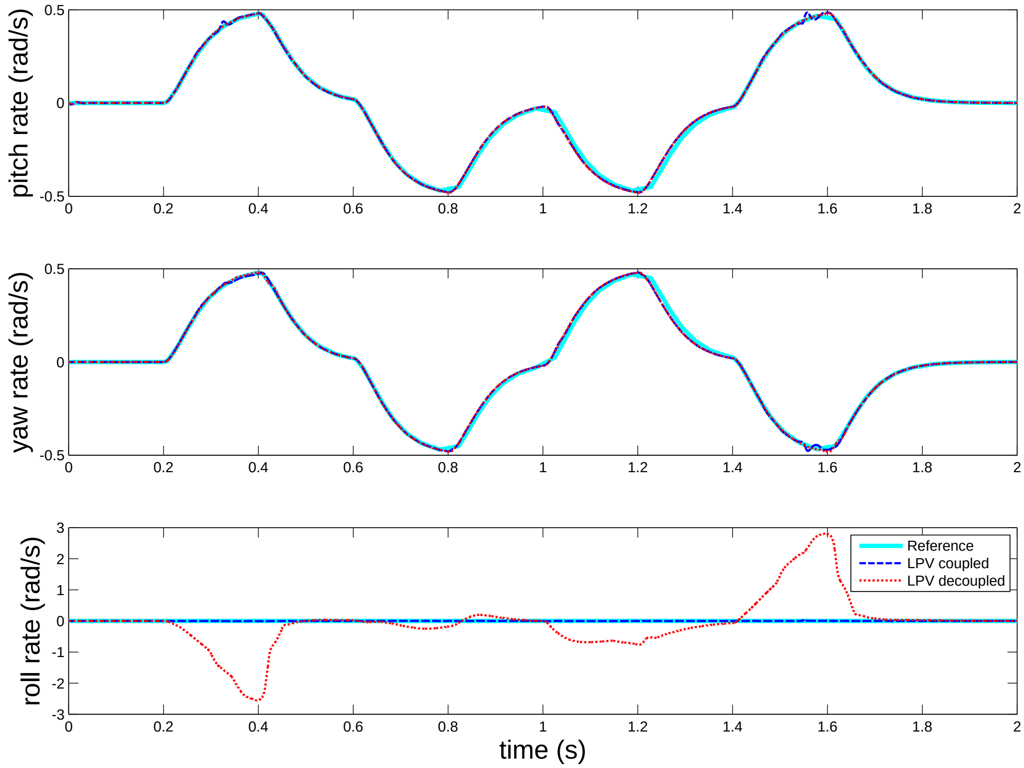


Figure 7.32: Skid-to-turn maneuver, simulation of angular rates of the vehicle.

The inner-loop control developed here serves as a basis for the homing/guidance problem. The architecture allows both bank-to-turn and skid-to-turn maneuvers to be executed. The higher level trajectory tracking control has the freedom to set the appropriate maneuver based on the actuator configuration and control authority.

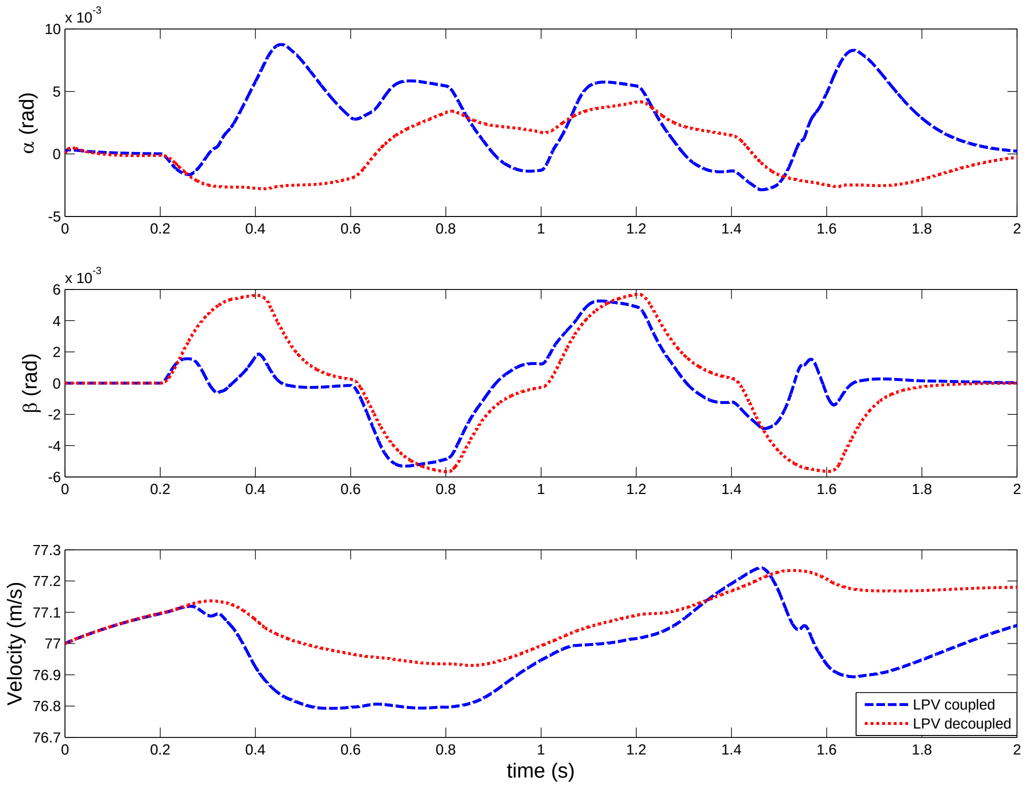


Figure 7.33: Skid-to-turn maneuver, simulation of aerodynamic angles of the vehicle.

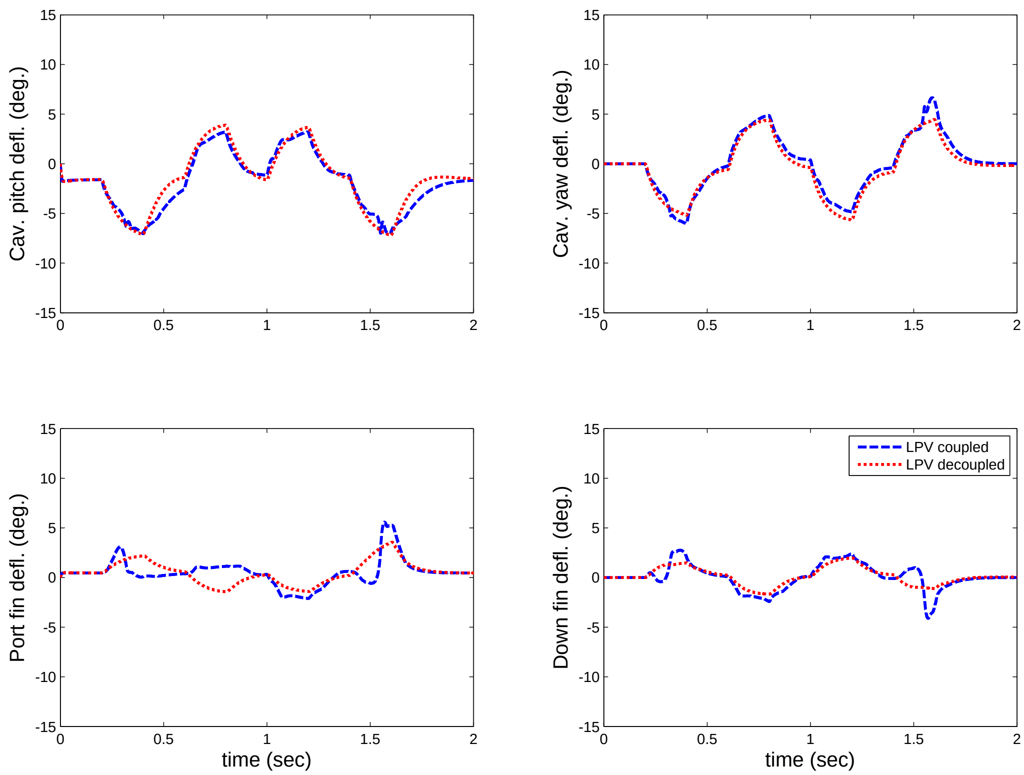


Figure 7.34: Skid-to-turn maneuver, simulation of control deflections of the vehicle.

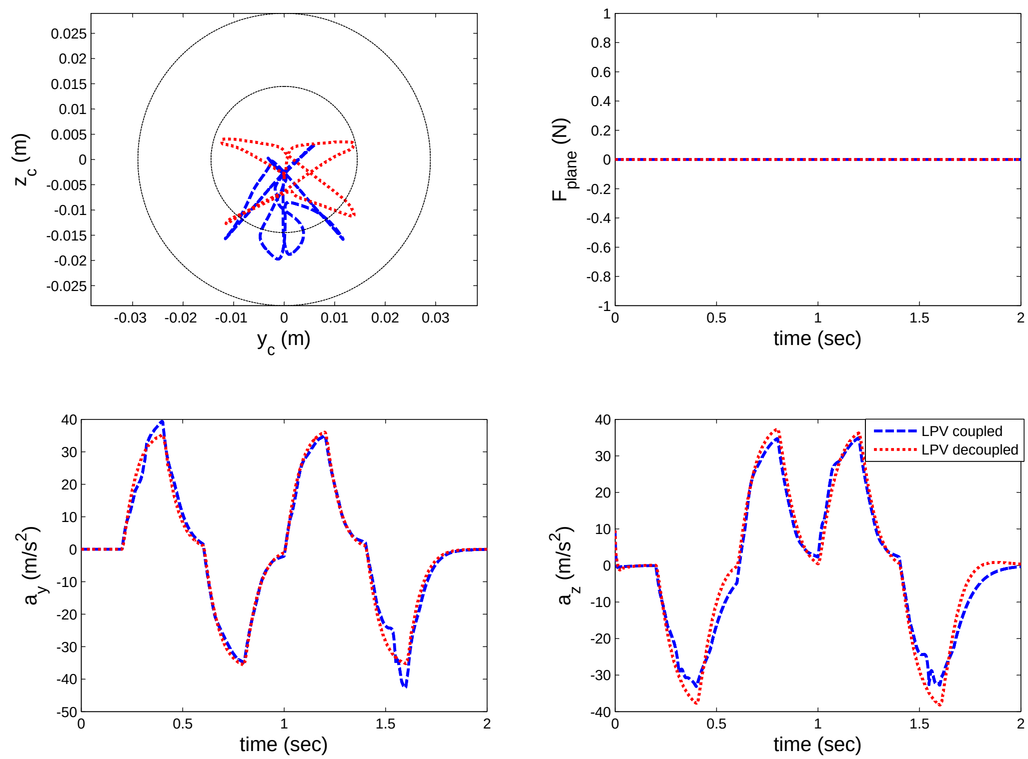


Figure 7.35: Skid-to-turn maneuver, simulation of cavity parameters of the vehicle.

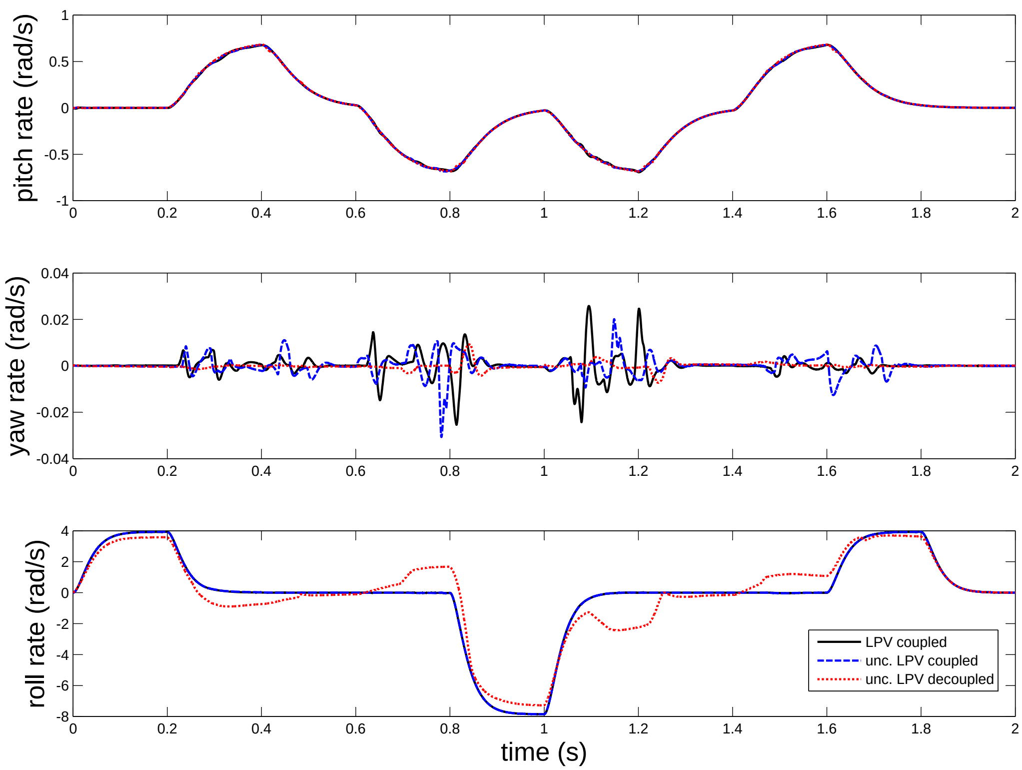


Figure 7.36: Impact of uncertainty, simulation of angular rates of the vehicle.

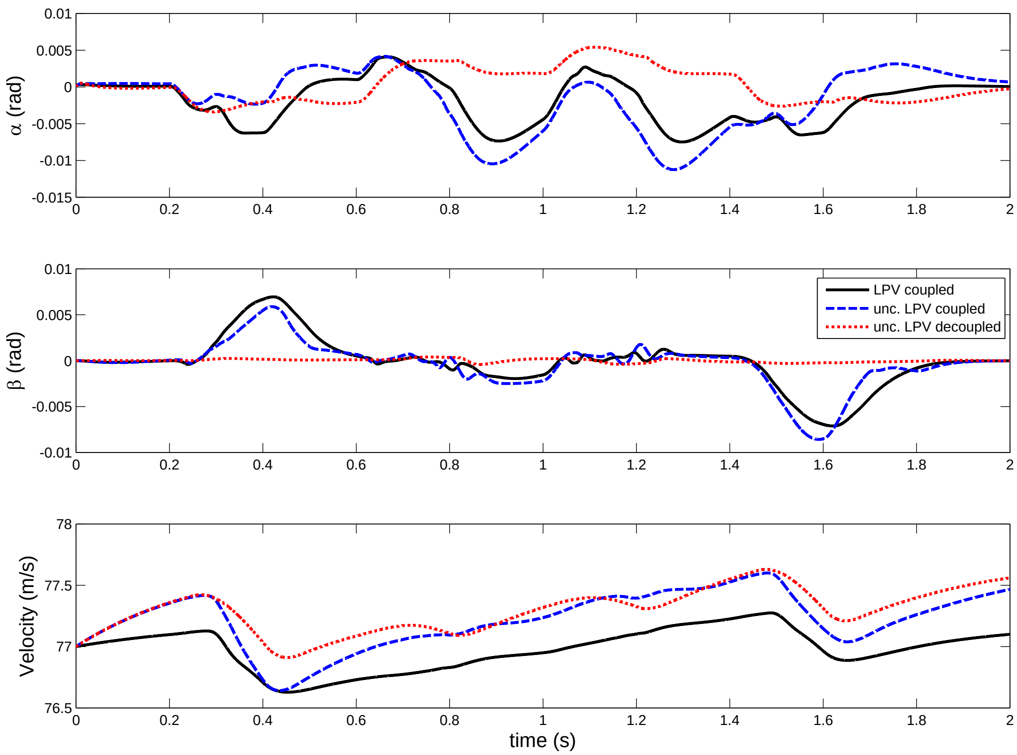


Figure 7.37: Impact of uncertainty, simulation of aerodynamic angles of the vehicle.

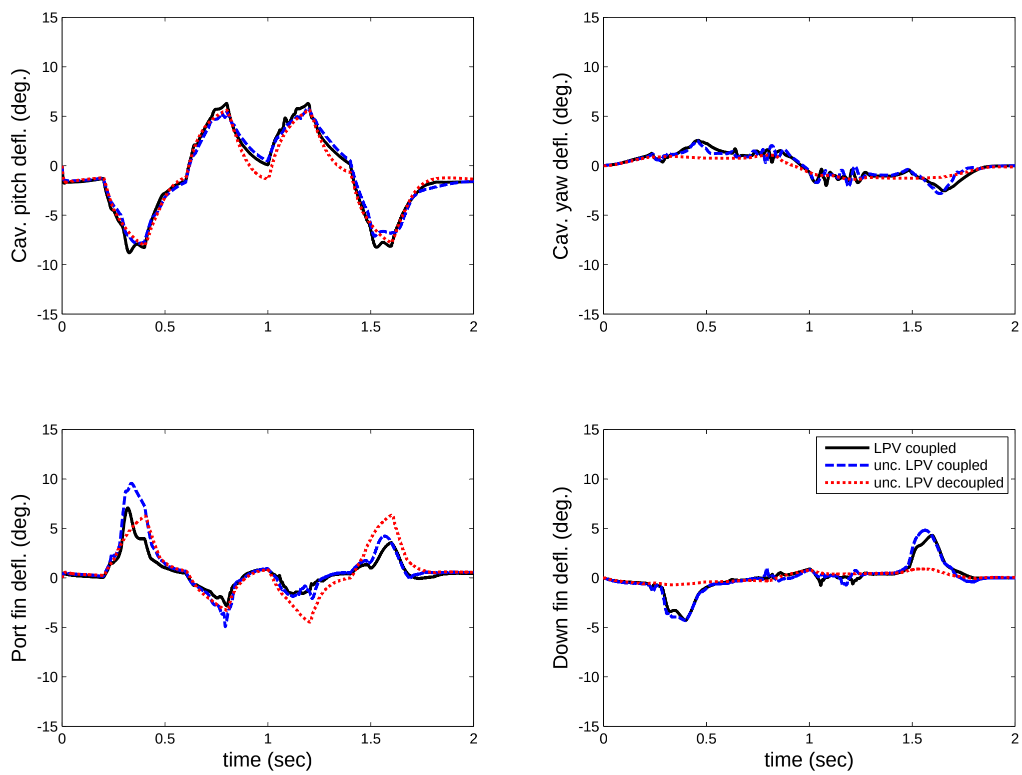


Figure 7.38: Impact of uncertainty, simulation of control deflections of the vehicle.

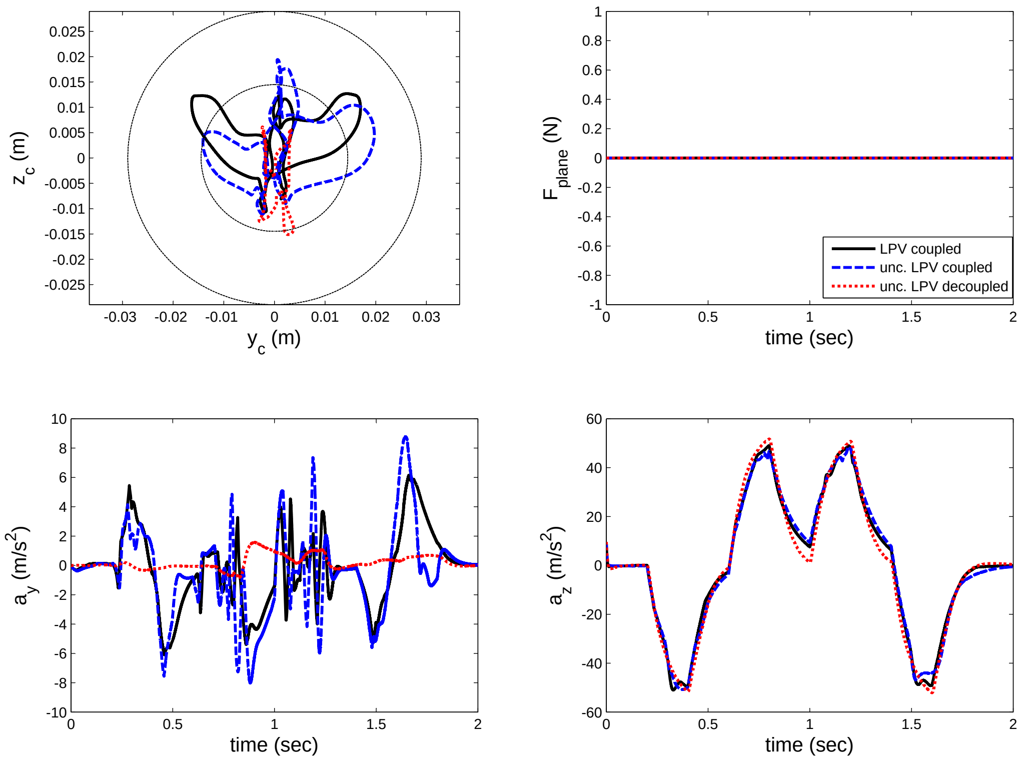


Figure 7.39: Impact of uncertainty, simulation of cavity parameters of the vehicle.

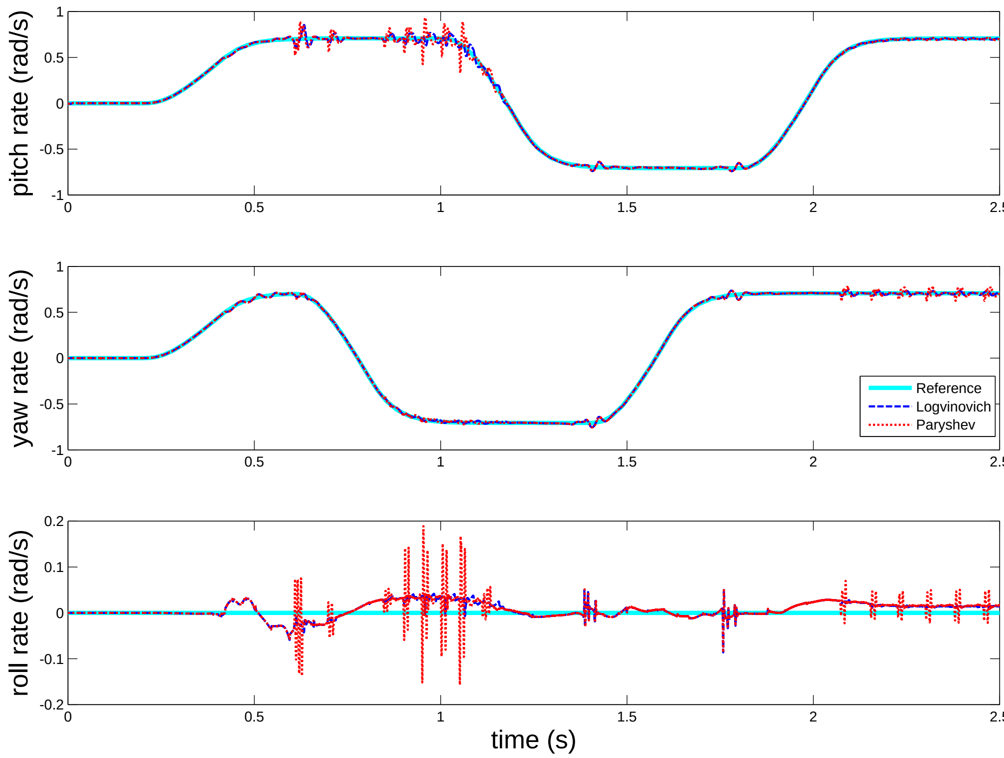


Figure 7.40: Impact of planing description, simulation of angular rates of the vehicle.

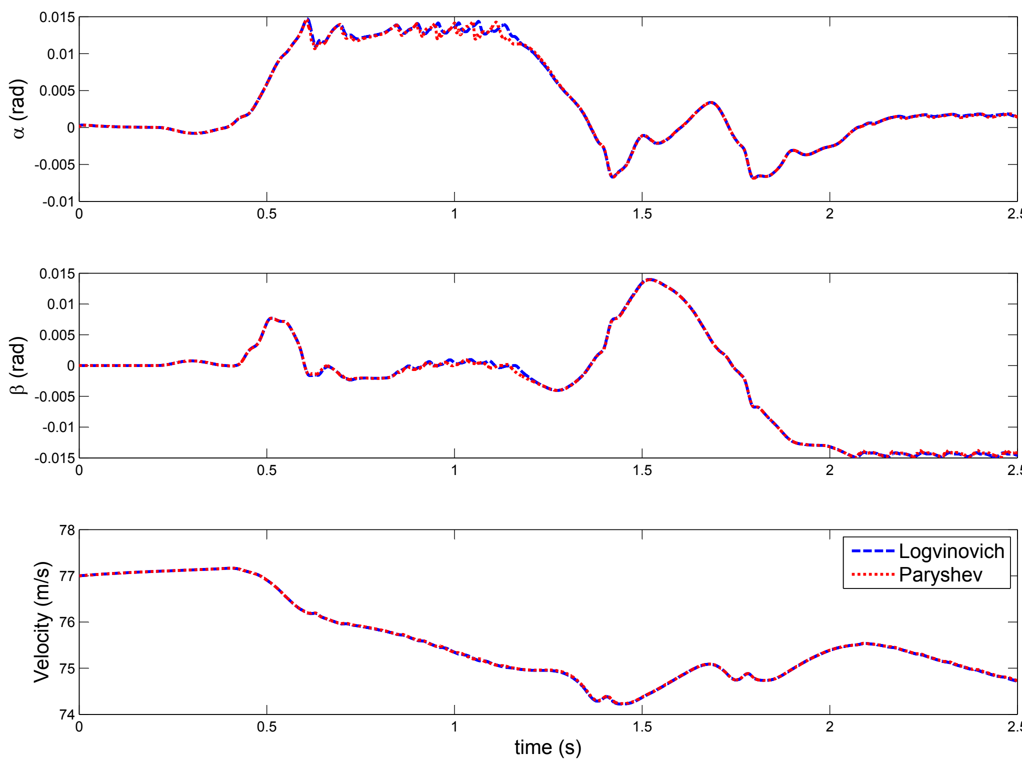


Figure 7.41: Impact of uncertainty, simulation of aerodynamic angles of the vehicle.

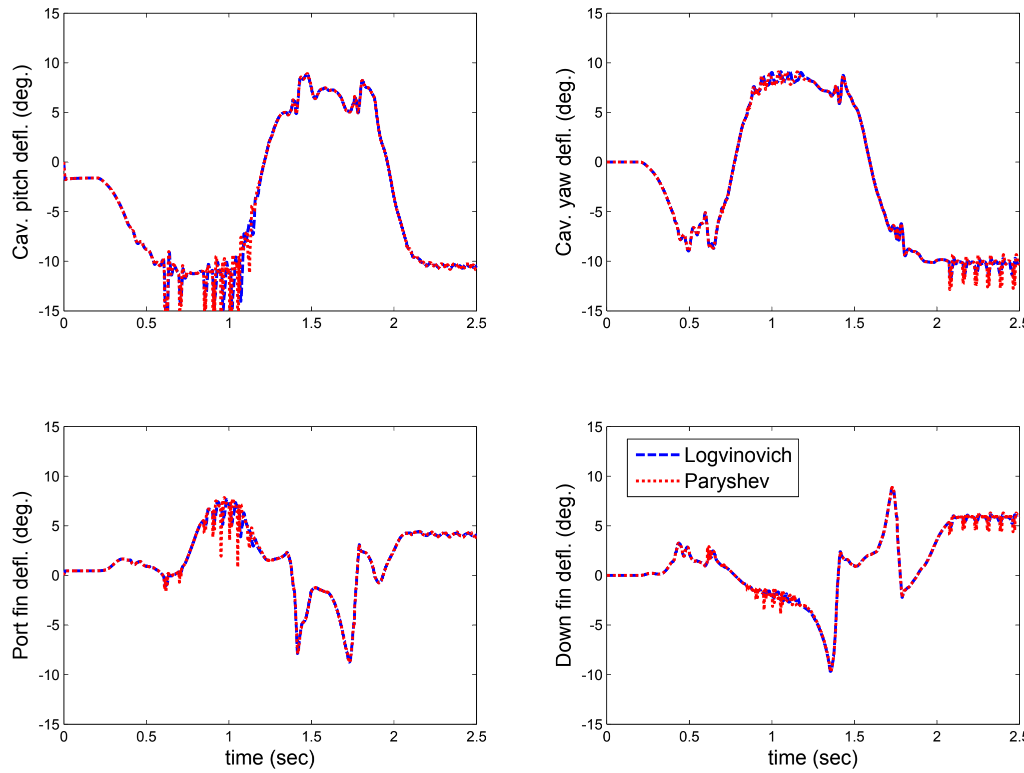


Figure 7.42: Impact of uncertainty, simulation of control deflections of the vehicle.

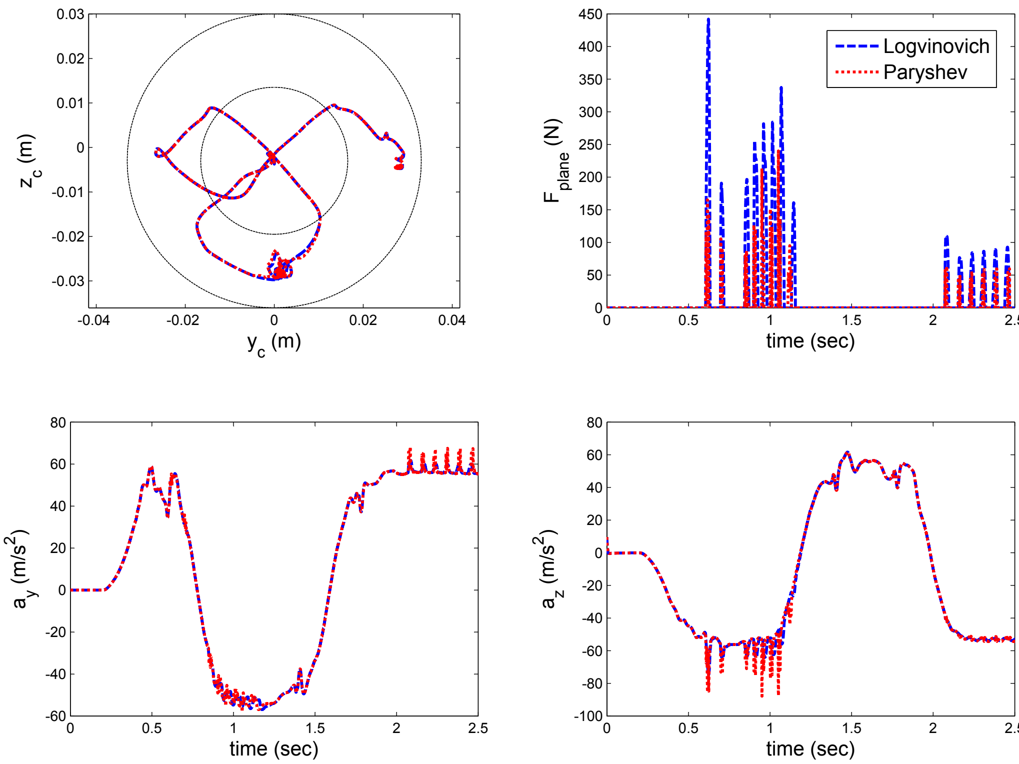


Figure 7.43: Impact of uncertainty, simulation of cavity parameters of the vehicle.

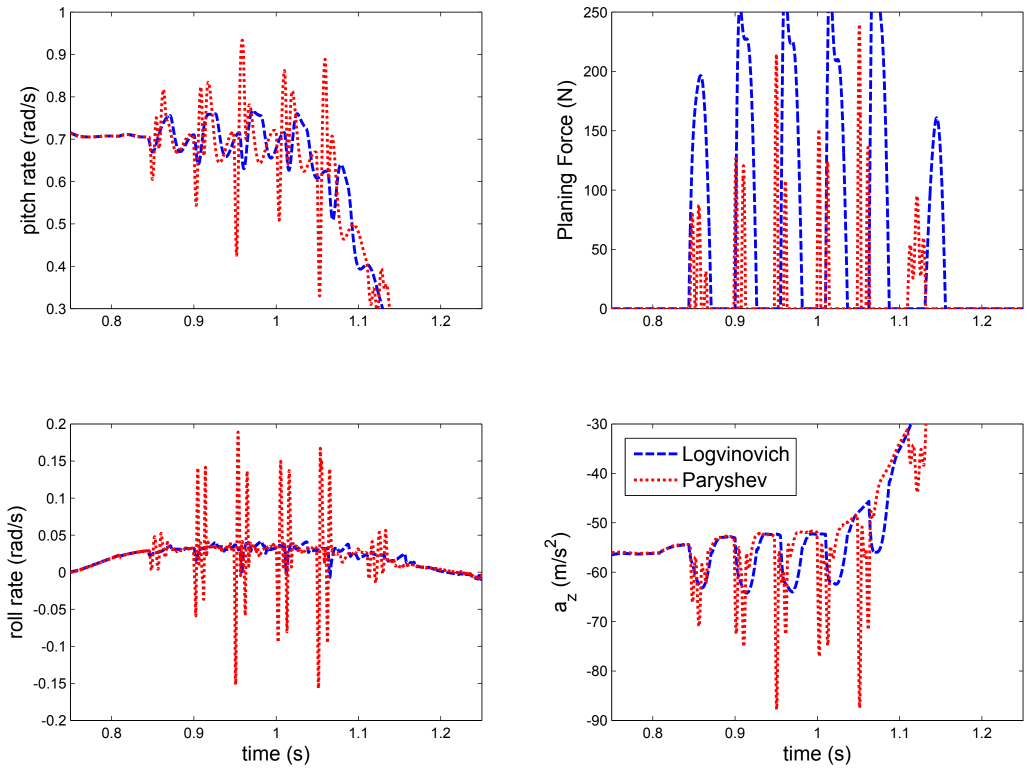


Figure 7.44: Impact of uncertainty, understanding the relation between planing and control.

# Chapter 8

# Conclusion

The dynamical modeling and control system development for the High-Speed Supercavitating Vehicle are discussed in this thesis. The focus is inner-loop control, stabilizing all body modes, which provides a platform for trajectory tracking guidance commands. The problem is solved in several steps building an overall understanding of the underlying problems.

Since model based control design approaches rely on the understanding of underlying dynamical behavior of the vehicle, an extensive analysis of the system behavior is performed first. The importance of gaining appropriate insight into the problem can be understood, as the unique characteristics of this vehicle type are relatively unknown, has not been sufficiently explored in the literature yet.

The equations-of-motion are derived from a control design point of view. The unique system dynamics are governed by nonlinear, time-delay differential equations. This model, including the memory effect associated with the cavity, written in state space form, provides a general framework for analysis and control design purposes. The structure allows rapid adaptation of the system parameters and governing equations due to modular structure, hence different vehicle configurations and the effect of system parameters on the dynamics, like planing models, can be better understood.

To understand the most fundamental properties of vehicle cavity interaction, including the memory effect, a simplified longitudinal model is derived for analysis. The analysis reveals the importance of cavity description, which using the Logvinovich independence principle is fundamentally different from the cavity descriptions described by only current states of the motion. The importance of uncertainty in cavity dimensions and physical properties of the vehicle are also investigated.

Feedback linearization is used to synthesize a controller for the switched delay-dependent problem. Controllability is guaranteed over the entire operating envelope, even on the time-delay dependent switching surface of the bimodal system, due to the control design approach. Position tracking in the longitudinal plane shows the importance of avoiding contact with the cavity surface. In the presence of planing the vehicle motion becomes oscillatory and the control actuators are often saturated. It is shown that this can lead to loss of stability. The destabilizing influence of planing is evident, since the control effectors can exert only a fraction of the peak planing force. This observation further strengthens the need for actively controlled fins on the vehicle, since the cavitator alone cannot guarantee planing free motion.

Using insight gained from the longitudinal dynamics and the associated control problem, a linear parameter-varying (LPV) description of the vehicle is derived for three dimensional flight. Local Jacobian linearizations are performed at coordinated maneuvers, along two parameter direction and serve as the baseline models for the LPV controller synthesis. The cavity offset parameters are correlated with the aerodynamic angles, providing scheduled steady-state approximation of the bubble dynamics. Analysis of the local Jacobian linearizations reveal a wide range of dynamics along the parameters. The stringent stability and performance requirements indicate that gain-scheduled controllers are necessary to achieve the desired objectives. Moreover, strong coupling observed between the pitch, roll and yaw channels point out the need for a multi-input multi-output control problem formulation, where the decoupled response can be stated explicitly.

Control synthesis is done using the LPV framework, which is particulary well suited to handle complex multi-input, multi-output systems, with nonlinear and parameter dependent dynamics. Robustness in the presence of model uncertainty is addressed as well as multiple performance objectives corresponding to handling qualities and desired requirements. Engineering insight, gained during the longitudinal control design and analysis of the open-loop dynamics, plays an important role in this approach.

Due to computational complexity the LPV control problem formulation for the 3-axis design cannot be obtained for the system in one step. Hence, two approaches are taken to synthesize MIMO, LPV controllers. The first scenario synthesizes decoupled , independent longitudinal and lateral directional controllers. These controllers, working in parallel on the nonlinear vehicle model, neglect the coupling between the lateral longitudinal and roll motion. The second approach, takes advantage of the coupling to synthesize a single controller for the lateral and longitudinal directional axis. A controller blending approach is used to synthesize the model following controller. The operating envelope is separated into eight overlapping regions. The blended LPV controller is obtained via combining the control synthesis solutions using parameter dependent weights on the eight overlapped regions.

The obtained LPV controllers are implemented on the nonlinear supercavitating vehicle model. Simulations are performed to determine the robustness and performance of the designs. The main difference between the performance of the coupled vs. decoupled LPV controllers is due to the neglected cross coupling. As expected, the coupled LPV controller handles complex maneuvers with more ease and copes with larger disturbances. The coupled LPV controller is also less sensitive to uncertainties in the system dynamics and able to provide robust tracking performance for a larger operating envelope. It is also demonstrated, that both parameter dependent controllers provide significant improvement in robustness and extend the limits of the operating envelope compared with traditional linear control approaches.

The main challenges, facing the real time implementation of the LPV controllers are related to the accuracy of the system description. First and foremost, no information is available on the quality of the sensors onboard the vehicle. Hence the assumption of full state measurement in the control design may be invalid. The other fundamental observation is related to the planing force, which has few different analytical descriptions, leading to distinct dynamical behavior, but experimental results does not verify the scope of these descriptions.

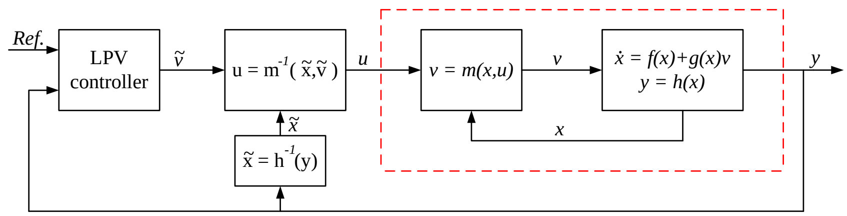


Figure 8.1: Control approach using decomposition of static non-affine mapping and affine dynamics

## 8.1 Further Work

The control synthesis results are obtained using local linear models. This might be a significant disadvantage, considering the wide range of transient responses the vehicle can exhibit. This problem might be eliminated by partitioning the system in a smart way. An important feature of the dynamics is that the controls are not entering the system in a linear manner, hence traditional control design techniques can not be applied straightforward to provide output tracking. This is often the case for highly nonlinear systems. For that reason it is showed by [66] that the output tracking problem can be solved in two steps. First the system is decomposed into a cascade connection of a state and control dependent nonlinear map followed by a smooth nonlinear dynamical system. More traditional nonlinear design techniques can then be applied, via an inverse of the nonlinear static map as shown in Figure 8.1. This approach is demonstrated to provide several advantages which is illustrated by the author on a passenger vehicle control problem. The results on switched, delay dependent systems obtained in Chapter 5 can be directly extended to this approach.

The future research direction in control of supercavitating vehicles has to focus on fusion between the outer loop guidance with the sensor suite onboard. The limited information obtained by the homing sensors, including the sonar, have to be aided by special maneuvers which help providing more information about the surrounding environment. The homing trajectories have to be properly designed, allowing the vehicle relative attitude to change with respect to the reference point, helping the observability of the underlying estimation problem.

In addition, the understanding of the trade-offs between control surface size, actuation rate and the possible operating envelope of the vehicle platform needs further effort. The initial acceleration phase, where tail-slapping might not be eliminated, is very sensitive to uncertainties in the system equations. A higher fidelity planing model with extensive experimental validation would be beneficial for analysis of the system and for the control design in the transition phase.

# Bibliography


[1] I. Kirschner, D. Kring, A. Stokes, and J. Uhlman, "Control strategies for supercavitating vehicles," *J Vibration and Control 8:219–242*, 2002.

[2] B. Vanek, J. Bokor, G. Balas, and R. Arndt, "Longitudinal motion control of a high-speed supercavitation vehicle," *Journal of Vibration and Control*, vol. 13, no. 2, pp. 159–184, 2007.

[3] S. Ashley, "Warp drive underwater," *Scientific American*, 2001.

[4] S. Ahn, "An integrated approach to the design of supercavitating underwater vehicles," Ph.D. dissertation, Georgia Institute of Technology, 2007.

[5] E. Euteneuer, "Further studies into the dynamics of a supercavitating torpedo," Master's thesis, University of Minnesota, 2003.

[6] M. Tulin, "Lecture notes on supercavitating flows," in *VKI Lecture Series on Supercavitating flows*, 2001.

[7] L. Rayleigh, "On the pressure developed in a liquid during the collapse of a spherical cavity," *Philos.Mag.*, pp. 94–98, 1917.

[8] R. Arndt, "Recent advances in cavitation research," *Advances in Hydroscience*, vol. 12, pp. 1–72, 1981.

[9] DARPA Advanced Technology Office, "Underwater express," in *BAA06-13 Proposer Information Pamphlet (PIP)*, 2005.

[10] K. Ng, "Overview of the onr supercavitating high-speed bodies program," in *AIAA GNC Conference*, Keystone,CO, 2006.

[11] Diehl-BGT Defence, "Underwater missile," in *http://www.diehl-bgt-defence.de*, 2007.

[12] Y. Shao, M. Mesbahi, and G. Balas, "Planing, switching and supercavitating flight control," *AIAA Guidance, Navigation and Control Conference, AIAA-2003-5724*, 2003.

[13] A. Goel, "Control strategies for supercavitating vehicles," Master's thesis, University of Florida, 2002.

[14] I. N. Kirschner, D. C. Kring, A. W. Stokes, N. E. Fine, and j. James S. Uhlman, "Control strategies for supercavitating vehicles," *Journal of Vibration and Control*, vol. 8, pp. 219–242, 2002.

[15] A. J. Kurdila, R. Lind, J. Dzielski, A. Jammulamadaka, and A. Goel, "Dynamics and control of supercavitating vehicles," Office of Naval Research Supercavitating High Speed Bodies Workshop, Tech. Rep., 2003.

[16] J. Dzielski and A. Kurdila, "A benchmark control problem for supercavitating vehicles and an initial investigation of solutions," *Journal of Vibration and Control*, vol. 9, no. 7, pp. 791–804, 2003.

[17] G. Lin, B. Rosenthal, E. Abed, and B. Balachandran, "Dynamics and control of supercavitating bodies," in *TECH2004*, 2004.

[18] J. Syrstad, M. Wosnik, G. Balas, and R. E. Arndt, "Control of a supercavity-piercing fin," in *58th Annual Meeting of the Division of Fluid Dynamics.* The American Physical Society, 2005.

[19] G. Logvinovich, "Hydrodynamics of free-boundary flows," *translated from the Russian (NASA-TT-F-658), US Department of Commerce, Washington D.C.*, 1972.

[20] Y. N. Savchenko, "Control of supercavitation flow and stability of supercavitating motion of bodies," in *VKI Lecture Series Supercavitating flows*, 2001.

[21] A. Vasin and E. Paryshev, "Immersion of a cylinder in a fluid through a cylindrical free surface," *Fluid Dynamics*, vol. 36, no. 2, pp. 169–177, 2001, translated from Russian.

[22] E. Paryshev, "The plane problem of immersion of an expanding cylinder through a cylindrical free surface of variable radius," in *International Summer Scientific School on High-Speed Hydrodynamics.* Cheboksary, Russia: National Academy of Sciences and Art of Chuvash Republic, 2002.

[23] D. Stinering, R. Cook, J. Dzielski, and R. Kunz, "High-speed supercavitating vehicles," in *AIAA Guidance Navigation and Control Conference*, Keystone,CO, 2007.

[24] R. Stengel, *Flight Dynamics.* Princeton University Press, 2004.

[25] H. Baruh, *Analytical Dynamics.* McGraw-Hill, 1999.

[26] P. Garabedian, "Calculation of axially symmetric cavities and jets," *Pacific Journal of Mathematics*, vol. 6, 1956.

[27] A. May, "Water entry and the cavity-running behavior of missiles," *SEAHAC TR 75-2*, 1975.

[28] H. Münzer and H. Reichardt, "Rotational symmetric source-sink bodies with predominantly constant pressure distributions," *ARE Translation 1/50 Aerospace Research Establishment, England*, 1950.

[29] R. Arndt, "From wageningen to minnesota and back: Perspectives on cavitation research," *Sixth International Symposium on Cavitation*, 2006, wageningen, The Netherlands.

[30] B. Vanek, J. Bokor, and G. J. Balas, "High-speed underwater vehicle control," in *AIAA Guidance, Navigation, and Control Conference, Keystone*, 2006.

[31] I. Kirschner, B. J. Rosenthal, and J. Uhlman, "Simplified dynamical systems analysis of supercavitating high-speed bodies," in *Fifth International Symposium on Cavitation (CAV2003)*, Osaka,Japan, 2003.

[32] G. Balas, J. Bokor, B. Vanek, and R. Arndt, *Control of Uncertain Systems: Modelling, Approximation, and Design*, ser. LNCIS. Springer-Verlag, 2006, ch. Control of High-Speed Underwater Vehicles, pp. 25–44.

[33] B. Vanek, J. Bokor, and G. J. Balas, "Theoretical aspects of high-speed supercavitation vehicle control," in *American Control Conference, Minneapolis*, 2006.

[34] S. Sastry, *Nonlinear Systems: Analysis, Stability and Control.* Springer, 1999.

[35] G. J. Balas, Z. Szabó, and J. Bokor, "Controllability of bimodal lti systems," in *IEEE International Conference on Control Applications*, 2006.

[36] M. Çamlibel, W. Heemels, and J. Schumacher, "On the controllability of bimodal piecewise linear systems," *In:Alur R, Pappas GJ (eds.) Hybrid Systems: Computationand Control LNCS 2993, Springer, Berlin, 250–264*, 2004.

[37] R. Brammer, "Controllability in linear autonomous systems with positive controllers," *SIAM J. Control, 10:329–353*, 1972.

[38] S. Saperstone and J. Yorke, "Controllability of linear oscillatory systems using positive controls," *SIAM J. Control, 9:253–262*, 1971.

[39] J. Doyle, K. Glover, P. Khargonekar, and B. Francis, "State-space solutions to standard $\mathcal{H}_2$ and $\mathcal{H}_\infty$ control problems," *IEEE Trans Auto Control 34:831–847*, 1989.

[40] D. MacFarlene and K. Glover, *Robust controller design using normalised coprime factor plant descriptions*, ser. Lecture Notes in Control and Information Sciences. Springer-Verlag, 1989, no. 138.

[41] G. Balas, R. Chiang, A. Packard, and M. Safanov, "Robust control toolbox," *MUSYN Inc. and The MathWorks, Natick MA*, 2005.

[42] D. Mayne, J. Rawlings, C. Rao, and P. Scokaert, "Constrained model predictive control: stability and optimality," *Automatica*, no. 36, pp. 789–814, 2000.

[43] J. Maciejowski, *Predictive Control with Constraints.* Prentice Hall, 2002.

[44] A. Bemporad, M. Morari, and N. Ricker, *Model Predictive Control Toolbox User's Guide.* The Mathworks, 2005.

[45] M. Safonov, *Modelling, Robustness and Sensitivity Reduction in Control Systems.* Springer-Verlag, 1987, ch. Imaginary-axis zeros in $\mathcal{H}_\infty$ optimal control, pp. 71–82.

[46] R. Arndt, G. Balas, and M. Wosnik, "Control of cavitating flows: A perspective," accepted for publication," *Japan Society of Mechanical Engineers International Journal, Japan*, 2005.

[47] S. Ganguli, A. Marcos, and G. Balas, "Reconfigurable lpv control design for boeing 747-100/200 longitudinal axis," in *Proceedings of the American Contol Conference, Anchorage*, 2002.

[48] J. Shin, "Worst-case analysis and linear parameter-varying gain-scheduled control of aerospace systems," Ph.D. dissertation, University of Minnesota, 2000.

[49] A. Marcos, "Linear parameter varying model of the boeing 747-100/200 longitudinal motion," Master's thesis, University of Minnesota, 2001.

[50] W. Rugh and J. Shamma, "Research on gain scheduling," *Automatica*, vol. 36, pp. 1401–1425, 2000.

[51] F. Wu, "Control of linear parameter varying systems," Ph.D. dissertation, University of California at Berkeley, 1995.

[52] G. Becker and A. Packard, "Robust performance of linear parametrically varying systems using parametrically-dependent linear feedback," *Systems and Control Letters*, vol. 23, no. 3, pp. 205–215, 1994.

[53] W. Tan, "Applications of linear parameter-varying control theory," Master's thesis, University of California at Berkeley, 1997.

[54] G. Papageorgiou, "Robust control system design: H-infinity loop shaping and aerospace applications," Ph.D. dissertation, University of Cambridge, 1998.

[55] B. Stevens and F. Lewis, *Aircraft Control and Simulation.* John Wiley & Sons, INC., 1992.

[56] J. Shamma and J. Cloutier, "Gain-scheduled missile autopilot design using linear parameter varying transformations," *Journal of Guidance,Control, and Dynamics*, vol. 16, no. 2, 1993.

[57] J. Taylor and A. Antoniotti, "Linearization algorithms for computer-aided control engineering," *IEEE Control*, vol. 13, no. 2, pp. 58–64, 1993.

[58] S. Skogestad and I. Postlethwaite, *Multivariable Feedback Control Analysis and Design*. Wiley, 2005.

[59] H. Khalil, *Nonlinear Systems*. Prentice Hall, 2002.

[60] W. Laboratory, "Applications of multivariable control theory to aircraft control laws: Multivariable control design guidelines," Flight Dynamics Directorate, Tech. Rep., 1996.

[61] J. Shamma and M. Athans, "Gain scheduling: Potential hazards and possible remedies," *Control Systems Magazine,IEEE*, vol. 12, pp. 101–107, 1992.

[62] A. Packard, "Gain scheduling via linear fractional transformations," *Systems and Control Letters*, vol. 22, pp. 79–92, 1994.

[63] K. Zhou, J. Doyle, and K. Glover, *Robust and Optimal Control*. Prentice Hall, 1996.

[64] L. Lee, "Identification and robust control of linear parameter-varying systems," Ph.D. dissertation, University of California, Berkeley, 1997.

[65] M. Chilali, P. Gahinet, and P. Apkarian, "Robust pole placement in lmi regions," in *Proceedings of the* $36^{th}$ *IEEE Conference on Decision and Control*, 1997.

[66] E. Grünbacher, "Robust inverse control of a class of nonlinear systems," Ph.D. dissertation, Johannes Kepler Universität Linz, 2005.